Interaction of light with quantum systems of different degrees of symmetry

Interaction of light with quantum systems of different degrees of symmetry

---

by
Piotr Gładysz
M.Sc. in Theoretical Physics
Nicolaus Copernicus University 2019

Dissertation submitted in total fulfillment
of the requirements for the degree of
Doctor of Physics

Doctoral School of Exact and Natural Sciences
Nicolaus Copernicus University in Toruń
Toruń, Poland

September 2024

Interaction of light with quantum systems
of different degrees of symmetry,

Author:
Piotr Gładysz

Supervisor:
Dr hab. Karolina Słowik

Doctoral School of Exact and Natural Sciences
Department of Quantum Mechanics
Faculty of Physics, Astronomy and Informatics
Nicolaus Copernicus University in Toruń

DEDICATION

To my wife, Joanna,
for being my support.

To my supervisor, Karolina,
for making me a scientist.

CONTENTS

ABSTRACT

This dissertation explores the interaction of light with quantum systems exhibiting different symmetry properties, specifically two-level polar systems without inversion symmetry, sustaining permanent dipole moments, and inversion-symmetric three-level systems. A comprehensive theoretical framework is developed to describe the dynamics of light-matter interactions in these systems as well as ensembles thereof, with a particular focus on the generation of low-frequency radiation and superluminal pulse propagation.

In two-level polar systems, the presence of permanent dipole moments introduces complex dynamical behaviors beyond traditional models. These include nonlinear Rabi oscillation frequencies with respect to the driving field amplitude and the generation of coherent low-frequency radiation. The proposed theory revisits and extends classical approaches, offering new insights into the role of permanent dipoles in light-matter interactions. By applying a series of unitary transformations, an analytically solvable model is derived, capturing the influence of the polarity of the system on its optical properties.

The thesis further investigates three-level systems, focusing on the phenomena of subluminal and superluminal propagation. A new, experimentally feasible scheme is proposed for achieving superluminal light propagation in rubidium vapors using a three-level ladder configuration by exploiting far-detuned two-photon transitions. This approach reduces pulse distortion and absorption compared to the scenarios exploiting single-photon transitions, enabling the observation of superluminal group velocities.

This research advances the understanding of light-matter interactions in both polar and nonpolar systems, offering new theoretical insights and proposing experimental scenarios in quantum optics. The findings have implications for coherent radiation generation, pulse propagation, and possible future applications in areas such as spectroscopy, imaging, and quantum communication.

STRESZCZENIE

Niniejsza rozprawa bada oddziaływanie światła z układami kwantowymi charakteryzowanymi różnym stopniem symetrii względem inwersji przestrzennej, w szczególności z dwupoziomowymi układami polarnymi z trwałymi momentami dipolowymi oraz z trójpoziomowymi układami o symetrii inwersyjnej. Opracowany w niej model teoretyczny opisuje dynamikę oddziaływania światła z materią zarówno w pojedynczych układach, jak i w ośrodkach cząsteczkowych, ze szczególnym uwzględnieniem generacji promieniowania o niskiej częstotliwości oraz propagacji impulsów z prędkościami nadświetlnymi.

W polarnych układach dwupoziomowych obecność trwałych momentów dipolowych w złożony sposób modyfikuje ich dynamikę, której opis stanowił wyzwanie w ramach tradycyjnych modeli. Należą do nich oscylacje Rabiego z częstością nieliniowo skalującą się z amplitudą pola działającego na układ, a także generacja spójnego promieniowania o niskiej częstotliwości. Zaproponowana teoria uogólnia klasyczne podejście, koncentrując się na roli trwałych momentów dipolowych w oddziaływaniu światło-materia. W jej ramach, po zastosowaniu serii przekształceń unitarnych uzyskano w pełni analityczny model uwzględniający wpływ polarności układu na jego właściwości optyczne.

Rozprawa bada również trójpoziomowe układy kwantowe, koncentrując się na zjawiskach podświetlnej i nadświetlnej propagacji. Zaproponowano nowy, możliwy do wdrożenia w eksperymencie schemat uzyskania tego typu propagacji światła w parach rubidu z wykorzystaniem konfiguracji poziomów energetycznych w formie trójpoziomowej drabinki. Dzięki zastosowaniu daleko odstrojonego dwufotonowego przejścia, możliwe jest zredukowanie zniekształceń impulsu i ograniczenie absorpcji w stosunku do scenariuszy eksperymentalnych wykorzystujących przejścia jednofotonowe, co umożliwia obserwację nadświetlnych prędkości grupowych.

Badania te poszerzają zrozumienie oddziaływania światła z materią zarówno w układach polarnych, jak i niepolarnych poprzez nowe podejścia teoretyczne oraz propozycje realizacji eksperymentalnych w optyce kwantowej. Wyniki mogą mieć istotne znaczenie dla realizacji scenariuszy generacji spójnego promieniowania, propagacji impulsów oraz możliwych przyszłych zastosowań w takich dziedzinach jak spektroskopia, obrazowanie i komunikacja kwantowa.

PUBLICATIONS

The articles considered as a part of the dissertation:

- A1 Piotr Gładysz, Karolina Słowik,
  "**Rabi frequency for polar systems interacting with light**",
  arXiv:2408.13011 (2024).
- A2 Piotr Gładysz, Piotr Wcisło, Karolina Słowik,
  "**Propagation of optically tunable coherent radiation in a gas of polar molecules**",
  Scientific Reports 10 (1), 17615 (2020).
- A3 Piotr Gładysz, Szymon Pustelny, Karolina Słowik,
  "**Superluminal light propagation in a three-level ladder system**",
  Scientific Reports 14 (1), 15151 (2024).

The articles not included in the dissertation:

- B1 Evgenia Rusak, Jakob Straubel, Piotr Gładysz, Mirko Göddel, Andrzej Kędziorski, Michael Kühn, Florian Weigend, Carsten Rockstuhl, Karolina Słowik,
  "**Enhancement of and interference among higher order multipole transitions in molecules near a plasmonic nanoantenna**",
  Nature Communications 10 (1), 5775 (2019).
- B2 Saeid Izadshenas, Piotr Gładysz, Karolina Słowik,
  "**Hybrid graphene-silver nanoantenna to control THz emission from polar quantum systems**",
  Optics Express 31 (18), 29037-29050 (2023).

1

INTRODUCTION

The interaction of light with matter is a fundamental phenomenon that underpins many fields of modern research, from quantum optics to materials science. This work focuses on exploring how light interacts with systems possessing different degrees of symmetry, specifically two-level systems with broken inversion symmetry (polar systems) sustaining permanent dipole moments (PDMs) and inversion-symmetric three-level systems. The propagation of electromagnetic pulses through the ensembles of such systems provides plenty of interesting phenomena such as those discussed in this thesis: generation of low-frequency radiation and superluminal group velocities.

In two-level systems, light-matter interaction is typically described by well-established models exploiting the electric-dipole and rotating-wave approximations. Historically, the role of permanent dipole moments in these interactions was considered minimal, leading to minor frequency shifts. However, attempts to describe the impact of the polar systems on evolution were made in the approximated form quite early, e.g., by G. F. Thomas [1] or W. J. Meth and collaborators [2, 3]. More recent research has revealed that these systems exhibit far more complex dynamical behaviors. O. Kibis et al. described analytically two-level polar system interacting with light in the wave function formalism [4] providing evidence for the low-frequency radiation generation, and later his work was extended to the tailored photonic environments such as an ensemble of quantum dots [5], gases [6] or cavities [7, 8]. In works [9–11] Meath et al. again investigated the polarity, now in the context of enhancement of two-photon interactions, while M. Koppenhöfer et al. [12] and M. Antón et al. [13] focused on light squeezing. Spatial asymmetry may have a significant impact on the optoelectronic properties of double quantum dots, including the spectral position of optical resonances [14]. PDMs also facilitate stimulated Raman adiabatic passage (STIRAP) [15, 16], establishing strong long-range interactions [17], population inversion [18] and many more [19–21]. These unique properties make polar systems highly intriguing for both theoretical studies and practical applications. The growing interest is fueled by the potential for generating coherent radiation at tunable frequencies, enabling new possibilities in fields such as spectroscopy, imaging, quantum information processing, and communication.

In this thesis, a comprehensive theoretical framework addressing this rich evolution is proposed which, through a series of unitary transformations, leads to an analytically solvable model. The model may involve approximations neglecting processes at high-order resonances, yet it well describes the dynamics in a physically relevant range of parameters. This result generalizes the analytical solution of the Rabi model without PDMs, obtained recently by D. Braak [22]. It additionally provides analytical expressions for observables such as the rich fluorescence spectrum sustained by polar systems. The analysis is then extended to polar molecule ensembles. The model requires rewriting the established Bloch–Maxwell set of equations beyond the standard approximations. Applied to a specific example system of LiH molecules, it extends the prediction of Kibis et al. regarding the emission of low-frequency radiation by polar molecules, shown to be coherent which may give rise to an overall stronger signal.

In addition to two-level systems, the behavior of light interacting with three-level systems opens a pathway to understanding more complex dynamics like electromagnetically induced transparency (EIT), slow light, and superluminal propagation. The investigation of phase and group velocities of pulse propagating in media has been a subject of extensive research since theoretical predictions of superluminal propagation sparked widespread interest. According to A. Sommerfeld and L. Brillouin [23], the idea of group velocity appeared already in 1839, while became broadly known due to the Lord Rayleigh book published in 1877 (first edition) [24] and later articles. Early debates as shown in books [23, 25], tied to the implications for Einstein's theory of relativity and many have claimed that the pulse distortion provides no physical significance of group velocity. However, in 1970 C. G. B. Garrett et. al showed that the output pulse can have nearly the same shape as an incoming one [26]. This later spurred the development of theoretical and experimental investigations of variety of electromagnetic pulse propagation aspects: slow light in the EIT process [27–31], fast light [32, 33], and even negative group velocities [34, 35].

The research described in the final part of this thesis builds on these foundational studies by proposing a new, experimentally feasible scheme for superluminal propagation using a three-level ladder configuration. This setup exploits the interaction between a control and probe beam in a far-detuned two-photon transition regime, allowing the anomalous dispersion necessary for superluminal behavior to appear. This project was triggered by heretofore unpublished experimental results conducted under the direction of Sz. Pustelny (Jagiellonian University, Cracow). Their results suggested superluminal propagation of probe pulses in suitably prepared rubidium vapors. This phenomenon was unexpected at the time, and the analysis eventually confirmed the possibility of superluminal propagation in the studied system. The propagation conditions in model three-level systems with different energy configurations were characterized in detail, and a scheme for superluminality without population inversion or nonlinearities was identified by exploiting the two-photon resonance regime.

Through these investigations, this work examines two core phenomena: the rich physics of light interactions with polar two-level systems, including low-frequency radiation generation, and superluminal propagation in nonpolar three-level systems. By focusing on these two distinct yet related systems, the thesis provides new insights into how symmetry in light-matter interactions influences coherent radiation generation and pulse propagation.

The dissertation is organized into several chapters that build upon the foundational theory of light-matter interaction, focusing on both two-level and three-level systems, as outlined below:

Chapter 2: Light-Matter Interaction Theory.
This is the most comprehensive part that presents the theoretical framework for understanding how light interacts with quantum systems on the basic level. Beginning with two- and three-level systems, several topics are covered: the electric-dipole approximation, non-dissipative and dissipative Bloch equations, the difference between energy level configurations, and the role of permanent dipole moments. Next, the ensembles of these systems are taken into account with discussed: dissipative Bloch–Maxwell equations, slowly varying envelope approximation (SVEA), and group velocity of pulses. These models provide a foundation for the subsequent analysis of more complex systems and act as an introduction to the articles presented in the following chapters.

Chapter 3: Permanent Dipole Moments in Two-Level Systems.
This chapter presents articles A1 and A2, focusing on the specific case of two-level systems with broken inversion symmetry, highlighting the effects of permanent dipole moments on the interaction with light. The generation of low-frequency radiation in such systems is a central topic of discussion, along with the implications for practical aspects of coherent radiation generation.

Chapter 4: Sub- and Superluminal Propagation in Three-Level Systems.
The interaction of light with three-level systems, specifically in the context of subluminal and superluminal pulse propagation, is explored in this chapter with the article A3. These phenomena arise in media with specific three-level configurations, leading to unique propagation effects that challenge the conventional understanding of light speed.

Chapter 5: Summary.
The final chapter summarizes the key findings of the thesis, with a focus on the novel effects arising from the interaction of light with systems of different degrees of symmetry. Potential future directions for research are also discussed, particularly in the realm of practical applications of the findings.

2

LIGHT-MATTER INTERACTION THEORY

This chapter introduces the background that facilitates the understanding of the articles comprising this thesis and the connections between them.

The first section describes quantum systems with two energy levels that interact with an external electromagnetic field. The theory explains the evolution of the population for both isolated and dissipative system cases. Ultimately, an additional interaction involving permanent dipole moments provided by polar systems is introduced.

The second section naturally continues by adding a third energy level to the system, which may significantly affect the system's behavior under certain conditions. All three possible level configurations are described, followed by a theory similar to that of the previous section.

The third section further extends the topic by using previously described systems as building blocks of the media. Specifically, ensembles of noninteracting systems are considered in a semi-classical description. Here, a theory of electric pulse propagation in such media is also introduced. Finally, the phase and group velocities, as well as sub- and superluminal propagation of such pulses are discussed.

2.1 TWO-LEVEL SYSTEMS

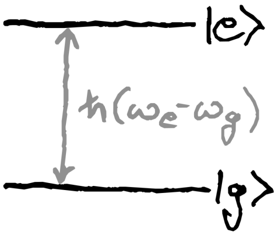

Figure 2.1: Schematic representation of the two-level system.

The simplest, yet scientifically interesting quantum system one can imagine consists of just two energy levels. Although this model might appear overly simplistic in some contexts, numerous research findings have demonstrated that it often aligns well with experimental results [36–39]. Notably, resonant interaction between matter and electromagnetic fields can frequently be described using this framework.

In nature, there are many exact and approximate realizations of two-level systems. The most pertinent to this work involves coupling electromagnetic radiation with two specific energy levels from a more complex system, such as an atom or molecule. By carefully adjusting the laser frequency to the energy levels of the system, and using selection rules, it is possible to focus solely on the two levels of interest.

Mathematically, such a system can be described using the tools provided by quantum mechanics. In this case, both levels, which in this thesis are considered nondegenerate, correspond to linearly independent vectors in a two-dimensional Hilbert space. The system's energy is described by the energy operator, the Hamiltonian. Throughout this thesis, Dirac notation is used, where the excited (upper-energy) and the ground (lower-energy) states are represented by kets $|e\rangle$ and $|g\rangle$, with corresponding energies $\hbar\omega_e$ and $\hbar\omega_g$ (Fig. 2.1), where $\hbar$ is the reduced Planck constant. It is convenient to use these states as a basis for this Hilbert space as they are orthonormal $\big(\langle e|g\rangle = 0, \langle e|e\rangle = \langle g|g\rangle = 1\big)$. The Hamiltonian of the system, expressed in this basis is

$$\hat{H}_{\text{sys}} = \hbar\omega_e |e\rangle\langle e| + \hbar\omega_g |g\rangle\langle g| \,. \tag{2.1}$$

On the other hand, the system's population is described by the density matrix of the form

$$\hat{\rho}_{\text{sys}} = \rho_{ee} |e\rangle\langle e| + \rho_{eg} |e\rangle\langle g| + \rho_{ge} |g\rangle\langle e| + \rho_{gg} |g\rangle\langle g| \,, \tag{2.2}$$

where $\rho_{ij} \equiv \rho_{ij}(t)$, $i, j \in \{e, g\}$ are the time-dependent coefficients describing the evolution. The terms $\rho_{ee,gg}$ contain information about the population in the excited and ground states, respectively. Hence, in the case of no leakage of population trace $\text{Tr}\big(\hat{\rho}_{\text{sys}}\big) = 1$, the probability of finding the system in any state is 1. The $\rho_{eg,ge}$ terms describe the coherence in the system, which is a purely quantum property, as setting these values to zero indicates that the system is just a classical mixture of states. Due to the Hermitian character of the operators $\hat{\rho}_{\mathrm{sys}}^{\dagger} = \hat{\rho}_{\mathrm{sys}}$, these coefficients are connected by the equality $\rho_{eg} = \rho_{ge}^{\star}$, where $\cdot^{\star}$ describes complex conjugation.

The description of the two-level system in the eigenstates basis (by the operators $|i\rangle\langle j|$, for $i, j \in e, g$) is simple and intuitive. Nevertheless, it is sometimes more convenient to use their linear combinations known as Pauli matrices:

$$\begin{aligned}
\hat{I} &= |e\rangle\langle e| + |g\rangle\langle g|\,, \\
\hat{\sigma}_z &= |e\rangle\langle e| - |g\rangle\langle g|\,, \\
\hat{\sigma}_x &= |g\rangle\langle e| + |e\rangle\langle g|\,, \\
\hat{\sigma}_y &= \mathrm{i}\left(|g\rangle\langle e| - |e\rangle\langle g|\right),
\end{aligned}$$

where i is an imaginary unit. However, the most common basis includes combinations of the above operators, where instead of $\hat{\sigma}_x$ and $\hat{\sigma}_y$, so-called flip operators are used

$$\begin{aligned}
\hat{\sigma}^{+} &= |e\rangle\langle g| = \frac{1}{2}\left(\hat{\sigma}_x + \mathrm{i}\hat{\sigma}_y\right), \\
\hat{\sigma}^{-} &= |g\rangle\langle e| = \frac{1}{2}\left(\hat{\sigma}_x - \mathrm{i}\hat{\sigma}_y\right).
\end{aligned}$$

The name of these operators describes their property as they "flip" one eigenstate vector to the other: $\hat{\sigma}^{+}|g\rangle = |e\rangle\langle g|g\rangle = |e\rangle$, $\hat{\sigma}^{-}|e\rangle = |g\rangle\langle e|e\rangle = |g\rangle$.

In this thesis, the basis $\{\hat{I}, \hat{\sigma}_z, \hat{\sigma}^{+}, \hat{\sigma}^{-}\}$ is used. Hence, the Hamiltonian (2.1) has a form

$$\hat{H}_{\mathrm{sys}} = \frac{1}{2}\hbar\underbrace{\left(\omega_e - \omega_g\right)}_{\omega_{eg}}\hat{\sigma}_z + \frac{1}{2}\hbar\left(\omega_e + \omega_g\right)\hat{I}, \tag{2.3}$$

and the density operator (2.2) takes the form

$$\hat{\rho}_{\mathrm{sys}} = \frac{1}{2}\left(\rho_{ee} - \rho_{gg}\right)\hat{\sigma}_z + \rho_{eg}\hat{\sigma}^{+} + \rho_{ge}\hat{\sigma}^{-} + \frac{1}{2}\underbrace{\left(\rho_{ee} + \rho_{gg}\right)}_{=\mathrm{Tr}\left(\hat{\rho}_{\mathrm{sys}}\right)=1}\hat{I}. \tag{2.4}$$

2.1.1 *Isolated, non-interacting system*

To calculate the evolution of the population, i.e., the time dependency of the density operator coefficients, the von Neumann equation [40] is required

$$\mathrm{i}\hbar\frac{\mathrm{d}}{\mathrm{d}t}\hat{\rho}(t) = \left[\hat{H}(t), \hat{\rho}(t)\right], \tag{2.5}$$

which is a general formula for any Hamiltonian $\hat{H}(t)$ (even time-dependent), and density operator describing any isolated quantum-mechanical system $\hat{\rho}(t)$. Here, $\mathrm{d}/\mathrm{d}t$ denotes the time derivative, while the $[\cdot,\cdot]$ bracket denotes the commutator of two operators. For pure states, this equation is fully equivalent to the Schrödinger equation.

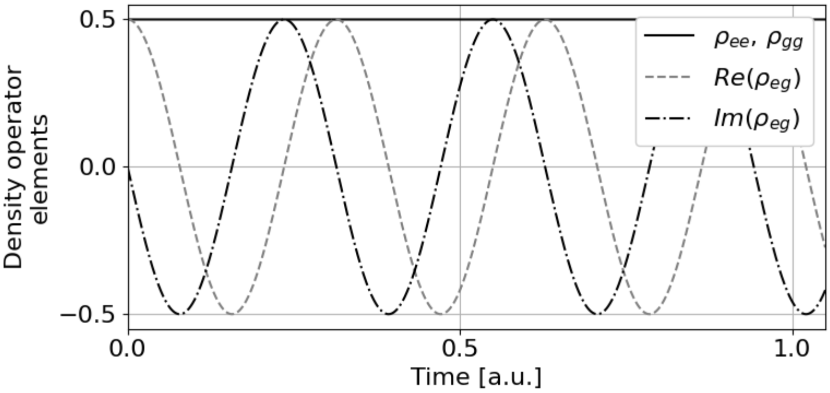

Figure 2.2: Illustrative presentation of the evolution of the density operator elements for the isolated two-level system initially prepared in the superposition of excited and ground states such that $\rho_{ee}(0) = \rho_{gg}(0) = 1/2$, and $\rho_{eg}(0) = 1/2$. The solid line corresponds to the excited state occupation, while the dashed and dot-dashed lines show the real and imaginary parts of the coherence in the system, respectively. All the units are arbitrarily chosen (a.u.).

For the case of a non-interacting two-level system described by (2.3), and (2.4), the von Neumann equation (2.5) has an explicit form of

$$\begin{aligned}
&\mathrm{i}\hbar\frac{\mathrm{d}}{\mathrm{d}t}\hat{\rho}_{\mathrm{sys}}(t) = \left[\hat{H}_{\mathrm{sys}}, \hat{\rho}_{\mathrm{sys}}(t)\right] \\
&= \frac{1}{2}\hbar\omega_{eg}\left(\frac{1}{2}\left(\rho_{ee}(t)-\rho_{gg}(t)\right)\underbrace{\left[\hat{\sigma}_z,\hat{\sigma}_z\right]}_{=0}+\rho_{eg}(t)\left[\hat{\sigma}_z,\hat{\sigma}^+\right]+\rho_{ge}(t)\left[\hat{\sigma}_z,\hat{\sigma}^-\right]+\frac{1}{2}\underbrace{\left[\hat{\sigma}_z,\hat{I}\right]}_{=0}\right) \\
&+\frac{1}{2}\hbar\left(\omega_e+\omega_g\right)\left(\frac{1}{2}\left(\rho_{ee}(t)-\rho_{gg}(t)\right)\underbrace{\left[\hat{I},\hat{\sigma}_z\right]}_{=0}+\rho_{eg}(t)\underbrace{\left[\hat{I},\hat{\sigma}^+\right]}_{=0}+\rho_{ge}(t)\underbrace{\left[\hat{I},\hat{\sigma}^-\right]}_{=0}+\frac{1}{2}\underbrace{\left[\hat{I},\hat{I}\right]}_{=0}\right) \\
&= \frac{1}{2}\hbar\omega_{eg}\left(\rho_{eg}(t)\left[\hat{\sigma}_z,\hat{\sigma}^+\right]+\rho_{ge}(t)\left[\hat{\sigma}_z,\hat{\sigma}^-\right]\right).
\end{aligned}$$

The equation simplifies significantly, as the terms with the identity operator do not contribute to the evolution of the system because this operator always commutes with any other one and the time derivative of a constant value is zero. This is a general behavior, so such terms can be entirely omitted directly in the Hamiltonian and density operators in the first place, which will be the approach taken for the rest of this thesis. Furthermore, the energies of the levels in the system ($\hbar\omega_e$, and $\hbar\omega_g$) do not appear in the equation; instead, the energy difference $\hbar\omega_{eg}$ is an important parameter.

An easily obtainable commutation relation $[\hat{\sigma}_z, \hat{\sigma}^\pm] = \pm 2\hat{\sigma}^\pm$ provides the final form of the equation for non-interacting, isolated two-level system

$$\mathrm{i}\left[\frac{\mathrm{d}}{\mathrm{d}t}\left(\rho_{ee}(t)-\rho_{gg}(t)\right)\hat{\sigma}_z+\frac{\mathrm{d}}{\mathrm{d}t}\rho_{eg}(t)\hat{\sigma}^++\frac{\mathrm{d}}{\mathrm{d}t}\rho_{ge}(t)\hat{\sigma}^-\right]=\omega_{eg}\left[\rho_{eg}(t)\hat{\sigma}^+-\rho_{ge}(t)\hat{\sigma}^-\right]. \quad (2.6)$$

Based on this result, the equations for the coefficients can be written as

$$\frac{\mathrm{d}}{\mathrm{d}t}\left(\rho_{ee}(t) - \rho_{gg}(t)\right) = 0 \Rightarrow \rho_{ee,gg}(t) = \rho_{ee,gg}(0), \tag{2.7a}$$

$$\frac{\mathrm{d}}{\mathrm{d}t}\rho_{eg}(t) = -\mathrm{i}\omega_{eg}\rho_{eg}(t) \Rightarrow \rho_{eg}(0)\mathrm{e}^{-\mathrm{i}\omega_{eg}t}, \tag{2.7b}$$

$$\rho_{ge}(t) = \rho^{\star}_{eg}(t). \tag{2.7c}$$

This solution is presented in Fig. 2.2, and two interesting features appear in it. First, the population in the system does not change in time, hence, in this ideal problem, the initial state is preserved forever. However, if, at the beginning, the system has coherence, it oscillates forever with the frequency corresponding to the energy difference between excited and ground levels.

2.1.2 *Electric-dipole approximation*

The quantum system alone is just one part of the problem in quantum-optical considerations. The other is the field with which it interacts. It is typically an electromagnetic field with frequencies in the visible range for the most frequently used atomic and molecular systems. Moreover, in this thesis, the semi-classical approach is considered, i.e., the classical description of the electromagnetic field is used as the field is strong, and hence quantum systems are altered significantly while the field is negligibly affected.

The general classical Hamiltonian for a non-relativistic electron in an atom (or molecule) interacting with an external electromagnetic field reads [41]

$$H(\vec{r},\vec{p},t) = \frac{1}{2m_e}\left(\vec{p} - \frac{e}{c}\vec{A}(\vec{r},t)\right)^2 + e\Phi(\vec{r},t) + V_{\mathrm{at}}(\vec{r}), \tag{2.8}$$

where $\vec{r}$ is the position vector, $\vec{p}$ is the electron's momentum, m_e is the electron's mass, and c is a speed of light in vacuum. The vector and scalar potentials of the external field are $\vec{A}$ and Φ, respectively, while V_{at} represents the static potential energy of the atom (with the nucleus at the origin of the coordinate system). However, the above form may be inconvenient for the interaction analysis with a directly given electromagnetic field (e.g. plane wave or Gaussian pulses extensively used in the experimental realizations). The fact that the electromagnetic field remains the same under the so-called gauge transformations $\vec{A} \to \vec{A} + \vec{\nabla} f$, $\Phi \to \Phi - \frac{1}{c}\frac{\partial}{\partial t} f$, where $f \equiv f(\vec{r},t)$ is any twice continuously differentiable function, provides some freedom in the formulation of the interaction Hamiltonian. The most useful, in the context of this dissertation, is the Göppert-Mayer transformation [42]

$$f(\vec{r},t) = -\vec{r} \cdot \vec{A}(\vec{0},t). \tag{2.9}$$

The transformed Hamiltonian (2.8) has a form [42]

$$\widetilde{H}(\vec{r},\vec{p},t) = \frac{1}{2m_e}\left(\vec{p} - \frac{e}{c}\left(\vec{A}(\vec{r},t) - \vec{A}(\vec{0},t)\right)\right)^2 + e\left(\Phi(\vec{r},t) + \vec{r}\frac{\partial}{c\partial t}\vec{A}(\vec{0},t)\right) + V_{\mathrm{at}}(\vec{r}). \tag{2.10}$$

Before it becomes clear why such a transformation is helpful, it is worth focusing on the electromagnetic field itself. The simplest example would be a pulse with a given carrier frequency ω_c and electric and magnetic envelopes $\vec{E}_0(\vec{r},t)$, $\vec{B}_0(\vec{r},t)$, respectively. Mathematically, it reads

$$\vec{E}(\vec{r},t) = \vec{E}_0(\vec{r},t)\cos\Big(\vec{k}\cdot\vec{r} \pm \omega_c t + \phi\Big), \tag{2.11a}$$

$$\vec{B}(\vec{r},t) = \vec{B}_0(\vec{r},t)\cos\Big(\vec{k}\cdot\vec{r} \pm \omega_c t + \phi\Big), \tag{2.11b}$$

where $\vec{r}$ is the position vector, $\vec{k}$ is a wave vector where $|\vec{k}| = \omega_c/c$, and ϕ is an additional field phase. The $\pm$ sign corresponds to different propagation directions. In most cases, the quantum system, which is the subject of the considerations, is much smaller compared to the wavelength of the external electromagnetic field. Hence, $\vec{k}\cdot\vec{r} \ll 1$ as $|\vec{r}|$ is at most of the size of the system, and it is assumed that the center of the system is in the origin of the coordinate system. Taylor series provides the following expansion

$$\begin{aligned}
\cos\Big(\vec{k}\cdot\vec{r} \pm \omega_c t + \phi\Big) &= \cos\Big(\vec{k}\cdot\vec{r}\Big)\cos(\omega_c t \pm \phi) \mp \sin\Big(\vec{k}\cdot\vec{r}\Big)\sin(\omega_c t \pm \phi) \\
&= \left(1 - \frac{\Big(\vec{k}\cdot\vec{r}\Big)^2}{2!} + \cdots\right)\cos(\omega_c t \pm \phi) \mp \left(\vec{k}\cdot\vec{r} - \frac{\Big(\vec{k}\cdot\vec{r}\Big)^3}{3!} + \cdots\right)\sin(\omega_c t \pm \phi) \\
&= \cos(\omega_c t \pm \phi) + \mathcal{O}\left(\vec{k}\cdot\vec{r}\right).
\end{aligned}$$

The approximation justifies neglecting the spatial variation along the system, and so $\vec{A}(\vec{r},t) \approx \vec{A}(\vec{0},t)$ (the system is placed in the origin). From now on, the additional phase term $\pm\phi$ can be neglected as it does not provide any qualitative changes.

Assuming $\Phi(\vec{r},t) = 0$ as there are no free charges in the vicinity of the system and recalling that the electric field in the Göppert-Mayer gauge (2.9) can be expressed in terms of a vector potential by the relation

$$\vec{E}(\vec{r},t) = -\frac{1}{c}\frac{\partial}{\partial t}\vec{A}(\vec{r},t),$$

after applying the previously used transformation, the Hamiltonian (2.10) simplifies to

$$H(\vec{r},\vec{p},t) = \underbrace{\frac{1}{2m_e}\vec{p}^2 + V_{\text{at}}(\vec{r})}_{H_{\text{sys}}} \underbrace{-e\vec{r}\cdot\vec{E}(\vec{0},t)}_{H_d}. \tag{2.12}$$

The first two terms represent the system Hamiltonian H_{sys}, which (after quantization) can be simplified e.g. to the form provided previously for the two-level system (2.3). The last term H_d is the interaction Hamiltonian between the system and the external field, where $e\vec{r} = \vec{d}$ is called the electric dipole moment, and the whole procedure describes the electric-dipole approximation.

The correspondence rule [43] allows going from a classic to a quantum interaction Hamiltonian by replacing the position vector with the adequate operator $\vec{r} \to \hat{\vec{r}} \Rightarrow \vec{d} \to \hat{\vec{d}}$, and the same for the system Hamiltonian $H_{\text{sys}} \rightarrow \hat{H}_{\text{sys}}$, giving quantum version of the Hamiltonian (2.12)

$$\hat{H}(t) = \hat{H}_{\text{sys}} - \hat{\vec{d}} \cdot \vec{E}. \tag{2.13}$$

The operator $\hat{\vec{d}}$ is known as the dipole moment operator.

To have a complete picture of the dipole-approximated interaction Hamiltonian, the absence of a magnetic field has to be explained. There are two reasons why, in this description, the magnetic part of the electromagnetic field is omitted.

First, the interaction of the magnetic field with the electron's momentum is incorporated in the full Hamiltonian (2.8). However, the Göppert Meyer transformation along with the small size of the system and non-relativistic electron description provide an approximation to the Hamiltonian that neglects this interaction, as it is much smaller compared to the electric one.

Second, the classical Hamiltonian cannot describe the interaction with the electron spin $\vec{S}$ as it is a purely quantum property of the particle. Hence it should be added by hand as

$$H_{\text{s}} = -\frac{e}{m_e} \vec{S} \cdot \vec{B}(\vec{r}, t).$$

The relation between the electric and magnetic amplitudes of the electromagnetic field reads $\left|\vec{B}\right| \propto \frac{1}{c}\left|\vec{E}\right|$, while the spin value reads $\left|\vec{S}\right| \propto \frac{1}{2}\hbar$. The comparison of the norms $||H_s||$ and $||H_d||$ for the typical parameters provides [44]

$$\frac{||H_s||}{||H_d||} \propto \frac{\left|\vec{S}\right|}{2m_e c} r^{-1} \approx 2 \times 10^{-13}\text{m} \times r^{-1},$$

which is also negligible for a typical system's size $|\vec{r}|$ of the order of 10^{-10} – 10^{-8}m. Hence, the magnetic part does not contribute to the description of the evolution of the quantum system.

2.1.3 *Non-dissipative Bloch equations*

Many atomic systems, such as atoms, homoatomic molecules, etc., are inversion symmetric. For many others, effects related to inversion symmetry breaking are negligible and it is enough to describe them as inversion-symmetric. Then, their eigenstates are either symmetric or antisymmetric with respect to the operation R of spatial inversion. For a single electron, $R(\psi(\vec{r})) = \pm\psi(-\vec{r})$, where $\psi(\vec{r})$ is a wavefunction in position representation given by

$$\psi_i(\vec{r}) = \langle\vec{r}|i\rangle = \pm\langle-\vec{r}|i\rangle = \pm\psi_i(-\vec{r}), \quad \text{for } i \in \{e, g\},$$

where $|\vec{r}\rangle$ is an eigenstate of the electron position operator $\hat{\vec{r}}$, and $\pm$ sign corresponds to symmetric and antisymmetric states, respectively. The form of the dipole operator in the basis of the eigenstates of the two-level system is then

$$\hat{\vec{d}} = \vec{d}_{eg}\hat{\sigma}^{+} + \vec{d}_{ge}\hat{\sigma}^{-}, \tag{2.14}$$

where $\vec{d}_{ge} = \vec{d}^{\star}_{eg}$.

The evolution of the two-level system can be calculated by the previously introduced von Neumann equation (2.5). Inserting the Hamiltonian (2.13) with the system Hamiltonian (2.3) and the dipole operator (2.14) interacting with the external field given by (2.11a) in the dipole approximation, the equation reads

$$i\hbar \frac{\mathrm{d}}{\mathrm{d}t}\hat{\rho}_{\mathrm{sys}}(t) = \left[\underbrace{\frac{1}{2}\hbar\omega_{eg}\hat{\sigma}_z - \left(\vec{d}_{eg}\hat{\sigma}^+ + \vec{d}_{ge}\hat{\sigma}^-\right)\vec{E}_0(t)\cos(\omega_c t)}_{\hat{H}(t)}, \hat{\rho}_{\mathrm{sys}}(t) \right]. \tag{2.15}$$

It can be split into a set of first-order differential equations for the expected values of the operators $\langle\hat{\sigma}_z\rangle$, $\langle\hat{\sigma}^+\rangle$, $\langle\hat{\sigma}^-\rangle$. The formula for the expected value of a given operator $\hat{A}$ under the evolution of the density matrix $\hat{\rho}(t)$ reads

$$\langle\hat{A}\rangle = \mathrm{Tr}\big(\hat{\rho}(t)\hat{A}\big),$$

where $\mathrm{Tr}(\cdot)$ stands for the trace operation. The useful properties

$$\begin{aligned}
&\frac{\mathrm{d}}{\mathrm{d}t}\langle\hat{A}\rangle = \frac{\mathrm{d}}{\mathrm{d}t}\mathrm{Tr}\big(\hat{\rho}(t)\hat{A}\big) = \mathrm{Tr}\left(\frac{\mathrm{d}}{\mathrm{d}t}\hat{\rho}(t)\hat{A}\right),\\
&\mathrm{Tr}\big(\alpha\hat{A} + \beta\hat{B}\big) = \alpha\,\mathrm{Tr}\big(\hat{A}\big) + \beta\,\mathrm{Tr}\big(\hat{B}\big),\\
&\mathrm{Tr}\big(\hat{A}\hat{B}\big) = \mathrm{Tr}\big(\hat{B}\hat{A}\big),
\end{aligned} \tag{2.16}$$

where $\hat{A}$, and $\hat{B}$ are two operators and $\alpha, \beta \in \mathbb{C}$. The equations for the evolution of the expected values of the σ-operators can be written by multiplying both sides of the evolution equation (2.15) by such an operator. Then, applying the trace operation, the output set is

$$i\hbar\frac{\mathrm{d}}{\mathrm{d}t}\langle\hat{\sigma}_z\rangle = -2\vec{E}_0(t)\cos(\omega_c t)\left(\vec{d}_{eg}\langle\hat{\sigma}^+\rangle - \vec{d}_{ge}\langle\hat{\sigma}^-\rangle\right), \tag{2.17a}$$

$$i\hbar\frac{\mathrm{d}}{\mathrm{d}t}\langle\hat{\sigma}^+\rangle = -\hbar\omega_{eg}\langle\hat{\sigma}^+\rangle - \vec{E}_0(t)\cos(\omega_c t)\vec{d}_{ge}\langle\hat{\sigma}_z\rangle, \tag{2.17b}$$

$$i\hbar\frac{\mathrm{d}}{\mathrm{d}t}\langle\hat{\sigma}^-\rangle = \hbar\omega_{eg}\langle\hat{\sigma}^-\rangle + \vec{E}_0(t)\cos(\omega_c t)\vec{d}_{eg}\langle\hat{\sigma}_z\rangle, \tag{2.17c}$$

where the trace properties (2.16) were used. The above equation set is a general form of the so-called Bloch equations for two-level systems. They allow calculating the evolution of the system and can be solved numerically.

To understand the meaning of these equations, one can show how the expected values of the sigma operators correspond to the matrix elements of the density operator. It is easily obtainable that $\langle\hat{\sigma}^{\pm}\rangle = \rho_{ge,eg}(t)$, while $\langle\hat{\sigma}_z\rangle = \rho_{ee}(t) - \rho_{gg}(t)$. Hence, $\langle\hat{\sigma}^{\pm}\rangle$ describes the evolution of coherence, while $\langle\hat{\sigma}_z\rangle$ provides information on the evolution of the population.

In a simple scenario, the envelope of the external field does not depend on time $\vec{E}_0(t) \equiv \vec{E}_0$, and the above set can be simplified if noted that the equations can be divided into rapidly and slowly oscillating terms. According to the solution presented in the absence of an external field (2.7), the off-diagonal (coherence) terms oscillate much faster compared to the diagonal (population) ones. This is true also for the evolution under external illumination. Moreover, in the usual case of interest, the external field's frequency is close to the transition frequency of the two-level system $\omega_c \approx \omega_{eg}$, which is described in the literature as a resonant or fluorescent regime. These conditions provide a significant interaction between the system and the electromagnetic field. Based on these observations, the coherence operators can be explicitly represented as a rapidly oscillating term and a slowly oscillating envelope (marked with $\sim$) by the ansatz

$$\langle\hat{\sigma}^{\pm}\rangle = \langle\tilde{\hat{\sigma}}^{\pm}\rangle \mathrm{e}^{\pm \mathrm{i}\omega_c t}. \tag{2.18}$$

Inserting this form into Bloch equations (2.17), and making use of the relation $\cos(\omega_c t) = \frac{1}{2}\left(\exp(\mathrm{i}\omega_c t) + \exp(-\mathrm{i}\omega_c t)\right)$ allows to separate terms with different temporal behavior

$$\mathrm{i}\hbar\frac{\mathrm{d}}{\mathrm{d}t}\langle\hat{\sigma}_z\rangle = -\vec{E}_0\left(\vec{d}_{eg}\langle\tilde{\hat{\sigma}}^{+}\rangle - \vec{d}_{ge}\langle\tilde{\hat{\sigma}}^{-}\rangle\right) - \underline{\vec{E}_0\left(\vec{d}_{eg}\langle\tilde{\hat{\sigma}}^{+}\rangle\mathrm{e}^{2\mathrm{i}\omega_c t} - \vec{d}_{ge}\langle\tilde{\hat{\sigma}}^{-}\rangle\mathrm{e}^{-2\mathrm{i}\omega_c t}\right)}, \tag{2.19a}$$

$$\mathrm{i}\hbar\frac{\mathrm{d}}{\mathrm{d}t}\langle\tilde{\hat{\sigma}}^{\pm}\rangle = \pm\hbar\underbrace{(\omega_c - \omega_{eg})}_{\delta}\langle\tilde{\hat{\sigma}}^{\pm}\rangle \mp \frac{1}{2}\vec{E}_0\vec{d}_{ge,eg}\langle\hat{\sigma}_z\rangle \mp \underline{\frac{1}{2}\vec{E}_0\vec{d}_{ge,eg}\mathrm{e}^{\mp 2\mathrm{i}\omega_c t}\langle\hat{\sigma}_z\rangle}, \tag{2.19b}$$

where the new symbol δ is used for the difference between driving and transition frequencies providing quantitative information about the detuning from the resonance. The underlined terms oscillate with high frequency $\pm 2\omega_c$, while the others depend on time slowly. In the typical case, these rapidly oscillating terms can be dropped as they average out for interesting evolution timescales.

The discussed approximation has its name – Rotating-Wave Approximation (RWA); nevertheless, from the reasoning presented above it is not clear where this name came from. However, there is another way to obtain the same set (2.19) by moving to a different frame, typically performed through unitary transformations in Hilbert space. For any unitary transformation $U(t)$ hold

$$\begin{aligned}
&U(t)U^{\dagger}(t) = I, \\
&\tilde{\hat{\rho}}(t) = U(t)\hat{\rho}(t)U^{\dagger}(t), \\
&\tilde{\hat{H}}(t) = U(t)\hat{H}(t)U^{\dagger}(t) + \mathrm{i}\hbar\frac{\mathrm{d}}{\mathrm{d}t}U(t)U^{\dagger}(t),
\end{aligned}$$

where $\cdot^{\dagger}$ represents the Hermitian conjugation, and the transformations of the density matrix operator and Hamiltonian preserve the form of the von-Neumann equation (the equation is invariant under unitary transformations). In this problem, the frame rotating with an external field frequency ω_c is useful as it leads to the same modification of the $\hat{\sigma}^{\pm}$ operators as in (2.18), namely

$$\begin{aligned}
&U_{\text{RWA}}(t) = \mathrm{e}^{\frac{1}{2}\mathrm{i}\omega_c t\hat{\sigma}_z}, \\
&U_{\text{RWA}}(t)\hat{\sigma}^{\pm}U^{\dagger}_{\text{RWA}}(t) = \tilde{\hat{\sigma}}^{\pm}\mathrm{e}^{\pm\mathrm{i}\omega_c t}, \\
&\mathrm{i}\hbar\frac{\mathrm{d}}{\mathrm{d}t}U_{\text{RWA}}(t)U^{\dagger}_{\text{RWA}}(t) = -\frac{1}{2}\omega_c\hat{\sigma}_z.
\end{aligned} \tag{2.20}$$

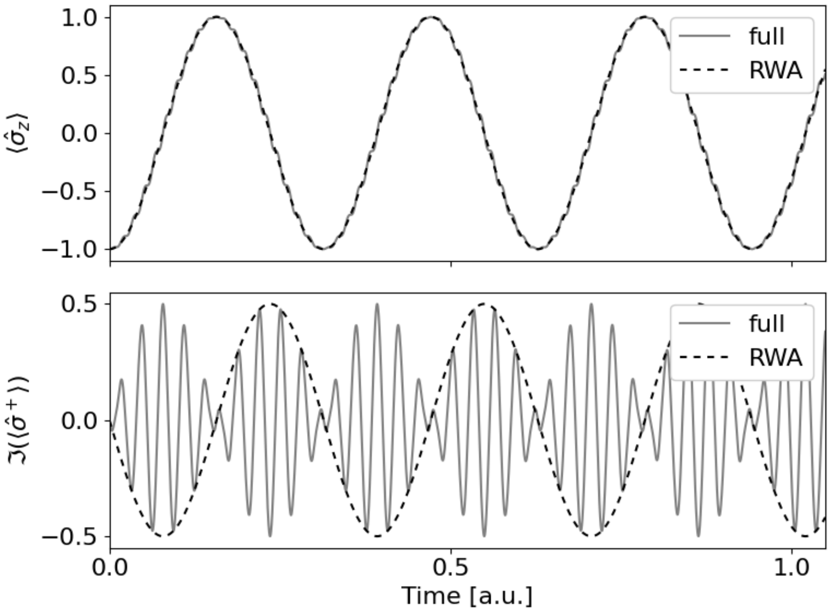

Figure 2.3: Illustrative presentation of the evolution of the expected values of the σ-operators for a two-level system interacting with a resonant electric field. Initially, the system is prepared in the ground state such that $\rho_{ee}(0) = 0$, $\rho_{gg}(0) = 1$, and $\rho_{eg}(0) = 0$. The solid lines correspond to the solution for the Hamiltonian without any approximations (labeled as *full*), while the dashed lines show the solution with the RWA included (labeled as *RWA*). Only the imaginary part of the coherence $\langle\hat{\hat{\sigma}}^+\rangle$ is shown, as the real one is negligible. All the units are arbitrarily chosen.

The rotated full Hamiltonian (2.15) has the form

$$\hat{\hat{H}}(t) = \underbrace{-\frac{1}{2}\hbar\delta\hat{\sigma}_z - \frac{1}{2}\vec{E}_0\left(\vec{d}_{eg}\hat{\hat{\sigma}}^+ + \vec{d}_{ge}\hat{\hat{\sigma}}^-\right)}_{\hat{H}_{\mathrm{RWA}}} - \frac{1}{2}\vec{E}_0\left(\vec{d}_{eg}\hat{\hat{\sigma}}^+\mathrm{e}^{2\mathrm{i}\omega_c t} + \vec{d}_{ge}\hat{\hat{\sigma}}^-\mathrm{e}^{-2\mathrm{i}\omega_c t}\right). \tag{2.21}$$

Note that σ_z is not modified by this transformation. Since the commutation relations between rotated operators are the same as in the original frame $\left[\hat{\sigma}_z, \hat{\hat{\sigma}}^\pm\right] = \pm 2\hat{\hat{\sigma}}^\pm$, $\left[\hat{\hat{\sigma}}^\pm, \hat{\hat{\sigma}}^\mp\right] = \pm\hat{\sigma}_z$, the procedure of finding Bloch equations is analogical, and provides exactly the same set of equations as (2.19). The difference is conceptual, as using $U(t)$ the splitting onto slowly- and rapidly- rotating terms is done already at the stage on the Hamiltonian description. The part $\hat{H}_{\mathrm{RWA}}$ is responsible for time-independent terms, hence rotating-wave approximation means dropping terms that counter-rotate to the (also rotating) frame incorporated by the unitary transformation. The approximated von Neumann equation has the form

$$\mathrm{i}\hbar\frac{\mathrm{d}}{\mathrm{d}t}\hat{\hat{\rho}}(t) = \left[\hat{H}_{\mathrm{RWA}}, \hat{\hat{\rho}}(t)\right]. \tag{2.22}$$

The comparison of the solutions with and without this approximation is shown in Fig. 2.3. The rapidly-oscillating terms provide a correction to the $\langle\hat{\sigma}_z\rangle$ visible as small wiggling along the approximated solution, while for the coherence the curve in the transformed frame $\langle\hat{\hat{\sigma}}^+\rangle$ is simply the envelope of the full solution $\langle\hat{\sigma}^+\rangle$. Most importantly, upon interaction with an external field, the population of the system oscillates. This phenomenon is known as Rabi oscillations, and the frequency reads

$$\Omega_R = \frac{\vec{E}_0 \cdot \vec{d}_{ge}}{\hbar}. \tag{2.23}$$

Hence, the Rabi frequency depends linearly on the amplitude of the electric field. It is worth noting, that this term is precisely the coupling constant between a system and a field. The linear dependence of the light-matter interaction constant on the field amplitude is important for the articles comprising this thesis.

The RWA provides proper results in the near-resonant regime, which is understood as $|\delta| \ll \omega_c,\ \omega_{eg}$, and for a weak coupling $|\Omega_R| \ll \omega_c,\ \omega_{eg}$. Beyond, counter-rotating terms cannot be neglected. Even with these restrictions, the RWA form of the Bloch equations is extremely useful as it does not contain any explicitly time-dependent terms and so can be solved analytically. Moreover, it provides a clear insight into the system's dynamics revealing the most significant property of a driven two-level system – Rabi oscillations.

2.1.4 *Dissipative Bloch equations*

In experimental conditions, it is challenging to achieve isolated systems (as in Sec. 2.1.1) or systems interacting with a single mode of the electric field (as in Sec. 2.1.3), as the quantum systems always interact with vacuum modes or with other systems in an ensemble. Hence, a quantitative description of such additional interactions has to be incorporated into the evolution equation. The solution to this problem is the usage of the so-called quantum master equation [45], which, in a general form, is extremely hard to solve. Instead, the most popular and broadly used is its approximated form named Gorini–Kossakowski–Sudarshan–Lindblad (GKLS or just Lindblad) equation [46]

$$i\hbar\frac{\mathrm{d}}{\mathrm{d}t}\hat{\rho}(t) = \left[\hat{H}(t),\hat{\rho}(t)\right] + \underbrace{i\hbar\sum_i \gamma_i \left(\hat{L}_i\rho(t)\hat{L}_i^\dagger - \frac{1}{2}\left(\hat{L}_i^\dagger\hat{L}_i\hat{\rho}(t) + \hat{\rho}(t)\hat{L}_i^\dagger\hat{L}_i\right)\right)}_{\mathcal{L}(\hat{\rho}(t))}, \tag{2.24}$$

where the first part is the regular von Neumann equation with a density operator of the system and the coherent evolution Hamiltonian. The additional sum corresponds to incoherent interactions with the modes outside the system, also called environment or reservoir, and is described by the operators $\sqrt{\gamma_i}\hat{L}_i$.

The environment provides additional ways for the system to evolve and is typically much larger (in a Hilbert space sense) than the quantum system itself. For this reason, in most cases, it is justified to assume that the environment evolution is negligible as the system does not impact it significantly. Moreover, it is assumed that system-environment interaction is Markovian (memoryless), i.e., coupling to it is relatively weak and can be treated as time-independent, which greatly reduces the computation complexity.

The easiest case the above equation can describe is the spontaneous emission – a random process of transition from excited to the ground state due to the interaction of the excited system with an environment in the form of virtual photons in vacuum. In that case, $\gamma_i \equiv \gamma_{\text{se}}$ is a decay rate or parameter that describes how fast, on average, the system will deexcite and is inversely proportional to the lifetime of the excited state. Since in the process system changes its state from $|e\rangle$ to $|g\rangle$, the spontaneous emission operator has the form of the flip operator $\hat{L}_{\text{se}} = |g\rangle\langle e| = \hat{\sigma}^-$.

To find additional terms for the Bloch equations derived in the previous section, the same procedure as with the von Neumann equation can be repeated for the Lindblad part. That is, multiplying by $\hat{\sigma} \in \{\hat{\sigma}_z,\ \hat{\sigma}^+,\ \hat{\sigma}^-\}$ and taking the trace gives

$$\mathcal{L}_{\text{se}}(\langle\hat{\sigma}\rangle) = \mathrm{i}\hbar\gamma_{\text{se}}\left(\mathrm{Tr}\big(\hat{\sigma}\hat{\sigma}^-\hat{\rho}(t)\hat{\sigma}^+\big) - \frac{1}{2}\left(\mathrm{Tr}\big(\hat{\sigma}\hat{\sigma}^+\hat{\sigma}^-\hat{\rho}(t)\big) + \mathrm{Tr}\big(\hat{\sigma}\hat{\rho}(t)\hat{\sigma}^+\hat{\sigma}^-\big)\right)\right)$$

$$= -\mathrm{i}\hbar\begin{cases}\gamma_{\text{se}}\left(\langle\hat{\sigma}_z\rangle + 1\right), & \text{if } \hat{\sigma} = \hat{\sigma}_z,\\ \frac{1}{2}\gamma_{\text{se}}\langle\hat{\sigma}^\pm\rangle, & \text{if } \hat{\sigma} = \hat{\sigma}^\pm.\end{cases}$$

Therefore, in the case of a two-level system interacting only with vacuum, the Bloch equations have the form

$$\mathrm{i}\hbar\frac{\mathrm{d}}{\mathrm{d}t}\langle\hat{\sigma}_z\rangle = -\mathrm{i}\hbar\gamma_{\text{se}}\left(\langle\hat{\sigma}_z\rangle + 1\right) \Rightarrow \langle\hat{\sigma}_z\rangle(t) = \left(\langle\hat{\sigma}_z\rangle(0) + 1\right)\mathrm{e}^{-\gamma_{\text{se}}t} - 1, \tag{2.25a}$$

$$\mathrm{i}\hbar\frac{\mathrm{d}}{\mathrm{d}t}\langle\hat{\sigma}^\pm\rangle = -\mathrm{i}\hbar\left(\mp\mathrm{i}\omega_{eg} + \frac{1}{2}\gamma_{\text{se}}\right)\langle\hat{\sigma}^\pm\rangle \Rightarrow \underbrace{\langle\hat{\sigma}^\pm\rangle(t)\mathrm{e}^{\mp\mathrm{i}\omega_{eg}t}}_{\langle\hat{\tilde{\sigma}}^\pm\rangle(t)} = \langle\hat{\sigma}^\pm\rangle(0)\mathrm{e}^{-\frac{1}{2}\gamma_{\text{se}}t}. \tag{2.25b}$$

Contrary to the solution of the isolated system, the population in the system does not stay the same (unless the initial state was $|g\rangle$) but rather decays eventually to the ground state as $\langle\hat{\sigma}_z\rangle \xrightarrow[t\to\infty]{} -1$. Moreover, the coherence also decreases but slower and eventually reaches zero. Such irreversible processes lead to a loss of information and energy and are called dissipative.

Complementary to the spontaneous emission, one can describe an incoherent pumping process, when the reservoir's energy is transferred into the system. It can happen e.g., when the system is in non-zero temperature and thermal photons can excite it. The description is similar to spontaneous emission, but the operator has a form $\hat{L}_{\text{pu}} = |e\rangle\langle g| = \hat{\sigma}^+$ with the pump rate γ_{pu}. Short calculations with use of the GKLS equation (2.24) show that the result is similar to (2.25), with $\gamma_{\text{se}} \to \gamma_{\text{pu}}$ and reversed signs next to "1"s. This time $\langle\hat{\sigma}_z\rangle \xrightarrow[t\to\infty]{} 1$. Hence, the population tends to transfer to the excited state. However, incoherent interaction with an environment always provides a loss of coherence, since the equation for $\langle\hat{\sigma}^\pm\rangle$ is the same as in the spontaneous emission case.

Another source of decoherence that occurs in atomic system ensembles are collisions with the sample walls and among the systems forming the ensemble. In this process, dephasing occurs and population transfer between states is not induced, contrary to the

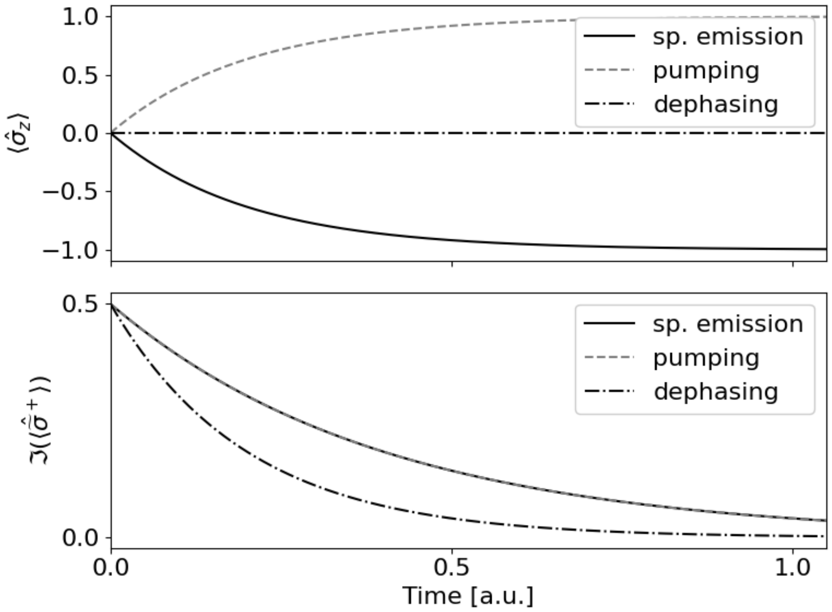

Figure 2.4: Illustrative presentation of the resonant evolution of the expected values of the σ-operators for the two-level system in incoherent interactions. The system is initially prepared in the superposition of excited and ground states such that $\rho_{ee}(0) = \rho_{gg}(0) = 1/2$, and $\rho_{eg}(0) = 1/2$. The solid lines correspond to the decay of the population and coherence in the spontaneous emission process (labeled *sp. emission*), while the dashed lines present evolution for the pumping process (labeled *pumping*), and dot-dashed lines show evolution with only dephasing process. In all the cases γ-rates are the same, and the $\hat{L}$-operators are introduced in the main text. All the units are arbitrarily chosen.

previous examples. The operator may have a form $\hat{L}_{\mathrm{de}} = \frac{1}{\sqrt{2}}\hat{\sigma}_z$ with the decay rate γ_{de}. In that case, the additional terms read

$$\begin{aligned}\mathcal{L}_{\mathrm{de}}(\langle\hat{\sigma}\rangle) = \mathrm{i}\hbar\gamma_{\mathrm{de}}\left(\frac{1}{2}\operatorname{Tr}(\hat{\sigma}\hat{\sigma}_z\hat{\rho}(t)\hat{\sigma}_z) - \frac{1}{2}\left(\frac{1}{2}\operatorname{Tr}(\hat{\sigma}\hat{\sigma}_z\hat{\sigma}_z\hat{\rho}(t)) + \frac{1}{2}\operatorname{Tr}(\hat{\sigma}\hat{\rho}(t)\hat{\sigma}_z\hat{\sigma}_z)\right)\right) \\ = -\mathrm{i}\hbar\begin{cases}0, & \text{if } \hat{\sigma} = \hat{\sigma}_z, \\ \gamma_{\mathrm{de}}\langle\hat{\sigma}^{\pm}\rangle, & \text{if } \hat{\sigma} = \hat{\sigma}^{\pm}.\end{cases}\end{aligned}$$

Indeed, only coherence is dumped in this process while the population is intact.

The graphical comparison of the evolution of the system for each incoherent process is presented in Fig. 2.4. While for the spontaneous emission and pumping cases the behavior of the population is tremendously different, the coherence behaves the same. For the dephasing process, as intended, the population is unchanged while the coherence decays at a double pace even though the γ-rates have been assumed to have the same values in each case.

Previously, the evolution equations under RWA (2.19) were presented, so it is also of interest to analyze the behavior of the transformed Lindblad terms $\hat{L}_i \to \hat{\tilde{L}}_i$. Under the transformation U_{RWA} the $\hat{\sigma}^{\pm}$ operators gain the phase terms $\exp\left(\pm\frac{1}{2}\mathrm{i}\omega_c t\right)$, while σ_z remains unmodified (2.20). Since $\hat{L}_i$ operators always appear in pairs ($\hat{L}_i$, $\hat{L}_i^{\dagger}$), these additional phase terms cancel out and, in consequence, the form of the GKLS part (2.24) is unchanged.

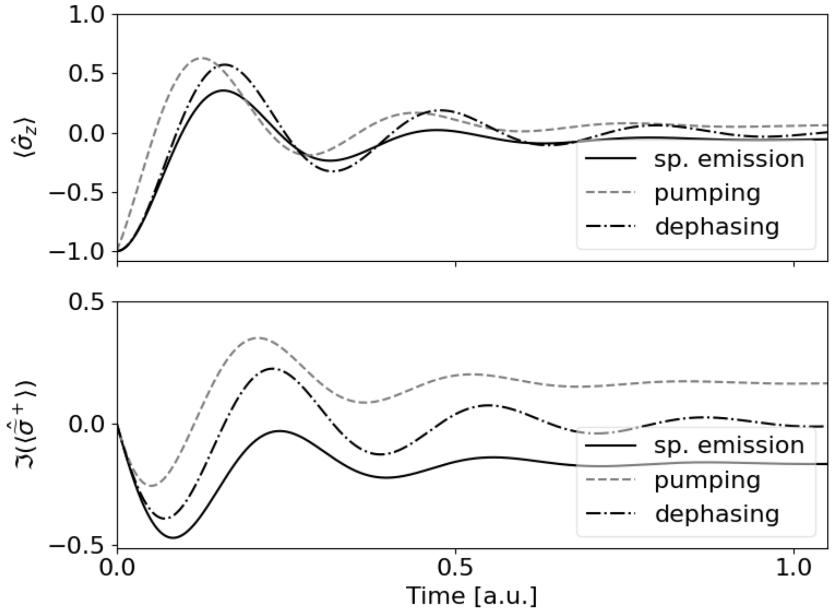

Figure 2.5: Illustrative presentation of the resonant evolution of the expected values of the σ-operators for the two-level system interacting with the external electric field with included different dissipation mechanisms. The lines descriptions are the same as in Fig. 2.4.

In summary, dissipative Bloch equations of the two-level system interacting with external coherent field in the form of the plane wave in the RWA regime and with dissipative processes included via GKLS equation read

$$i\hbar\frac{\mathrm{d}}{\mathrm{d}t}\langle\hat{\sigma}_z\rangle = -\hbar\left(\Omega_R^{\star}\langle\hat{\tilde{\sigma}}^{+}\rangle - \Omega_R\langle\hat{\tilde{\sigma}}^{-}\rangle\right) - i\hbar\left(\Gamma + \gamma_{\mathrm{pu}}\right)\langle\hat{\sigma}_z\rangle - i\hbar\left(\Gamma - \gamma_{\mathrm{pu}}\right), \tag{2.26a}$$

$$i\hbar\frac{\mathrm{d}}{\mathrm{d}t}\langle\hat{\tilde{\sigma}}^{\pm}\rangle = \pm\hbar\delta\langle\hat{\tilde{\sigma}}^{\pm}\rangle \mp \frac{1}{2}\hbar\Omega_R^{;\star}\langle\hat{\sigma}_z\rangle - i\hbar\gamma_{\perp}\langle\hat{\tilde{\sigma}}^{\pm}\rangle, \tag{2.26b}$$

where Γ is called the longitudinal decay rate in literature and takes into account all incoherent processes of population decay to the ground state. In this thesis, it corresponds to spontaneous emission $\Gamma = \gamma_{\mathrm{se}}$, while the pumping process is added separately. On the other hand, $\gamma_{\perp}$ is named the transverse decay rate and contains all the information about the incoherent processes that affect the coherence in the system (with pumping included). In this thesis, it reads $\gamma_{\perp} = \frac{1}{2}\left(\gamma_{\mathrm{se}} + \gamma_{\mathrm{pu}}\right) + \gamma_{\mathrm{de}}$. In light of these results, it is justified to write $\gamma_{\perp} \geq \frac{1}{2}\Gamma$ with equality holding if no pure dephasing or pumping processes affect the evolution of the two-level system.

The solutions to Bloch equations (2.26) are illustrated in Fig. 2.5, with each line representing a different decoherence mechanism for easy comparison. Both spontaneous emission and pumping processes result in a faster decay of population and coherence than dephasing alone. Moreover, the population eventually reaches a stationary value, unlike solutions without an external field. In each case, a stationary state is eventually reached: the highest values occur with pumping, the lowest with spontaneous emission, and intermediate values with dephasing. Regardless of the mechanism, the decay in the population is due to the external field coupling the ground and excited states, causing the system to oscillate between them. Thus, coherence influences the population and decay in coherence impacts population evolution. The decoherence does not affect the population directly in the dephasing process, preserving oscillations for the longest time.

2.1.5 *Permanent dipole moments*

So far, the dipole operator in the form (2.14) has been considered. As has been stated, this is justified for the systems with inversion symmetry since the wavefunctions have certain parities. The natural generalization pertains to a description of the evolution of a system with broken inversion symmetry, i.e., polar systems. Broken symmetry provides additional dipole moments in the system: permanent dipole moments $\vec{d}_{ee}$, $\vec{d}_{gg}$ in each of the eigenstates. The connection between the geometry of the system and the appearance of PDMs can be found in Section S1 in Supplement to the article A2. The generalized form of the dipole operator reads

$$\hat{\vec{d}} = \vec{d}_{eg}\hat{\sigma}^{+} + \vec{d}_{ge}\hat{\sigma}^{-} + \frac{1}{2}\left(\vec{d}_{ee} - \vec{d}_{gg}\right)\hat{\sigma}_z + \frac{1}{2}\left(\vec{d}_{ee} + \vec{d}_{gg}\right)\hat{I}. \tag{2.27}$$

The Hamiltonian describing the interaction between such a system with the external electric field has a more complex form compared to the one from (2.15)

$$\hat{H}(t) = \frac{1}{2}\hbar\underbrace{\left(\omega_{eg} - \left(\vec{d}_{ee} - \vec{d}_{gg}\right)\frac{\vec{E}_0(t)}{\hbar}\cos(\omega_c t)\right)}_{\omega_{eg}(t)}\hat{\sigma}_z - \left(\vec{d}_{eg}\hat{\sigma}^{+} + \vec{d}_{ge}\hat{\sigma}^{-}\right)\vec{E}_0(t)\cos(\omega_c t), \tag{2.28}$$

where the term with the identity operator $\hat{I}$ operator is dropped as it does not contribute to the evolution equations (as was shown in Sec. 2.1.1). The difference between non-polar and polar systems is manifested in the transition frequency. For the polar case, it becomes time-dependent, as it starts to oscillate with the external field's frequency ω_c, and with the amplitude proportional to the permanent dipole moments difference between the excited and ground states $\vec{d}_{ee} - \vec{d}_{gg}$.

The goal is to find the time-independent Bloch equations in the spirit of the previous section. However, in addition to RWA, there is a need to apply a unitary transformation to deal with the time dependency of the transition frequency. The proper form reads [4]

$$\begin{aligned}
U_{\text{PDM}}(t) &= \mathrm{e}^{-\mathrm{i}\frac{1}{2}\kappa_z\sin(\omega_c t)\hat{\sigma}_z},\\
U_{\text{PDM}}(t)\hat{\sigma}^{\pm}U^{\dagger}_{\text{PDM}}(t) &= \hat{\hat{\sigma}}^{\pm}\mathrm{e}^{\mp\mathrm{i}\kappa_z\sin(\omega_c t)},\\
\mathrm{i}\hbar\frac{\mathrm{d}}{\mathrm{d}t}U_{\text{PDM}}(t)U^{\dagger}_{\text{PDM}}(t) &= \frac{1}{2}\hbar\kappa_z\omega_c\cos(\omega_c t)\hat{\sigma}_z,
\end{aligned} \tag{2.29}$$

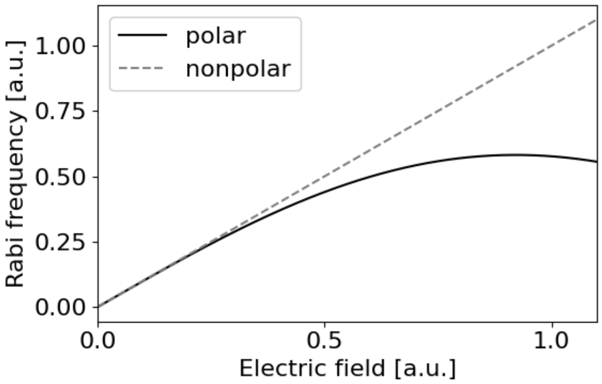

Figure 2.6: Illustrative presentation of the difference between Rabi frequency for polar (solid line) and non-polar (dashed line) systems as a function of electric field amplitude. The transition dipoles in both cases are the same, and all parameters are in arbitrary units.

where $\kappa_z = \left(\vec{d}_{ee} - \vec{d}_{gg}\right) \vec{E}_0 / \hbar\omega_c$, and again, the plane wave assumption is in use $\vec{E}_0(t) \equiv \vec{E}_0$. Indeed, the transformed Hamiltonian (2.28) has time-independent $\hat{\sigma}_z$-term

$$\hat{\tilde{H}}(t) = \frac{1}{2}\hbar\omega_{eg}\hat{\sigma}_z - \left(\vec{d}_{eg}\hat{\tilde{\sigma}}^{+}\mathrm{e}^{-\mathrm{i}\kappa_z \sin(\omega_c t)} + \vec{d}_{ge}\hat{\tilde{\sigma}}^{-}\mathrm{e}^{\mathrm{i}\kappa_z \sin(\omega_c t)}\right) \vec{E}_0 \cos(\omega_c t). \tag{2.30}$$

The complicated form next to the $\hat{\sigma}^{\pm}$ operators can be expressed by the sum of Bessel functions of the first kind $\mathrm{J}_n(x)$ for $n \in \mathbb{Z}$

$$\mathrm{e}^{\pm\mathrm{i}\kappa_z \sin(\omega_c t)} = \sum_{n=-\infty}^{\infty} \mathrm{J}_n(\kappa_z)\mathrm{e}^{\pm \mathrm{i}n\omega_c t}.$$

It is convenient to write the Hamiltonian using this expression as terms that oscillate with different frequencies $n\omega_c$ are easily separable. Additionally, making use of the property $\mathrm{J}_{n-1}(x) + \mathrm{J}_{n+1}(x) = \frac{2n}{\kappa_z}\mathrm{J}_n(x)$, and the unitary transformation U_{RWA} (2.20), the full Hamiltonian (2.30) transforms to

$$\begin{aligned}\hat{\tilde{\tilde{H}}}(t) = &\underbrace{-\frac{1}{2}\hbar\delta\hat{\sigma}_z - \frac{1}{2}\hbar\frac{2}{\kappa_z}\mathrm{J}_1(\kappa_z)\left(\Omega_R^{\star}\hat{\tilde{\tilde{\sigma}}}^{+} + \Omega_R\hat{\tilde{\tilde{\sigma}}}^{-}\right)}_{\hat{H}_{\mathrm{RWA}}} \\ &- \frac{1}{2}\hbar\sum_{\substack{n=-\infty \\ n\neq 0}}^{\infty} \frac{2(n+1)}{\kappa_z}\mathrm{J}_{n+1}(\kappa_z)\left(\Omega_R^{\star}\hat{\tilde{\tilde{\sigma}}}^{+}\mathrm{e}^{-\mathrm{i}n\omega_c t} + \Omega_R\hat{\tilde{\tilde{\sigma}}}^{-}\mathrm{e}^{\mathrm{i}n\omega_c t}\right),\end{aligned} \tag{2.31}$$

where $\tilde{\tilde{\cdot}}$ highlights application of both unitary transformations.

The important difference between this result and the RWA Hamiltonian for the nonpolar system (2.21) is the nonlinear dependence of the coupling on the external field and hence the nonlinear Rabi frequency. Note that κ_z is a function of the field amplitude.

$$\tilde{\Omega}_R = \frac{2}{\kappa_z}\mathrm{J}_1(\kappa_z)\Omega_R. \tag{2.32}$$

The form above is general and recreates the previous one (2.23) for $\left(\vec{d}_{ee} - \vec{d}_{gg}\right) \to 0$ as the additional term vanishes $\frac{2}{\kappa_z}\mathrm{J}_1(\kappa_z) \to 1$. Besides that, the RWA Hamiltonian looks the same as previously, hence the Bloch equations for the polar system under all the approximations described earlier have the same form as in Eqs. (2.26)

$$\mathrm{i}\hbar\frac{\mathrm{d}}{\mathrm{d}t}\langle\hat{\sigma}_z\rangle = -\hbar\left(\widetilde{\Omega}_R^{\star}\langle\hat{\tilde{\tilde{\sigma}}}^{+}\rangle - \widetilde{\Omega}_R\langle\hat{\tilde{\tilde{\sigma}}}^{-}\rangle\right) - \mathrm{i}\hbar\left(\Gamma + \gamma_{\mathrm{pu}}\right)\langle\hat{\sigma}_z\rangle - \mathrm{i}\hbar\left(\Gamma - \gamma_{\mathrm{pu}}\right), \tag{2.33a}$$

$$\mathrm{i}\hbar\frac{\mathrm{d}}{\mathrm{d}t}\langle\hat{\tilde{\tilde{\sigma}}}^{\pm}\rangle = \pm\hbar\delta\langle\hat{\tilde{\tilde{\sigma}}}^{\pm}\rangle \mp \frac{1}{2}\hbar\widetilde{\Omega}_R^{;\star}\langle\hat{\sigma}_z\rangle - \mathrm{i}\hbar\gamma_{\perp}\langle\hat{\tilde{\tilde{\sigma}}}^{\pm}\rangle. \tag{2.33b}$$

The comparison for the arbitrarily chosen parameters of Rabi frequency in polar and non-polar systems is shown in Fig. 2.6. The nonlinear behavior is an interesting and intriguing phenomenon that may influence the description of the most basic light-matter interaction and is a starting point for the article **A1**.

2.2 THREE-LEVEL SYSTEMS

The discussion now naturally continues to the exploration of three-level quantum systems, extending the concepts discussed in the previous chapter. These systems provide a richer framework compared to their two-level counterparts, allowing for more complex interaction scenarios, e.g., involving multiple driving fields. The study of three-level systems reveals new phenomena that are not present in simpler systems and offers insights into more advanced topics such as coherent population trapping [47], EIT [27–30], STIRAP [15], and many more [48–51].

In the context of this dissertation, the most important is the ability to control the dynamics of the system *via* a driving field, i.e., dressing the system optically to impact the propagation of probe pulses. These possibilities are investigated for three-level systems with inversion symmetry.

2.2.1 *Configurations V, Λ, and Ξ*

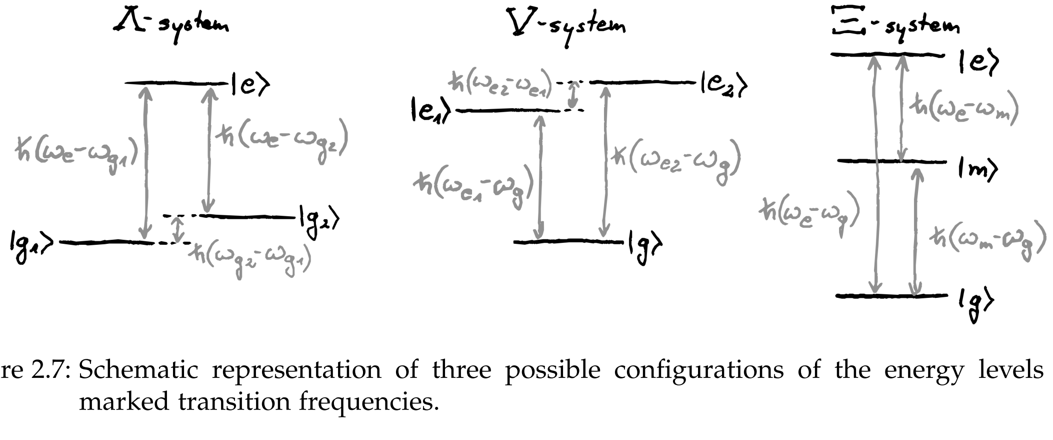

Figure 2.7: Schematic representation of three possible configurations of the energy levels with marked transition frequencies.

There are three ways to organize the three levels that provide significantly different responses to the external electromagnetic field. In the literature, they are named Λ, V, and Ξ systems with graphical representation in Fig. 2.7, and the Hamiltonians respectively read

$$\hat{H}^{\Lambda}_{\text{sys}} = \hbar\omega_{g_1} \left|g_1\right\rangle \left\langle g_1\right| + \hbar\omega_{g_2} \left|g_2\right\rangle \left\langle g_2\right| + \hbar\omega_e \left|e\right\rangle \left\langle e\right|, \tag{2.34a}$$

$$\hat{H}^{V}_{\text{sys}} = \hbar\omega_{g} \left|g\right\rangle \left\langle g\right| + \hbar\omega_{e_1} \left|e_1\right\rangle \left\langle e_1\right| + \hbar\omega_{e_2} \left|e_2\right\rangle \left\langle e_2\right|, \tag{2.34b}$$

$$\hat{H}^{\Xi}_{\text{sys}} = \hbar\omega_{g} \left|g\right\rangle \left\langle g\right| + \hbar\omega_{m} \left|m\right\rangle \left\langle m\right| + \hbar\omega_e \left|e\right\rangle \left\langle e\right|. \tag{2.34c}$$

The systems dynamics are significantly different and the energy levels are named accordingly, to highlight their role. Hence, the bases are $\mathcal{B}^{\Lambda} = \{\left|g_1\right\rangle, \left|g_2\right\rangle, \left|e\right\rangle\}$, $\mathcal{B}^{V} = \{\left|g\right\rangle, \left|e_1\right\rangle, \left|e_2\right\rangle\}$, and $\mathcal{B}^{\Xi} = \{\left|g\right\rangle, \left|m\right\rangle, \left|e\right\rangle\}$. In this thesis, the orders of the energy levels are such that $\omega_{g_1} \leq \omega_{g_2} \leq \omega_e$, $\omega_g \leq \omega_{e_1} \leq \omega_{e_2}$, $\omega_g \leq \omega_m \leq \omega_e$, for Λ, V, and Ξ configurations, respectively.

The additional energy level, compared to the two-level system, provides space for interaction with three external fields, one for each energy-level pair. However, in the typical scenario involving an inversion-symmetric system, the wave function of each energy level has a certain parity. Hence, the direct transition between the same-parity levels is suppressed. Especially, in the dipole approximation introduced in the previous section, the following transitions are assumed to be forbidden: $\left|g_1\right\rangle \not\to \left|g_2\right\rangle$, $\left|e_1\right\rangle \not\to \left|e_2\right\rangle$, and $\left|g\right\rangle \not\to \left|e\right\rangle$ for the configurations Λ, V, and Ξ, respectively.

The electric-dipole-allowed transitions along with fields that couple them are shown in Fig. 2.8 for each configuration. Usually, one of the fields is stronger compared to the other and is called in the literature the control field (here described with Rabi frequency Ω_c) which leads to the optical dressing of the system mentioned earlier. This field controls the system behavior in the interaction with the second weaker probe field (Rabi frequency Ω_p). Moreover, to describe near-resonant dynamics, detunings for control and probe fields are allowed and described by $\delta_c = \omega_c - \omega_i$, and $\delta_p = \omega_p - \omega_j$, where ω_c is the control field frequency, ω_p corresponds to the probe field frequency, and $\omega_{i,j}$ are respective transition frequencies where $i \in \{eg_2, e_2g, em\}$, and $j \in \{eg_1, e_1g, mg\}$.

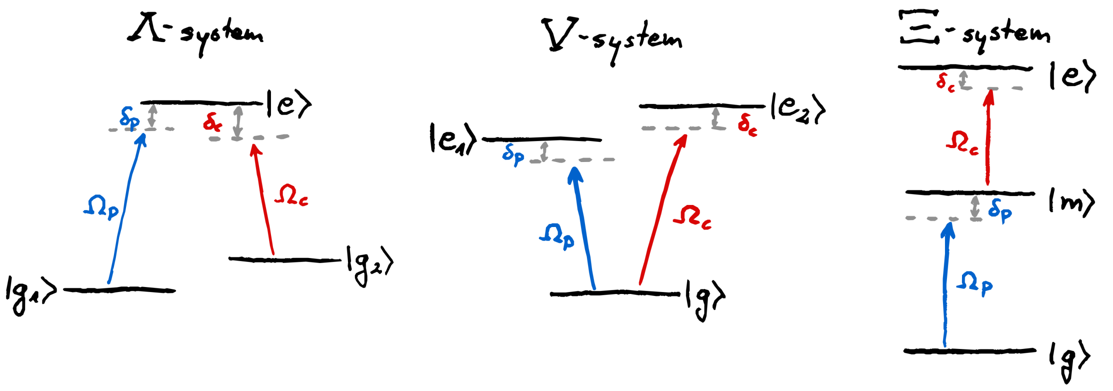

Figure 2.8: Schematic presentation of the three-level systems driven by control (red) and probe (blue) fields coupled to selected pairs of states. For each field and configuration, the corresponding detuning is also marked.

The Hilbert space in this case is larger; hence, instead of four operators describing the two-level system, nine are required. However, the flip operators $(\hat{\sigma}^{-})^{\dagger} = \hat{\sigma}^{+}$ are connected, and the probability preservation, $\mathrm{Tr}(\hat{\rho}_{\mathrm{sys}}) = 1$, is assumed, and so only five are independent. For convenience, the operators are presented in tabular form in Tab. 2.1, and σ-operators have subscripts p and c corresponding to the energy level pairs coupled via probe and control fields, while f depicts pairs with forbidden transitions.

Table 2.1: Collective definitions of the operators used in the thesis.

	Λ system	V system	Ξ system
$\hat{I}$	$\sum_{i\in\{g_1,\, g_2,\, e\}} \|i\rangle\langle i\|$	$\sum_{i\in\{g,\, e_1,\, e_2\}} \|i\rangle\langle i\|$	$\sum_{i\in\{g,\, m,\, e\}} \|i\rangle\langle i\|$
$\hat{\sigma}_p^z$	$\|e\rangle\langle e\| - \|g_1\rangle\langle g_1\|$	$\|e_1\rangle\langle e_1\| - \|g\rangle\langle g\|$	$\|m\rangle\langle m\| - \|g\rangle\langle g\|$
$\hat{\sigma}_c^z$	$\|e\rangle\langle e\| - \|g_2\rangle\langle g_2\|$	$\|e_2\rangle\langle e_2\| - \|g\rangle\langle g\|$	$\|e\rangle\langle e\| - \|m\rangle\langle m\|$
$\hat{\sigma}_p^+$	$\|e\rangle\langle g_1\|$	$\|e_1\rangle\langle g\|$	$\|m\rangle\langle g\|$
$\hat{\sigma}_c^+$	$\|e\rangle\langle g_2\|$	$\|e_2\rangle\langle g\|$	$\|e\rangle\langle m\|$
$\hat{\sigma}_f^+$	$\|g_2\rangle\langle g_1\|$	$\|e_2\rangle\langle e_1\|$	$\|e\rangle\langle g\|$

The Hamiltonians from (2.34) can be then expressed as

$$\hat{H}_{\mathrm{sys}}^{\Lambda} = \frac{1}{3}\hbar\left(\underbrace{(\omega_{eg_1} + \omega_{g_2g_1})}_{\omega_p^{\Lambda}}\hat{\sigma}_p^z + \underbrace{(\omega_{eg_2} - \omega_{g_2g_1})}_{\omega_c^{\Lambda}}\hat{\sigma}_c^z\right), \tag{2.35a}$$

$$\hat{H}_{\mathrm{sys}}^{V} = \frac{1}{3}\hbar\left(\underbrace{(\omega_{e_1g} - \omega_{e_2e_1})}_{\omega_p^{V}}\hat{\sigma}_p^z + \underbrace{(\omega_{e_2g} + \omega_{e_2e_1})}_{\omega_c^{V}}\hat{\sigma}_c^z\right), \tag{2.35b}$$

$$\hat{H}_{\mathrm{sys}}^{\Xi} = \frac{1}{3}\hbar\left(\underbrace{(\omega_{mg} + \omega_{eg})}_{\omega_p^{\Xi}}\hat{\sigma}_p^z + \underbrace{(\omega_{em} + \omega_{eg})}_{\omega_c^{\Xi}}\hat{\sigma}_c^z\right), \tag{2.35c}$$

where $\hat{I}$-elements are dropped. Introducing new frequencies shown above, the general Hamiltonian of the three-level system in any configuration can be expressed shortly as

$$\hat{H}_{\mathrm{sys}}^{\alpha} = \frac{1}{3}\hbar\left(\omega_p^{\alpha}\hat{\sigma}_p^z + \omega_c^{\alpha}\hat{\sigma}_c^z\right), \quad \text{for } \alpha \in \{\Lambda, V, \Xi\}. \tag{2.36}$$

The advantage of such choice of the operators is that for energy levels coupled via probe and control fields the corresponding flip operators have the same commutation relations as in the two-level system $[\hat{\sigma}_{p,c}^{+}, \hat{\sigma}_{p,c}^{-}] = \hat{\sigma}_{p,c}^{z}$, $[\hat{\sigma}_{p,c}^{z}, \hat{\sigma}_{p,c}^{\pm}] = \pm 2\hat{\sigma}_{p,c}^{\pm}$.

2.2.2 *Non-dissipative Bloch equations*

The evolution of the three-level system driven by two external electric fields, in analogy to the previously investigated two-level system in Sec. 2.1.3, is described by the Bloch equations. However, additional energy level and coupling field, and three possible configurations significantly complicate the general derivation. Nevertheless, this problem is well-known in the literature [52–54].

The systems are coupled to the probe and control fields defined with the use of their Rabi frequencies as follows

$$\begin{aligned}\Omega_p(t) &= \Omega_p \cos(\omega_p t),\\ \Omega_c(t) &= \Omega_c \cos(\omega_c t),\end{aligned}$$

where $\hbar\Omega_p = \vec{E}_p \cdot \vec{d}_{ij}$ for $(i,j) \in \{(g_1,e),(g,e_1),(g,m)\}$, and $\hbar\Omega_c = \vec{E}_c \cdot \vec{d}_{kl}$ for $(k,l) \in \{(g_2,e),(g,e_2),(m,e)\}$. Vectors $\vec{d}_{ij}$, and $\vec{d}_{kl}$ are the transition dipole moments of the corresponding energy levels pairs. From now, for the simplicity of notation, these dipole moments will have subscripts p and c indicating pairs coupled by the probe and control fields $\vec{d}_{ij} \equiv \vec{d}_p$, $\vec{d}_{kl} \equiv \vec{d}_c$. Hence, the total dipole moment operator reads

$$\hat{\vec{d}} = \vec{d}_p^{\star}\hat{\sigma}_p^{+} + \vec{d}_p\hat{\sigma}_p^{-} + \vec{d}_c^{\star}\hat{\sigma}_c^{+} + \vec{d}_c\hat{\sigma}_c^{-}. \tag{2.37}$$

The general Hamiltonian including (2.36) reads

$$\hat{H}^{\alpha}(t) = \hat{H}^{\alpha}_{\text{sys}} - \hbar\Omega_p^{\star}\cos(\omega_p t)\hat{\sigma}_p^{+} - \hbar\Omega_c^{\star}\cos(\omega_c t)\hat{\sigma}_c^{+} + h.c. \quad \text{for } \alpha \in \{\Lambda, V, \Xi\}, \tag{2.38}$$

where *h.c.* means *Hermitian conjugation*, and contains additional $\hat{\sigma}^{-}_{p,c}$ terms. The time-dependent form of the Hamiltonian can be approximated similarly to the unitary transformation (2.20) used for the two-level system. However, the appearance of two external fields with two different frequencies complicates the problem and the unitary transformation cannot be expressed just with $\hat{\sigma}^{z}_{p,c}$ operators. The most convenient is to use, for the moment, the sets of operators of the form $\{|i\rangle\langle i|\}_{|i\rangle \in \mathcal{B}^{\alpha}}$ for $\alpha \in \{\Lambda, V, \Xi\}$. The unitary transformations for each configuration read [54]

$$\begin{aligned}
U^{\Lambda}_{\text{RWA}}(t) &= \mathrm{e}^{\mathrm{i}\omega_p t}\,|e\rangle\langle e| + \mathrm{e}^{\mathrm{i}(\omega_p-\omega_c)t}\,|g_2\rangle\langle g_2| + |g_1\rangle\langle g_1|\,,\\
\mathrm{i}\hbar\frac{\mathrm{d}}{\mathrm{d}t}U^{\Lambda}_{\text{RWA}}(U^{\Lambda}_{\text{RWA}})^{\dagger} &= -\hbar\omega_p\,|e\rangle\langle e| - \hbar(\omega_p-\omega_c)\,|g_2\rangle\langle g_2|\,,\\
U^{V}_{\text{RWA}}(t) &= \mathrm{e}^{\mathrm{i}\omega_p t}\,|e_1\rangle\langle e_1| + \mathrm{e}^{\mathrm{i}\omega_c t}\,|e_2\rangle\langle e_2| + |g\rangle\langle g|\,,\\
\mathrm{i}\hbar\frac{\mathrm{d}}{\mathrm{d}t}U^{V}_{\text{RWA}}(U^{V}_{\text{RWA}})^{\dagger} &= -\hbar\omega_p\,|e_1\rangle\langle e_1| - \hbar\omega_c\,|e_2\rangle\langle e_2|\,,\\
U^{\Xi}_{\text{RWA}}(t) &= \mathrm{e}^{\mathrm{i}\omega_p t}\,|m\rangle\langle m| + \mathrm{e}^{\mathrm{i}(\omega_p+\omega_c)t}\,|e\rangle\langle e| + |g\rangle\langle g|\,,\\
\mathrm{i}\hbar\frac{\mathrm{d}}{\mathrm{d}t}U^{\Xi}_{\text{RWA}}(U^{\Xi}_{\text{RWA}})^{\dagger} &= -\hbar\omega_p\,|m\rangle\langle m| - \hbar(\omega_p+\omega_c)\,|e\rangle\langle e|\,.
\end{aligned} \tag{2.39}$$

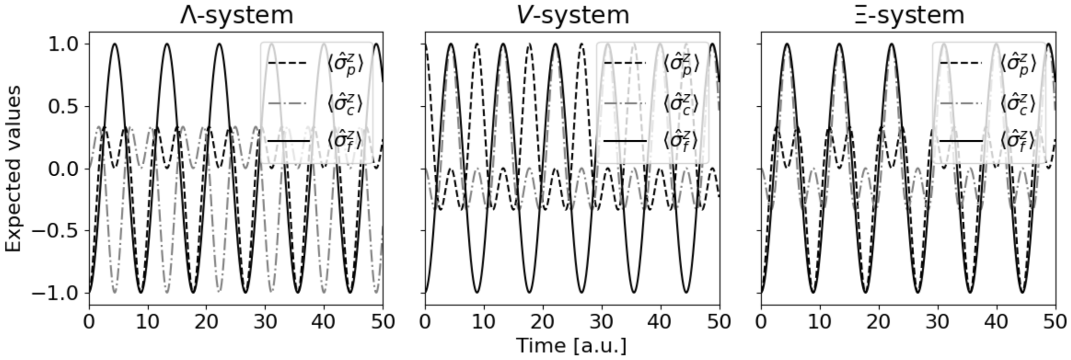

Figure 2.9: The evolution of the populations in three-level systems driven by plane-wave probe and control fields.

This definition provides the following transformations of the σ-operators

$$
\begin{aligned}
U^{\alpha}_{\mathrm{RWA}}\hat{\sigma}^{z}_{p,c}(U^{\alpha}_{\mathrm{RWA}})^{\dagger} &= \hat{\sigma}^{z}_{p,c},\\
U^{\alpha}_{\mathrm{RWA}}\hat{\sigma}^{\pm}_{p,c}(U^{\alpha}_{\mathrm{RWA}})^{\dagger} &= \mathrm{e}^{\pm\mathrm{i}\omega_{p,c}t}\hat{\hat{\sigma}}^{\pm}_{p,c},\\
U^{\alpha}_{\mathrm{RWA}}\hat{\sigma}^{\pm}_{f}(U^{\alpha}_{\mathrm{RWA}})^{\dagger} &= \begin{cases} \mathrm{e}^{\pm\mathrm{i}(\omega_p-\omega_c)t}\hat{\hat{\sigma}}^{\pm}_{f}, & \text{for } \Lambda,\\ \mathrm{e}^{\mp\mathrm{i}(\omega_p-\omega_c)t}\hat{\hat{\sigma}}^{\pm}_{f}, & \text{for } V,\\ \mathrm{e}^{\pm\mathrm{i}(\omega_p+\omega_c)t}\hat{\hat{\sigma}}^{\pm}_{f} & \text{for } \Xi, \end{cases}
\end{aligned}
$$

for $\alpha \in \{\Lambda, V, \Xi\}$. Although the unitary transformation (2.39) is significantly different from the one for two-level system (2.20), it has the same effect on the dynamics of the $\hat{\sigma}^z$ and flip operators, transforming the latter to slowly varying envelopes. The transformed Hamiltonians can be expressed as

$$
\begin{aligned}
\hat{\hat{H}}^{\alpha}(t) = &\underbrace{-\frac{1}{3}\hbar\left(\left(2\delta_p \mp \delta_c\right)\hat{\sigma}^{z}_{p} + \left(2\delta_c \mp \delta_p\right)\hat{\sigma}^{z}_{c}\right) - \frac{1}{2}\hbar\left(\Omega^{\star}_{p}\hat{\hat{\sigma}}^{+}_{p} + \Omega^{\star}_{c}\hat{\hat{\sigma}}^{+}_{c}\right) + h.c.}_{\hat{H}^{\alpha}_{\mathrm{RWA}}}\\
&-\frac{1}{2}\hbar\left(\Omega^{\star}_{p}\hat{\hat{\sigma}}^{+}_{p} + \Omega^{\star}_{c}\hat{\hat{\sigma}}^{+}_{c}\right)\mathrm{e}^{2\mathrm{i}\omega_p t} + h.c. \quad \text{for } \alpha \in \{\Lambda, V, \Xi\}.
\end{aligned} \tag{2.40}
$$

The ∓ signs in the first brackets differentiate between the Λ and V configurations, where the minus sign applies, and the Ξ configuration, where the plus sign is correct. The Hamiltonian $\hat{H}^{\alpha}_{\mathrm{RWA}}$ evaluated in Eq. (2.40) can be divided into two parts: one involving operators corresponding to the evolution under the influence of the probe field and the other involving analogous operators for the control field. However, operators in these separate parts do not commute as $[\hat{\sigma}^{z}_{p,c}, \hat{\hat{\sigma}}^{\pm}_{c,p}] = \pm\hat{\hat{\sigma}}^{\pm}_{c,p}$ for Λ and V, and $[\hat{\sigma}^{z}_{p,c}, \hat{\hat{\sigma}}^{\pm}_{c,p}] = \mp\hat{\hat{\sigma}}^{\pm}_{c,p}$ for Ξ.

The Bloch equations can be evaluated as previously in (2.22) by using von Neumann equation

$$
\mathrm{i}\hbar\frac{\mathrm{d}}{\mathrm{d}t}\hat{\hat{\rho}}(t) = [\hat{H}^{\alpha}_{\mathrm{RWA}}, \hat{\hat{\rho}}(t)].
$$

The expected values of five operators: $\hat{\sigma}^z_{p,c}$, and $\hat{\sigma}^+_{p,c,f}$, provide full information on the evolution of the system as $\hat{\sigma}^-_{p,c,f} = (\hat{\sigma}^+_{p,c,f})^\dagger$, and $\hat{\sigma}^z_f$ can be expressed as $\hat{\sigma}^z_p - \hat{\sigma}^z_c$, $\hat{\sigma}^z_c - \hat{\sigma}^z_p$, and $\hat{\sigma}^z_p + \hat{\sigma}^z_c$ for Λ, V, and Ξ, respectively. The generally written explicit Bloch equations for these expected values of the operators read

$$\mathrm{i}\hbar\frac{\mathrm{d}}{\mathrm{d}t}\langle\hat{\sigma}^z_p\rangle = -\hbar\left(\Omega^\star_p\langle\hat{\sigma}^+_p\rangle - \Omega_p\langle\hat{\sigma}^-_p\rangle\right) \mp \frac{1}{2}\hbar\left(\Omega^\star_c\langle\hat{\sigma}^+_c\rangle - \Omega_c\langle\hat{\sigma}^-_c\rangle\right), \tag{2.41a}$$

$$\mathrm{i}\hbar\frac{\mathrm{d}}{\mathrm{d}t}\langle\hat{\sigma}^z_c\rangle = -\hbar\left(\Omega^\star_c\langle\hat{\sigma}^+_c\rangle - \Omega_c\langle\hat{\sigma}^-_c\rangle\right) \mp \frac{1}{2}\hbar\left(\Omega^\star_p\langle\hat{\sigma}^+_p\rangle - \Omega_p\langle\hat{\sigma}^-_p\rangle\right), \tag{2.41b}$$

$$\mathrm{i}\hbar\frac{\mathrm{d}}{\mathrm{d}t}\langle\hat{\sigma}^+_p\rangle = \hbar\delta_p\langle\hat{\sigma}^+_p\rangle - \frac{1}{2}\hbar\Omega_p\langle\hat{\sigma}^z_p\rangle + \begin{cases} +\frac{1}{2}\hbar\Omega_c\langle\hat{\sigma}^+_f\rangle, & \text{for } \Lambda, \\ -\frac{1}{2}\hbar\Omega_c\langle\hat{\sigma}^-_f\rangle, & \text{for } V, \\ +\frac{1}{2}\hbar\Omega^\star_c\langle\hat{\sigma}^+_f\rangle, & \text{for } \Xi, \end{cases} \tag{2.41c}$$

$$\mathrm{i}\hbar\frac{\mathrm{d}}{\mathrm{d}t}\langle\hat{\sigma}^+_c\rangle = \hbar\delta_c\langle\hat{\sigma}^+_c\rangle - \frac{1}{2}\hbar\Omega_c\langle\hat{\sigma}^z_c\rangle + \begin{cases} +\frac{1}{2}\hbar\Omega_p\langle\hat{\sigma}^-_f\rangle, & \text{for } \Lambda, \\ -\frac{1}{2}\hbar\Omega_p\langle\hat{\sigma}^+_f\rangle, & \text{for } V, \\ -\frac{1}{2}\hbar\Omega^\star_p\langle\hat{\sigma}^+_f\rangle, & \text{for } \Xi, \end{cases} \tag{2.41d}$$

$$\mathrm{i}\hbar\frac{\mathrm{d}}{\mathrm{d}t}\langle\hat{\sigma}^+_f\rangle = \begin{cases} +\hbar\left(\delta_p - \delta_c\right)\langle\hat{\sigma}^+_f\rangle - \frac{1}{2}\hbar\Omega_p\langle\hat{\sigma}^-_c\rangle + \frac{1}{2}\hbar\Omega^\star_c\langle\hat{\sigma}^+_p\rangle, & \text{for } \Lambda, \\ -\hbar\left(\delta_p - \delta_c\right)\langle\hat{\sigma}^+_f\rangle - \frac{1}{2}\hbar\Omega^\star_p\langle\hat{\sigma}^+_c\rangle + \frac{1}{2}\hbar\Omega_c\langle\hat{\sigma}^-_p\rangle, & \text{for } V, \\ +\hbar\left(\delta_p + \delta_c\right)\langle\hat{\sigma}^+_f\rangle - \frac{1}{2}\hbar\Omega_p\langle\hat{\sigma}^+_c\rangle + \frac{1}{2}\hbar\Omega_c\langle\hat{\sigma}^+_p\rangle, & \text{for } \Xi. \end{cases} \tag{2.41e}$$

Once again, the $\mp$ sign provides distinction between configurations. As an example, Fig. 2.9 presents the evolution of the σ^z-operators (and hence the population) for the systems driven by equally strong probe and control fields in the form of plane waves. The population is initially in $|g_1\rangle$, $|e_1\rangle$, and $|g\rangle$ states for Λ, V, and Ξ configurations, respectively. Note that for the sake of symmetry in the figures, in the V-system, the excited state is the initial one. Surprisingly, even if there is no field that directly couples levels of the $\hat{\sigma}^z_f$ operator, the Rabi oscillations between them appear with maximal amplitude providing effective transfer of population.

Even more interesting and counterintuitive behavior can be observed for Gaussian-shaped pulses. If the same initial states as previously are used for each case and an adiabatic control field is switched on first, it will couple unoccupied levels. Switching on an adiabatic probe field later provides an ideal transfer of population between states noncoupled by any field. Moreover, the third state will be unoccupied during the entire process. In Fig. 2.10 shapes and temporal positions of such pulses are shown, while the resulting population transfer for each configuration can be found in Fig. 2.11. This provides direct evidence of the significance of the coherence built-up even between unoccupied levels. The process is known as the mentioned earlier Stimulated Raman Adiabatic Passage [15, 16] and is used broadly in quantum optics.

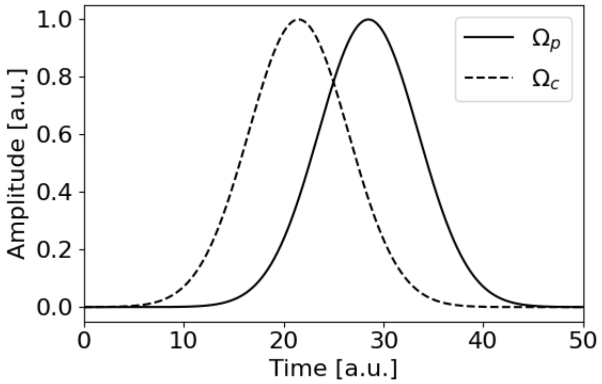

Figure 2.10: Shapes and order of probe and control fields driving three-level systems. Note that the control pulse is sent before the probe one.

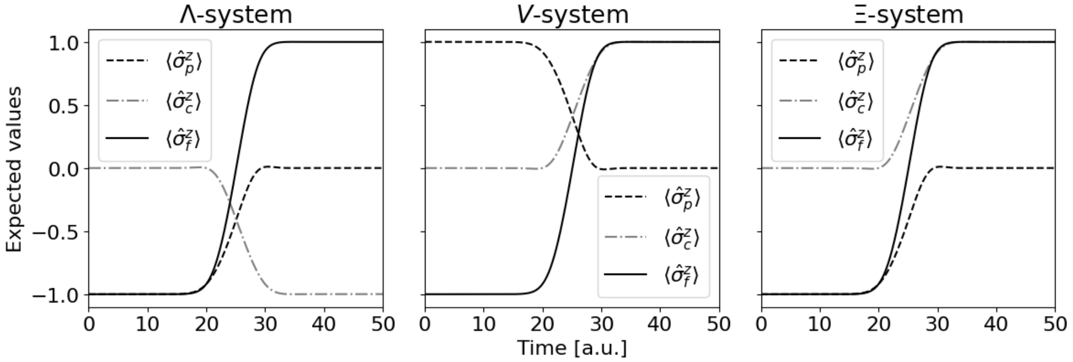

Figure 2.11: STIRAP process for each configuration. The evolution of the operators provides evidence that in each case the levels coupled to both fields ($|e\rangle$, $|g\rangle$, and $|m\rangle$, respectively) are not occupied while the population is fully transferred from initial to final states.

2.2.3 *Dissipative Bloch equations*

In analogy to the two-level system case, the dissipation processes can be incorporated into the evolution calculations by the GKLS equation (2.24) described in Sec. 2.1.4. However, this time, due to the higher number of energy levels, and hence available configurations, the incoherent system–reservoir interactions are described by more $\hat{L}$ operators. Moreover, the description is qualitatively different for each case.

For the spontaneous emission process, in each configuration, a pair of the $\hat{L}$ operators describes the evolution. Due to the existence of the forbidden transition (given by $\hat\sigma_f^\pm$), these operators correspond to the flip operators as $\hat{L}_p^{\text{se}} = \hat\sigma_p^-$ and $\hat{L}_c^{\text{se}} = \hat\sigma_c^-$ with respective gamma rates $\gamma_{p,c}^{\text{se}}$. The additional terms that have to be added to the Bloch equations (2.41) for a given operator $\hat\sigma$ can be calculated using the equation

$$\mathcal{L}_{\text{se}}(\langle\hat\sigma\rangle) = \mathrm{i}\hbar \sum_{i\in\{p,c\}} \gamma_i^{\text{se}} \left(\text{Tr}\big(\hat\sigma\hat\sigma_i^-\hat\rho(t)\hat\sigma_i^+\big) - \frac{1}{2}\left(\text{Tr}\big(\hat\sigma\hat\sigma_i^+\hat\sigma_i^-\hat\rho(t)\big) + \text{Tr}\big(\hat\sigma\hat\rho(t)\hat\sigma_i^+\hat\sigma_i^-\big)\right)\right).$$

Hence, the results read

$$\mathcal{L}_{\text{se}}(\langle\hat{\sigma}_p^z\rangle) = -\frac{1}{3}\mathrm{i}\hbar \begin{cases} \left(2\gamma_p^{\text{se}} + \gamma_c^{\text{se}}\right)\langle\hat{\sigma}_p^z\rangle + \left(2\gamma_p^{\text{se}} + \gamma_c^{\text{se}}\right)\langle\hat{\sigma}_c^z\rangle + \left(2\gamma_p^{\text{se}} + \gamma_c^{\text{se}}\right) & \text{for } \Lambda, \\ \left(4\gamma_p^{\text{se}} - \gamma_c^{\text{se}}\right)\langle\hat{\sigma}_p^z\rangle - \left(2\gamma_p^{\text{se}} - 2\gamma_c^{\text{se}}\right)\langle\hat{\sigma}_c^z\rangle + \left(2\gamma_p^{\text{se}} + \gamma_c^{\text{se}}\right) & \text{for } V, \\ \left(2\gamma_p^{\text{se}} - \gamma_c^{\text{se}}\right)\langle\hat{\sigma}_p^z\rangle - \left(2\gamma_p^{\text{se}} + 2\gamma_c^{\text{se}}\right)\langle\hat{\sigma}_c^z\rangle + \left(2\gamma_p^{\text{se}} - \gamma_c^{\text{se}}\right) & \text{for } \Xi, \end{cases} \tag{2.42a}$$

$$\mathcal{L}_{\text{se}}(\langle\hat{\sigma}_c^z\rangle) = -\frac{1}{3}\mathrm{i}\hbar \begin{cases} \left(2\gamma_c^{\text{se}} + \gamma_p^{\text{se}}\right)\langle\hat{\sigma}_c^z\rangle + \left(2\gamma_c^{\text{se}} + \gamma_p^{\text{se}}\right)\langle\hat{\sigma}_p^z\rangle + \left(2\gamma_c^{\text{se}} + \gamma_p^{\text{se}}\right) & \text{for } \Lambda, \\ \left(4\gamma_c^{\text{se}} - \gamma_p^{\text{se}}\right)\langle\hat{\sigma}_c^z\rangle - \left(2\gamma_c^{\text{se}} - 2\gamma_p^{\text{se}}\right)\langle\hat{\sigma}_p^z\rangle + \left(2\gamma_c^{\text{se}} + \gamma_p^{\text{se}}\right) & \text{for } V, \\ \left(4\gamma_c^{\text{se}} + \gamma_p^{\text{se}}\right)\langle\hat{\sigma}_c^z\rangle + \left(2\gamma_c^{\text{se}} - \gamma_p^{\text{se}}\right)\langle\hat{\sigma}_p^z\rangle + \left(2\gamma_c^{\text{se}} - \gamma_p^{\text{se}}\right) & \text{for } \Xi, \end{cases} \tag{2.42b}$$

$$\mathcal{L}_{\text{se}}(\langle\hat{\tilde{\sigma}}_p^{\pm}\rangle) = -\frac{1}{2}\mathrm{i}\hbar \begin{cases} \left(\gamma_p^{\text{se}} + \gamma_c^{\text{se}}\right)\langle\hat{\tilde{\sigma}}_p^{\pm}\rangle & \text{for } \Lambda, \\ \gamma_p^{\text{se}}\langle\hat{\tilde{\sigma}}_p^{\pm}\rangle & \text{for } V, \\ \gamma_p^{\text{se}}\langle\hat{\tilde{\sigma}}_p^{\pm}\rangle & \text{for } \Xi, \end{cases} \tag{2.42c}$$

$$\mathcal{L}_{\text{se}}(\langle\hat{\tilde{\sigma}}_c^{\pm}\rangle) = -\frac{1}{2}\mathrm{i}\hbar \begin{cases} \left(\gamma_p^{\text{se}} + \gamma_c^{\text{se}}\right)\langle\hat{\tilde{\sigma}}_c^{\pm}\rangle & \text{for } \Lambda, \\ \gamma_c^{\text{se}}\langle\hat{\tilde{\sigma}}_c^{\pm}\rangle & \text{for } V, \\ \left(\gamma_p^{\text{se}} + \gamma_c^{\text{se}}\right)\langle\hat{\tilde{\sigma}}_c^{\pm}\rangle & \text{for } \Xi, \end{cases} \tag{2.42d}$$

$$\mathcal{L}_{\text{se}}(\langle\hat{\tilde{\sigma}}_f^{\pm}\rangle) = -\frac{1}{2}\mathrm{i}\hbar \begin{cases} 0 & \text{for } \Lambda, \\ \left(\gamma_p^{\text{se}} + \gamma_c^{\text{se}}\right)\langle\hat{\tilde{\sigma}}_f^{\pm}\rangle & \text{for } V, \\ \gamma_c^{\text{se}}\langle\hat{\tilde{\sigma}}_f^{\pm}\rangle & \text{for } \Xi. \end{cases} \tag{2.42e}$$

It is worth noticing the appearance of the term $\mathcal{L}_{\text{se}}(\langle\hat{\tilde{\sigma}}_f^{\pm}\rangle)$, which affects the evolution of the coherence of states not directly coupled to the external fields nor the reservoir. Surprisingly, for the Λ configuration, this coherence is protected from being suppressed in a spontaneous emission process, whereas the opposite happens for the V configuration – decoherence is fast due to the contribution from both pairs. The Ξ configuration is between these two, as only the decoherence of the upper pair affects it.

In the same way, one can find terms that describe incoherent pumping in the system. However, contrary to the two-level system, due to the two available transition channels, pumping can be realized by operator $\hat{L}_p^{\text{pu}} = \hat{\sigma}_p^{+}$ or $\hat{L}_c^{\text{pu}} = \hat{\sigma}_c^{+}$ or both at the same time with corresponding gamma rates $\gamma_{p,c}^{\text{pu}}$, as below

$$\mathcal{L}_{\mathrm{pu}}(\langle\hat{\sigma}_p^z\rangle) = -\frac{1}{3}\mathrm{i}\hbar \begin{cases} -\left(2\gamma_p^{\mathrm{pu}} - 2\gamma_c^{\mathrm{pu}}\right)\langle\hat{\sigma}_p^z\rangle + \left(4\gamma_p^{\mathrm{pu}} - \gamma_c^{\mathrm{pu}}\right)\langle\hat{\sigma}_c^z\rangle - \left(2\gamma_p^{\mathrm{pu}} + \gamma_c^{\mathrm{pu}}\right) & \text{for } \Lambda, \\ \left(2\gamma_p^{\mathrm{pu}} + \gamma_c^{\mathrm{pu}}\right)\langle\hat{\sigma}_p^z\rangle + \left(2\gamma_p^{\mathrm{pu}} + \gamma_c^{\mathrm{pu}}\right)\langle\hat{\sigma}_c^z\rangle - \left(2\gamma_p^{\mathrm{pu}} + \gamma_c^{\mathrm{pu}}\right) & \text{for } V, \\ \left(4\gamma_p^{\mathrm{pu}} + \gamma_c^{\mathrm{pu}}\right)\langle\hat{\sigma}_p^z\rangle + \left(2\gamma_p^{\mathrm{pu}} - \gamma_c^{\mathrm{pu}}\right)\langle\hat{\sigma}_c^z\rangle - \left(2\gamma_p^{\mathrm{pu}} - \gamma_c^{\mathrm{pu}}\right) & \text{for } \Xi, \end{cases} \tag{2.43a}$$

$$\mathcal{L}_{\mathrm{pu}}(\langle\hat{\sigma}_c^z\rangle) = -\frac{1}{3}\mathrm{i}\hbar \begin{cases} -\left(2\gamma_c^{\mathrm{pu}} - 2\gamma_p^{\mathrm{pu}}\right)\langle\hat{\sigma}_c^z\rangle + \left(4\gamma_c^{\mathrm{pu}} - \gamma_p^{\mathrm{pu}}\right)\langle\hat{\sigma}_p^z\rangle - \left(2\gamma_c^{\mathrm{pu}} + \gamma_p^{\mathrm{pu}}\right) & \text{for } \Lambda, \\ \left(2\gamma_c^{\mathrm{pu}} + \gamma_p^{\mathrm{pu}}\right)\langle\hat{\sigma}_c^z\rangle + \left(2\gamma_c^{\mathrm{pu}} + \gamma_p^{\mathrm{pu}}\right)\langle\hat{\sigma}_p^z\rangle - \left(2\gamma_c^{\mathrm{pu}} + \gamma_p^{\mathrm{pu}}\right) & \text{for } V, \\ \left(2\gamma_c^{\mathrm{pu}} - \gamma_p^{\mathrm{pu}}\right)\langle\hat{\sigma}_c^z\rangle - \left(2\gamma_c^{\mathrm{pu}} + 2\gamma_p^{\mathrm{pu}}\right)\langle\hat{\sigma}_p^z\rangle - \left(2\gamma_c^{\mathrm{pu}} - \gamma_p^{\mathrm{pu}}\right) & \text{for } \Xi, \end{cases} \tag{2.43b}$$

$$\mathcal{L}_{\mathrm{pu}}(\langle\hat{\tilde{\sigma}}_p^{\pm}\rangle) = -\frac{1}{2}\mathrm{i}\hbar \begin{cases} \gamma_p^{\mathrm{pu}}\langle\hat{\tilde{\sigma}}_p^{\pm}\rangle & \text{for } \Lambda, \\ \left(\gamma_p^{\mathrm{pu}} + \gamma_c^{\mathrm{pu}}\right)\langle\hat{\tilde{\sigma}}_p^{\pm}\rangle & \text{for } V, \\ \left(\gamma_p^{\mathrm{pu}} + \gamma_c^{\mathrm{pu}}\right)\langle\hat{\tilde{\sigma}}_p^{\pm}\rangle & \text{for } \Xi, \end{cases} \tag{2.43c}$$

$$\mathcal{L}_{\mathrm{pu}}(\langle\hat{\tilde{\sigma}}_c^{\pm}\rangle) = -\frac{1}{2}\mathrm{i}\hbar \begin{cases} \gamma_c^{\mathrm{pu}}\langle\hat{\tilde{\sigma}}_c^{\pm}\rangle & \text{for } \Lambda, \\ \left(\gamma_p^{\mathrm{pu}} + \gamma_c^{\mathrm{pu}}\right)\langle\hat{\tilde{\sigma}}_c^{\pm}\rangle & \text{for } V, \\ \gamma_c^{\mathrm{pu}}\langle\hat{\tilde{\sigma}}_c^{\pm}\rangle & \text{for } \Xi, \end{cases} \tag{2.43d}$$

$$\mathcal{L}_{\mathrm{pu}}(\langle\hat{\tilde{\sigma}}_f^{\pm}\rangle) = -\frac{1}{2}\mathrm{i}\hbar \begin{cases} \left(\gamma_p^{\mathrm{pu}} + \gamma_c^{\mathrm{pu}}\right)\langle\hat{\tilde{\sigma}}_f^{\pm}\rangle & \text{for } \Lambda, \\ 0 & \text{for } V, \\ \gamma_p^{\mathrm{pu}}\langle\hat{\tilde{\sigma}}_f^{\pm}\rangle & \text{for } \Xi. \end{cases} \tag{2.43e}$$

In this case, pumping does not affect the coherence between the two excited states in the V configuration. This can be understood by viewing pumping as the reverse of spontaneous emission. As a result, the V system described in the pumping process is mathematically analogous to the Λ system with included spontaneous emission.

Finally, similarly to the previous processes, the pure dephasing is also described by two operators $\hat{L}_p^{\mathrm{de}} = \frac{1}{\sqrt{2}}\hat{\sigma}_p^z$ and $\hat{L}_c^{\mathrm{de}} = \frac{1}{\sqrt{2}}\hat{\sigma}_c^z$ with $\gamma_{p,c}^{\mathrm{de}}$, respectively, providing following results

$$\mathcal{L}_{\mathrm{de}}(\langle\hat{\sigma}_p^z\rangle) = 0, \tag{2.44a}$$

$$\mathcal{L}_{\mathrm{de}}(\langle\hat{\sigma}_c^z\rangle) = 0, \tag{2.44b}$$

$$\mathcal{L}_{\mathrm{de}}(\langle\hat{\tilde{\sigma}}_p^{\pm}\rangle) = -\frac{1}{4}\left(4\gamma_p^{\mathrm{de}} + \gamma_c^{\mathrm{de}}\right)\langle\hat{\tilde{\sigma}}_p^{\pm}\rangle, \tag{2.44c}$$

$$\mathcal{L}_{\mathrm{de}}(\langle\hat{\tilde{\sigma}}_c^{\pm}\rangle) = -\frac{1}{4}\left(4\gamma_c^{\mathrm{de}} + \gamma_p^{\mathrm{de}}\right)\langle\hat{\tilde{\sigma}}_c^{\pm}\rangle, \tag{2.44d}$$

$$\mathcal{L}_{\mathrm{de}}(\langle\hat{\tilde{\sigma}}_f^{\pm}\rangle) = -\frac{1}{4}\left(\gamma_p^{\mathrm{de}} + \gamma_c^{\mathrm{de}}\right)\langle\hat{\tilde{\sigma}}_f^{\pm}\rangle. \tag{2.44e}$$

As in the two-level system case, the dephasing process does not affect the population and only coherence is dumped. Moreover, the forbidden direct transition given by $\langle\hat{\sigma}_f^{\pm}\rangle$ is affected even if the $\hat{\sigma}_f^z$ operator was not explicitly involved, similarly to the spontaneous emission and pumping processes.

In summary, the full Bloch equations that describe the evolution of the three-level systems with coherent and incoherent external fields are given by Eqs. (2.41 – 2.44).

2.3 MEDIA CONSISTING OF TWO- AND THREE-LEVEL SYSTEMS

In this section, the generalization of previously introduced concepts continues by describing the interaction between classical light and ensembles of quantum two- and three-level systems, as introduced in Sections 2.1 and 2.2, respectively. The focus is on the behavior of these systems when subjected to classical electromagnetic fields and on how their collective response shapes the properties of light propagating through the medium.

For polar two-level systems driven by near-resonant fields, the medium acts as a source of low-frequency radiation, highlighting the fundamental impact of the permanent dipoles on the emission spectra. On the other hand, besides all variety of concepts, the ensembles of three-level systems dressed by strong control fields support slow and fast propagation of the probe field.

2.3.1 *Electric susceptibility*

Electric susceptibility χ characterizes the response of an atomic ensemble to an external electromagnetic field. Specifically, it describes the polarization $\vec{P}$ of the medium induced by such a field $\vec{E}$. This property plays a crucial role in determining how light propagates through the medium by influencing the absorption and dispersion relations. In classical electrodynamics, for the linear, isotropic, and dielectric media, the relation between these quantities is given in the frequency domain as

$$\vec{P}(\vec{r},\omega) = \epsilon_0\chi(\omega)\vec{E}(\vec{r},\omega), \tag{2.45}$$

where ϵ_0 is the vacuum permittivity constant and $\vec{r}$ is the position vector. Note that χ does not depend on position, as the isotropy of the medium ensures the same properties at each point. Additionally, for the electric field in the form of the plane wave $\vec{E}(\vec{r},t) = \vec{E}_0\cos\left(\vec{k}\vec{r} - \nu t\right)$, the transformation to the spectral domain reads

$$\begin{aligned}\vec{E}(\vec{r},\omega) &= \frac{1}{2}\vec{E}_0 e^{-i\vec{k}\vec{r}}\int_{-\infty}^{\infty} e^{i(\nu-\omega)t}dt + \frac{1}{2}\vec{E}_0 e^{i\vec{k}\vec{r}}\int_{-\infty}^{\infty} e^{-i(\nu+\omega)t}dt\\ &= \frac{1}{2}\vec{E}_0 e^{-i\vec{k}\vec{r}}\delta(\nu-\omega) + \frac{1}{2}\vec{E}_0 e^{i\vec{k}\vec{r}}\delta(\nu+\omega),\end{aligned}$$

where $\vec{k}$ is the wave vector, ν is a frequency, and $\delta(x)$ is the Dirac delta. The propagation direction was chosen arbitrary, and will be the same for all fields along the chapter. The polarization can be split into two terms regarding positive and negative frequencies ω: $\vec{P}(\vec{r},\omega) = \vec{P}^{+}(\vec{r},\omega)\delta(\nu-\omega) + \vec{P}^{-}(\vec{r},-\omega)\delta(\nu+\omega)$, where

$$\vec{P}^{+}(\vec{r},\omega) = \frac{1}{2}\epsilon_0\chi(\omega)\vec{E}_0 \mathrm{e}^{-\mathrm{i}\vec{k}\vec{r}}, \tag{2.46a}$$

$$\vec{P}^{-}(\vec{r},-\omega) = \frac{1}{2}\epsilon_0\chi(-\omega)\vec{E}_0 \mathrm{e}^{\mathrm{i}\vec{k}\vec{r}}. \tag{2.46b}$$

The electric susceptibility function contains full information about the medium regardless of whether classical or quantum theory describes it. Hence, the quantum description of the polarization has to be used to obtain it in the case of two- or three-energy-level system ensembles. The induced polarization $\vec{P}$ represents the induced dipole moment per unit volume, according to the formula [41]

$$\vec{P}(\vec{r},t) = N\langle\hat{\vec{d}}(\vec{r},t)\rangle, \tag{2.47}$$

where N stands for the density of quantum systems, and $\hat{\vec{d}}$ is the dipole moment operator defined by Eq. (2.27) for polar two-level systems and by Eq. (2.37) for nonpolar three-level systems. In this case, due to the large number of systems, the position vector $\vec{r}$ is treated as a continuous quantity. To find the exact formula for the polarization, the Bloch equations have to be used: Eq. (2.33) for the two-level systems, and Eqs. (2.41 – 2.44) for three-level systems. As a result, polarization can be found as a linear combination of density matrix element describing the medium.

By combining the two expressions for polarization, (2.45) and (2.47), the susceptibility function for a given medium can be found. However, note that these expressions are written in two different domains: frequency and time, and are related by a Fourier transform, which makes the general problem rather complicated. Yet, in the special case of time-independent media, the problem reduces to solving the stationary form of the Bloch equations for $t \to \infty$, which will be relatively simple to transform. For the equations with included incoherent processes, it means that terms with time derivatives are equal to zero. Due to that, in the matrix form, set of the polar two-level system equations (2.33) read

$$\vec{0} = \begin{pmatrix} -\mathrm{i}\delta - \gamma_\perp & 0 & \frac{1}{2}\mathrm{i}\widetilde{\Omega}_R \\ 0 & \mathrm{i}\delta - \gamma_\perp & -\frac{1}{2}\mathrm{i}\widetilde{\Omega}_R^\star \\ \mathrm{i}\widetilde{\Omega}_R^\star & -\mathrm{i}\widetilde{\Omega}_R & -(\Gamma + \gamma_{\mathrm{pu}}) \end{pmatrix} \begin{pmatrix} \langle\hat{\tilde{\sigma}}^{+}\rangle_s \\ \langle\hat{\tilde{\sigma}}^{-}\rangle_s \\ \langle\hat{\sigma}_z\rangle_s \end{pmatrix} - \begin{pmatrix} 0 \\ 0 \\ (\Gamma - \gamma_{\mathrm{pu}}) \end{pmatrix},$$

where subscript s indicates stationary solution. At this point stationary states are easy to find

$$\langle\hat{\tilde{\sigma}}^{\pm}\rangle_s = -\frac{\frac{1}{2}\widetilde{\Omega}_R\left(\delta \pm \mathrm{i}\gamma_\perp\right)\left(\Gamma - \gamma_{\mathrm{pu}}\right)}{\left(\delta^2 + \gamma_\perp^2\right)\left(\Gamma + \gamma_{\mathrm{pu}}\right) + |\widetilde{\Omega}_R|^2\gamma_\perp}, \tag{2.48a}$$

$$\langle\hat{\sigma}_z\rangle_s = -\frac{\left(\delta^2 + \gamma_\perp^2\right)\left(\Gamma - \gamma_{\mathrm{pu}}\right)}{\left(\delta^2 + \gamma_\perp^2\right)\left(\Gamma + \gamma_{\mathrm{pu}}\right) + |\widetilde{\Omega}_R|^2\gamma_\perp}. \tag{2.48b}$$

For the nonpolar three-level system described by equations (2.41 – 2.44) the solutions for each configuration are significantly more complicated, thus important assumptions have to be made. First, the control field has a form of the plane wave and is strong enough that it does not change along the medium. Second, it modifies the medium for the much weaker probe field $\Omega_p \ll \Omega_c$, which can have a spatio-temporal shape. This provides following forms of the electric fields

$$\vec{E}_c(\vec{r},t) = \vec{E}_c^0 \cos\Big(\vec{k}_c\vec{r} - \nu_c t\Big), \tag{2.49a}$$

$$\vec{E}_p(\vec{r},t) = \vec{E}_p^0(\vec{r},t) \cos\Big(\vec{k}_p\vec{r} - \nu_p t\Big), \tag{2.49b}$$

where $\vec{k}_{c,p}$ and $\nu_{c,p}$ are the control and probe fields wave vectors and frequencies, respectively. Additionally, it will be assumed that the shape $\vec{E}_p^0(\vec{r},t)$ is spectrally narrow, i.e., the Fourier transformation gives the same result as for the plane wave. Due to the above, the medium response to the probe pulse is determined by the matrix element $\langle\hat{\tilde{\sigma}}_p^{\pm}\rangle$ [41]. Finally, the last assumption that probe pulse is also weaker than total γ-rates appearing in the system, and so the Taylor expansion can be used regarding Ω_p variable. Thus, the series can be truncated on the linear terms, and the exact form, for included incoherent process in the form of only spontaneous emission for the sake of simplicity, read

$$\langle\hat{\tilde{\sigma}}_p^{+}\rangle_s^{\Lambda} = \frac{\frac{1}{2}\mathrm{i}\Omega_p}{-\mathrm{i}\delta_p + \frac{1}{2}(\gamma_p+\gamma_c) + \frac{\frac{1}{4}|\Omega_c|^2}{-\mathrm{i}(\delta_p-\delta_c)}} + \mathcal{O}(\Omega_p^3), \tag{2.50a}$$

$$\langle\hat{\tilde{\sigma}}_p^{+}\rangle_s^{V} = \frac{1}{2}\mathrm{i}\Omega_p \frac{\left(\frac{1}{4}\gamma_c^2 + \delta_c^2 + \frac{1}{4}|\Omega_c|^2\right) + \left(\mathrm{i}\delta_c - \frac{1}{2}\gamma_c\right)\frac{\frac{1}{4}|\Omega_c|^2}{-\mathrm{i}(\delta_p-\delta_c)+\frac{1}{2}(\gamma_p+\gamma_c)}}{\left(\frac{1}{4}\gamma_c^2 + \delta_c^2 + \frac{1}{2}|\Omega_c|^2\right)\left(-\mathrm{i}\delta_p + \frac{1}{2}\gamma_p + \frac{\frac{1}{4}|\Omega_c|^2}{-\mathrm{i}(\delta_p-\delta_c)+\frac{1}{2}(\gamma_p+\gamma_c)}\right)} + \mathcal{O}(\Omega_p^3), \tag{2.50b}$$

$$\langle\hat{\tilde{\sigma}}_p^{+}\rangle_s^{\Xi} = \frac{\frac{1}{2}\mathrm{i}\Omega_p}{-\mathrm{i}\delta_p + \frac{1}{2}(\gamma_p+\gamma_c) + \frac{\frac{1}{4}|\Omega_c|^2}{-\mathrm{i}(\delta_p+\delta_c)+\frac{1}{2}\gamma_c}} + \mathcal{O}(\Omega_p^3). \tag{2.50c}$$

Note the absence of Ω_p^2-terms.

As mentioned above, the polarization given by Eq. (2.46) is expressed in the spectral domain, whereas quantum theory provides a temporal form in Eq. (2.47). To be able to compare these two, the stationary solutions were found, and now the Fourier transformation can be performed. In the two-level system (2LS) case

$$\begin{aligned}
\vec{P}_{\mathrm{2LS}}(\omega) &= \int\limits_{-\infty}^{\infty} \vec{P}_{\mathrm{2LS}}(t)\mathrm{e}^{-\mathrm{i}\omega t}\mathrm{d}t \\
&= N\int\limits_{-\infty}^{\infty}\left(\vec{d}_{eg}\langle\hat{\tilde{\tilde{\sigma}}}^{+}\rangle_s \mathrm{e}^{\mathrm{i}\omega_c t}\mathrm{e}^{-\mathrm{i}\kappa_z\sin(\omega_c t)} + \vec{d}_{ge}\langle\hat{\tilde{\tilde{\sigma}}}^{-}\rangle_s \mathrm{e}^{-\mathrm{i}\omega_c t}\mathrm{e}^{\mathrm{i}\kappa_z\sin(\omega_c t)} + \left(\vec{d}_{ee} - \vec{d}_{gg}\right)\langle\hat{\sigma}_z\rangle_s\right)\mathrm{e}^{-\mathrm{i}\omega t}\mathrm{d}t \\
&\approx N\Bigg(\vec{d}_{eg}\langle\hat{\tilde{\tilde{\sigma}}}^{+}\rangle_s \underbrace{\int\limits_{-\infty}^{\infty}\mathrm{e}^{\mathrm{i}(\omega_c-\omega)t}\mathrm{d}t}_{\delta(\omega_c-\omega)} + \vec{d}_{ge}\langle\hat{\tilde{\tilde{\sigma}}}^{-}\rangle_s \underbrace{\int\limits_{-\infty}^{\infty}\mathrm{e}^{-\mathrm{i}(\omega_c+\omega)t}\mathrm{d}t}_{\delta(\omega_c+\omega)} + \left(\vec{d}_{ee} - \vec{d}_{gg}\right)\langle\hat{\sigma}_z\rangle_s \underbrace{\int\limits_{-\infty}^{\infty}\mathrm{e}^{-\mathrm{i}\omega t}\mathrm{d}t}_{\delta(\omega)}\Bigg),
\end{aligned}$$

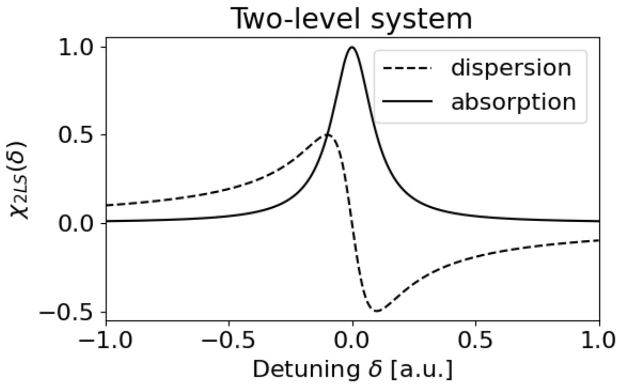

Figure 2.12: Imaginary (solid line) and real (dashed line) parts of the electric susceptibility for the medium of two-level systems. The imaginary part is responsible for the absorption in the medium, while real part provides information about the dispersion.

where the assumption of weak driving field was used as $\kappa_z \ll 1$, and hence $e^{\pm i\kappa_z \sin(\omega_c t)} \approx J_0(\kappa_z) \approx 1$. For convenience, the polarization can be split into three parts $\vec{P}_{2LS}(\omega) = \vec{P}^{+}_{2LS}(\omega)\delta(\omega_c - \omega) + \vec{P}^{-}_{2LS}(-\omega)\delta(\omega_c + \omega) + \vec{P}^{0}_{2LS}(0)\delta(\omega)$, for which

$$\vec{P}^{+}_{2LS}(\omega) = N\vec{d}_{eg}\langle\hat{\tilde{\tilde{\sigma}}}^{+}\rangle_s, \tag{2.51a}$$

$$\vec{P}^{-}_{2LS}(-\omega) = N\vec{d}_{ge}\langle\hat{\tilde{\tilde{\sigma}}}^{-}\rangle_s, \tag{2.51b}$$

$$\vec{P}^{0}_{2LS}(0) = N\left(\vec{d}_{ee} - \vec{d}_{gg}\right)\langle\hat{\sigma}_z\rangle_s. \tag{2.51c}$$

Since term $\vec{P}^{0}_{2LS}(0)$ does not depend linearly on the external field, it is negligible in the derivation of the electric susceptibility in the optical regime. Comparing fromulas for the polarizations in (2.46) and (2.51) (by realizing that $\nu = \omega_c$), using (2.48), recalling definitions of the Rabi frequency $\Omega_R(\vec{r})$ (2.23) and $\widetilde{\Omega}_R(\vec{r})$ (2.32) for the field amplitude $\vec{E}_0 \rightarrow \vec{E}_0 e^{i\vec{k}\vec{r}}$, the expression for the electric susceptibility for $\omega = \omega_c$ reads

$$\begin{aligned}\chi_{2LS}(\omega_c) &= \frac{N|\vec{d}_{eg}|^2}{\hbar\epsilon_0}\frac{2}{\kappa_z}J_1(\kappa_z)\frac{2\langle\hat{\tilde{\tilde{\sigma}}}^{+}\rangle_s(\vec{r})}{\widetilde{\Omega}_R(\vec{r})}\\ &= \frac{N|\vec{d}_{eg}|^2}{\hbar\epsilon_0}\frac{2}{\kappa_z}J_1(\kappa_z)\frac{i\left(\Gamma - \gamma_{pu}\right)}{\left(-i\delta - \gamma_\perp\right)\left(\Gamma + \gamma_{pu}\right) + \frac{|\widetilde{\Omega}_R|^2\gamma_\perp}{(i\delta - \gamma_\perp)}} \equiv \chi_{2LS}(\delta).\end{aligned} \tag{2.52}$$

Note that even for the assumption $\kappa_z \ll 1$, the influence of the permanent dipoles is visible. Moreover, there is no spatial dependency, as intended. The resulting plot of electric susceptibility is shown in Fig. 2.12. The real part of this complex quantity describes dispersion in the system, whereas imaginary part provides absorption. Note that at resonance $\delta = 0$ the absorption is the highest which is an indication of strong interaction between the medium and field. Also in that region the dispersion is anomalous – descreases with the increase of the field's frequency, which is discussed in details in Sec. 2.3.3.

Further analysis of the polar two-level medium regarding low-frequency radiation emission is investigated in article **A2**.

In the three-level systems case, two fields are present, hence in analogy to the Eq. (2.46), there are pairs of plus and minus polarization terms for the probe, and control fields given in Eq. (2.49)

$$\vec{P}_p^+(\vec{r},\omega) \approx \frac{1}{2}\epsilon_0\chi_p(\omega)\vec{E}_p^0(\vec{r},\omega)\mathrm{e}^{-\mathrm{i}\vec{k}_p\vec{r}}, \tag{2.53a}$$

$$\vec{P}_p^-(\vec{r},-\omega) \approx \frac{1}{2}\epsilon_0\chi_p(-\omega)\vec{E}_p^0(\vec{r},\omega)\mathrm{e}^{\mathrm{i}\vec{k}_p\vec{r}}, \tag{2.53b}$$

$$\vec{P}_c^+(\vec{r},\omega) = \frac{1}{2}\epsilon_0\chi_c(\omega)\vec{E}_c^0\mathrm{e}^{-\mathrm{i}\vec{k}_c\vec{r}}, \tag{2.53c}$$

$$\vec{P}_c^-(\vec{r},-\omega) = \frac{1}{2}\epsilon_0\chi_c(-\omega)\vec{E}_c^0\mathrm{e}^{\mathrm{i}\vec{k}_c\vec{r}}. \tag{2.53d}$$

where assumption of the spectrally narrow temporal envelope of the probe field holds. Subsequently, based on the polarization in the quantum systems given by Eq. (2.47), and making use of the approach given for the two-level system, the polarization in the three-level case read

$$\begin{aligned}
\vec{P}_{3\mathrm{LS}}(\omega) &= \int_{-\infty}^{\infty} \vec{P}_{3\mathrm{LS}}(t)\mathrm{e}^{-\mathrm{i}\omega t}\mathrm{d}t \\
&= N\int_{-\infty}^{\infty} \left(\vec{d}_p^\star\langle\hat{\tilde{\sigma}}_p^+\rangle_s\mathrm{e}^{\mathrm{i}\omega_p t} + \vec{d}_p\langle\hat{\tilde{\sigma}}_p^-\rangle_s\mathrm{e}^{-\mathrm{i}\omega_p t} + \vec{d}_c^\star\langle\hat{\tilde{\sigma}}_c^+\rangle_s\mathrm{e}^{\mathrm{i}\omega_c t} + \vec{d}_c\langle\hat{\tilde{\sigma}}_c^-\rangle_s\mathrm{e}^{-\mathrm{i}\omega_c t}\right)\mathrm{e}^{-\mathrm{i}\omega t}\mathrm{d}t \\
&= N\Big(\vec{d}_p^\star\langle\hat{\tilde{\sigma}}_p^+\rangle_s \underbrace{\int_{-\infty}^{\infty}\mathrm{e}^{\mathrm{i}(\omega_p-\omega)t}\mathrm{d}t}_{\delta(\omega_p-\omega)} + \vec{d}_p\langle\hat{\tilde{\sigma}}_p^-\rangle_s \underbrace{\int_{-\infty}^{\infty}\mathrm{e}^{-\mathrm{i}(\omega_p+\omega)t}\mathrm{d}t}_{\delta(\omega_p+\omega)}\Big) \\
&+ N\Big(\vec{d}_c^\star\langle\hat{\tilde{\sigma}}_c^+\rangle_s \underbrace{\int_{-\infty}^{\infty}\mathrm{e}^{\mathrm{i}(\omega_c-\omega)t}\mathrm{d}t}_{\delta(\omega_c-\omega)} + \vec{d}_c\langle\hat{\tilde{\sigma}}_c^-\rangle_s \underbrace{\int_{-\infty}^{\infty}\mathrm{e}^{-\mathrm{i}(\omega_c+\omega)t}\mathrm{d}t}_{\delta(\omega_c+\omega)}\Big).
\end{aligned}$$

By splitting into terms respective to the probe and control fields $\vec{P}_{3\mathrm{LS}}(\omega) = \vec{P}_p(\omega) + \vec{P}_c(\omega) \equiv \vec{P}_p^+(\omega)\delta(\omega_p-\omega) + \vec{P}_p^-(-\omega)\delta(\omega_p+\omega) + \vec{P}_c^+(\omega)\delta(\omega_c-\omega) + \vec{P}_c^-(\omega)\delta(\omega_c+\omega)$, the form of polarizations is easily obtainable

$$\vec{P}_p^+(\omega) = N\vec{d}_p^\star\langle\hat{\tilde{\sigma}}_p^+\rangle_s, \tag{2.54a}$$

$$\vec{P}_p^-(-\omega) = N\vec{d}_p\langle\hat{\tilde{\sigma}}_p^-\rangle_s, \tag{2.54b}$$

$$\vec{P}_c^+(\omega) = N\vec{d}_c^\star\langle\hat{\tilde{\sigma}}_c^+\rangle_s, \tag{2.54c}$$

$$\vec{P}_c^-(-\omega) = N\vec{d}_c\langle\hat{\tilde{\sigma}}_c^-\rangle_s. \tag{2.54d}$$

As stated previously, the control field is assumed to be much stronger compared to the probe field, and so it modifies the properties of the medium in χ_p, whereas weak probe field does not affect it significantly. As the propagation of the probe field is of the interest of this thesis, only the electric susceptibility for this field is going to be derived. Similarly to

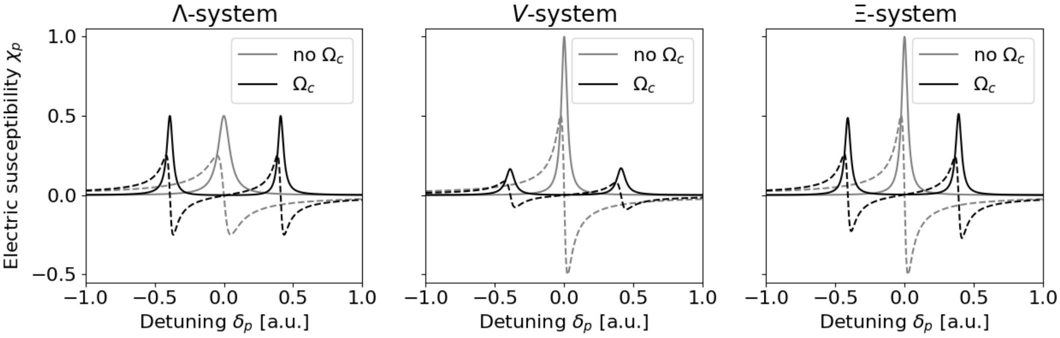

Figure 2.13: Imaginary (solid line) and real (dashed line) parts of the electric susceptibilities for media of three-level systems and for each configuration. In case of no control field, the result is the same as for the two-level systems, while strong control field provides splitting of the absorption peak into two symmetric peaks providing transparency window in former position of the resonance. In each case γ-rates are the same and $\delta_c = 0$.

the derivation of $\chi_{2\mathrm{LS}}(\delta)$ in Eq. (2.52), comparing fomulas in (2.53) and (2.54) (by realizing that $\nu_p = \omega_p$, $\nu_c = \omega_c$) the electric susceptibility for the probe field and for $\omega = \omega_p$, reads

$$\chi_p(\omega_p) = \frac{N|\vec{d}_p|^2}{\hbar\epsilon_0}\frac{2\langle\hat{\tilde{\sigma}}_p^+\rangle_s(\vec{r})}{\Omega_p(\vec{r})} \equiv \chi_p(\delta_p), \tag{2.55}$$

hence, for each configuration the explicit forms with the use of Eqs. (2.50) read

$$\chi_p^\Lambda(\delta_p) = \frac{N|\vec{d}_p|^2}{\hbar\epsilon_0}\frac{\mathrm{i}}{-\mathrm{i}\delta_p + \frac{1}{2}(\gamma_p+\gamma_c) + \frac{\frac{1}{4}|\Omega_c|^2}{-\mathrm{i}(\delta_p-\delta_c)}}, \tag{2.56a}$$

$$\chi_p^V(\delta_p) = \frac{N|\vec{d}_p|^2}{\hbar\epsilon_0}\mathrm{i}\frac{\left(\frac{1}{4}\gamma_c^2+\delta_c^2+\frac{1}{4}|\Omega_c|^2\right)+\left(\mathrm{i}\delta_c-\frac{1}{2}\gamma_c\right)\frac{\frac{1}{4}|\Omega_c|^2}{-\mathrm{i}(\delta_p-\delta_c)+\frac{1}{2}(\gamma_p+\gamma_c)}}{\left(\frac{1}{4}\gamma_c^2+\delta_c^2+\frac{1}{2}|\Omega_c|^2\right)\left(-\mathrm{i}\delta_p+\frac{1}{2}\gamma_p+\frac{\frac{1}{4}|\Omega_c|^2}{-\mathrm{i}(\delta_p-\delta_c)+\frac{1}{2}(\gamma_p+\gamma_c)}\right)}, \tag{2.56b}$$

$$\chi_p^\Xi(\delta_p) = \frac{N|\vec{d}_p|^2}{\hbar\epsilon_0}\frac{\mathrm{i}}{-\mathrm{i}\delta_p + \frac{1}{2}(\gamma_p+\gamma_c) + \frac{\frac{1}{4}|\Omega_c|^2}{-\mathrm{i}(\delta_p+\delta_c)+\frac{1}{2}\gamma_c}}. \tag{2.56c}$$

As expected, even though the stationary state of the coherence $\hat{\tilde{\sigma}}_p^+$ depends on $\vec{r}$, the resulted electric susceptibility function is spatially independent for the linear term of the Taylor series.

The electric susceptibility functions (2.56) are a powerful tool for analyzing the propagation of the probe pulse (Ω_p). The control field Ω_c, treated as a parameter, allows for a dramatic change in the response of the medium. One of the examples is Elecromagnetically Induced Transparency. In Fig. 2.13 plots of the $\chi^\alpha(\delta_p)$ control field with switched off (gray lines) and on (black lines) control field are shown. Note that for no control, the function for the two-level system is recovered, which is an intuitive result. However, the appearance of Ω_c creates a dip in absorption (EIT) with a slowly varying dispersion, providing slow probe pulse propagation or even trapping pulse inside the medium. Moreover, split peaks have the same size as an original one only for the Λ configuration, while for the Ξ

and V configurations they are suppressed. This behavior reflects the resulted equations of evolution with spontaneous emission for $\hat{\tilde{\sigma}}_f^+$ operator given in (2.42e).

2.3.2 *Bloch–Maxwell equations*

In the previous sections, equations describing the evolution of the quantum systems or ensembles of such, driven by external field(s), have been provided. However, the field evolution can also be a subject of investigation. In classical electrodynamics, propagation of the electromagnetic field is described by the Maxwell equations in matter

$$\begin{aligned}
&\vec{\nabla} \cdot \vec{D}(\vec{r},t) = \rho_f(\vec{r},t), \\
&\vec{\nabla} \cdot \vec{B}(\vec{r},t) = 0, \\
&\vec{\nabla} \times \vec{E}(\vec{r},t) = -\frac{\partial}{\partial t}\vec{B}(\vec{r},t), \\
&\vec{\nabla} \times \vec{H}(\vec{r},t) = \vec{J}_f(\vec{r},t) + \frac{\partial}{\partial t}\vec{D}(\vec{r},t).
\end{aligned}$$

where $\vec{E}$ and $\vec{B}$ are electric and magnetic fields, respectively, while ρ_f is the free charge density and $\vec{J}_f$ is the free current density in the medium. The auxiliary fields $\vec{D}$ and $\vec{H}$ account for the bound charges and currents in the medium, and are of the form

$$\begin{aligned}
\vec{D}(\vec{r},t) &= \epsilon_0\vec{E}(\vec{r},t) + \vec{P}(\vec{r},t), \\
\vec{H}(\vec{r},t) &= \frac{1}{\mu_0}\vec{B}(\vec{r},t) - \vec{M}(\vec{r},t),
\end{aligned}$$

where $\vec{P}$ is the polarization and $\vec{M}$ is the magnetization, both induced in the medium.

In this thesis, of the interest are linear dielectric media $\vec{M} = \vec{0}$ without free charges $\rho_f = 0$ and currents $\vec{J}_f = \vec{0}$, hence the wave equation for the electric field can be found

$$\vec{\nabla}^2\vec{E}(\vec{r},t) - \frac{1}{c^2}\frac{\partial^2}{\partial t^2}\vec{E}(\vec{r},t) = \mu_0\frac{\partial^2}{\partial t^2}\vec{P}(\vec{r},t), \tag{2.59}$$

where c is the speed of light in vacuum and the identity $c^2 = 1/(\mu_0\epsilon_0)$ was used. As a consequence, the wave equation contains the source term in the form of polarization on the right-hand side. As shown in the previous section, polarization in the medium is described by coherences and can be solved using Bloch equations; therefrom the name Bloch–Maxwell equations is used.

As the control field is considered to be strong, we focus on the propagation effects in the probe beam, driven by the part of polarization oscillating at the probe frequency. The probe field can be expressed as given in Eq. (2.49b). Without loss of generality, the assumption that $\vec{k}$ is parallel to the z axis can be used, provided that $\vec{k}_p\vec{r} = k_p z$, and hence $\vec{\nabla}^2 \to \partial^2/\partial z^2$. Thus, the left-hand-side of the wave equation (2.59) can be rewritten into the form

$$\left(\frac{\partial}{\partial z} + \frac{1}{c}\frac{\partial}{\partial t}\right)\left(\frac{\partial}{\partial z} - \frac{1}{c}\frac{\partial}{\partial t}\right)\vec{E}_p(z,t) = \mu_0\frac{\partial^2}{\partial t^2}\vec{P}_p(z,t),$$

The explicit form of the right-hand-side bracket acting on the electric field reads

$$\begin{aligned}\left(\frac{\partial}{\partial z}-\frac{1}{c}\frac{\partial}{\partial t}\right)\vec{E}_p(z,t)&=\left(\frac{\partial}{\partial z}-\frac{1}{c}\frac{\partial}{\partial t}\right)\frac{1}{2}\vec{E}^0_p(z,t)\left(\mathrm{e}^{\mathrm{i}(k_pz-\nu_pt)}+\mathrm{e}^{-\mathrm{i}(k_pz-\nu_pt)}\right)\\&=\frac{1}{2}\left(\frac{\partial}{\partial z}\vec{E}^0_p(z,t)-\frac{1}{c}\frac{\partial}{\partial t}\vec{E}^0_p(z,t)\right)\left(\mathrm{e}^{\mathrm{i}(k_pz-\nu_pt)}+\mathrm{e}^{-\mathrm{i}(k_pz-\nu_pt)}\right)\\&+\frac{1}{2}\vec{E}^0_p(z,t)\mathrm{i}\left(k_p+\frac{\nu_p}{c}\right)\left(\mathrm{e}^{\mathrm{i}(k_pz-\nu_pt)}-\mathrm{e}^{-\mathrm{i}(k_pz-\nu_pt)}\right)\\&\approx \mathrm{i}k_p\vec{E}^0_p(z,t)\left(\mathrm{e}^{\mathrm{i}(k_pz-\nu_pt)}-\mathrm{e}^{-\mathrm{i}(k_pz-\nu_pt)}\right),\end{aligned}\tag{2.60}$$

where free-space relation $k_p=\nu_p/c$ was used, and the assumptions $|\partial\vec{E}^0_p/\partial t|\ll\nu_p\vec{E}^0_p$ and $|\partial\vec{E}^0_p/\partial z|\ll k_p\vec{E}^0_p$ were used. They are justified for pulses whose envelopes change slowly compared to the carrier-frequency oscillations. The resulting procedure in (2.60) is known as the Slowly Varying Envelope Approximation (SVEA). The SVEA applies in particular to spectrally narrow pulses mentioned earlier. For the polarization term corresponding to the probe field in the temporal domain

$$\begin{aligned}\vec{P}_p(z,t)&=\int_{-\infty}^{\infty}\vec{P}^p_{3\mathrm{LS}}(z,\omega)\mathrm{e}^{\mathrm{i}\omega t}\mathrm{d}\omega=\int_{-\infty}^{\infty}\left(\vec{P}^+_p(z,\omega)\delta(\omega_p-\omega)+\vec{P}^-_p(z,-\omega)\delta(\omega_p+\omega)\right)\mathrm{e}^{\mathrm{i}\omega t}\mathrm{d}\omega\\&=\vec{P}^+_p(z,\omega_p)\mathrm{e}^{\mathrm{i}\omega_pt}+\vec{P}^-_p(z,-\omega_p)\mathrm{e}^{-\mathrm{i}\omega_pt}.\end{aligned}$$

Hence, the right-hand-side of the wave equation (2.59)

$$\mu_0\frac{\partial^2}{\partial t^2}\vec{P}_p(z,t)\approx-\mu_0\omega_p^2\left(\vec{P}^+_p(z,\omega_p)\mathrm{e}^{\mathrm{i}\omega_pt}+\vec{P}^-_p(z,-\omega_p)\mathrm{e}^{-\mathrm{i}\omega_pt}\right),\tag{2.61}$$

where SVEA holds as provides direct connection between the polarization terms and the electric field given by Eq. (2.53). Inserting into Eq. (2.59) approximated forms from (2.60) and (2.61), replacing $\vec{P}^\pm_p(z,\omega_p)$ with forms from (2.53) and making use of the electric susceptibility equation (2.55), the approximated probe field propagation in the ensemble of quantum systems is obtained

$$\left(c\frac{\partial}{\partial z}+\frac{\partial}{\partial t}\right)\Omega_p(z,t)=\mathrm{i}\frac{N\omega_p|\vec{d}_p|^2}{\hbar\epsilon_0}\langle\hat{\sigma}^+_p\rangle_s(z),\tag{2.62}$$

for the probe field's envelope $\Omega_p=\vec{E}^0_p\vec{d}_p/\hbar$. Accompanied by the Bloch equations describing evolution of the ensemble, the whole set is called the Bloch–Maxwell equations.

2.3.3 *Phase and group velocities*

When a wave propagates through a medium, two key velocities characterize its motion: the phase velocity v and the group velocity v_g. While the phase velocity describes the speed at which the carrier wave moves, the group velocity refers to the speed at which the envelope or overall shape of a modulated wave packet propagates. Both quantities are connected via an electric susceptibility function χ discussed in Sec. 2.3.1.

In free space, the wave equation (2.59) simplifies as $\vec{P} = \vec{0}$. One of the solutions is the plane wave of the form $\vec{E}_0 \cos\left(\vec{k}\vec{r} - \omega t\right)$ as it gives

$$-|\vec{k}|^2 \vec{E}_0 \cos\left(\vec{k}\vec{r} - \omega t\right) = -\frac{1}{c^2}\omega^2 \vec{E}_0 \cos\left(\vec{k}\vec{r} - \omega t\right) \Rightarrow |\vec{k}| = \frac{\omega}{c}.$$

The resulting formula is called the dispersion relation, and in free space has the linear form $k(\omega) = \omega/c$. However, the presence of a medium significantly changes this relation as an additional term appears

$$\mu_0 \frac{\partial^2}{\partial t^2}\vec{P} = \mu_0 \frac{\partial^2}{\partial t^2}\epsilon_0 \chi \vec{E} \cos\left(\vec{k}\vec{r} - \omega t\right) = -\frac{1}{c^2}\chi\omega^2 \vec{E} \cos\left(\vec{k}\vec{r} - \omega t\right),$$

which provides a modified dispersion relation

$$k(\omega) = \underbrace{\sqrt{1 + \chi(\omega)}}_{n(\omega)} \frac{\omega}{c}. \tag{2.63}$$

The square root is known as complex refractive index n. Its real part is responsible for the phase velocity of the electric field $v(\omega) = c/\operatorname{Re}(n(\omega))$ so the dispersion relation has a familiar form $k(\omega) = \omega/v(\omega)$. On the other hand, the imaginary part is related to the absorption in the medium. [25]

In the previous chapters, considerable effort was put to decouple the envelope Ω_p of the probe pulse from the carrier wave $\cos\left(k_p z - \omega_p t\right)$ in the evolution equations. Since the phase velocity refers to the carrier and is described by the refractive index n, the analogous formula for the envelope movement has to be found. Conceptually, as the pulse can be composed of plane waves with different frequencies, this new index should take into account how the refractive index varies with the frequency of light. Because of that property of capturing many frequencies at once, it is called group index in the literature [25].

Starting with the pulse written as a superposition of plane waves with amplitudes $F(k)$

$$f(z,t) = \int_{-\infty}^{\infty} F(k) \mathrm{e}^{\mathrm{i}(kz - \omega(k)t)} \mathrm{d}k, \tag{2.64}$$

and assuming the wave packet to be spectrally narrow, i.e., almost monochromatic, it has a peak at central wavenumber k_0. Thus, Taylor series for the frequency truncated at the linear term gives

$$\omega(k) \approx \underbrace{\omega(k_0)}_{\omega_0} + \underbrace{\left.\frac{\partial \omega(k)}{\partial k}\right|_{k=k_0}}_{\omega_0'} (k - k_0).$$

Inserting it into the wave packet equation (2.64) gives

$$f(z,t) = \mathrm{e}^{\mathrm{i}(k_0 z - \omega_0 t)} \int_{-\infty}^{\infty} F(k) \mathrm{e}^{\mathrm{i}(k - k_0)(z - \omega_0' t)} \mathrm{d}k,$$

where term before the integral is a monochromatic wave with the central wavenumber k_0. It describes oscillations at the carrier frequency in both space and time and is followed by the envelope defined by the integral. The form of the exponent inside the integral resembles that of the plane wave $\sim \exp(ik(z - vt))$, where v describes the wave velocity. In analogy, ω_0' can be interpreted as the velocity of the envelope, and hence, the group velocity and index are defined as

$$v_g = \omega_0' = \frac{\partial \omega}{\partial k} \Rightarrow n_g = \frac{c}{v_g}. \tag{2.65}$$

Moreover, the relation between the group velocity and refractive index can be easily found by using real part of the dispersion relation (2.63)

$$v_g = c \left(\frac{\partial k}{\partial \omega} \right)^{-1} = \frac{c}{\mathrm{Re}(n) + \omega \frac{\partial \, \mathrm{Re}(n)}{\partial \omega}}. \tag{2.66}$$

The above form of the group velocity provides an important insight into the pulse propagation by its connection to the refractive index $\mathrm{Re}(n)$. In consequence, velocity can be controlled by tailoring the shape of dispersion. From the analysis of the group velocity equation (2.66), several crucial pieces of information can be obtained. In case of both $\mathrm{Re}(n)$ and its frequency derivative being positive and at least one of them large, the pulse is slowed down significantly – slow-light regime is achieved with subluminal propagation $v_g < c$. This is the case for the EIT, where suppressed absorption accompanied with a positive frequency derivative can drastically slow down or even "stop" a light pulse [55]. On the other hand, fast light (superluminal) appears either by obtaining small values of $\mathrm{Re}(n)$ and its derivative or by anomalous dispersion, i.e., negative value of the frequency derivative of the refractive index. Note, that this is always the case for the resonance peaks, where absorption is the greatest and can distort the pulse significantly. However, in that case, the denominator in Eq. (2.66) can have any value below 1, providing propagation with a group velocity exceeding the vacuum speed of light $v_g > c$ or even a negative group velocity if $v_g < 0$.

The considerations regarding superluminal propagation and ways to suppress the impact of the high absorption are further explained in article **A3**.

3

PERMANENT DIPOLE MOMENTS IN TWO-LEVEL SYSTEMS

The theory described in detail in the previous chapter allows for an understanding of the basics of further investigations in articles A1 and A2. The permanent dipole moments play a crucial role in the evolution of the two-level system driven by the external electromagnetic field, giving rise to phenomena that are otherwise absent: The dynamics of the single system is enriched due to dynamic eigenstate energies, whose effect can be captured in an effective model developed in A1. For this purpose, we have used the density-matrix formalism and applied a series of unitary transformations to find a reference frame simplifying the description and leading to approximate analytical expressions for observables such as the fluorescence spectra. An ensemble of systems with permanent dipole moments, on the other hand, gives rise to a buildup of coherent radiation emitted at the Rabi frequency, as shown and discussed in A2 using the adapted Bloch–Maxwell's equations, which include a variety of dissipative processes in semi-analytical solutions and numerical simulations applicable to model experimental realizations.

3.1 BLOCH EQUATIONS FOR SINGLE SYSTEM

In article A1, we investigate the dynamics of polar systems with permanent dipole moments when coupled to classical light in the ultrastrong coupling regime. This is the continuation of the introduction provided in Section 2.1. We have derived an analytical framework similar to the Jaynes–Cummings model to describe the complex behavior of these systems, particularly focusing on nonlinear light-matter interactions.

Key elements of this work:

- In polar systems, nonlinear interaction strength replaces the traditional linear scaling of the light-matter coupling strength with the driving field amplitude.
- The developed analytical model provides effective parameters like frequency shifts, coupling strength, and rescaled relaxation rates.
- This approach simplifies understanding of these interactions and reduces computational costs, even in regimes where full Hamiltonian calculations would be highly complex.
- The analysis shows potential for enhancing coherence in quantum systems with permanent dipole moments subject to fields rapidly varying in space and opens new pathways for exploring light-matter interactions in quantum optics. A follow-up article summarizing our results on this subject is in preparation and is beyond the scope of this thesis.

I was the principal investigator of the scientific project within which this research was performed (Preludium grant no. 2021/41/N/ST2/02068, National Science Centre, Poland). In the article, I contributed to the conception of the idea, I am fully responsible for the theory development and made the dominant contributions to the results analysis and manuscript preparation.

The theory developed in A1 is fundamental to article B2, where plasmonic nanostructures are proposed as a means to tune the Rabi frequency in polar two-level systems to the THz range and enhance the power of the generated low-frequency radiation. However, due to the article's focus on engineering aspects, which were primarily the responsibility of the first author, I have chosen not to include it in this dissertation.

Rabi frequency for polar systems interacting with light

Piotr Gladysz[*] and Karolina Slowik[†]
Institute of Physics, Faculty of Physics, Astronomy and Informatics,
Nicolaus Copernicus University in Toruń, Grudziadzka 5/7, 87-100 Toruń, Poland

We investigate the dynamics of polar systems coupled to classical external beams in the ultrastrong coupling regime. The permanent dipole moments (PDMs) sustained by polar systems can couple to the electromagnetic field, giving rise to a variety of processes such as difference-frequency and harmonic generation, reflected in complicated dynamics of the atomic system. Here, we demonstrate that the dynamics can be described simply in a dynamic reference frame. We derive a Jaynes–Cummings-like framework with effective parameters describing frequency shift, coupling strength with the driving field, and a rescaled relaxation rate. The familiar linear scaling of the interaction strength with the field amplitude is replaced with a nonlinear dependence, suggesting potential applications for improving the coherence of quantum system ensembles with permanent dipoles.

The interaction of light with matter is a fundamental phenomenon in physics, which underpins many modern quantum optics and photonics [1–4]. Polar systems, characterized by the presence of the PDMs due to the lack of inversion symmetry, offer unique opportunities and challenges in this domain [5–9]. Unlike transition dipole moments that occur between pairs of system eigenstates, permanent dipoles are inherent properties of individual eigenstates and can significantly influence the system's response to external electromagnetic fields [10–15].

Traditionally, the role of permanent dipoles in light-matter interaction has been considered minor, often relegated to causing trivial frequency shifts. However, recent studies have shown that these dipoles can induce coherent radiation at the Rabi frequency, leading to more complex and rich dynamical behaviors than previously understood [10, 14, 16]. Polar systems have been suggested for lasing at tunable frequencies [12], radiation generation in tailored photonic environments [17, 18], efficient two-photon excitation [16, 19] and light squeezing [11, 13]. Materials with inherent $\chi^{(2)}$ nonlinearity were proposed for difference-frequency generation in a related mechanism [20]. Similar effects were also studied in the magnetic context, where a rescaling of the Landé g factor was found in atoms dressed with radiofrequency magnetic fields [21].

In this manuscript, we investigate the dynamics of polar systems in the ultrastrong coupling regime with external beams, where the interaction strength between the electromagnetic field and the system is comparable to or exceeds the transition frequency of the system itself [22]. Despite the variety of processes that can occur in this regime, we reveal, through a series of unitary operations rotating the reference frame, that the system's behavior can be elegantly captured using a Jaynes–Cummings-type analytically solvable model. This description, set in a dynamic reference frame, is based on three key parameters: the rescaled frequency shift, coupling strength, and the relaxation rate. The rescaling is a qualitative change: For example, the traditional linear dependence of interaction strength with the driving field amplitude is replaced by a nonlinear one, suggesting new potential regimes for the exploration of light-matter interactions. We thoroughly verify the applicability range of the effective analytical description, confirming the robustness and accuracy of the model up to the ultrastrong coupling, where it shows good agreement with the full Hamiltonian dynamics but significantly reduces the computational cost. Finally, based on the effective Hamiltonian, we find analytical expressions for resonance fluorescence spectra that would otherwise be challenging to access, due to the involvement of processes occurring at time scales that may differ by orders of magnitude, making the numerical integration challenging.

We consider a two-level polar quantum system (TLS) with the excited $|e\rangle$ and ground $|g\rangle$ states separated with the transition frequency ω_{eg}. It is subject to a classical plane-wave laser drive $\vec{E}(t) = \vec{E}_0 \cos(\omega_c t)$ with the amplitude $\vec{E}_0$ and frequency $\omega_c \approx \omega_{eg}$ near-resonant with the system transition. For a polar system, light couples with the full dipole moment $\vec{d} = \sum_{ij} \vec{d}_{ij} |i\rangle \langle j|$ with $i, j \in \{e, g\}$, which includes the transition $\vec{d}_{i \neq j}$ and permanent $\vec{d}_{ii}$ elements. The Hamiltonian reads

$$\begin{aligned} H(t)/\hbar &= \frac{1}{2}\omega_{eg}\sigma_z + \vec{E}(t) \cdot \vec{d} \\ &= \frac{1}{2}\underbrace{\left(\omega_{eg} + g_z \cos(\omega_c t)\right)}_{\omega_{eg}(t)}\sigma_z + g_x \cos(\omega_c t)\sigma_x \end{aligned} \tag{1}$$

Here, $\sigma_{x,z}$ are standard Pauli matrices. The drive induces transitions between the eigenstates with the strength $g_x = \vec{E}_0 \vec{d}_{eg}/\hbar$, and a sinusoidal energy shift with the amplitude $g_z = \vec{E}_0 \Delta\vec{d}/\hbar$, where $\Delta\vec{d} = \vec{d}_{ee} - \vec{d}_{gg}$. Although the g_x term also occurs in the standard nonpolar case, the term proportional to g_z is unique to systems with PDMs and is key to the effects investigated in this work. To quantify its impact, we introduce a parameter $\kappa_z = g_z/\omega_c$ which reduces to 0 for nonpolar systems and is of the order of 1 for polar systems in the ultrastrong coupling regime, in which the dynamics is qualitatively altered.

A nonpolar system driven by light undergoes Rabi pop-

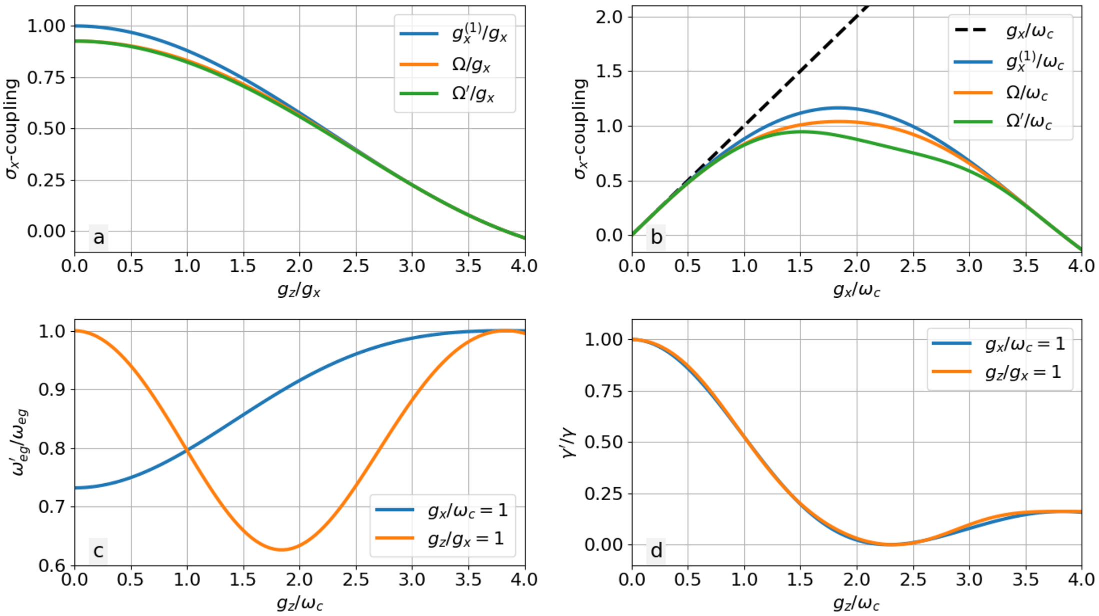

FIG. 1. The upper plots show comparisons of the $\hat{\sigma}_x$-coupling strengths for different corrections as a function of: **a.** PDMs difference (for $g_x/\omega_c = 1$), **b.** driving field amplitude (for $g_z/\omega_c = 1$). The lower plots present: **c.** the normalized effective transition frequency, **d.** the normalized effective gamma rate, as functions of g_z coupling, both in cases of fixed driving field (blue) or PDMs difference (orange), respectively.

ulation oscillations with the Rabi frequency that for weak relaxation is given by $\Omega_{\mathrm{R}} \approx \sqrt{|g_x|^2 + \delta^2}$, and depends on the drive amplitude and detuning $\delta = \omega_c - \omega_{eg}$ [23]. In a polar system, the eigenstate energies oscillate inducing a time-dependent detuning according to Eq. (1) $\delta(t) = \delta + g\cos\omega_c t$, leading to complicated dynamics mixing a range of oscillation frequencies. In the ultrastrong coupling regime, these contributions should not be neglected *a priori* through a rotating-wave-type approximation. In Supplementary Material Section I, we document in detail a transition to a reference frame that allows one to capture this complicated behavior in an analytically solvable model. The transition involves a series of noncommutative reference frame rotations. These rotations subsequently simplify the form of the Hamiltonian. With the first transformation $U_1 = \exp\left(\frac{1}{2}\mathrm{i}\kappa_z \sin(\omega_c t)\sigma_z\right)$, the terms proportional to g_z are incorporated in the parameters of an effective Rabi-like model,

$$H_1/\hbar = \frac{1}{2}\omega_{eg}\sigma_z + g_x^{(1)}\sigma_x \cos\omega_c t + H_{\mathrm{multi}}/\hbar, \tag{2}$$

corrected by higher-order terms H_{multi} related to resonances at $n\omega_c = \omega_{eg}$, $n \geq 2$ [Supplementary Material Eq. (S7)] which can be associated with multiphoton processes. The coupling constant describing effects resonant at $n\omega_c$ is given by

$$g_x^{(n)}(\vec{E}_0, \vec{d}_{eg}, \Delta\vec{d}, \omega_c) \equiv g_x^{(n)}(\kappa_z) = \frac{2n}{\kappa_z}\mathrm{J}_n(\kappa_z)g_x, \tag{3}$$

where $\mathrm{J}_n(x)$ is the nth-order Bessel function of the first kind. This step involves no approximations and the polar terms are fully included. However, in a frame rotating with a sinusoidally varying frequency, the system behaves as if it were not polar but coupled with an electromagnetic field through a modified coupling strength $g_x^{(1)}$, nonlinearly dependent on the field amplitude. As we verify in Fig. 5, the corrections arising from H_{multi} may become important for the case of the ultrastrong σ_x-coupling.

In the following steps, counter-rotating terms are similarly incorporated in effective parameters through the pair of transformations $U_2 = \exp(\mathrm{i}\xi\kappa_x \sin(\omega_c t)\sigma_x)$ [24] and $U_3 = \exp\left(\frac{1}{2}\mathrm{i}\kappa'_z \sin(\omega_c t)\sigma_z\right)$. Here, $\kappa_x = g_x^{(1)}/\omega_c$, and κ'_z is a cumbersome function of dipole moment elements and the driving field, defined in the Supplementary Material Section I. The parameter $\xi \in (0, 1)$ fulfills the equation [24]

$$\omega_{eg}\mathrm{J}_1(2\xi\kappa_x) = (1 - \xi)g_x^{(1)} \equiv \frac{1}{2}\Omega, \tag{4}$$

where Ω plays the role of an effective coupling strength

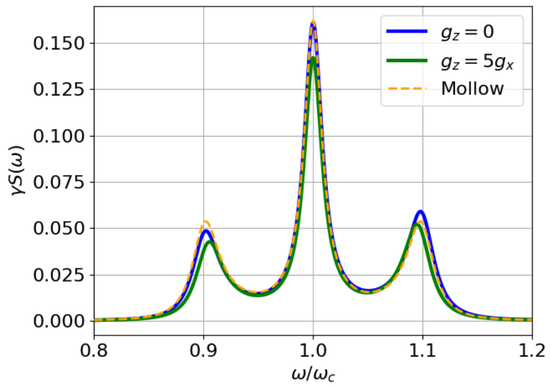

FIG. 2. Comparison of spectra calculated for the two-level system with (green line), and without (blue line) PDMs, and the Mollow-triplet (dashed line), calculated for the resonant case $\omega_c = \omega_{eg}$. The coupling strength $g_x/\omega_c = 0.1$ and the relaxation rates $\gamma/\omega_c = \gamma'/\omega_c = 0.02$ were assumed to be the same for all cases. In the polar case, $g_z = 5g_x$.

obtained in the intermediate step. The resulting Hamiltonian has the Jaynes–Cummings form as it occurs in the Schrödinger-picture. The transformation $U_4 = \exp\left(\frac{1}{2}\mathrm{i}\omega_c t\sigma_z\right)$ brings it to the interaction picture, where it is time-independent and acquires the final analytically solvable form

$$H_{\mathrm{eff}}/\hbar = -\frac{1}{2}\delta'\sigma_z + \frac{1}{2}\Omega'\sigma_x. \tag{5}$$

Here, we have omitted multiphoton corrections negligible in the regime investigated below. The Hamiltonian (5) is analytically solvable, and yet, accounts for a plethora of physical effects related to the system's asymmetry *via* PDMs, ultrastrong coupling, Bloch–Siegert shift, and beyond, and is exact up to multiphoton effects. The rich variety of the captured phenomena is reflected in the effective parameters that we now discuss. The field detuning $\delta' = \omega_c - \omega'_{eg}$ is defined with respect to the effective transition frequency $\omega'_{eg} = \omega_{eg} J_0(2\xi\kappa_x)$, whose dominant Taylor expansion coefficient

$$\xi^2\omega_{eg}\frac{J_1(\kappa_z)^2|2g_x|^2}{\kappa_z^2\omega_c^2} \xrightarrow[\kappa_z\to 0]{} \xi^2\omega_{eg}|g_x|^2\omega_c^2$$

can be recognized as the Bloch–Siegert shift [25]. The scaling of the effective frequency ω'_{eg} with normalized g_z coupling is shown in Fig. 1(c).

The effective coupling strength has a complicated functional dependence on the field amplitude and atomic dipole moments

$$\Omega' = \mathrm{J}_0(\kappa'_z)\Omega \approx g_x^{(1)}. \tag{6}$$

where the latter approximate expression is valid for moderately strong interactions with $\vec{E}_0\Delta\vec{d} < \hbar\omega_c$. Therefore, we have found an iterative sequence of coupling strengths $g_x^{(1)} \to \Omega \to \Omega'$ obtained through subsequent rotations. The effective coupling strengths are plotted in Fig. 1(a,b) respectively as a function of the PDMs difference in the TLS eigenstates and of the electric field amplitude. The blue, orange, and green lines represent coupling strengths after subsequent frame rotations, and the black dashed line is the usual coupling strength linearly scaled with the field amplitude in the original reference frame.

To account for dissipative dynamics, we have augmented the Hamiltonian (1) with a coupling to a bosonic thermal bath and performed the same reference frame rotations. These steps are described in detail in Supplementary Material Section II. As a result, following the Weisskopf-Wigner theory with the Markovian approximation, we find a rescaled spontaneous emission rate which for $\vec{E}_0\Delta\vec{d} \leq \hbar\omega_c$ takes the approximate form

$$\gamma' \approx \mathrm{J}_0(\kappa_z)^2\mathrm{J}_0(\kappa'_z)^2\gamma, \tag{7}$$

and is further modified for strong fields (see Supplementary Material Section II for exact formulas). Thus, in the dynamic frame, the spontaneous emission rate in polar systems depends on the external field amplitude E_0 [see Fig. 1(d), where the rate is shown without approximations]. The emission rate keeps its original value γ for vanishing PDMs or in the absence of an external field.

The simple form of the effective Hamiltonian (5) allows us to analytically evaluate the stationary expectation values of the population inversion and the induced dipole moment in the rotated frame, as derived in Supplementary Material Section III

$$\langle\sigma^{\pm}\rangle_s = \frac{\Omega'(2\delta' \pm \mathrm{i}\gamma')}{2\Omega'^2 + 4\delta'^2 + \gamma'^2}, \tag{8a}$$

$$\langle\sigma_z\rangle_s = -\frac{(4\delta'^2 + \gamma'^2)}{2\Omega'^2 + 4\delta'^2 + \gamma'^2}. \tag{8b}$$

Building upon stationary solutions, we use the Onsager-Lax theorem to evaluate the fluorescence spectrum of the system following the approach proposed by [24] for nonpolar systems. At this step, the price for the simplicity of the Hamiltonian is the complicated form of the evolution operator in the rotating frame that makes the resulting expressions quite complex. Yet, we obtain their analytical forms predicting a sequence of Mollow triplets centered at multiples $n\omega_c$ of the illumination frequency, with sidebands separated by the effective Rabi frequency $\widetilde{\Omega}$, which is calculated based on the coupling strength Ω' and γ'-rate such that $\widetilde{\Omega} \to \Omega'$ for $\gamma' \to \gamma$. For the full derivation of the lineshapes and $\widetilde{\Omega}$ parameter see Supplementary Material Section IV.

Let us first analyze the resulting spectrum of a polar system illuminated at $\omega_c = \omega_{eg}$ around the original peak, i.e., in the vicinity of the illumination frequency. This result is compared with the one obtained for the non-polar

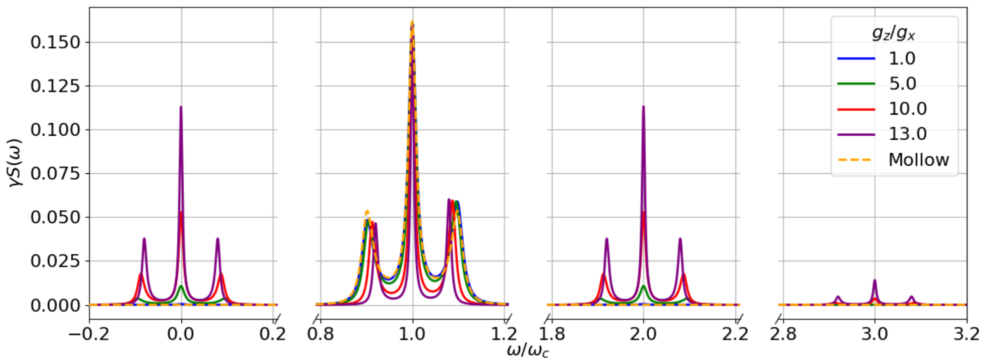

FIG. 3. Comparison of spectra for several different values of the PDMs (g_z/g_x ratios) and compared to the results obtained by Mollow (dashed line), obtained for the resonant case $\omega_c = \omega_{eg}$, $\gamma/\omega_c = 0.02$, $g_x/\omega_{eg} = 0.1$. In the plot, calculated γ' values are used.

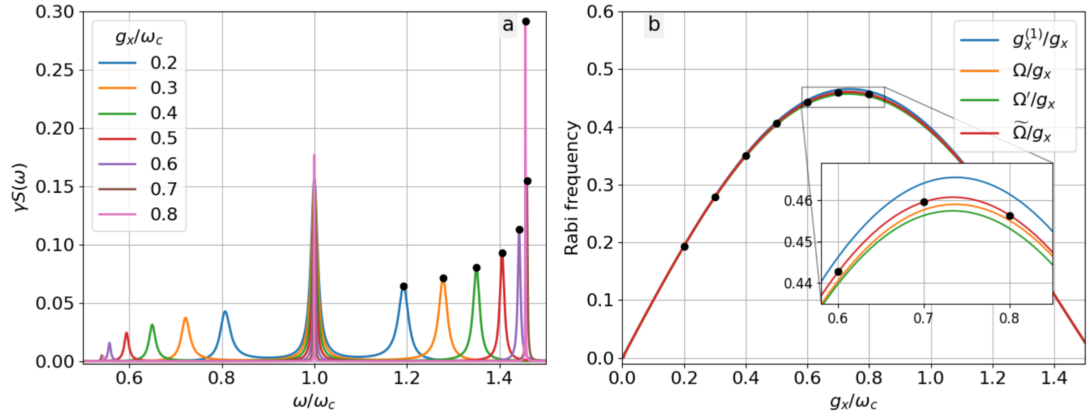

FIG. 4. **a.** Resonance fluorescence spectra for different values of the $\hat{\sigma}_x$-coupling g_x and fixed PDMs difference $g_z/g_x = 2.5$. For each spectrum $\omega_c = \omega_{eg}$, and spontaneous emission rates γ's are calculated based on $\gamma/\omega_c = 0.02$. **b.** Position of the peaks of the right sidebands shown on top of the curves with approximations to the evaluation of the Rabi frequency.

case [24] and the analytical results derived by Mollow [26] (Fig. 2). The relatively strong field, and hence the significant correction to the atomic frequency and nonzero effective detuning are responsible for the asymmetry of the sidebands in both polar and nonpolar cases but are not captured by the Mollow solution. This asymmetry is comparable in the two former cases, hence we conclude that the existence of the PDMs does not impact significantly the resonance shift. However, it is crucial for the correct evaluation of the peak amplitudes and spectral positions of the sidebands, given by the effective coupling $\widetilde{\Omega}$.

We now proceed to discuss the spectral features centered at $n\omega_c$. Neglecting multiphoton corrections, the relevant terms correspond to $n = 0, 1, 2, 3$, as predicted in earlier studies [15]. In systems without PDMs, the emission at even multiples of the laser frequency does not occur [16]. The peak at $3\omega_{eg}$ is induced in this case by the counter-rotating terms in the Rabi Hamiltonian [15, 27]. Polarity in the system reduces the Hamiltonian symmetry, gives rise to the even-order fluorescence peaks, and modifies the odd ones. The low-energy emission at Rabi frequency $\widetilde{\Omega}$ discussed previously in various contexts [10, 12, 14], is captured here as the Mollow sideband of the triplet corresponding to $n = 0$. In Fig. 3, we demonstrate the spectra for $g_x/\omega_c = 0.1$ and $g_z/\omega_c = 0.1$, 0.5, 1.0 and 1.3. We assume the laser is tuned to the original atomic resonance $\omega_c = \omega_{eg}$. Again, the field gives rise to a large frequency shift, hence, a significant effective detuning responsible for the asymmetry of the sidebands. With increasing PDMs difference, the light interaction with the atomic system becomes dominated by related terms, in the original Hamiltonian proportional to g_z. This is reflected in the emission spectrum through the modified relative intensity of the peaks: The original Mollow triplet at ω_c, dominant for weakly polar systems with small PDMs, is gradually suppressed as the emission is directed to other frequency channels.

Finally, Fig. 4(a) shows how the spectral position of the sidebands can be tuned with the driving field amplitude. Here, we assume again the illumination at $\omega_c = \omega_{eg}$. The ratio of permanent- and transition-dipole moment element components parallel to the field is equivalent to the ratio of coupling constants, that we fix at $g_z/g_x = 2.5$. The relaxation rate is evaluated according to Eq. (7) with $\gamma/\omega_c = 0.02$. We find that as the field amplitude increases, the sidebands are initially pulled away from the central peak at a decreasing pace and eventually turn back towards the center at ω_c. Additionally, by increasing the field amplitude we decrease both the transition frequency ω' and spontaneous emission γ'-rates according to the results from Fig. 1(a,b). As a result, we observe the narrowing and growth (shrinking) of the right (left) sidebands.

In the Jaynes–Cummings model, the difference in the spectral position of the sideband and the central peak corresponds to the coupling strength. Naturally, the same is expected from the effective description that we have reduced to the Jaynes–Cummings form. Indeed, as can be seen in Fig. 4(b), the position of spectral sidebands given by $\widetilde{\Omega}$ is in good agreement with the prediction of the effective coupling strength Ω'. For comparison, we also show the coupling strengths' predictions evaluated after subsequent transformations $U_1 - U_4$. As it is clear from the inset, all frame rotations need to be performed to eventually obtain the excellent agreement of $\widetilde{\Omega}$ (red line) with the calculated spectral positions of sidebands (black dots). However, already the first transformation provides a qualitatively correct expression for the effective coupling strength $g_x^{(1)}$, as can be concluded from the examination of the blue line.

We aim to comment on the applicability of the derived model in Fig. 5. Each panel corresponds to a selected spectrum from Fig. 4a for a fixed value of g_x/ω_c and $g_z = 2.5g_x$ (matching colors are used). Note that for $g_x/\omega_c = 0.4$, ultra-strong σ_z-coupling is already reached with $g_z = \omega_c$. Despite the simplicity of the effective Hamiltonian described with a pair of effective parameters, we obtain very good agreement with the full Hamiltonian dynamics even near the Bessel function peak. We can thus capture the complex dynamics of systems with permanent dipoles subjected to extremely strong electromagnetic fields with this simple model. Beyond $g_x/\omega_c = 0.6$ [Fig. 5(c)], multiphoton corrections begin to play a more important role so that the effective dynamics ceases to predict the qualitative behaviour of the system. Moreover, in this regime the suppression of the γ'-rate is significant and in Fig. 5(c,d) leads to the reduction of the oscillations' damping. The involvement of the multiphoton corrections could also alter this behavior.

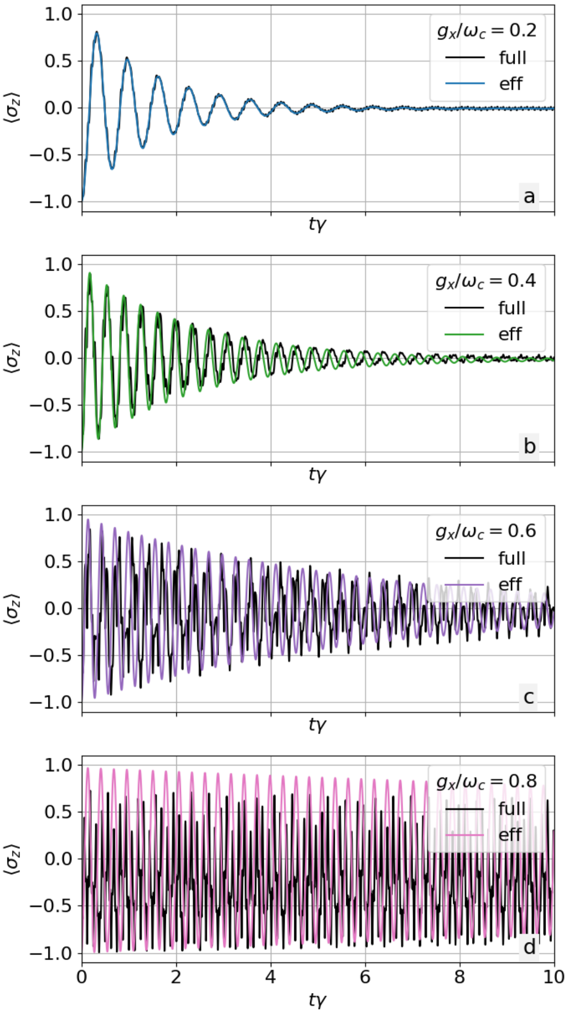

FIG. 5. Evolution of the population represented by $\langle\hat{\sigma}_z\rangle$. Each plot corresponds to one of the spectral lineshapes presented in Fig. 4a (color matching),

In conclusion, we explored the behavior of polar systems under ultrastrong coupling with classical external beams. By switching to a dynamic reference frame using a series of unitary operations, we derived an analytically solvable Jaynes–Cummings-like model. This model captures the impact of PDMs, counter-rotating terms, and strong fields in effective frequency shift, coupling strengths, and relaxation rate, helping us understand the complex interactions in these systems.

Our findings show that permanent dipoles play a crucial role in changing how the system interacts with external fields, leading to a nonlinear interaction strength. This shift from traditional linear scaling suggests new avenues for research on light interactions with polar matter, especially in enhancing the coherence of multiple quantum systems with permanent dipoles. Future research should investigate the identified nonlinear effects and their practical applications, explore more complex quantum systems, and study their behavior under different external conditions. Additionally, expanding this framework to include multiphoton interactions and multipartite dynamics could offer further insights into the principles that govern this interesting interaction regime.

Acknowledgement: The authors acknowledge the support from the National Science Centre, Poland, PRELUDIUM programme (grant number 2021/41/N/ST2/02068).

---

[*] glad@doktorant.umk.pl
[†] karolina@fizyka.umk.pl

[1] D. Dovzhenko, S. Ryabchuk, Y. P. Rakovich, and I. Nabiev, Light–matter interaction in the strong coupling regime: configurations, conditions, and applications, Nanoscale **10**, 3589 (2018).

[2] M. Hertzog, M. Wang, J. Mony, and K. Börjesson, Strong light–matter interactions: a new direction within chemistry, Chemical Society Reviews **48**, 937 (2019).

[3] N. Rivera and I. Kaminer, Light–matter interactions with photonic quasiparticles, Nature Reviews Physics **2**, 538 (2020).

[4] A. Marinho, M. de Paula, and A. Dodonov, Approximate analytic solution of the dissipative semiclassical rabi model near the three-photon resonance and comparison with the quantum behavior, Physics Letters A , 129608 (2024).

[5] M. A. Kmetic and W. J. Meath, Perturbative corrections to the rotating-wave approximation for two-level molecules and the effects of permanent dipoles on single-photon and multiphoton spectra, Physical Review A **41**, 1556 (1990).

[6] D. DeMille, Quantum computation with trapped polar molecules, Physical Review Letters **88**, 067901 (2002).

[7] S. A. Moses, J. P. Covey, M. T. Miecnikowski, D. S. Jin, and J. Ye, New frontiers for quantum gases of polar molecules, Nature Physics **13**, 13 (2017).

[8] J. F. Triana and J. L. Sanz-Vicario, Polar diatomic molecules in optical cavities: Photon scaling, rotational effects, and comparison with classical fields, The Journal of Chemical Physics **154** (2021).

[9] R. González-Férez, J. Shertzer, and H. Sadeghpour, Ultralong-range rydberg bimolecules, Physical Review Letters **126**, 043401 (2021).

[10] O. Kibis, G. Y. Slepyan, S. Maksimenko, and A. Hoffmann, Matter coupling to strong electromagnetic fields in two-level quantum systems with broken inversion symmetry, Physical review letters **102**, 023601 (2009).

[11] M. Koppenhöfer and M. Marthaler, Creation of a squeezed photon distribution using artificial atoms with broken inversion symmetry, Physical Review A **93**, 023831 (2016).

[12] I. Y. Chestnov, V. A. Shahnazaryan, A. P. Alodjants, and I. A. Shelykh, Terahertz lasing in ensemble of asymmetric quantum dots, Acs Photonics **4**, 2726 (2017).

[13] M. Antón, S. Maede-Razavi, F. Carreño, I. Thanopulos, and E. Paspalakis, Optical and microwave control of resonance fluorescence and squeezing spectra in a polar molecule, Physical Review A **96**, 063812 (2017).

[14] P. Gładysz, P. Wcisło, and K. Słowik, Propagation of optically tunable coherent radiation in a gas of polar molecules, Scientific reports **10**, 17615 (2020).

[15] G. Scala, K. Słowik, P. Facchi, S. Pascazio, and F. V. Pepe, Beyond the rabi model: Light interactions with polar atomic systems in a cavity, Physical Review A **104**, 013722 (2021).

[16] W. J. Meath and B. Jagatap, On the effects of permanent molecular dipoles in the simultaneous absorption of two photons: Full generalized rotating wave approximation versus analytical results, The Journal of Chemical Physics **139** (2013).

[17] I. Savenko, O. Kibis, and I. A. Shelykh, Asymmetric quantum dot in a microcavity as a nonlinear optical element, Physical Review A—Atomic, Molecular, and Optical Physics **85**, 053818 (2012).

[18] S. Izadshenas, P. Gładysz, and K. Słowik, Hybrid graphene-silver nanoantenna to control thz emission from polar quantum systems, Optics Express **31**, 29037 (2023).

[19] W. J. Meath, On the optimization, and the intensity dependence, of the excitation rate for the absorption of two-photons due to the direct permanent dipole moment excitation mechanism, AIP Advances **6** (2016).

[20] F. Barachati, S. De Liberato, and S. Kéna-Cohen, Generation of rabi-frequency radiation using exciton-polaritons, Physical Review A **92**, 033828 (2015).

[21] C. Landré, C. Cohen-Tannoudji, J. Dupont-Roc, and S. Haroche, Anisotropie des propriétés magnétiques d'un atome habillé par des photons de rf, Journal de Physique **31**, 971 (1970).

[22] P. Forn-Díaz, L. Lamata, E. Rico, J. Kono, and E. Solano, Ultrastrong coupling regimes of light-matter interaction, Rev. Mod. Phys. **91**, 025005 (2019).

[23] R. Loudon, *The Quantum Theory of Light*, Oxford science publications (Clarendon Press, 1983).

[24] Y. Yan, Z. Lü, and H. Zheng, Effects of counter-rotating-wave terms of the driving field on the spectrum of resonance fluorescence, Physical Review A—Atomic, Molecular, and Optical Physics **88**, 053821 (2013).

[25] F. Bloch and A. Siegert, Magnetic resonance for nonrotating fields, Physical Review **57**, 522 (1940).

[26] B. Mollow, Power spectrum of light scattered by two-level systems, Physical Review **188** (1969).

[27] D. Braak, Integrability of the rabi model, Physical Review Letters **107**, 100401 (2011).

Supplementary Material for the Article *Rabi frequency for polar systems interacting with light*

Piotr Gładysz* and Karolina Słowik†
Institute of Physics, Nicolaus Copernicus University in Toruń, Gagarina 11, 87-100 Toruń, Poland

This supplement contains derivations of equations discussed in the main text and additional results.

CONTENTS

In this supplement, we present detailed derivations of the Hamiltonian, relaxation rates and spectra in the transformed reference frame. We arrive at exact formulas and discuss approximations that lead to Eqs. (5) and (7) in the main article. For the readers' convenience, we fully re-introduce the notation so that all symbols are explained in this document. We also comment on the physical interpretation and consequences of subsequent mathematical steps.

I. DERIVATION OF HAMILTONIAN EQ.(5)

Our model considers a two-level polar quantum system (TLS) with orthogonal excited $|e\rangle$ and ground $|g\rangle$ states with transition frequency ω_{eg}. A classical plane wave $\vec{E}(t) = \vec{E}_0 \cos(\omega_c t)$ with amplitude $\vec{E}_0$ and frequency $\omega_c \approx \omega_{eg}$ is coupled to the TLS via the transition dipole moment $\vec{d}_{eg}$, and the permanent dipole moments (PDMs) $\vec{d}_{ee}$, $\vec{d}_{gg}$ in excited and ground states, respectively. The Hamiltonian reads

$$\begin{aligned} H(t)/\hbar &= \frac{1}{2}\omega_{eg}\sigma_z + \vec{E}(t)\cdot\hat{\vec{d}}, \\ &= \frac{1}{2}\underbrace{\left(\omega_{eg} + g_z\cos(\omega_c t)\right)}_{\omega_{eg}(t)}\sigma_z + g_x\cos(\omega_c t)\sigma_x + \frac{1}{2}g_I\cos(\omega_c t)I, \end{aligned} \tag{S1}$$

where $\sigma_z = |e\rangle\langle e| - |g\rangle\langle g|$ is the inversion operator, $\sigma_x = |e\rangle\langle g| + |g\rangle\langle e|)$ is the transition operator, $I = |e\rangle\langle e| + |g\rangle\langle g|$ is the identity operator, $\hat{\vec{d}} = \sum_{ij}\vec{d}_{ij}|i\rangle\langle j|$ for $i, j \in \{e, g\}$ is the dipole moment operator, $g_x = \vec{E}_0\vec{d}_{eg}/\hbar$, $g_z = \vec{E}_0\left(\vec{d}_{ee} - \vec{d}_{gg}\right)/\hbar$, and $g_I = \vec{E}_0\left(\vec{d}_{ee} + \vec{d}_{gg}\right)/\hbar$ are the coupling strengths. Effectively, coupling to the PDMs is manifested as the modification of the transition frequency $\omega_{eg} \rightarrow \omega_{eg}(t)$.

In the next steps, we introduce a series of unitary transformations and justify approximations to simplify the Hamiltonian eventually resulting in a time-independent, Jaynes-Cummings-like form given by Eq. (5) of the main text.

---

* glad@umk.pl
† karolina@umk.pl

A. Transformation U_1 – revealing higher-order resonances

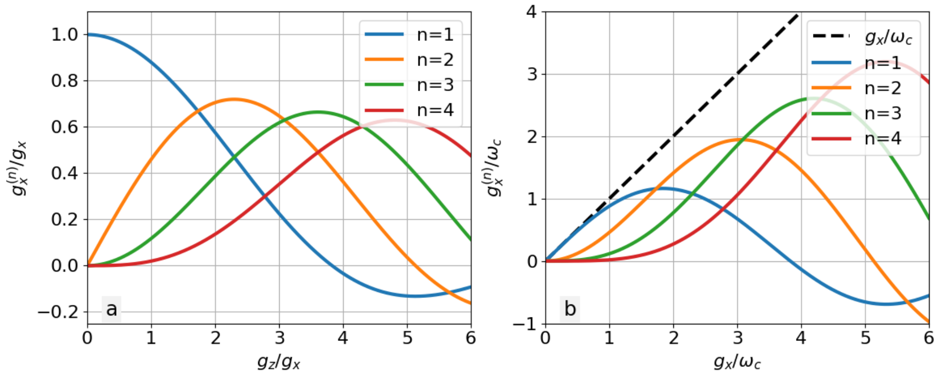

FIG. S1. Coupling strengths of single- (blue), and multi- (orange, green, red) photon resonances in two cases. **a.** As functions of PDMs difference g_z/g_x for a fixed value of the σ_x-coupling $g_x/\omega_c = 1.$ and relative to g_x. **b.** As functions of the field's amplitude g_x/ω_c for a fixed value of PDMs difference $g_z/g_x = 1$. The dashed line corresponds to the nonpolar system.

First, we remove the time dependence of the term proportional to the σ_z operator using the unitary transformation proposed in this context in Ref. [1]

$$\begin{aligned} U_1 &= \mathrm{e}^{\frac{1}{2}\mathrm{i}\kappa_z \sin(\omega_c t)\sigma_z}, \\ U_1\sigma^{\pm}U_1^{\dagger} &= \mathrm{e}^{\pm\mathrm{i}\kappa_z \sin(\omega_c t)}\sigma^{\pm}, \end{aligned} \tag{S2}$$

where $\kappa_z = g_z/\omega_c$ is the key parameter measuring the degree of asymmetry of the system with respect to spatial inversion and reduces to 0 for non-polar systems with vanishing PDMs. The transformed Hamiltonian reads as

$$H_1/\hbar = U_1 H U_1^{\dagger}/\hbar + \mathrm{i}\dot{U}_1 U_1^{\dagger} = \frac{1}{2}\omega_{eg}\sigma_z + g_x\cos(\omega_c t)(\mathrm{e}^{\mathrm{i}\kappa_z\sin(\omega_c t)}\sigma^+ + \mathrm{e}^{-\mathrm{i}\kappa_z\sin(\omega_c t)}\sigma^-), \tag{S3}$$

where $\dot{U}_1 \equiv \frac{\mathrm{d}}{\mathrm{d}t}U_1$. Using the Jacoby-Anger identity $\mathrm{e}^{\pm\mathrm{i}\kappa_z\sin(\omega_c t)} = \sum_{n=-\infty}^{\infty}\mathrm{J}_n(\kappa_z)\mathrm{e}^{\pm\mathrm{i}n\omega_c t}$, we can rewrite the Hamiltonian, with use of the Bessel functions of the first kind J_n, in the form

$$H_1/\hbar = \frac{1}{2}\omega_{eg}\sigma_z + \frac{1}{2}g_x\left(\mathrm{e}^{\mathrm{i}\omega_c t} + \mathrm{e}^{-\mathrm{i}\omega_c t}\right)\sum_{n=-\infty}^{\infty}\left(\mathrm{J}_n(\kappa_z)\mathrm{e}^{\mathrm{i}n\omega_c t}\sigma^+ + \mathrm{J}_n(\kappa_z)\mathrm{e}^{-\mathrm{i}n\omega_c t}\sigma^-\right). \tag{S4}$$

Taking advantage of the Bessel function properties $\mathrm{J}_{-n}(x) = (-1)^n\mathrm{J}_n(x)$, and $\mathrm{J}_{n-1}(x) + \mathrm{J}_{n+1}(x) = \frac{2n}{x}\mathrm{J}_n(x)$, and splitting the equation into terms with different oscillation frequencies, we rewrite

$$H_1/\hbar = \frac{1}{2}\omega_{eg}\sigma_z + \frac{1}{2}g_x\sum_{n=1}^{\infty}\frac{2n}{\kappa_z}\mathrm{J}_n(\kappa_z)\left(\mathrm{e}^{\mathrm{i}n\omega_c t} + (-1)^{n+1}\mathrm{e}^{-\mathrm{i}n\omega_c t}\right)\times\left(\sigma^+ + (-1)^{n+1}\sigma^-\right). \tag{S5}$$

Note that so far we have not introduced any approximations in the Hamiltonian. In this form, Hamiltonian (S5) separates terms that can be interpreted as n-photon resonances with the effective coupling strengths

$$g_x^{(n)}(\vec{E}_0, \vec{d}_{eg}, \Delta\vec{d}, \omega_c) \equiv g_x^{(n)}(\kappa_z) = \frac{2n}{\kappa_z}\mathrm{J}_n(\kappa_z)g_x, \tag{S6}$$

where we have denoted $\Delta\vec{d} = \vec{d}_{ee} - \vec{d}_{gg}$. Hence,

$$H_1/\hbar = \frac{1}{2}\omega_{eg}\sigma_z + \frac{1}{2}g_x^{(1)}\left(\mathrm{e}^{\mathrm{i}\omega_c t} + \mathrm{e}^{-\mathrm{i}\omega_c t}\right)\sigma_x + \underbrace{\frac{1}{2}\sum_{n=2}^{\infty}g_x^{(n)}\left(\mathrm{e}^{\mathrm{i}n\omega_c t} + (-1)^{n+1}\mathrm{e}^{-\mathrm{i}n\omega_c t}\right)\times\left(\sigma^+ + (-1)^{n+1}\sigma^-\right)}_{H_{\mathrm{multi}}/\hbar}. \tag{S7}$$

It is worth noticing that the polarity of the system "unlocks" even-photon-number transitions forbidden in inversion-symmetric systems with nonzero d_{eg}. The H_{multi} Hamiltonian gathers all the multiphoton resonance terms.

For the fixed arbitrarily σ_x-coupling strength $g_x/\omega_c = 1$, the values of the couplings as functions of the polarity g_z/g_x of the system are presented illustratively in Fig. S1a. For small PDMs and field amplitudes – typical in optical experiments and calculations – the single photon coupling $g_x^{(1)}$ is dominant. However, highly polarized systems coupled to strong fields may require accounting for higher-order transitions through terms with $n > 1$. Most importantly, as shown in Fig. S1b, for arbitrary and fixed PDMs difference $g_z/g_x = 1$, the coupling strength $g_x^{(1)}$ significantly deviates from standard g_x (dashed line) as we increase the driving field's amplitude g_x/ω_c. This nonlinear behavior is investigated further in the following parts.

In conclusion, transformation U_1 rotates the reference frame sinusoidally in time. The system defined by the Hamiltonian H is described exactly by the Hamiltonian H_1 in the dynamic frame of reference, where resonances at $n\omega_c \approx \omega$, which we will refer to as "higher-order resonances", are explicit.

B. Transformation U_2 – dealing with counter-rotating terms

At this point, the usual step is to disregard the higher-order- and counter-rotating terms in the rotating-wave approximation (RWA). However, the effects at the focus of this work become relevant in strong fields, for which RWA may not be justified. Hence, we are going to incorporate counter-rotating-term corrections following the idea introduced in Ref. [2] by the second unitary transformation

$$U_2 = \mathrm{e}^{\mathrm{i}\xi\kappa_x \sin(\omega_c t)\sigma_x}, \tag{S8}$$

where $\kappa_x = g_x^{(1)}/\omega_c$. The parameter $\xi \in (0, 1)$ will be evaluated later.

In the frame transformed through U_2, the inversion operator σ_z acquires terms proportional to the Pauli flip operators in form of $\sigma_y = -\mathrm{i}\,(\sigma^+ - \sigma^-)$, and *vice versa*

$$\begin{aligned} U_2\sigma_z U_2^\dagger &= \cos(2\xi\kappa_x \sin(\omega_c t))\sigma_z + \sin(2\xi\kappa_x \sin(\omega_c t))\sigma_y \\ U_2\sigma_y U_2^\dagger &= \cos(2\xi\kappa_x \sin(\omega_c t))\sigma_y - \sin(2\xi\kappa_x \sin(\omega_c t))\sigma_z. \end{aligned} \tag{S9}$$

We make use of the Bessel expansion once again

$$U_2\sigma_{z,y}U_2^\dagger = \left(\mathrm{J}_0(2\xi\kappa_x) + \sum_{k=1}^{\infty} \mathrm{J}_{2k}(2\xi\kappa_x)\left(\mathrm{e}^{\mathrm{i}2k\omega_c} + \mathrm{e}^{-\mathrm{i}2k\omega_c}\right)\right)\sigma_{z,y} \mp \mathrm{i}\sum_{k=0}^{\infty} \mathrm{J}_{2k+1}(2\xi\kappa_x)\left(\mathrm{e}^{\mathrm{i}(2k+1)\omega_c} - \mathrm{e}^{-\mathrm{i}(2k+1)\omega_c}\right)\sigma_{y,z}. \tag{S10}$$

From the form of the expansions we conclude that the rotated Hamiltonian consists of terms with different oscillation frequencies (ω_c, $2\omega_c$, $3\omega_c$, ...). The full form reads

$$\begin{aligned} &H_2/\hbar = U_2 H_1 U_2^\dagger/\hbar + \mathrm{i}\dot{U}_2 U_2^\dagger = \\ &\frac{1}{2}\omega_{eg}\left[\left(\mathrm{J}_0(2\xi\kappa_x) + \sum_{k=1}^{\infty}\mathrm{J}_{2k}(2\xi\kappa_x)\left(\mathrm{e}^{\mathrm{i}2k\omega_c t} + \mathrm{e}^{-\mathrm{i}2k\omega_c t}\right)\right)\sigma_z - \mathrm{i}\sum_{2k+1}^{\infty}(2\xi\kappa_x)\left(\mathrm{e}^{\mathrm{i}(2k+1)\omega_c t} - \mathrm{e}^{-\mathrm{i}(2k+1)\omega_c t}\right)\sigma_y\right] \\ &+ \frac{1}{2}\sum_{k=0}^{\infty} g_x^{(2k)}(\kappa_z)\left(\mathrm{e}^{\mathrm{i}(2k+1)\omega_c t} + \mathrm{e}^{-\mathrm{i}(2k+1)\omega_c t}\right)\sigma_x - \xi g_x^{(1)}\cos(\omega_c t)\sigma_x \\ &+ \frac{\mathrm{i}}{2}\sum_{k=1}^{\infty} g_x^{2k}(\kappa_z)\left(\mathrm{e}^{\mathrm{i}2k\omega_c t} - \mathrm{e}^{-\mathrm{i}2k\omega_c t}\right)\times \\ &\left[\left(\mathrm{J}_0(2\xi\kappa_x) + \sum_{k=1}^{\infty}\mathrm{J}_{2k}(2\xi\kappa_x)\left(\mathrm{e}^{\mathrm{i}2k\omega_c t} + \mathrm{e}^{-\mathrm{i}2k\omega_c t}\right)\right)\sigma_y + \mathrm{i}\sum_{2k+1}^{\infty}(2\xi\kappa_x)\left(\mathrm{e}^{\mathrm{i}(2k+1)\omega_c t} - \mathrm{e}^{-\mathrm{i}(2k+1)\omega_c t}\right)\sigma_z\right]. \end{aligned} \tag{S11}$$

We separated the different frequency terms in the spirit of the RWA. Keeping time-independent terms and terms oscillating with the frequency ω_c, we arrive at an approximated Hamiltonian relevant for the resonance fluorescence problem

$$\begin{aligned} H_2/\hbar \approx \frac{1}{2}\underbrace{\omega_{eg}\mathrm{J}_0(2\xi\kappa_x)}_{\omega'_{eg}}\sigma_z + \underbrace{\sum_{k=1}^{\infty} g_x^{(2k)}(\kappa_z)\frac{4k}{2\xi\kappa_x}\mathrm{J}_{2k}(2\xi\kappa_x)\cos(\omega_c t)}_{g'_z}\sigma_z \\ + \omega_{eg}\mathrm{J}_1(2\xi\kappa_x)\sin(\omega_c t)\sigma_y + (1-\xi)g_x^{(1)}(\kappa_z)\cos(\omega_c t)\sigma_x. \end{aligned} \tag{S12}$$

Here, we introduced ω'_{eg}, which is the modified resonance frequency shifted due to the influence of the counter-rotating terms. The main contribution to this shift is the well-known Bloch-Siegert shift $\xi^2(g_x^{(1)})^2\frac{\omega_{eg}}{\omega_c^2}$, however, the form provided here is more general. We also introduced coupling g'_z which is a correction from the counter-rotating terms to the polar coupling of the system.

At this point, we find the value of the parameter ξ introduced earlier by comparing coupling terms

$$\omega_{eg}\mathrm{J}_1(2\xi\kappa_x) = (1-\xi)g_x^{(1)}(\kappa_z) \equiv \frac{1}{2}\Omega. \tag{S13}$$

This condition simplifies the form of the resulting Hamiltonian and defines the effective coupling strength Ω. After simple transformations, the rewritten Hamiltonian reads

$$H_2/\hbar = \frac{1}{2}\omega'_{eg}\sigma_z + g'_z\cos(\omega_c t)\sigma_z + \frac{1}{2}\Omega\left(\mathrm{e}^{-\mathrm{i}\omega_c t}\sigma^+ + \mathrm{e}^{\mathrm{i}\omega_c t}\sigma^-\right). \tag{S14}$$

With the second transformation, we have taken into account the counter-rotating terms in the effective parameters ω'_{eg}, g'_z and Ω. We now proceed to effectively remove the σ_z-coupling.

C. Transformation U_3 – effectively removing the σ_z coupling

The above form is very similar to the one given in the initial Hamiltonian (S1). Hence, the oscillating σ_z term can be treated with a transformation analogous to (S2)

$$U_3 = \mathrm{e}^{\frac{1}{2}\mathrm{i}\kappa'_z\sin(\omega_c t)\sigma_z}, \tag{S15}$$

where $\kappa'_z = g'_z/\omega_c$. The transformed Hamiltonian takes the form which we refer to as Jaynes-Cummings-like since the field is in this case treated classically unlike in the original Jaynes-Cummings model

$$H_3/\hbar \approx \frac{1}{2}\omega'_{eg}\sigma_z + \frac{1}{2}\underbrace{\Omega\mathrm{J}_0(\kappa'_z)}_{\Omega'}\left(\mathrm{e}^{-\mathrm{i}\omega_c t}\sigma^+ + \mathrm{e}^{\mathrm{i}\omega_c t}\sigma^-\right). \tag{S16}$$

Here, Ω' is the effective coupling strength.

D. Transformation U_4 – moving to the interaction picture

Finally, by applying interaction picture transformation

$$U_4 = \mathrm{e}^{\frac{1}{2}\mathrm{i}\omega_c t\sigma_z}, \tag{S17}$$

and setting effective detuning $\delta' = \omega_c - \omega'_{eg}$, we end up with the final, time-independent form same as Eq. (5) in the main text

$$H_{\mathrm{eff}}/\hbar = -\frac{1}{2}\delta'\sigma_z + \frac{1}{2}\Omega'\sigma_x. \tag{S18}$$

To conclude, we have applied a series of noncommutative unitary transformations or Bloch sphere rotations around the z and x axes. Each of these transformations introduces a Hamiltonian simplification and captures subsequent Hamiltonian terms in effective parameters. As a result, we have arrived at the Hamiltonian H_{eff}, whose simple form captures the rich physics of interactions of light with transition and permanent dipole moments in the ultrastrong coupling regime, including the influence of counter-rotating terms, Bloch-Siegert frequency shift, and beyond. In H_{eff}, we have neglected higher-order resonances of the type $n\omega_c \approx \omega_{eg}$, which is justified with our original assumption that $\omega_c \approx \omega_{eg}$.

II. DERIVATION OF RELAXATION RATE EQ. (7)

To take into account dissipation processes (e.g., spontaneous emission), we consider an additional interaction between the TLS and a bosonic reservoir

$$H_R/\hbar = \sum_p \omega_p b_p^\dagger b_p + \frac{1}{2}\sum_p g_p (b_p^\dagger + b_p)\sigma_x. \tag{S19}$$

The reservoir modes are described by the creation $b^\dagger$ and annihilation b_p operators with corresponding mode frequencies ω_p. The coupling strength between these modes and the system is given by g_p.

We move to the interaction picture for the reservoir by making use of the unitary transformation

$$U_{\text{int}}^R = \mathrm{e}^{\mathrm{i}\sum_m \omega_m b_m^\dagger b_m t} \tag{S20}$$

that does not affect the system and, therefore, does not interfere with our previous calculations. The interaction-picture Hamiltonian takes the form

$$H_{R,\text{int}}/\hbar = \frac{1}{2}\sum_p g_p \left(b_p^\dagger \mathrm{e}^{\mathrm{i}\omega_p t} + b_p \mathrm{e}^{-\mathrm{i}\omega_p t}\right)\sigma_x. \tag{S21}$$

We now apply all the transformations U_1–U_4 to the system operators $\sigma_{x,y,z}$, and list below the nontrivial transformation prescriptions:

$$\begin{aligned}
U_1\sigma_x U_1^\dagger &= \left(\mathrm{J}_0(\kappa_z) + \sum_{k=1}^{\infty}\mathrm{J}_{2k}(\kappa_z)\left(\mathrm{e}^{\mathrm{i}2k\omega_c t} + \mathrm{e}^{-\mathrm{i}2k\omega_c t}\right)\right)\sigma_x + \sum_{k=0}^{\infty}\mathrm{J}_{2k+1}(\kappa_z)\left(\mathrm{e}^{\mathrm{i}(2k+1)\omega_c t} - \mathrm{e}^{-\mathrm{i}(2k+1)\omega_c t}\right)\mathrm{i}\sigma_y,\\
U_2\mathrm{i}\sigma_y U_2^\dagger &= \left(\mathrm{J}_0(2\xi\kappa_x) + \sum_{k=1}^{\infty}\mathrm{J}_{2k}(2\xi\kappa_x)\left(\mathrm{e}^{\mathrm{i}2k\omega_c t} + \mathrm{e}^{-\mathrm{i}2k\omega_c t}\right)\right)\mathrm{i}\sigma_y - \sum_{k=0}^{\infty}\mathrm{J}_{2k+1}(2\xi\kappa_x)\left(\mathrm{e}^{\mathrm{i}(2k+1)\omega_c t} - \mathrm{e}^{-\mathrm{i}(2k+1)\omega_c t}\right)\sigma_z,\\
U_3\sigma_1 U_3^\dagger &= \left(\mathrm{J}_0(\kappa_z') + \sum_{k=1}^{\infty}\mathrm{J}_{2k}(\kappa_z')\left(\mathrm{e}^{\mathrm{i}2k\omega_c t} + \mathrm{e}^{-\mathrm{i}2k\omega_c t}\right)\right)\sigma_1 + \sum_{k=0}^{\infty}\mathrm{J}_{2k+1}(\kappa_z')\left(\mathrm{e}^{\mathrm{i}(2k+1)\omega_c t} - \mathrm{e}^{-\mathrm{i}(2k+1)\omega_c t}\right)\sigma_2,\\
U_4\sigma_x U_4^\dagger &= \left(\sigma^+\mathrm{e}^{\mathrm{i}\omega_c t} + \sigma^-\mathrm{e}^{-\mathrm{i}\omega_c t}\right),\\
U_4\mathrm{i}\sigma_y U_4^\dagger &= \left(\sigma^+\mathrm{e}^{\mathrm{i}\omega_c t} - \sigma^-\mathrm{e}^{-\mathrm{i}\omega_c t}\right).
\end{aligned} \tag{S22}$$

where the third line above applies for pairs $(\sigma_1, \sigma_2) = (\sigma_x, \mathrm{i}\sigma_y),\ (\mathrm{i}\sigma_y, \sigma_x)$.

Putting together all the pieces, we end up with a fully transformed Hamiltonian describing system-reservoir interaction

$$
\begin{aligned}
H_{R,\mathrm{int}}/\hbar = {} & \frac{1}{2}\sum_p g_p \underline{\left(b_p^\dagger \mathrm{e}^{\mathrm{i}\omega_p t} + b_p \mathrm{e}^{-\mathrm{i}\omega_p t}\right)} \times \\
\Bigg[& -\sum_{k=0}^{\infty}\sum_{l=0}^{\infty} \mathrm{J}_{2k+1}(\kappa_z)\mathrm{J}_{2l+1}(2\xi\kappa_x)\left(\mathrm{e}^{\mathrm{i}(2k+1)\omega_c t} - \mathrm{e}^{-\mathrm{i}(2k+1)\omega_c t}\right)\left(\mathrm{e}^{\mathrm{i}(2l+1)\omega_c t} - \mathrm{e}^{-\mathrm{i}(2l+1)\omega_c t}\right)\sigma_z \\
& + \Bigg[\left(\mathrm{J}_0(\kappa_z) + \sum_{k=1}^{\infty}\mathrm{J}_{2k}(\kappa_z)\left(\mathrm{e}^{\mathrm{i}2k\omega_c t} + \mathrm{e}^{-\mathrm{i}2k\omega_c t}\right)\right)\left(\mathrm{J}_0(\kappa_z') + \sum_{l=1}^{\infty}\mathrm{J}_{2l}(\kappa_z')\left(\mathrm{e}^{\mathrm{i}2l\omega_c t} + \mathrm{e}^{-\mathrm{i}2l\omega_c t}\right)\right) \\
& \quad + \sum_{k=0}^{\infty}\mathrm{J}_{2k+1}(\kappa_z)\left(\mathrm{e}^{\mathrm{i}(2k+1)\omega_c t} - \mathrm{e}^{-\mathrm{i}(2k+1)\omega_c t}\right)\left(\mathrm{J}_0(2\xi\kappa_x) + \sum_{l=1}^{\infty}\mathrm{J}_{2l}(2\xi\kappa_x)\left(\mathrm{e}^{\mathrm{i}2l\omega_c t} + \mathrm{e}^{-\mathrm{i}2l\omega_c t}\right)\right)\times \\
& \quad \sum_{m=0}^{\infty}\mathrm{J}_{2m+1}(\kappa_z')\left(\mathrm{e}^{\mathrm{i}(2m+1)\omega_c t} - \mathrm{e}^{-\mathrm{i}(2m+1)\omega_c t}\right)\Bigg]\underline{\left(\sigma^+\mathrm{e}^{\mathrm{i}\omega_c t} + \sigma^-\mathrm{e}^{-\mathrm{i}\omega_c t}\right)} \\
& + \Bigg[\left(\mathrm{J}_0(\kappa_z) + \sum_{k=1}^{\infty}\mathrm{J}_{2k}(\kappa_z)\left(\mathrm{e}^{\mathrm{i}2k\omega_c t} + \mathrm{e}^{-\mathrm{i}2k\omega_c t}\right)\right)\sum_{l=0}^{\infty}\mathrm{J}_{2l+1}(\kappa_z')\left(\mathrm{e}^{\mathrm{i}(2l+1)\omega_c t} - \mathrm{e}^{-\mathrm{i}(2l+1)\omega_c t}\right) \\
& \quad + \sum_{k=0}^{\infty}\mathrm{J}_{2k+1}(\kappa_z)\left(\mathrm{e}^{\mathrm{i}(2k+1)\omega_c t} - \mathrm{e}^{-\mathrm{i}(2k+1)\omega_c t}\right)\left(\mathrm{J}_0(2\xi\kappa_x) + \sum_{l=1}^{\infty}\mathrm{J}_{2l}(2\xi\kappa_x)\left(\mathrm{e}^{\mathrm{i}2l\omega_c t} + \mathrm{e}^{-\mathrm{i}2l\omega_c t}\right)\right)\times \\
& \quad \left(\mathrm{J}_0(\kappa_z') + \sum_{m=1}^{\infty}\mathrm{J}_{2m}(\kappa_z')\left(\mathrm{e}^{\mathrm{i}2m\omega_c t} + \mathrm{e}^{-\mathrm{i}2m\omega_c t}\right)\right)\Bigg]\underline{\left(\sigma^+\mathrm{e}^{\mathrm{i}\omega_c t} - \sigma^-\mathrm{e}^{-\mathrm{i}\omega_c t}\right)}\Bigg].
\end{aligned}
\tag{S23}
$$

Since we consider a thermal reservoir in the vacuum state weakly coupled to the system, the terms oscillating at $\mathrm{e}^{\pm\mathrm{i}(\omega_p-\omega_c)}$ are significant, while other rapidly oscillating terms in the above equation can be disregarded. Moreover, we can also exclude the whole second rectangular bracket, as all the multiplications provide time-dependent terms. Hence, the complexity of the problem reduces significantly and we arrive at

$$
H_{R,\mathrm{int}}/\hbar \approx \frac{1}{2}\sum_p g_p\alpha\left(b_p^\dagger\sigma^-\mathrm{e}^{\mathrm{i}(\omega_p-\omega_c)t} + b_p\sigma^+\mathrm{e}^{-\mathrm{i}(\omega_p-\omega_c)t}\right), \tag{S24}
$$

with

$$
\begin{aligned}
\alpha(\kappa_z,\kappa_x,\kappa_z') = {} & \mathrm{J}_0(\kappa_z)\mathrm{J}_0(\kappa_z') + 2\sum_{k=1}^{\infty}\mathrm{J}_{2k}(\kappa_z)\mathrm{J}_{2k}(\kappa_z') - 2\mathrm{J}_0(2\xi\kappa_x)\sum_{k=0}^{\infty}\mathrm{J}_{2k+1}(\kappa_z)\mathrm{J}_{2k+1}(\kappa_z') \\
& - 2\sum_{k=0}^{\infty}\sum_{l=1}^{\infty}\mathrm{J}_{2k+1}(\kappa_z)\mathrm{J}_{2l}(2\xi\kappa_x)\mathrm{J}_{2(k+l)+1}(\kappa_z') + 2\sum_{k=0}^{\infty}\sum_{m=0}^{\infty}\mathrm{J}_{2k+1}(\kappa_z)\mathrm{J}_{2(k+m+1)}(2\xi\kappa_x)\mathrm{J}_{2m+1}(\kappa_z') \\
& - 2\sum_{l=1}^{\infty}\sum_{m=0}^{\infty}\mathrm{J}_{2(l+m)+1}(\kappa_z)\mathrm{J}_{2l}(2\xi\kappa_x)\mathrm{J}_{2m+1}(\kappa_z').
\end{aligned}
\tag{S25}
$$

Following the Weisskopf-Wigner theory [3], we find the effective spontaneous emission rate to be the same as Eq. (7) from the main text

$$
\gamma' = \alpha^2\gamma \approx \left(\mathrm{J}_0(\kappa_z)\mathrm{J}_0(\kappa_z')\right)^2\gamma, \tag{S26}
$$

where γ is the emission rate for the non-polar case. Note that in the resulting frame, due to the PDMs, the effective spontaneous emission rate becomes dependent on the external field amplitude $\vec{E}_0$. The emission rate keeps its original value γ without PDMs or the external field. The result given by Eq. (S26) without the approximation is presented graphically in the main text in Fig. 1d. The appearance of the PDMs in the system significantly reduces the gamma rate, while strong field interaction incorporates small correction (compare the blue and orange curves).

III. STATIONARY SOLUTION

Based on the above expressions, we can write the master equation for the polar system's density matrix ρ which also undergoes the unitary transformations

$$\rho \to U_4(t)U_3(t)U_2(t)U_1(t)\rho U_1^\dagger(t)U_2^\dagger(t)U_3^\dagger(t)U_4^\dagger(t) \tag{S27}$$

under the evolution of the approximated Hamiltonian Eq. (S18)

$$\dot{\rho} = [H_{\text{eff}}/\hbar, \rho] - \mathrm{i}\frac{\gamma'}{2}\left(\sigma^+\sigma^-\rho + \rho\sigma^+\sigma^- - 2\sigma^-\rho\sigma^+\right). \tag{S28}$$

To solve this equation for the stationary state ($\dot{\rho}(t) = 0$), we rewrite it in the matrix form for the expectation values of the operators $\sigma_z, \sigma^\pm$

$$\vec{0} = \begin{pmatrix} -\mathrm{i}\delta' - \frac{1}{2}\gamma' & 0 & -\frac{1}{2}\mathrm{i}\Omega' \\ 0 & \mathrm{i}\delta' - \frac{1}{2}\gamma' & \frac{1}{2}\mathrm{i}\Omega' \\ -\mathrm{i}\Omega' & \mathrm{i}\Omega' & -\gamma' \end{pmatrix} \begin{pmatrix} \langle\sigma^+\rangle_s \\ \langle\sigma^-\rangle_s \\ \langle\sigma_z\rangle_s \end{pmatrix} - \begin{pmatrix} 0 \\ 0 \\ \gamma' \end{pmatrix}, \tag{S29}$$

where subscript s indicates stationary solution

$$\begin{aligned} \langle\sigma^\pm\rangle_s &= \frac{\Omega'(2\delta' \pm \mathrm{i}\gamma')}{2\Omega'^2 + 4\delta'^2 + \gamma'^2}, \\ \langle\sigma_z\rangle_s &= -\frac{(4\delta'^2 + \gamma'^2)}{2\Omega'^2 + 4\delta'^2 + \gamma'^2}. \end{aligned} \tag{S30}$$

IV. FLUORESCENCE SPECTRA

The general formula for the emission spectrum reads [3]

$$S(\omega) = \frac{1}{2\pi}\lim_{T\to\infty}\frac{1}{T}\int_0^T dt \int_0^T dt' g^{(1)}(t,t')\mathrm{e}^{-\mathrm{i}\omega(t-t')}, \tag{S31}$$

where $g^{(1)}$ is the first-order correlation function

$$g^{(1)}(t,t') = \langle U^\dagger(t)\sigma^+ U(t) U^\dagger(t')\sigma^- U(t')\rangle, \tag{S32}$$

where $U(t)$ is an evolution operator of Hamiltonian Eq. (S1). The further calculations in this section provide generalization of the work done in Ref. [2]. The correlation function can be found analytically in the reference frame rotated according to the sequence of operators U_1–U_4

$$\begin{aligned} \sigma^\pm \to & U_4(t)U_3(t)U_2(t)U_1(t)\sigma^\pm U_1^\dagger(t)U_2^\dagger(t)U_3^\dagger(t)U_4^\dagger(t) \\ = & \frac{1}{2}\sum_{m\ \text{odd}}^{\infty}\left(j'_{m+1}\mathrm{e}^{\pm\mathrm{i}m\omega_c t} + j_{m+1}\mathrm{e}^{\mp\mathrm{i}m\omega_c t}\right)\sigma_z \\ & + \frac{1}{2}\sum_{m=0}^{\infty}\left[\left(\alpha_m\mathrm{e}^{\pm\mathrm{i}m\omega_c t} + \beta_m\mathrm{e}^{\mp\mathrm{i}m\omega_c t}\right)\sigma^\pm + \left(\alpha'_m\mathrm{e}^{\pm\mathrm{i}m\omega_c t} + \beta'_m\mathrm{e}^{\mp\mathrm{i}m\omega_c t}\right)\sigma^\mp\right], \end{aligned} \tag{S33}$$

where the $\sigma^\pm$ operators on the right-hand side are given in the rotated reference frame. Above, we have used the following symbols

$$\begin{aligned} j_n &= \begin{cases} 1 + \mathrm{J}_0(2\xi\kappa_x), & n = 1 \\ \mathrm{J}_{n-1}(2\xi\kappa_x), & n \neq 1 \end{cases} \\ j'_n &= \begin{cases} 1 - \mathrm{J}_0(2\xi\kappa_x), & n = 1 \\ -\mathrm{J}_{n-1}(2\xi\kappa_x), & n \neq 1 \end{cases} \end{aligned} \tag{S34}$$

and

$$\alpha_m = \begin{cases} \frac{1}{2}\sum\limits_{n\ \text{odd}}^{\infty} \mathrm{J}_n(\kappa_z^{\Sigma})(j_{n+2} - j_n), & m = 0 \\ \mathrm{J}_0(\kappa_z^{\Sigma})j_1 + \sum\limits_{n\ \text{odd}}^{\infty} \left[\mathrm{J}_{n+1}(\kappa_z^{\Sigma})j_{n+2} + \mathrm{J}_{\underset{(n>1)}{n-1}}(\kappa_z^{\Sigma})j_n\right], & m = 1 \\ \sum\limits_{n\ \text{odd}}^{\infty} \left[\mathrm{J}_{\underset{(m>n)}{m-n}}(\kappa_z^{\Sigma})j_n + \mathrm{J}_{m+n}(\kappa_z^{\Sigma})j_{n+2} - \mathrm{J}_{\underset{(n>m)}{n-m}}(\kappa_z^{\Sigma})j_n\right], & m\ \text{even} \\ \sum\limits_{n\ \text{odd}}^{\infty} \left[\mathrm{J}_{\underset{(m>n)}{m-n}}(\kappa_z^{\Sigma})j_n + \mathrm{J}_{m+n}(\kappa_z^{\Sigma})j_{n+2} + \mathrm{J}_{\underset{(n>m)}{n-m}}(\kappa_z^{\Sigma})j_n\right] + J_0(\kappa_z^{\Sigma})j_m, & m\ \text{odd} \end{cases} \tag{S35}$$

$$\beta_m = \begin{cases} \frac{1}{2}\sum\limits_{n\ \text{odd}}^{\infty} \mathrm{J}_n(\kappa_z^{\Sigma})(j_{n+2} - j_n), & m = 0 \\ \mathrm{J}_0(\kappa_z^{\Sigma})j_{1+2} + \sum\limits_{n\ \text{odd}}^{\infty} \left[\mathrm{J}_{n+1}(\kappa_z^{\Sigma})j_n + \mathrm{J}_{\underset{(n>1)}{n-1}}(\kappa_z^{\Sigma})j_{n+2}\right], & m = 1 \\ -\sum\limits_{n\ \text{odd}}^{\infty} \left[\mathrm{J}_{\underset{(m>n)}{m-n}}(\kappa_z^{\Sigma})j_{n+2} + \mathrm{J}_{m+n}(\kappa_z^{\Sigma})j_n - \mathrm{J}_{\underset{(n>m)}{n-m}}(\kappa_z^{\Sigma})j_{n+2}\right], & m\ \text{even} \\ \sum\limits_{n\ \text{odd}}^{\infty} \left[\mathrm{J}_{\underset{(m>n)}{m-n}}(\kappa_z^{\Sigma})j_{n+2} + \mathrm{J}_{m+n}(\kappa_z^{\Sigma})j_n + \mathrm{J}_{\underset{(n>m)}{n-m}}(\kappa_z^{\Sigma})j_{n+2}\right] + J_0(\kappa_z^{\Sigma})j_{m+2}. & m\ \text{odd} \end{cases} \tag{S36}$$

The relation between the primed and non-primed parameters is

$$\alpha_m,\ \beta_m \xrightarrow[\substack{j_n \to j'_{n+2} \\ j_{n+2} \to j'_n \\ \kappa_z^{\Sigma} \to \kappa_z^{\Delta}}]{} \alpha'_m,\ \beta'_m. \tag{S37}$$

Above, $\kappa_z^{\Sigma} = \kappa_z + \kappa'_z$, and $\kappa_z^{\Delta} = \kappa_z - \kappa'_z$.

Eventually, the correlation function reads as

$$\begin{aligned} g^{(1)}(t,t') = \Bigg\langle \Bigg(&\frac{1}{2}\sum_{m'\ \text{odd}}^{\infty} \left(j'_{m'+1}\mathrm{e}^{\mathrm{i}m'\omega_c t} + j_{m'+1}\mathrm{e}^{-\mathrm{i}m'\omega_c t}\right)\sigma_z \\ &+ \frac{1}{2}\sum_{m'=0}^{\infty} \left[\left(\alpha_{m'}\mathrm{e}^{\mathrm{i}m'\omega_c t} + \beta_{m'}\mathrm{e}^{-\mathrm{i}m'\omega_c t}\right)\sigma^+ + \left(\alpha'_{m'}\mathrm{e}^{\mathrm{i}m'\omega_c t} + \beta'_{m'}\mathrm{e}^{-\mathrm{i}m'\omega_c t}\right)\sigma^-\right]\Bigg) \\ \times \Bigg(&\frac{1}{2}\sum_{m\ \text{odd}}^{\infty} \left(j'_{m+1}\mathrm{e}^{-\mathrm{i}m\omega_c t'} + j_{m+1}\mathrm{e}^{\mathrm{i}m\omega_c t'}\right)\sigma_z \\ &+ \frac{1}{2}\sum_{m=0}^{\infty} \left[\left(\alpha_m\mathrm{e}^{-\mathrm{i}m\omega_c t'} + \beta_m\mathrm{e}^{\mathrm{i}m\omega_c t'}\right)\sigma^- + \left(\alpha'_m\mathrm{e}^{-\mathrm{i}m\omega_c t'} + \beta'_m\mathrm{e}^{\mathrm{i}m\omega_c t'}\right)\sigma^+\right]\Bigg)\Bigg\rangle. \end{aligned} \tag{S38}$$

We have obtained an expression with two types of terms with exponents: $\mathrm{e}^{\pm\mathrm{i}m'\omega_c t}\mathrm{e}^{\mp\mathrm{i}m\omega_c t'}$, and $\mathrm{e}^{\pm\mathrm{i}m'\omega_c t}\mathrm{e}^{\pm\mathrm{i}m\omega_c t'}$. To calculate the spectrum based on Eq. (S31), we integrate each of these terms, approximating as follows

$$\begin{aligned} I(\omega) &= \lim_{T\to\infty}\frac{1}{T}\int_0^T dt \int_0^T dt' \mathrm{e}^{\pm\mathrm{i}m'\omega_c t}\mathrm{e}^{\mp\mathrm{i}m\omega_c t'}\mathrm{e}^{-\mathrm{i}\omega(t-t')} \times \langle\sigma_\mu(t-t')\sigma_\nu(0)\rangle \\ &= \lim_{T\to\infty}\frac{1}{T}\int_0^T dt' \mathrm{e}^{\pm\mathrm{i}(m'-m)\omega_c t'} \int_{-t'}^{T-t'} d\tau \mathrm{e}^{\pm\mathrm{i}(m'\omega_c \mp \omega)\tau} \times \langle\sigma_\mu(\tau)\sigma_\nu(0)\rangle \\ &\approx \delta_{m',m}\int_{-\infty}^{\infty} d\tau \mathrm{e}^{\pm\mathrm{i}(m'\omega_c \mp \omega)\tau}\langle\sigma_\mu(\tau)\sigma_\nu(0)\rangle_s, \end{aligned} \tag{S39}$$

where $\tau = t - t'$, $\mu, \nu \in \{z, +, -\}$ and we moved to the stationary state for the expectation values $\langle\sigma_\mu(\tau)\sigma_\nu(0)\rangle \to \langle\sigma_\mu(\tau)\sigma_\nu(0)\rangle_s$ by setting integral limits $T - t' \to \infty$, $-t' \to -\infty$. Due to this approximation, we simplified the correlation function by removing one of the sums, as only the terms with $m = m'$ contribute. Moreover, following the same procedure for terms $\mathrm{e}^{\pm \mathrm{i}m'\omega_c t}\mathrm{e}^{\pm \mathrm{i}m\omega_c t'}$, we end up with $\delta_{m',-m}$ which leaves only one term with $m' = -m = 0$, as $m, m' \geq 0$.

We end up with a compact form of the expression for the fluorescence spectrum

$$S(\omega) = \frac{1}{4\pi}\,\mathrm{Re}\int\limits_0^\infty d\tau \sum_{n=0}^{\infty}\sum_{\mu,\nu}\left(A^+_{\mu\nu}(n)\mathrm{e}^{\mathrm{i}n\omega_c\tau} + A^-_{\mu\nu}(n)\mathrm{e}^{-\mathrm{i}n\omega_c\tau}\right) \times \langle\sigma_\mu(\tau)\sigma_\nu(0)\rangle, \tag{S40}$$

where

$$\begin{aligned}
A^+_{zz}(n) &= \begin{cases} 0, & n \text{ even} \\ j'^2_{n+1}, & n \text{ odd} \end{cases} \\
A^+_{z-}(n) = A^+_{+z}(n) &= \begin{cases} 0, & n \text{ even} \\ j'_{n+1}\alpha_n, & n \text{ odd} \end{cases} \\
A^+_{z+}(n) = A^+_{-z}(n) &= \begin{cases} 0, & n \text{ even} \\ j'_{n+1}\alpha'_n, & n \text{ odd} \end{cases} \\
A^+_{--}(n) = A^+_{++}(n) &= \begin{cases} \alpha_n\alpha'_n + \alpha'_n\beta_n, & n = 0 \\ \alpha_n\alpha'_n, & n \neq 0 \end{cases} \\
A^+_{-+}(n) &= \begin{cases} \alpha'^2_n + \alpha'_n\beta'_n, & n = 0 \\ \alpha'^2_n, & n \neq 0 \end{cases} \\
A^+_{+-}(n) &= \begin{cases} \alpha^2_n + \alpha_n\beta_n, & n = 0 \\ \alpha^2_n, & n \neq 0 \end{cases} \\
A^+_{\mu\nu}(n) &\xrightarrow[\substack{j'_n \to j_n \\ \alpha_n,\, \alpha'_n \to \beta_n,\, \beta'_n \\ \beta_n,\, \beta'_n \to \alpha_n,\, \alpha'_n}]{} A^-_{\mu\nu}(n).
\end{aligned} \tag{S41}$$

Finally, we evaluate the expectation values for the operators. We are interested in the incoherent part of the spectrum, hence, we use the quantity

$$\langle\langle\sigma_\mu(\tau)\sigma_\nu(0)\rangle\rangle = \langle\sigma_\mu(\tau)\sigma_\nu(0)\rangle_s - \langle\sigma_\mu\rangle_s\langle\sigma_\nu\rangle_s. \tag{S42}$$

Using the quantum regression theorem [3] and following reasoning in Ref. [2] for the master equation Eq. (S28), we find that

$$\frac{d}{d\tau}\langle\langle\sigma_\mu(\tau)\sigma_\nu(0)\rangle\rangle = \sum_\lambda M_{\mu\lambda}\langle\langle\sigma_\lambda(\tau)\sigma_\nu(0)\rangle\rangle, \tag{S43}$$

where M is the matrix responsible for the homogeneous evolution in the GKLS equation (S29)

$$M = \begin{pmatrix} -\mathrm{i}\delta' - \frac{1}{2}\gamma' & 0 & -\frac{1}{2}\mathrm{i}\Omega' \\ 0 & \mathrm{i}\delta' - \frac{1}{2}\gamma' & \frac{1}{2}\mathrm{i}\Omega' \\ -\mathrm{i}\Omega' & \mathrm{i}\Omega' & -\gamma' \end{pmatrix}. \tag{S44}$$

Making use of the Laplace transformation $\mathcal{L}(f(t)) = \int_0^\infty f(t)\mathrm{e}^{-s\tau}\mathrm{d}\tau = \mathcal{L}[f](s)$, this set of equations can be written as

$$\left(M - \frac{1}{s}I\right)\mathcal{L}[X_\nu](s) = X_{0\nu}, \tag{S45}$$

where $X_{0\nu}$ provides initial conditions

$$X_{0\nu} = \begin{pmatrix} \langle\langle\sigma^+(0)\sigma_\nu(0)\rangle\rangle \\ \langle\langle\sigma^-(0)\sigma_\nu(0)\rangle\rangle \\ \langle\langle\sigma_z(0)\sigma_\nu(0)\rangle\rangle \end{pmatrix}, \quad X_\nu = \begin{pmatrix} \langle\langle\sigma^+(\tau)\sigma_\nu(0)\rangle\rangle \\ \langle\langle\sigma^-(\tau)\sigma_\nu(0)\rangle\rangle \\ \langle\langle\sigma_z(\tau)\sigma_\nu(0)\rangle\rangle \end{pmatrix}. \tag{S46}$$

The solutions can be expressed as [2]

$$\langle\langle\sigma_\mu(\tau)\sigma_\nu(0)\rangle\rangle = \sum_{l=1}^{3} R^l_{\mu\nu} \mathrm{e}^{s_l \tau} \tag{S47}$$

where $R^l_{\mu\nu} = \lim_{s\to s_l}(s - s_l)\mathcal{L}[\langle\langle\sigma_\mu(\tau)\sigma_\nu(0)\rangle\rangle](s)$, for s_l beeing the roots of the determinant

$$\det\left(M - \frac{1}{s}I\right) = s^3 + 2\gamma' s^2 + (\Omega'^2 + \delta'^2 + \frac{5}{4}\gamma'^2)s + \gamma'(\frac{1}{2}\Omega'^2 + \delta'^2 + \frac{1}{4}\gamma'^2), \tag{S48}$$

which are of the form $s_1 = -\gamma_1$, $s_2 = -\gamma_2 + \mathrm{i}\widetilde{\Omega}$, $s_3 = -\gamma_2 - \mathrm{i}\widetilde{\Omega}$, and $\gamma_{1,2}, \widetilde{\Omega} \geq 0$.

Hence, the spectrum can be written as

$$S(\omega) = \frac{1}{4\pi}\,\mathrm{Re}\sum_{n=0}^{\infty}\sum_{\mu,\nu}\sum_{l=1}^{3}\left[A^+_{\mu\nu}(n)R^l_{\mu\nu}\int_0^\infty d\tau \mathrm{e}^{-\mathrm{i}(\omega - n\omega_c)\tau + s_l\tau} + A^-_{\mu\nu}(n)R^l_{\mu\nu}\int_0^\infty d\tau \mathrm{e}^{-\mathrm{i}(\omega + n\omega_c)\tau + s_l\tau}\right], \tag{S49}$$

With that, we can calculate the above integrals which describe the lineshapes $L^\pm_{n,l}(\omega)$

$$L^\pm_{n,l}(\omega) = \begin{cases} \dfrac{\gamma_1 - \mathrm{i}(\omega \mp n\omega_c)}{\gamma_1^2 + (\omega \mp n\omega_c)^2}, & l = 1 \\ \dfrac{\gamma_2 - \mathrm{i}(\omega \mp n\omega_c - \widetilde{\Omega})}{\gamma_2^2 + (\omega \mp n\omega_c - \widetilde{\Omega})^2}, & l = 2 \\ \dfrac{\gamma_2 - \mathrm{i}(\omega \mp n\omega_c + \widetilde{\Omega})}{\gamma_2^2 + (\omega \mp n\omega_c + \widetilde{\Omega})^2}, & l = 3. \end{cases} \tag{S50}$$

Lineshape intensities $I^\pm_{n,l}$ are given by

$$I^\pm_{n,l} = \sum_{\mu,\nu} A^\pm_{\mu\nu}(n)R^l_{\mu\nu}. \tag{S51}$$

Finally, the full spectrum can be calculated as

$$S(\omega) = \frac{1}{4\pi}\sum_{n=0}^{\infty}\sum_{l=1}^{3}\left(I^+_{n,l}L^+_{n,l}(\omega) + I^-_{n,l}L^-_{n,l}(\omega)\right). \tag{S52}$$

[1] O. Kibis, G. Y. Slepyan, S. Maksimenko, and A. Hoffmann, Matter coupling to strong electromagnetic fields in two-level quantum systems with broken inversion symmetry, Physical review letters **102**, 023601 (2009).

[2] Y. Yan, Z. Lü, and H. Zheng, Effects of counter-rotating-wave terms of the driving field on the spectrum of resonance fluorescence, Physical Review A—Atomic, Molecular, and Optical Physics **88**, 053821 (2013).

[3] M. O. Scully and M. S. Zubairy, *Quantum optics* (Cambridge university press, 1997).

3.2 LOW-FREQUENCY RADIATION GENERATION

In article A2, we investigate the generation and propagation of low-frequency coherent radiation in a medium of polar molecules. This is the continuation of the theory described in Sections 2.1 and 2.3. The emphasis is on using polar molecules with broken inversion symmetry to produce tunable radiation in the microwave domain driven by coherent light. This makes it useful for various applications in quantum optics and communications.

Key elements of this work:

- A theoretical model describes how a resonant driving field causes Rabi oscillations in the molecules, generating low-frequency radiation.
- Bloch–Maxwell equations beyond SVEA are used to simulate the build-up and propagation of the signal, demonstrating tunable coherent output, with potential applications in microwave and terahertz radiation sources.
- The frequency of the generated radiation can be controlled by adjusting the drive's amplitude and detuning.
- The model is applied to a realistic medium of LiH molecules, for which the effect of external polarizing DC field on the average orientation of dipole moments is thoroughly evaluated.
- The solver used for this work was written in Python and is available online [56].

In the article, I contributed to the conception of the idea, followed by the dominant contributions to the development of the theory, results analysis, and manuscript preparation. I am fully responsible for the numerical software implementation.

www.nature.com/scientificreports

scientific reports

OPEN

Propagation of optically tunable coherent radiation in a gas of polar molecules

Piotr Gładysz✉, Piotr Wcisło & Karolina Słowik

Coherent, optically dressed media composed of two-level molecular systems without inversion symmetry are considered as all-optically tunable sources of coherent radiation in the microwave domain. A theoretical model and a numerical toolbox are developed to confirm the main finding: the generation of low-frequency radiation, and the buildup and propagation dynamics of such low-frequency signals in a medium of polar molecules in a gas phase. The physical mechanism of the signal generation relies on the permanent dipole moment characterizing systems without inversion symmetry. The molecules are polarized with a DC electric field yielding a permanent electric dipole moment in the laboratory frame; the direction and magnitude of the moment depend on the molecular state. As the system is resonantly driven, the dipole moment oscillates at the Rabi frequency and, hence, generates microwave radiation. We demonstrate the tuning capability of the output signal frequency with the drive amplitude and detuning. We find that even though decoherence mechanisms such as spontaneous emission may damp the output field, a scenario based on pulsed illumination yields a coherent, pulsed output of tunable temporal width. Finally, we discuss experimental scenarios exploiting rotational levels of gaseous ensembles of heteronuclear diatomic molecules.

Analysis of the propagation of an electric field in various types of media is a well-known problem in quantum optics, especially in the context of coherent phenomena[1]. Typically, an ensemble of atoms is dressed with a coherent electromagnetic beam modifying the atomic optical properties probed by a weak beam of light. Attractive examples include stimulated Raman adiabatic passage[2,3], magneto-optical rotation[4–6] electromagnetically induced transparency[7–9], light slowdown[10,11] and storage[12–14]. Coherent atomic systems support quantum interference in emission or absorption channels, exploited e.g. in the phenomenon of lasing without inversion[15–17]. An alternative scenario for lasing closely related to this work is based on a resonant amplification of a high-frequency signal generated in a superradiant ensemble of atoms coherently driven by a low-frequency beam[18,19]. Despite the long record of investigation, there is still room in the field for fundamental and uncharted research ideas for even the simplest possible models. One such example is a one-dimensional medium consisting of two-level systems with broken inversion symmetry, coupled to an electromagnetic field.

A two-level system, obeying inversion symmetry, driven by a resonant electromagnetic field is a canonical example considered in quantum optics. Such a system undergoes Rabi oscillations of populations of the two levels as the system subsequently exchanges energy with the driving field. This induces oscillations of a transition dipole moment at the transition frequency. This can be understood in terms of AC Stark effect. The resulting emission spectrum has the form of a Mollow triplet[20], with a central peak at the transition frequency of the atomic system and sidebands detuned by the Rabi frequency. If the two-level system is polar, its inversion symmetry is broken and radiation is additionally generated at the Rabi frequency, i.e., much below the transition frequency between the eigenstates. This can be explained by noting that the permanent electric dipole moment characterizing the system can, in general, be different in the excited and ground states (polar molecules have to be subjected to an external DC electric field to have the electric dipole moment in the laboratory frame). Thus, the population exchange between the eigenstates results in oscillations of the permanent dipole moment at the Rabi frequency. Such behaviour was first shown by Kibis et al.[21], where the coupling of a single asymmetric system (a quantum dot) with classical light was considered. The discussion was extended to the cases of single-mode[22] and bichromatic light[23]. Nonlinear effects were also considered in terms of polarizabilities of asymmetric systems[24]. Moreover, two-level systems with broken inversion symmetry were suggested for lasing or for generation of squeezed light[25–27].

Institute of Physics, Faculty of Physics, Astronomy and Informatics, Nicolaus Copernicus University in Toruń, Grudziadzka 5, 87-100 Torun, Poland. ✉email: glad@doktorant.umk.pl

Until now, the analysis neglected field propagation effects. This approach limited the possible physical realizations to small amounts of relatively large quantum systems and excluded commonly available molecular clouds or solids. In this paper, we extend that research to scenarios in which a resonant driving beam illuminates an ensemble of two-level systems with broken inversion symmetry, e.g., polar molecules in a gaseous phase. As a result, a coherent beam of low-frequency radiation is generated throughout the length of the sample and propagates parallel to the drive.

We investigate the performance of the proposed system as an all-optically-controlled source of coherent radiation. Its frequency could be optically tuned within the microwave domain by modulation of the amplitude of the drive. In an opposite strategy, modulation of the driving field's detuning from resonance with the atomic transition would provide a knob to suppress the outgoing signal at a fixed frequency. To investigate these effects, we develop a method based on the semiclassical Bloch–Maxwell equations derived under a generalized form of the rotating wave approximation. The usual slowly varying envelope approximation is not applied because it does not hold for low-frequency pulses. The theory is applied to a realistic model of a gaseous medium of molecules, which support a permanent dipole moment.

Method

Medium. We consider a quasi-one-dimensional sample containing a medium of uniformly distributed polar molecules. To generate a signal the dipole moments have to be oriented in the laboratory frame which can be done by applying an external DC electric field. The simplest examples of molecules well suited for this purpose include heteronuclear molecules with large electric dipole moment which can be relatively easily polarized in the laboratory frame, such as: methylidyne (CH)[28] or carbon fluoride (CF)[29] both in a ground state $X\ ^2\Pi_{1/2}$, hydroxide (OH)[30] in a $X\ ^2\Pi_{3/2}$ state, or lithium hydride (LiH)[31] in a $X\ ^1\Sigma^+$ state. For such systems the dipole moment operator in the laboratory frame $\hat{\mathbf{d}} = \sum_{ij} \mathbf{d}_{ij} |i\rangle\langle j|$ with $i, j \in \{e, g\}$ has nonzero diagonal elements: $|\mathbf{d}_{ii}| \neq 0$ (for a proof, see the "Supplementary Information"). The diagonal elements correspond to *permanent* dipole moments, in contrast to the usually considered off-diagonal elements describing *transition* dipole moments $\mathbf{d}_{ij}$ with $i \neq j$. A crucial for this work feature is that the permanent dipole moments of the two eigenstates are not equal: $\mathbf{d}_{ee} \neq \mathbf{d}_{gg}$. Naturally, the transition dipole moment $\mathbf{d}_{eg} = \mathbf{d}_{ge}^{\star}$ should be nonzero to enable efficient coupling with the driving electric field, which we describe in the following subsection. For the purpose of describing how the DC electric field polarizes the molecules in the laboratory frame we use the full set of relevant molecular levels, see "Supplementary Information". However, for the purpose of describing the light-molecules interaction and light propagation it suffices to focus only on the two levels coupled by light (the drive beam), hence the medium is described with 2×2 density matrix $\rho(z, t)$ dependent on position z and time t, which we describe on the basis of excited (e) and ground (g) states $\{|e\rangle, |g\rangle\}$. The free Hamiltonian of the system can be written as $H_{\text{medium}} = \hbar\omega_0 |e\rangle\langle e|$, where $\hbar$ stands for the reduced Planck constant, ω_0 is the transition frequency, and we have set the energy of the lower state to zero.

Electromagnetic field. The electromagnetic field is treated classically. It consists of two components corresponding to the driving and signal fields (in this section we skip the DC electric field that is used to polarize the molecular medium). Thus, the electric part of the field can be written as

$$\mathbf{E}(z, t) = \mathbf{E}_{\text{drive}}(z, t) + \mathbf{E}_{\text{signal}}(z, t). \tag{1}$$

The drive

$$\mathbf{E}_{\text{drive}}(z, t) = \mathscr{E}\ (z, t)\mathbf{e}\cos(kz - \omega t) \tag{2}$$

is a strong coherent laser beam of carrier frequency ω close to resonance with the two-level system's transition frequency ω_0. Depending on the system, it may belong to the optical, near- or even far-infrared regime. Here, $\mathbf{e}$ indicates the polarization of the driving field, which we assume is constant. The beam propagates along the z direction, and on resonance the wavenumber k equals $\frac{\omega}{c}$ with c being the speed of light in vacuum. Tuned close to the resonance with the two-level systems, the driving field induces coherent Rabi oscillations of their population between the ground and excited states. Either due to back-action from the medium or due to external tuning, the envelope $\mathscr{E}$ can be modulated at timescales comparable to the inverse Rabi frequency. This observation will be important in later parts of this work.

Due to coherent oscillations of the population between the eigenstates with unequal permanent dipole moments, a coherent signal field $\mathbf{E}_{\text{signal}}(z, t)$ may be generated in the medium. Its source is the permanent dipole oscillating at the Rabi frequency Ω_R, whose exact form is derived later. It is typically in the microwave regime. Formally, we can distinguish the signal field envelope and a harmonic term

$$\mathbf{E}_{\text{signal}} = \mathscr{E}_{\text{s}}(z, t)\mathbf{e}_{\text{s}} e^{\mathrm{i}\Omega_R(\frac{z}{c} - t)} + \text{c.c.}, \tag{3}$$

where $\mathbf{e}_{\text{s}}$ represents the polarization vector of the signal field, which is constant and parallel to the permanent dipole moments of the medium. In realistic scenarios, the timescales of modulations of the signal field envelope may be comparable to the inverse Rabi frequency $\left|\frac{\partial}{\partial t}\mathscr{E}_{\text{s}}\right| \lesssim \mathscr{E}_{\text{s}}\Omega_R$, which means that the slowly varying envelope approximation may not be valid for this part of the field and will not be applied. We make the reasonable assumption that initially the signal field is absent throughout the entire sample $\left|\mathbf{E}_{\text{signal}}(z, t = 0)\right| = 0$ for all $z \in [0, L]$, where L is the sample length. In the following section, we derive the equations describing the buildup and propagation of the signal field.

Medium coupled to the field. The goal of this subsection is to find the coupled Bloch–Maxwell equations that govern the evolution of the density matrix of the medium as well as the propagation of the signal field. In many cases, the propagation effects for the drive can be neglected. Here, we will nevertheless allow temporal tuning of the drive amplitude at reasonable timescales: $\left|\frac{\partial}{\partial t}\mathscr{E}\right| \ll \mathscr{E}\ \omega$.

Our starting point is the one-dimensional form of the propagation equation for the total field given by Eq. (1)

$$-\frac{\partial^2}{\partial z^2}\mathbf{E}(z,t) + \frac{1}{c^2}\frac{\partial^2}{\partial t^2}\mathbf{E}(z,t) = -\mu_0\frac{\partial^2}{\partial t^2}\mathbf{P}(z,t), \tag{4}$$

where μ_0 is the vacuum permeability, and $\mathbf{P}(z,t)$ is the polarization of the medium. For this equation to be valid, the medium must be nonmagnetic, linear, and isotropic, without free charges and currents. We make these assumptions here as they describe a rather wide class of molecular vapors and solids.

The polarization at the right-hand-side of Eq. (4) can be expressed as

$$\mathbf{P}(z,t) = N\mathrm{Tr}(\rho(z,t)\mathbf{d}) = N\sum_{i,j\in\{e,g\}}\rho_{ij}(z,t)\mathbf{d}_{ji}, \tag{5}$$

where N is the concentration of the two-level systems in the medium, $\mathrm{Tr}(\cdot)$ stands for the trace operation, and $\rho_{ij}(z,t)$ are elements of the density matrix of the medium $\rho(z,t)$. Note that contrary to the usually considered symmetric case, all density matrix elements contribute to the polarization, including the diagonal ones that give rise to the signal buildup.

To find the explicit form of the source term in Eq. (4), we model the evolution of the density matrix with the master equation

$$\mathrm{i}\hbar\frac{\partial}{\partial t}\rho(z,t) = [H(z,t),\rho(z,t)] + \mathscr{L}[\rho(z,t)], \tag{6}$$

where H is the full Hamiltonian

$$H(z,t) = H_{\text{medium}} - \mathbf{d}\cdot\mathbf{E}(z,t), \tag{7}$$

H_{medium} was introduced at the end of subsection "Medium", and the electric dipole approximation has been assumed for the interaction term. The relaxation term is given by[32,33]

$$\mathscr{L}[\rho(z,t)] = 2\mathrm{i}\hbar\sum_{p=\text{se,coll}}\gamma_p\left(L_p\rho L_p^\dagger - \frac{1}{2}\rho L_p^\dagger L_p - \frac{1}{2}L_p^\dagger L_p\rho\right), \tag{8}$$

where in our system the index p = "se" corresponds to spontaneous emission with $L_{\text{se}} = |g\rangle\langle e|$, while p = "coll" describes collisional relaxation: $L_{\text{coll}} = |e\rangle\langle e| - |g\rangle\langle g|$. To simplify the notation, we have omitted the arguments of the density matrix on the right-hand side.

From now on, we assume that all matrix elements of the dipole moment operator $\mathbf{d}_{ij}$ are oriented in the same direction, parallel to the polarization direction of the fields. Hence, we can omit the vector notation. Please note, however, that the analysis could be equivalently performed for perpendicular orientations of permanent and transition dipoles: $\mathbf{d}_{ii}\perp\mathbf{d}_{ij}$, $j\neq i$.

To separate slowly varying and rapidly-oscillating components of the coherence ρ_{eg}, we adjust the ansatz introduced in the previous work[21]

$$\rho_{eg(z,t)} = r_{eg}(z,t)\mathrm{e}^{\mathrm{i}(kz-\omega t)}\mathrm{e}^{-\mathrm{i}\kappa(z,t)\sin(kz-\omega t)}, \tag{9}$$

where the dimensionless parameter $\kappa(z,t) = \frac{\mathscr{E}\ (z,t)(d_{ee}-d_{gg})}{\hbar\omega}$ is a measure of asymmetry. As we will see from the Bloch equations, the timescale for variations of the envelope function r_{eg} is on the order of Ω_R^{-1}.

The last exponent in Eq. (9) can be expressed using the identity $\mathrm{e}^{-\mathrm{i}\kappa\sin x} = \sum_{n=-\infty}^{+\infty}\mathrm{J}_n(\kappa)\mathrm{e}^{-\mathrm{i}nx}$, where J_n refers to the Bessel function of the first kind. Making use of this form and inserting Eqs. (7–9) into the master Eq. (6), with the field in the form given by Eq. (1), we arrive at a set of Bloch equations whose general form and detailed derivation are given in the "Supplementary Information". The rotating wave approximation leads to the following form of the Bloch equations:

$$\frac{\partial}{\partial t}\rho_{ee} = 2\Im(\Omega_R^\star r_{eg}) + 2\frac{E_{\text{signal}}}{\hbar}\mathrm{J}_1(\kappa)\Im(d_{eg}^\star r_{eg}) - 2\gamma_{\text{se}}\rho_{ee}, \tag{10a}$$

$$\frac{\partial}{\partial t}r_{eg} = \mathrm{i}\left[-\delta + \frac{\partial}{\partial t}\kappa + \frac{E_{\text{signal}}}{\hbar}(d_{ee}-d_{gg})\right]r_{eg} + \mathrm{i}\left[\Omega_R + \frac{E_{\text{signal}}}{\hbar}\mathrm{J}_1(\kappa)d_{eg}\right](1-2\rho_{ee}) - (\gamma_{\text{se}}+\gamma_{\text{coll}})r_{eg}, \tag{10b}$$

where we have introduced the detuning $\delta = \omega_0 - \omega \ll \omega_0$ and derived the explicit form of the Rabi frequency $\Omega_R = \frac{d_{eg}\omega}{d_{ee}-d_{gg}}\mathrm{J}_1(\kappa)$. This form implies that the signal frequency can be controlled with external parameters, in particular the amplitude of the drive, as well as—to a smaller extent—its frequency. Note that if the diagonal and off-diagonal terms of the dipole moment are comparable, the order of magnitude for κ corresponds to the ratio of the Rabi frequency to the transition frequency in the system. This means that κ is typically small, and the Bessel function can be approximated by the linear term $\mathrm{J}_1(\kappa)\approx\frac{1}{2}\kappa$. In this regime, the Rabi frequency reverts to the familiar form $\Omega_R \approx \frac{\mathscr{E}(z,t) d_{eg}}{2\hbar}$. It is now clear that the elements ρ_{ee}, r_{eg} of the density matrix vary at timescales set by Ω_R^{-1} and the inverse decoherence rates γ_p^{-1}. From Eq. (10b), it follows that the signal field gives rise to a time- and space-dependent energy shift of the levels that is proportional to the difference between the permanent dipole moments of the eigenstates. In addition, the time dependence of the envelope of the driving field is included in the term $\frac{\partial}{\partial t}\kappa$. This part is negligible for slow changes of the drive's envelope and vanishes for a constant amplitude.

Once we have found the evolution of the density matrix elements, we can specify the form of the medium polarization induced by the driving field. Making use of the density matrix normalization $\rho_{gg} + \rho_{ee} = 1$, combining Eqs. (9) and (5) yields

$$P(z,t) = N\left[d_{gg} + \rho_{ee}(d_{ee} - d_{gg}) + r_{eg} d_{ge} \sum_{n=-\infty}^{\infty} \mathrm{J}_n(\kappa) \mathrm{e}^{-\mathrm{i}(n-1)(kz-\omega t)} + \text{c.c.}\right]. \tag{11}$$

We can insert this form into the right-hand side of Eq. (4). To extract the equation for the signal rather than the total field, we insert Eq. (1) in the left-hand-side of Eq. (4). Next, we separate contributions on both sides of the wave equation that oscillate at different harmonic frequencies. This step is based on the assumption that the components of the field oscillating at the Rabi frequency that contribue to the signal have their source in the polarization components oscillating at the Rabi frequency, while their coupling with the polarization components at the carrier frequency is negligible[24]. The details of this step are given in the "Supplementary Information". As a result, we obtain the propagation equation of the signal field:

$$\begin{aligned} -\frac{\partial^2}{\partial z^2} E_{\text{signal}} + \frac{1}{c^2}\frac{\partial^2}{\partial t^2} E_{\text{signal}} = {} & -\mu_0 N (d_{ee} - d_{gg}) \frac{\partial^2}{\partial t^2}\rho_{ee} \\ & - 2\mu_0 N \Re\left\{ d_{ge}\left[\mathrm{J}_1(\kappa)\frac{\partial^2}{\partial t^2} r_{eg} + 2\mathrm{J}_1'(\kappa)\frac{\partial}{\partial t}\kappa \frac{\partial}{\partial t} r_{eg} + \left(\mathrm{J}_1''(\kappa)\left(\frac{\partial}{\partial t}\kappa\right)^2 + \mathrm{J}_1'(\kappa)\frac{\partial^2}{\partial t^2}\kappa\right) r_{eg}\right]\right\}. \end{aligned} \tag{12}$$

here, $\mathrm{J}_1'(\kappa)$ and $\mathrm{J}_1''(\kappa)$ are respectively the first and second derivatives of the Bessel function over the argument κ. These terms represent the influence of the temporal modulations of the drive envelope. For a continuous-wave drive, all time derivatives of κ disappear, and the equation is significantly simplified. In general, $\mathrm{J}_1'(\kappa) = \frac{1}{2}[\mathrm{J}_0(\kappa) - \mathrm{J}_2(\kappa)]$ and $\mathrm{J}_1''(\kappa) = \frac{1}{4}[\mathrm{J}_3(\kappa) - 3\mathrm{J}_1(\kappa)]$. Because κ is typically small, the part proportional to $\mathrm{J}_0(\kappa)$ is the dominant contribution. Then, the correction arising from the time dependence of the drive envelope can be rewritten as $\mathrm{J}_0(\kappa)\frac{\partial}{\partial t}\kappa\frac{\partial}{\partial t} r_{eg}$.

From Eq. (12), it follows that both the diagonal and the off-diagonal parts of the density matrix contribute to the generation of low-frequency radiation. Assuming comparable values of permanent and transition dipole moments, we see that the oscillation of the population has a major impact on the signal buildup, in particular in the case of the slowly varying drive envelope, i.e., negligible $\frac{\partial}{\partial t}\kappa$. This observation is one of the key points of this work: the physical origin of the generated signal is the permanent dipole moment associated with the eigenstates of the system and oscillating at the Rabi frequency. This is the carrier frequency of the output signal. The Rabi frequency is determined by the drive amplitude $\mathscr{E}$, which provides a knob for spectral tuning of the signal.

In Eq. (12) we assume co-linear orientation of molecules. To include a distribution of the orientation directions of the molecules, one would need to replace the density N with a distribution function $N(\theta, \phi)$, and integrate over the orientations (θ, ϕ). In practice, this would suppress the coherence of the generated signal due to the distribution of coupling strengths between the differently oriented molecules and the drive.

Note that in many other works the field propagation equation in the Bloch–Maxwell set is a first-order differential equation[8,14,34]. That simplified form is obtained under the slowly varying envelope approximation in which the signal envelope is assumed to vary both in time and space much more slowly than its inverse carrier frequency and wave vector, respectively. Here, this approximation may not be justified, because the carrier frequency Ω_R is of the same order as the inverse timescales of the system's dynamics, and therefore we chose to retain the more complicated second-order propagation equation.

Results and discussion

In this section, we first perform calculations for parameters that do not describe any specific molecule, but rather represent orders of magnitude characterizing standard molecular or atomic ensembles, in order to present the typical output provided by the model. To explore the possibilities and limitations, in some investigations we even neglected decoherence or consider very large concentrations. Next, we investigate the performance of a LiH molecular ensemble as a low-frequency signal source.

Model parameters. We apply the theory to a model sample of a gaseous molecular medium. We focus on an electronic transition at $\omega_0 = 660$ THz, with dipole moments set to 1 atomic unit ($d_{ee} = d_{eg} = 8.5 \times 10^{-30}$ Cm). The spontaneous emission rate $\gamma_{\text{se}} = 3.4$ MHz is calculated according to the Weisskopf–Wigner theorem[34], and the collisional decoherence lifetime $\gamma_{\text{coll}}^{-1} = 65$ kHz has been chosen in accordance with experiments on diluted atomic vapors[35]. The sample of length $L = 53$ cm is illuminated with a driving beam with the envelope

$$\mathscr{E}(t,z) = A\frac{1}{\pi}\left(\arctan\left(-\alpha(z - z_0 - ct)\right) + \frac{\pi}{2}\right), \tag{13}$$

where the arctan function is chosen to model a smooth ramp-up of the beam. The parameter $\alpha = 0.019$/cm is a scaling factor controlling the slope and $z_0 = -5.3$ m. The amplitude $A = 1550$ V/cm corresponds to

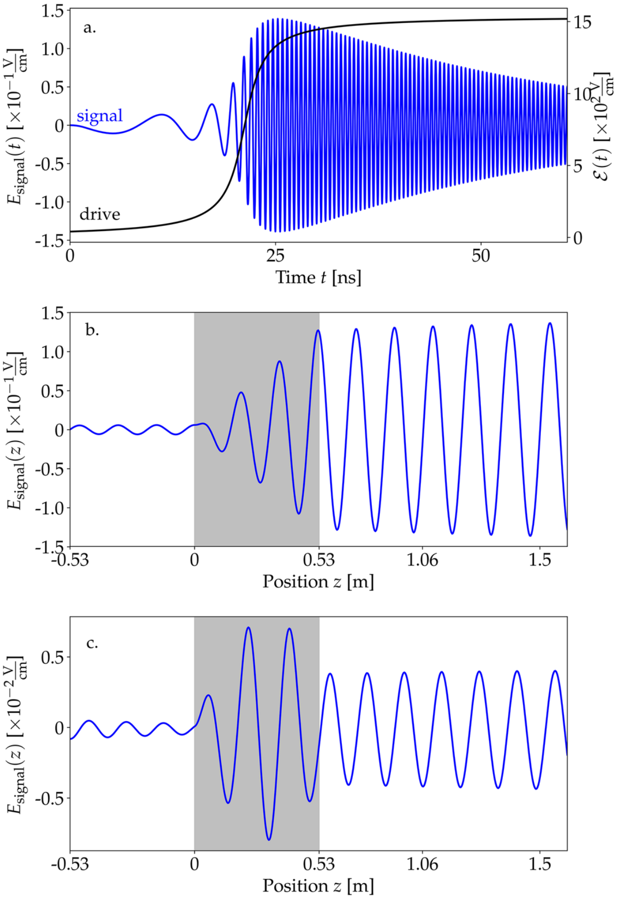

Figure 1. (**a**) Envelope of the driving field $\mathcal{E}$ (black) and generated signal E_{signal} (blue) as functions of time at the end of the sample $(z = L)$ for $\gamma_{\text{se}} = 3.4$ MHz, $\gamma_{\text{coll}} = 65$ kHz, and $\delta = 0$. (**b**) The signal E_{signal} in the spatial domain at $t = 30$ ns. The gray rectangle represents the sample with the active medium (between 0 and 0.53 m). (**c**) Spatial behavior of the generated radiation for the same γ_{se} and γ_{coll} coefficients but in the presence of detuning $\delta = 460$ MHz.

continuous-wave laser power of 32 W for a beam area of 1 mm^2. The carrier frequency of the drive will be chosen around the medium resonance.

We solve the Bloch–Maxwell equations (10, 12) with a self-developed Python code, which we made available on a public repository[36]. The Bloch and the Maxwell equations are alternately iterated in time, so that their coupling is fully accounted for, allowing one in particular to observe the effects of back-action of the signal on a dense medium, as it is discussed later. First, we discuss the case of a relatively low concentration $N = 6.7 \times 10^{12}$ molecules/cm^3. The time dependence of the generated low-frequency signal at the position fixed at the end of the sample $z = L$ is shown with the blue line in Fig. 1a. As the drive enters the medium, the signal builds up. Note that the signal frequency $\Omega_R(z = L, t)$ varied in time proportionally to the drive envelope $\mathcal{E}(z = L, t)$ and reached the stable value of 1.97 GHz after approximately 30 ns. The amplitude of the signal is significantly weaker than the drive, but well beyond the detection threshold in the microwave domain[37,38]. Naturally, the weak amplitude of the signal is a result of the small medium density we chose and could be improved in denser samples. Note that for very large densities at which the mean spatial separation between the molecules would be below the transition wavelength, dipole–dipole interactions of molecules may become relevant, but are not included in our model. They could be taken into account, e.g., through local-field corrections[39].

Figure 1b shows the generated signal at a fixed time $E(z, t = 30\,\text{ns})$. The gray area corresponds to $z \in [0, L]$ and represents the active medium, where the amplitude of the signal grows steadily. We find the dominant component of the signal to propagate toward the positive-z direction, in accordance with the propagation direction of the drive. This indicates the coherent character of the generated signal. Outside the sample the signal amplitude retains its value.

Figure 1c shows the same dependence as Fig. 1b, but for a drive detuned by $\delta = 460$ MHz. Naturally, the generated signal field amplitude is decreased in this case and its frequency shifted, as we will discuss below. In

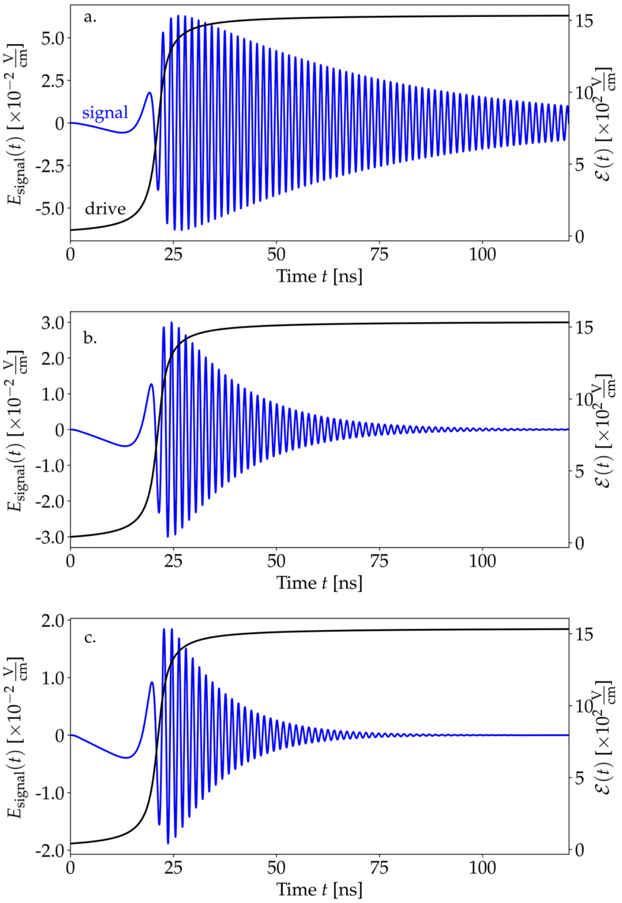

Figure 2. Shapes of the signal field (blue) for enhanced values of relaxation parameters. The envelope of the driving field is shown in black. (**a**) Only collisional relaxation present: $\gamma_{\text{coll}} = 6.6$ MHz, $\gamma_{\text{se}} = 0$. (**b**) Only spontaneous emission involved: $\gamma_{\text{se}} = 6.6$ MHz, $\gamma_{\text{coll}} = 0$. (**c**) Both mechanisms included: $\gamma_{\text{se}} = 6.6$ MHz, $\gamma_{\text{coll}} = 6.6$ MHz.

addition, the detuning induces a beating of the signal field inside the sample, now modulated with a sinusoidal envelope of the spatial period corresponding to the detuning. In consequence, the amplitude of the output signal outside the sample is suppressed depending on the phase of the envelope of the signal at the end of the sample.

Due to decoherence, the signal decays at timescales determined mostly by γ_{se}^{-1}, while γ_{coll} is a relatively less important correction (see Fig. 2). The reason is that the relaxation γ_{coll} does not directly affect the population (i.e., it does not appear in Eq. (10a), which is the main source of the low-frequency signal. The impact of relaxation is through a modification of the coherence term r_{eg}. The decay of the signal is a direct consequence of the decay of population oscillations. This means that decoherence channels, in particular a strong spontaneous emission, might prevent the possibility of low-frequency signal generation in a continuous manner. Instead, the signal could be generated pulse-wise, with drive impulses as discussed at the end of this subsection.

A close analysis of Eq. (10b) reveals that an effective detuning $\delta_{\text{eff}}(z,t) = \delta - \frac{\partial}{\partial t}\kappa - \frac{E_{\text{signal}}}{\hbar}(d_{ee} - d_{gg})$ can be induced by additional effects: a time modulation of the drive and a back-action from the generated signal field. While the former is weak for the modulation timescales considered in our examples, we analyze the impact of the signal back-action in samples with increased concentration N in Fig. 3. The calculations were performed for a weaker drive ($A = 514$ V/cm), longer time period, and the same decoherence parameters for better visualisation. In the case of small concentrations, the back-action is not observed at the investigated time scales (Fig. 3a). For larger medium concentrations, we find a clear indication of the back-action from the signal only if we do not include the spontaneous emission (gray curves in Fig. 3b,c): the modulations of the signal amplitude originate from time- and space-dependent effective frequency fluctuations (δ_{eff}) of the atomic transition induced by the signal. However, this effect is blurred in the presence of spontaneous emission (blue curves in Fig. 3b,c). The back-action of the signal also appears in Eq. (10) next to the Rabi frequency Ω_R, modifying it to the effective value $\Omega_{\text{eff}} = \Omega_R + \frac{E_{\text{signal}}}{\hbar}\mathrm{J}_1(\kappa)d_{eg}$. Yet, this impact is considerably smaller due to the proportionality of the correction applied to the Bessel function $\mathrm{J}_1(\kappa) \ll 1$.

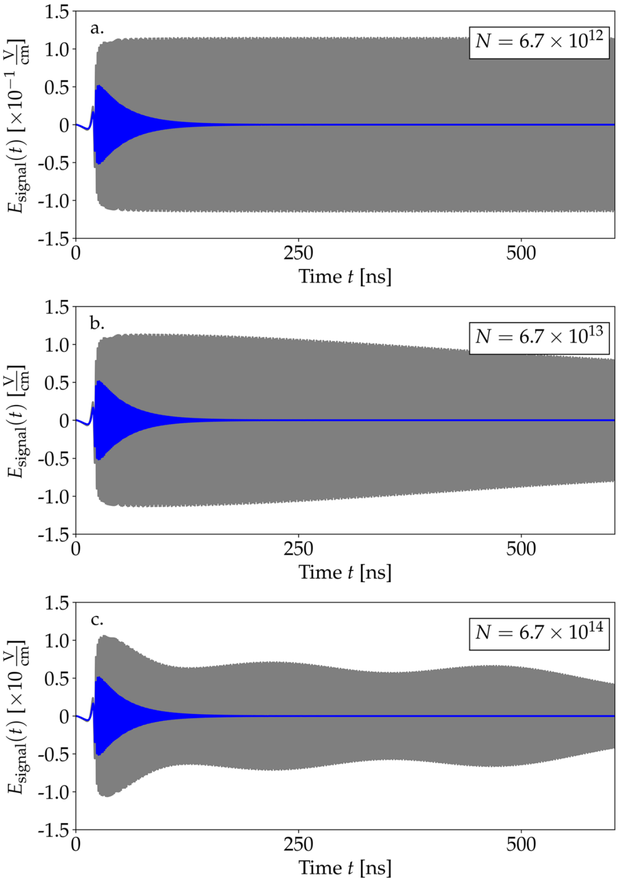

Figure 3. Generated signal for different concentrations N in the medium with (blue) and without (gray) relaxations. The driving field's amplitude was set to $A = 515$ V/cm. (**a**) Concentration $N = 6.7 \times 10^{12}$ molecules/cm^3. (**b**) $N = 6.7 \times 10^{13}$ molecules/cm^3. (**c**) $N = 6.7 \times 10^{14}$ molecules/cm^3.

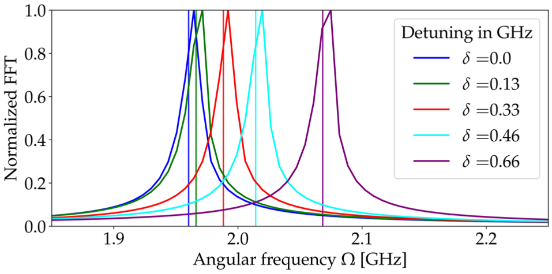

Figure 4. Fast Fourier transforms (FFTs) of the generated signals reveal frequencies of the signals for the resonant case (blue line) and for several values of detuning (other lines), all for $\Omega_R = 1.97$ GHz. The vertical lines indicate frequencies calculated according to Eq. (14).

To quantify the impact of the drive detuning on the signal frequency, we evaluate Fourier transforms of the stationary parts of the generated signals (the integration of the signal field $E_{\text{signal}}(z = L, t)$ was performed over times between 72 and 121 ns). Their normalized values are shown in Fig. 4. We compare the results obtained numerically for different values of detuning up to $\delta = 657$ MHz, with the theoretical prediction of the oscillation frequency of medium populations[40]

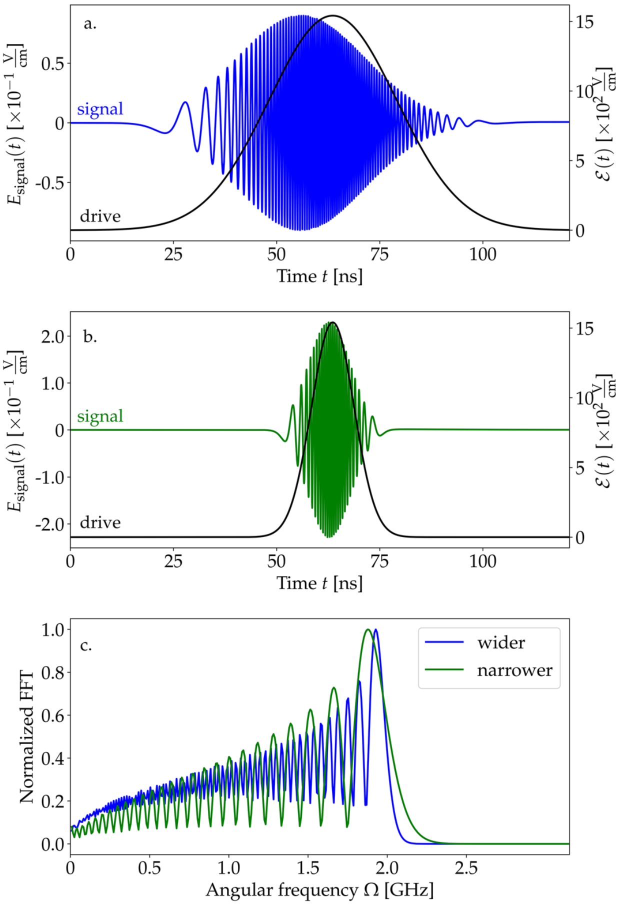

Figure 5. Results of the simulation for the impulse driving field with amplitude $A = 515$ V/cm. Blue and green lines represent the generated signal while black ones are envelopes of the drive in the form of Gaussians with respective FWHMs of (**a**) 36 ns and (**b**). 12 ns. (**c**) Fast Fourier transform performed on signal impulses.

$$\Omega = 2\sqrt{\Omega_R^2 + \delta^2/4}. \tag{14}$$

The factor of 2 appears because Ω_R corresponds to the frequency of oscillations of probability amplitudes, while the population probabilities are modulated at twice the pace. The formula above is valid for the case of vanishing relaxation rates, while in the studied case $\gamma_{\mathrm{se,coll}}$ are approximately two orders of magnitude smaller than δ. Therefore, the main consequence of relaxation is a spectral broadening of the signal rather than a frequency shift. In the above expression, we did not take into consideration the effective parameters $\Omega_{\mathrm{eff}}, \delta_{\mathrm{eff}}$ because their influence at the relevant timescale is negligible with respect to the impact of spontaneous emission. The theoretical results are in very good agreement with the numerical ones, with offsets at the third significant digit, i.e., exactly at the level at which we expect corrections from the relaxations.

The derived Bloch–Maxwell equations allow us to study the generation of low-frequency radiation under more complex illumination schemes than a smooth step function. In Fig. 5, we present the temporal shape of signals generated under illumination with Gaussian impulses defined as

$$\mathscr{E}\ (z, t) = A e^{-\alpha(z - z_0 - ct)^2}, \tag{15}$$

where $\alpha = a^2 \times 2.3 \times 10^{-6}/\mathrm{cm}^2$ hence, the full temporal width at half-maximum FWHM(a)=$a \times 12$ ns. The signals have Gaussian envelopes. The frequency chirp results from the drive modulation. The shift of the maximum of the signal with respect to the peak of the drive is due to decoherence and disappears in the absence of spontaneous emission and relaxation. Fig. 5c presents fast Fourier transforms (FFTs) of both signals. The main frequencies are $\Omega = 1.93$ GHz and 1.88 GHz for wider and narrower impulses, respectively. We observe that for increasing temporal FWHMs of the drive, the main frequency of the signal corresponds to the value of 1.97 GHz, which is the continuous-wave limit.

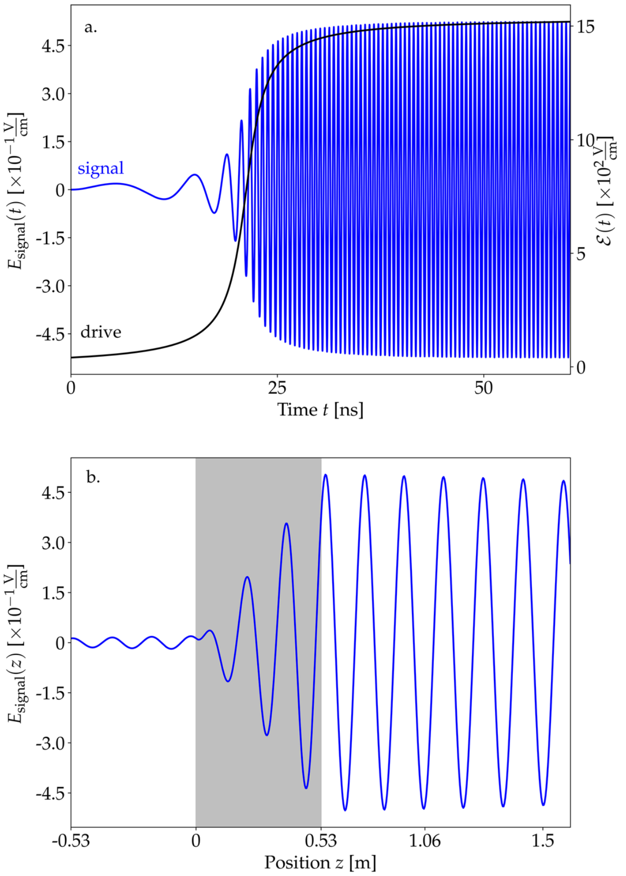

Figure 6. (**a**) Envelope of the driving field $\mathscr{E}$ (black) and generated signal E_{signal} (blue) as functions of time at the end of the sample ($z = L$) for $\gamma_{\mathrm{se}} = 0.75$ Hz, $\gamma_{\mathrm{coll}} = 65$ kHz, and $\delta = 0$. (**b**) The signal E_{signal} in the spatial domain at $t = 30$ ns. The gray rectangle represents the sample with the active medium (between 0 and 0.53 m).

Note that a pulsed drive brings into perspective a considerable increase in the driving field power, and therefore the frequency of the signal. In particular, signals in the terahertz domain could be achieved for the drive peak powers from 3.5 MW, assuming the other system parameters as selected above.

LiH molecule. In this section we discuss an example of a polar molecule of lithium hydride LiH that well suits the purpose of this project, i.e., it has a large permanent electric dipole moment that can be relatively easily oriented in the laboratory frame with an external electric field. We consider two selected rotational states $|NM\rangle = |00\rangle$ and $|N'M'\rangle = |10\rangle$ of a LiH molecule in its ground vibrational and electronic state $X^1\Sigma^+$. N and M denote the rotational angular momentum of the molecule and its projection on the quantization axis determined by the external DC field. The details of the calculations of the dipole moments (in the laboratory frame) and energies are as a function of applied DC electric field, E_{DC}, are provided in the "Supplementary Information". At the experimentally achievable electric field $E_{DC} = 150$ kV/cm the energy gap between the levels is $\Delta E = 0.642$ THz, the difference between the electric dipole moments in the ground and excited levels reads $d_{ee} - d_{gg} = 4.05$ D, and the transition electric dipole moment $d_{eg} = 2.51$ D. The concentration and the collisional decoherence rate of the molecules remain the same as before. We deem the concentration realistic with the method described in Ref.[31]. The results of our calculations are depicted in Fig. 6. We find a relatively high amplitude of the generated microwave radiation (the signal beam) of approximately 0.45 V/cm. The low energy gap between the levels yields low spontaneous emission coefficient and as a result, a relatively long coherence time of the signal (the decay is not visible at time scales shown in the figure).

Conclusions

We have shown how coherent radiation at the Rabi frequency is generated and propagates through a one-dimensional medium consisting of two-level systems with broken inversion symmetry. The underlying mechanism is associated with the Rabi oscillations of the population between the eigenstates induced as the resonant drive illuminates the medium, and of the corresponding permanent dipole moments.

To quantify the effect, we derived Bloch–Maxwell equations governing the dynamics of the system. The equations were solved numerically for sets of parameters representing standard molecular media. The results confirm that the generation of low-frequency radiation is mostly caused by oscillations of the population in the medium, while other contributions can be considered as corrections. The output signal amplitude and frequency can be tuned with drive intensity modulation, allowing for an all-optical control of the signal properties. In our examples, the signal frequency belongs to the microwave regime, while the amplitude is small but detectable. A pulsed illumination scheme allows one to increase both the intensity and frequency of the signal, potentially leading to tunable sources of coherent terahertz radiation.

Received: 13 March 2020; Accepted: 22 September 2020

References

1. Mandel, L. & Wolf, E. *Optical coherence and quantum optics* (Cambridge University Press, Cambridge, 1995).
2. Drummond, P., Kheruntsyan, K., Heinzen, D. J. & Wynar, R. Stimulated Raman adiabatic passage from an atomic to a molecular bose-einstein condensate. *Phys. Rev. A* **65**, 063619 (2002).
3. Vitanov, N. V., Rangelov, A. A., Shore, B. W. & Bergmann, K. Stimulated raman adiabatic passage in physics, chemistry, and beyond. *Rev. Modern Phys.* **89**, 015006 (2017).
4. Budker, D., Kimball, D., Rochester, S., Yashchuk, V. & Zolotorev, M. Sensitive magnetometry based on nonlinear magneto-optical rotation. *Phys. Rev. A* **62**, 043403 (2000).
5. Petrosyan, D. & Malakyan, Y. P. Magneto-optical rotation and cross-phase modulation via coherently driven four-level atoms in a tripod configuration. *Phys. Rev. A* **70**, 023822 (2004).
6. Pustelny, S. *et al.* Pump-probe nonlinear magneto-optical rotation with frequency-modulated light. *Phys. Rev. A* **73**, 023817 (2006).
7. Harris, S. E. *et al.* Electromagnetically induced transparency. In *Coherence and Quantum Optics VII*, 295–304 (Springer, 1996).
8. Paspalakis, E., Kylstra, N. & Knight, P. Transparency of a short laser pulse via decay interference in a closed v-type system. *Phys. Rev. A* **61**, 045802 (2000).
9. Fleischhauer, M., Imamoglu, A. & Marangos, J. P. Electromagnetically induced transparency: Optics in coherent media. *Rev. Modern Phys.* **77**, 633 (2005).
10. Hau, L. V., Harris, S. E., Dutton, Z. & Behroozi, C. H. Light speed reduction to 17 m per s in an ultracold atomic gas. *Nature* **397**, 594–598 (1999).
11. Fleischhauer, M. & Lukin, M. D. Dark-state polaritons in electromagnetically induced transparency. *Phys. Rev. Lett.* **84**, 5094 (2000).
12. Phillips, D., Fleischhauer, A., Mair, A., Walsworth, R. & Lukin, M. D. Storage of light in atomic vapor. *Phys. Rev. Lett.* **86**, 783 (2001).
13. Raczyński, A., Słowik, K., Zaremba, J. & Zielińska-Kaniasty, S. Controlling statistical properties of stored light. *Opt. Commun.* **279**, 324–329 (2007).
14. Słowik, K., Raczyński, A., Zaremba, J. & Zielińska-Kaniasty, S. Light storage in a tripod medium as a basis for logical operations. *Opt. Commun.* **285**, 2392–2396 (2012).
15. Scully, M. O., Zhu, S.-Y. & Gavrielides, A. Degenerate quantum-beat laser: Lasing without inversion and inversion without lasing. *Phys. Rev. Lett.* **62**, 2813 (1989).
16. Harris, S. E. Lasers without inversion: Interference of lifetime-broadened resonances. *Phys. Rev. Lett.* **62**, 1033 (1989).
17. Kocharovskaya, O. Amplification and lasing without inversion. *Phys. Rep.* **219**, 175–190 (1992).
18. Svidzinsky, A. A., Yuan, L. & Scully, M. O. Quantum amplification by superradiant emission of radiation. *Phys. Rev. X* **3**, 041001 (2013).
19. Shchedrin, G., Rostovtsev, Y., Zhang, X. & Scully, M. O. New approach to quantum amplification by superradiant emission of radiation. In *From Atomic to Mesoscale: The Role of Quantum Coherence in Systems of Various Complexities*, 193–203 (World Scientific, 2015). https://www.worldscientific.com/doi/abs/10.1142/9789814678704_0009.
20. Grove, R., Wu, F. & Ezekiel, S. Measurement of the spectrum of resonance fluorescence from a two-level atom in an intense monochromatic field. *Phys. Rev. A* **15**, 227 (1977).
21. Kibis, O., Slepyan, G. Y., Maksimenko, S. & Hoffmann, A. Matter coupling to strong electromagnetic fields in two-level quantum systems with broken inversion symmetry. *Phys. Rev. Lett.* **102**, 023601 (2009).
22. Savenko, I., Kibis, O. & Shelykh, I. A. Asymmetric quantum dot in a microcavity as a nonlinear optical element. *Phys. Rev.A* **85**, 053818 (2012).
23. Kryuchkyan, G. Y., Shahnazaryan, V., Kibis, O. V. & Shelykh, I. Resonance fluorescence from an asymmetric quantum dot dressed by a bichromatic electromagnetic field. *Phys. Rev. A* **95**, 013834 (2017).
24. Paspalakis, E., Boviatsis, J. & Baskoutas, S. Effects of probe field intensity in nonlinear optical processes in asymmetric semiconductor quantum dots. *J. Appl. Phys.* **114**, 153107. https://doi.org/10.1063/1.4825320 (2013).
25. Marthaler, M., Koppenhöfer, M., Słowik, K. & Rockstuhl, C. Lasing at arbitrary frequencies with atoms with broken inversion symmetry and an engineered electromagnetic environment. *arXiv preprint*arXiv:1601.01511 *(2016).*
26. Koppenhöfer, M. & Marthaler, M. Creation of a squeezed photon distribution using artificial atoms with broken inversion symmetry. *Phys. Rev. A* **93**, 023831 (2016).
27. Chestnov, I. Y., Shahnazaryan, V. A., Alodjants, A. P. & Shelykh, I. A. Terahertz lasing in ensemble of asymmetric quantum dots. *ACS Photon.* **4**, 2726–2737 (2017).
28. Takezaki, M., Ohoyama, H., Kasai, T. & Kuwata, K. Formation of the state-selected ch radical beam and its application to the ch+ no reaction. *Laser Chem.* **15**, 113–121 (1995).
29. Weibel, M. A., Hain, T. D. & Curtiss, T. J. Generation of intense, hexapole-selected, supersonic beams of fluorocarbon radicals: Cf, cf 2, and cf 3. *J. Vacuum Sci. Technol. A Vacuum Surfaces Films* **15**, 2238–2246 (1997).
30. Hain, T. D., Weibel, M. A., Backstrand, K. M. & Curtiss, T. J. Rotational state selection and orientation of oh and od radicals by electric hexapole beam-focusing. *J. Phys. Chem. A* **101**, 7674–7683 (1997).
31. Dagdigian, P. J., Wilcomb, B. E. & Alexander, M. H. Lih state-to-state rotationally inelastic cross sections in collisions with hcl and dcl. *J. Chem. Phys.* **71**, 1670–1682 (1979).

32. Lindblad, G. On the generators of quantum dynamical semigroups. *Commun. Math. Phys.* **48**, 119–130 (1976).
33. Gorini, V., Kossakowski, A. & Sudarshan, E. C. G. Completely positive dynamical semigroups of n-level systems. *J. Math. Phys.* **17**, 821–825 (1976).
34. Scully, M. & Zubairy, M. *Quantum Optics* (Cambridge University Press, Cambridge, 1997).
35. Dziczek, D. & Chwirot, S. Dual control of slow light in reciprocal electromagnetically-induced-transparency conditions. *Phys. Rev. A* **79**, 043807 (2009).
36. Gıadysz, P. Bloch–Maxwell simulation software. https://github.com/gladysz-piotr/Low-frequency_propagation.git (2020). (Accessed 29 July 2020).
37. Inomata, K. *et al.* Single microwave-photon detector using an artificial λ-type three-level system. *Nat. Commun.* **7**, 1–7 (2016).
38. Besse, J.-C. *et al.* Single-shot quantum nondemolition detection of individual itinerant microwave photons. *Phys. Rev. X* **8**, 021003. https://doi.org/10.1103/PhysRevX.8.021003 (2018).
39. Bowden, C. M. & Dowling, J. P. Near-dipole–dipole effects in dense media: Generalized Maxwell–Bloch equations. *Phys. Rev. A* **47**, 1247 (1993).
40. Loudon, R. *The Quantum Theory of Light* (OUP Oxford, Oxford, 2000).

Acknowledgements

The authors thank D. Ziemkiewicz for support on numerical aspects of this work. K.S and P.G. acknowledge the National Science Centre, Poland, Grant number 2018/31/D/ST3/01487. P.W. contribution was supported by the National Science Centre, Poland, through Project No. 2019/35/B/ST2/01118.

Author contributions

P.G. and K.S. equally contributed to idea conception, theory development and results analysis. P.G. implemented the code and performed all simulations. P.W. provided support on molecular physics. All authors contributed to the preparation of the manuscript.

Competing interests

The authors declare no competing interests.

Additional information

Supplementary information is available for this paper at https://doi.org/10.1038/s41598-020-74569-w.

Correspondence and requests for materials should be addressed to P.G.

Propagation of optically tunable coherent radiation in a gas of polar molecules: supplementary information

Piotr Gładysz[1,*], **Piotr Wcisło**[1], **and Karolina Słowik**[1]

[1]Institute of Physics, Faculty of Physics, Astronomy and Informatics, Nicolaus Copernicus University in Toruń, Grudziadzka 5, 87-100 Torun, Poland
[*]glad@doktorant.umk.pl

ABSTRACT

This file contains the following supplementary information:
S1. Relation between broken inversion symmetry and dipole moment
S2. Derivation of the Bloch-Maxwell equations
S3. Details of the numerical approach
S4. Lithium hydride example

S1 Relation between broken inversion symmetry and dipole moment

A diagonal element of the dipole moment operator with $i = e, g$ is given by

$$\mathbf{d}_{ii} = \langle i|\, \hat{\mathbf{d}}\, |i\rangle = \int d\mathbf{r} \sum_{\alpha} q_\alpha \mathbf{r}_\alpha \langle i|\mathbf{r}\rangle \langle \mathbf{r}|i\rangle \,, \tag{S1}$$

where $\mathbf{r} = \{\mathbf{r}_\alpha\}_{\alpha=1,\ldots,N}$ represents the set of positions $\mathbf{r}_\alpha$ of all N charges q_α contributing to the dipole moment of the system. For simplicity, in this proof we assume a single charge q at position $\mathbf{r}_1$. The proof for multiple charges is a straightforward generalization.

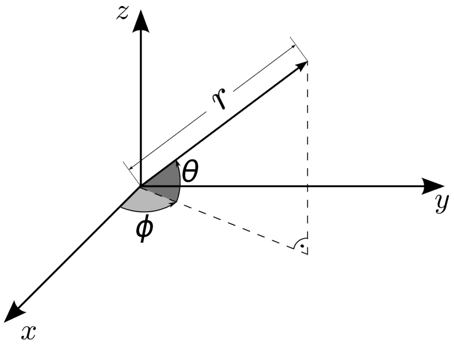

Figure S1. Spherical coordinate system used in calculations according to (S2). The unusual choice of directed angles θ and ϕ (notice the arrows in the picture) was intentional to set symmetric limits of integration in the equations.

To evaluate this quantity, we express $\mathbf{r}_1$ in spherical coordinates defined as follows (Fig. S1):

$$\begin{aligned} x &= r\cos\phi\cos\theta, \\ y &= r\sin\phi\cos\theta, \\ z &= r\sin\theta. \end{aligned} \tag{S2}$$

to obtain

$$\begin{aligned}\mathbf{d}_{ii} &= q\int_0^{\infty} dr_1 \int_{-\pi}^{\pi} d\phi_1 \int_{-\pi/2}^{\pi/2} d\theta_1\, r_1^2 \cos\theta_1\, \mathbf{r}_1\, |\langle \mathbf{r}_1|i\rangle|^2 \\ &= q\int_0^{\infty} dr_1 \int_{-\pi}^{\pi} d\phi_1 \int_{0}^{\pi/2} d\theta_1\, r_1^2 \cos\theta_1\, \mathbf{r}_1\, |\langle \mathbf{r}_1|i\rangle|^2 + q\int_0^{\infty} dr_1 \int_{-\pi}^{\pi} d\phi_1 \int_{-\pi/2}^{0} d\theta_1\, r_1^2 \cos\theta_1\, \mathbf{r}_1\, |\langle \mathbf{r}_1|i\rangle|^2\end{aligned} \tag{S3}$$

By substituting angles $\phi \to -\phi$, $\theta \to -\theta$ in the second term and making use of the relation $\cos(-\theta) = \cos(\theta)$, we obtain

$$\mathbf{d}_{ii} = q\int_0^{\infty} dr_1 \int_{-\pi}^{\pi} d\phi_1 \int_{0}^{\pi/2} d\theta_1\, r_1^2 \cos\theta_1\, \mathbf{r}_1 \left(|\langle \mathbf{r}_1|i\rangle|^2 - |\langle -\mathbf{r}_1|i\rangle|^2 \right), \tag{S4}$$

where $-\mathbf{r}_1 = (r_1, -\phi_1, -\theta_1)$. If the wave function $\langle \mathbf{r}_1|i\rangle$ has inversion symmetry, $|\langle \mathbf{r}_1|i\rangle| = |\langle -\mathbf{r}_1|i\rangle|$ holds, and the bracket at the end disappears. This implies that the diagonal elements d_{ee} and d_{gg} are equal to zero. This means that broken inversion symmetry is required to create a permanent dipole moment.

For the off-diagonal elements, we simply have

$$\mathbf{d}_{ij} = \langle i|\hat{\mathbf{d}}|j\rangle = \int \mathrm{d}\mathbf{r}\, \mathbf{r}\, \langle i|\mathbf{r}\rangle \langle \mathbf{r}|q\hat{\mathbf{r}}|\mathbf{r}_1\rangle \langle \mathbf{r}_1|j\rangle = \mathbf{d}^{\star}_{ji}, \tag{S5}$$

regardless of the wave function's symmetry. Due to the odd character of the position operator, if both wave functions share the same symmetry, the integral is equal to zero, and the transition is electric-dipole-forbidden.

S2 Bloch–Maxwell equations

Here, we provide a detailed derivation of the Bloch–Maxwell equations. First, let us insert the form of the field given by Eq. (1) into the master equation (6). The set of equations for the density matrix elements has the following form:

$$\mathrm{i}\hbar\frac{\partial}{\partial t}\rho_{ee} = \left(\mathscr{E}\cos(kz-\omega t) + E_{\text{signal}}\right)\left(d_{ge}\rho_{eg} - d_{eg}\rho_{ge}\right) - 2\mathrm{i}\hbar\gamma_{\text{se}}\rho_{ee}, \tag{S6a}$$

$$\mathrm{i}\hbar\frac{\partial}{\partial t}\rho_{eg} = \hbar\omega_0\rho_{eg} - \left(\mathscr{E}\cos(kz-\omega t) + E_{\text{signal}}\right)\left((d_{ee}-d_{gg})\rho_{eg} - d_{eg}(2\rho_{ee}-1)\right) - \mathrm{i}\hbar(\gamma_{\text{se}}+\gamma_{\text{dec}})\rho_{eg}. \tag{S6b}$$

The dynamics of the other elements can be found based on the density matrix properties: $\rho_{ee} + \rho_{gg} = 1$ and $r_{ge} = r^{\star}_{eg}$. Next, we make use of the ansatz (9) and expand the κ-dependent term into a series of Bessel functions $e^{-\mathrm{i}\kappa\sin x} = \sum_{n=-\infty}^{+\infty} \mathrm{J}_n(\kappa)e^{-\mathrm{i}nx}$:

$$\mathrm{i}\hbar\frac{\partial}{\partial t}\rho_{ee} = \left[\frac{1}{2}\mathscr{E}\left(\mathrm{e}^{2\mathrm{i}(kz-\omega t)}+1\right) + E_{\text{signal}}\mathrm{e}^{\mathrm{i}(kz-\omega t)}\right]\sum_{n=-\infty}^{\infty}\mathrm{J}_n(\kappa)\mathrm{e}^{-\mathrm{i}n(kz-\omega t)}d^{\star}_{eg}r_{eg} + \text{c.c.} - 2\mathrm{i}\hbar\gamma_{\text{se}}\rho_{ee}, \tag{S7a}$$

$$\begin{aligned}\mathrm{i}\hbar\frac{\partial}{\partial t}r_{eg} &= \hbar\left[\delta - \frac{\partial}{\partial t}\kappa - E_{\text{signal}}(d_{ee}-d_{gg})\right]r_{eg} \\ &\quad + \left[\frac{1}{2}\mathscr{E}\left(\mathrm{e}^{2\mathrm{i}(kz-\omega t)}+1\right) + E_{\text{signal}}\mathrm{e}^{-\mathrm{i}(kz-\omega t)}\right]d_{eg}(2\rho_{ee}-1)\sum_{n=-\infty}^{+\infty}\mathrm{J}_n(\kappa)\mathrm{e}^{\mathrm{i}n(kz-\omega t)} - \mathrm{i}(\gamma_{\text{es}}+\gamma_{\text{dec}})r_{eg}.\end{aligned} \tag{S7b}$$

If $\Omega_R \ll \omega$, the oscillatory terms on the right-hand side of the above equations make negligible contributions. We neglect them under the rotating wave approximation, in which out of the infinite sums the only surviving terms correspond to $n = 0, 2$ if they are multiplied by the drive envelope $\mathscr{E}$, or correspond to $n = 1$ if they are multiplied by the signal field. We arrive at the equations (10) from the article.

To derive formula (12), we insert Eq. (1) into the right-hand side of Eq. (4). Performing all the derivatives, we obtain

$$\begin{aligned}-\frac{\partial^2}{\partial z^2}E + \frac{1}{c^2}\frac{\partial^2}{\partial t^2}E &= -\frac{\partial^2}{\partial z^2}E_{\text{signal}} + \frac{1}{c^2}\frac{\partial^2}{\partial t^2}E_{\text{signal}} \\ &\quad + \frac{1}{2}\left(-\frac{\partial^2}{\partial z^2} + \frac{1}{c^2}\frac{\partial^2}{\partial t^2} - 2\mathrm{i}k\frac{\partial}{\partial z} + 2\mathrm{i}\frac{\omega}{c^2}\frac{\partial}{\partial t} + k^2 - \frac{\omega^2}{c^2}\right)\mathscr{E}\left(e^{\mathrm{i}(kz-\omega t)} - \mathrm{e}^{-\mathrm{i}(kz-\omega t)}\right).\end{aligned} \tag{S8}$$

Clearly, the slowly varying terms of the expression correspond to the signal, while the terms related to the drive envelope are multiplied by rapidly oscillating factors.

Let us now investigate the right-hand-side of the wave equation with the second time derivative of polarization. The fastest method is to apply the derivatives to the form of polarization given by Eq. (11). We introduce the symbol

$$R = \sum_{n=-\infty}^{\infty} \mathrm{J}_n(\kappa)\mathrm{e}^{-\mathrm{i}(n-1)(kz-\omega t)}. \tag{S9}$$

The second time derivative of the polarization is

$$\frac{\partial^2}{\partial t^2}P = N\left[(d_{ee}-d_{gg})\frac{\partial^2}{\partial t^2}\rho_{ee} + 2\frac{\partial^2}{\partial t^2}\mathrm{Re}(d_{eg}^\star r_{eg}R)\right]. \tag{S10}$$

The second term in the bracket reads

$$\begin{aligned}\frac{\partial^2}{\partial t^2}(d_{eg}^\star r_{eg}R) &= d_{eg}^\star\left(R\frac{\partial^2}{\partial t^2}r_{eg} + 2\frac{\partial}{\partial t}r_{eg}\frac{\partial}{\partial t}R + r_{eg}\frac{\partial^2}{\partial t^2}R\right)\\ &= \sum_{n=-\infty}^{\infty}\left[\left(\frac{\partial^2}{\partial t^2}r_{eg} + 2\frac{\partial}{\partial t}r_{eg}\left(\mathrm{J}_n'(\kappa)\frac{\partial}{\partial t}\kappa + \mathrm{i}(n-1)\omega\mathrm{J}_n(\kappa)\right) + r_{eg}\left(\mathrm{J}_n''(\kappa)\left(\frac{\partial}{\partial t}\kappa\right)^2 + \mathrm{J}_n'(\kappa)\frac{\partial^2}{\partial t^2}\kappa\right.\right.\right.\\ &\qquad \left.\left.\left. + 2\mathrm{i}(n-1)\omega\mathrm{J}_n'(\kappa)\frac{\partial}{\partial t}\kappa + [\mathrm{i}(n-1)\omega]^2\mathrm{J}_n(\kappa)\right)\right)d_{eg}^\star\mathrm{e}^{-\mathrm{i}(n-1)(kz-\omega t)}\right],\end{aligned} \tag{S11}$$

where we have explicitly inserted the first and second derivatives of R in accordance with Eq. (S9). We insert this result back into Eq. (S10).

Now, in analogy with the procedure conducted for the left-hand side (S8) of the wave equation, we can separate on the right-hand-side terms proportional to different powers of the oscillating factor $\exp[i(kz-\omega t)]$. In the rotating wave approximation, we neglect powers other than 0 and 1, as only these two are present on the left-hand side given by Eq. (S8). Now, we make the important assumption that any cross-talk between the slowly varying terms and those oscillating at the frequency ω can be neglected: The polarization terms oscillating at ω are coupled to the drive, while the slowly varying terms act as the source for the signal. This assumption is valid if $\left|\frac{\partial\mathscr{E}_{\text{signal}}}{\partial t}\right| \ll \omega\mathscr{E}_{\text{signal}}$ and similarly for the slowly varying part of the polarization. As a result, we can separate two wave equations, describing respectively the dynamics of the drive and of the signal. However, we assume the drive to be strong enough not to be affected by the coupling to the medium. The only relevant field equation is therefore the one for the drive, given by (12). On its right-hand side appear the terms corresponding to $n=1$ in Eq. (S11).

S3 Numerical approach

The solution of the coupled set of Bloch–Maxwell equations (10, 12) can be found numerically.

The wave equation has the form

$$-\frac{\partial^2}{\partial z^2}f(z,t) + \frac{1}{c^2}\frac{\partial^2}{\partial t^2}f(z,t) = s(z,t), \tag{S12}$$

where f is the function we wish to find, s is a source term, and c is the speed of the envelope in vacuum. Introducing discretization, we end up with a time-space grid of evenly distributed points (z_j, t_i) with respective spatial and temporal steps Δz and Δt. Hence, for the space variable, we have $z_j = z_0 + j\Delta z$, where $j \in [0,1,\ldots,N_L]$, and N_L is the number of the point at the end of the sample of length L, so $N_L\Delta z = L$. Similarly, $t_i = t_0 + i\Delta t$ for $i \in [0,1,\ldots]$ but with no upper bound. For convenience, we denote values of the functions at grid points $f(z_j,t_i) \equiv f_{i,j}$ and $s(z_j,t_i) \equiv s_{i,j}$. By the solution at time t_{i+1}, we understand the set of values $\{f_{i+1,j}\}$ for all j, and hence we have to find an expression that depends only on the previously calculated values. This can be done by expressing the second-order derivatives by the three-point (midpoint) formula[1]. Because we solve a second-order partial differential equation, two initial conditions for each space point are required. We introduce values $f_{j,0}$, $s_{j,0}$ and velocities $\partial f_{j,0}/\partial t \equiv g_j$ for the initial time t_0. To reach an accuracy on the order of $(\Delta t)^2$, we express $f_{1,j}$ as[2]

$$f_{1,j} = \frac{1}{2}\eta^2(f_{0,j-1}+f_{0,j+1}) + (1-\eta^2)f_{0,j} + \Delta t g_j + \frac{1}{2}c^2(\Delta t)^2 s_{0,j}, \quad \text{for } j \neq 0, N_L, \tag{S13}$$

and we find

$$f_{i+1,j} = \eta^2(f_{i,j+1}+f_{i,j-1}) + 2(1-\eta^2)f_{i,j} - f_{i-1,j} + c^2(\Delta t)^2 s_{i,j}, \quad \text{for } i>0, j\neq 0, N_L. \tag{S14}$$

Obviously, the foregoing expressions are not valid at the ends of the sample. There, we apply transparent boundary conditions[3] for the radiation exiting the sample (for $j = 0, N_L$):

$$f_{1,0/N_L} = \eta^2 f_{0,1/N_L-1} + (1-\eta^2) f_{0,0/N_L} + (1-\eta)\Delta t g_{0/N_L}, \tag{S15a}$$

$$f_{i+1,0/N_L} = \frac{2\eta^2 f_{i,1/N_L-1} + 2(1-\eta^2) f_{i,0/N_L} + (\eta-1) f_{i-1,0/N_L}}{1+\eta}, \tag{S15b}$$

where we assumed no sources at the ends of the sample. In addition, we have introduced the parameter $\eta = c\Delta t/\Delta z$, the so-called Courant number first described in Ref. 4, whose value is crucial for numerical stability. In our case, $\eta = 1$ corresponds to the so-called "magic step"[5] and leads to a solution that is not affected by the numerical dispersion problem.

The source term $s(z,t)$ corresponds to the solution of the Bloch Eqs. (10). The latter is a set of first-order differential equations of one variable for each point in space. At each time step, we calculate the solution using the Python build-in method *odeint* from the *scipy.integrate* library. It is a RK4 method, snd so the order of accuracy is $(\Delta t)^4$. This high level of accuracy is required because the source term is eventually differentiated twice, reducing the accuracy to the order of $(\Delta t)^2$. The differentiation is performed using the three-point (midpoint) method.

Our solver is written in Python 2.7, where two sets of equations (S14, S15) were implemented. A comparison between Eqs. (12) and (S12) reveals that $f \equiv E_{\text{signal}}$, and s is the right-hand side of Eq. (12). The solver is available on a public repository[6]. We draw the readers attention to another existing solver[7].

S4 Lithium hydride example

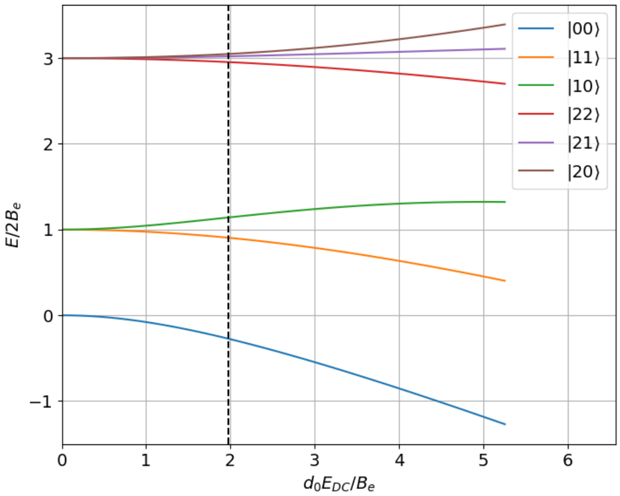

Figure S2. Energies of the rotational states in the ground electronic and vibrational state of the LiH molecule, as a function of electric field. The dashed line represents $E_{DC} = 150$ kV/cm. Levels represented by the blue and green lines were selected for the calculations in the main text.

To perform calculations based on a real system we have chosen the LiH molecule in ground state $X^1\Sigma^+$. We investigate its rotational states $|NM\rangle$. Since in the ground state the electronic angular momentum is zero, N and M denote the rotational angular momentum of the molecule and its projection. The permanent electric dipole moment in the molecule's frame is $d_0 = 5.88$ D[8] and the rotational constant $B_e = 7.513$ cm^{-1}[9]. In general, the orientation of a molecule in the gaseous ensemble is random and as the result, in the lab frame, the average dipole moment cancels out. To distinguish one of the directions (e.g. z-axis in the lab frame) and orient molecules we may apply an additional, constant electric field E_{DC}. This results in the DC

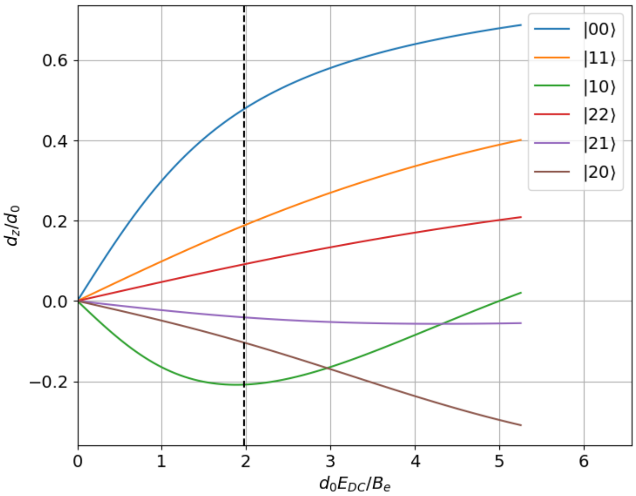

Figure S3. Projections of the permanent dipole moments in different rotational states as functions of applied electric field. The dashed line represents the amplitude $E_{DC} = 150$ kV/cm. The blue and green curves represent results for the states selected for the calculations in the main text.

Stark effect which leads to mixing of rotational states. The coupling matrix elements between states $|NM\rangle$ and $|N'M'\rangle$ read[10]

$$V_{NM;N'M'} = -E_{DC} d_0 \sqrt{\frac{4\pi}{3}} \langle NM| \mathrm{Y}_{10} |N'M'\rangle , \tag{S16}$$

where the spherical harmonic Y_{10} has been used. The $3-j$ Wigner symbols may now be used to evaluate the transition elements. As a result, the following matrix representation of the Hamiltonian is obtained

$$H_{\text{stark}} = \begin{array}{c} \\ |00\rangle \\ |10\rangle \\ |20\rangle \\ |30\rangle \\ |11\rangle \\ |21\rangle \\ |31\rangle \\ |22\rangle \\ |32\rangle \\ |33\rangle \end{array} \begin{array}{c} \begin{array}{cccccccccc} |00\rangle & |10\rangle & |20\rangle & |30\rangle & |11\rangle & |21\rangle & |31\rangle & |22\rangle & |32\rangle & |33\rangle \end{array} \\ \begin{bmatrix} 0 & E_{DC}d_1 & 0 & 0 & 0 & 0 & 0 & 0 & 0 & 0 \\ E_{DC}d_1 & 2B_e & E_{DC}d_3 & 0 & 0 & 0 & 0 & 0 & 0 & 0 \\ 0 & E_{DC}d_3 & 6B_e & E_{DC}d_6 & 0 & 0 & 0 & 0 & 0 & 0 \\ 0 & 0 & E_{DC}d_6 & 12B_e & 0 & 0 & 0 & 0 & 0 & 0 \\ 0 & 0 & 0 & 0 & 2B_e & E_{DC}d_2 & 0 & 0 & 0 & 0 \\ 0 & 0 & 0 & 0 & E_{DC}d_2 & 6B_e & E_{DC}d_5 & 0 & 0 & 0 \\ 0 & 0 & 0 & 0 & 0 & E_{DC}d_5 & 12B_e & 0 & 0 & 0 \\ 0 & 0 & 0 & 0 & 0 & 0 & 0 & 6B_e & E_{DC}d_4 & 0 \\ 0 & 0 & 0 & 0 & 0 & 0 & 0 & E_{DC}d_4 & 12B_e & 0 \\ 0 & 0 & 0 & 0 & 0 & 0 & 0 & 0 & 0 & 12B_e \end{bmatrix} \end{array} , \tag{S17}$$

where $d_1 = -\frac{1}{\sqrt{3}}d_0$, $d_2 = -\frac{1}{\sqrt{5}}d_0$, $d_3 = -\frac{2}{\sqrt{15}}d_0$, $d_4 = -\frac{1}{\sqrt{7}}d_0$, $d_5 = -\frac{2\sqrt{2}}{\sqrt{35}}d_0$, $d_6 = -\frac{3}{\sqrt{35}}d_0$.

A diagonalization of the presented Hamiltonian allows us to find new eigenstates and eigenenergies of the system for different values of the DC electric field. The new eigenstates are superpositions of the original states $|NM\rangle$, and for the studied range of fields each eigenstate has one dominant contribution. The eigenenergies are presented in Fig. S2 for the amplitude E_{DC} in the range between 0 and 400 kV/cm. The label corresponds to the state $|NM\rangle$ whose contribution to the eigenstate dominates. As can be seen, the energy gap between the levels of interest grows with the electric field in the considered range.

The new eigenstates are characterized with a nonzero permanent electric dipole moment in the lab frame, oriented along the z-axis (the direction of the E_{DC}) as presented in Fig. S3. The black dashed line indicates the field amplitude used in the main text. Additionally, transition dipole moments between pairs of states can be induced. In Fig. S4 we present all components of the transition dipole moments between the ground state to a set of possible excited states. As expected, for $M = M' = 0$ the transition dipole moments are parallel to the z-axis while transitions between levels with $M' \neq 0$ correspond to dipoles in

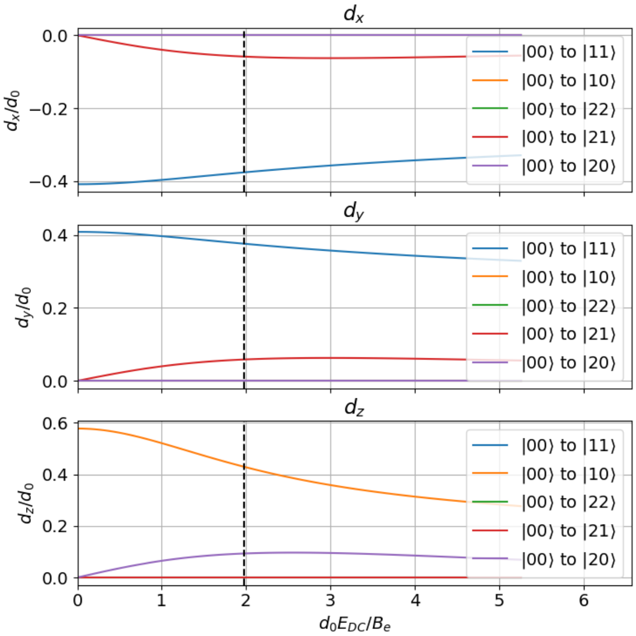

Figure S4. Projections on the laboratory frame axes of the transition electric dipole moments for transitions between the ground and selected excited states. The dashed line represents the amplitude $E_{DC} = 150$ kV/cm. The orange curve representes the results for the pair of states selected for the calculations in the main text.

oriented in the xy plane. These dipole moments decrease with the growing field due to the increasing contribution of states different than the dominant one.

References

1. Burden, R. L. & Faires, J. D. *Numerical Analysis* (Brooks/Cole, Cengage Learning, 2011).
2. Oliver, P. J. Numerical analysis lecture notes. http://www-users.math.umn.edu/~olver/num_/lnp.pdf (2008). [Online; accessed 29 July 2020].
3. Ionescu, D.-C. & Igel, H. Transparent boundary conditions for wave propagation on unbounded domains. In *International Conference on Computational Science*, 807–816 (Springer, 2003).
4. Courant, R., Friedrichs, K. & Lewy, H. On the partial difference equations of mathematical physics. *IBM journal Res. Dev.* **11**, 215–234 (1967).
5. Min, M. & Teng, C. The instability of the yee scheme for the “magic time step”. *J. Comput. Phys.* **166**, 418–424 (2001).
6. Gładysz, P. Bloch–Maxwell simulation software. https://github.com/gladysz-piotr/Low-frequency_propagation.git (2020). [Online; accessed 29 July 2020].
7. Riesch, M. & Jirauschek, C. mbsolve: An open-source solver tool for the maxwell-bloch equations. *arXiv preprint arXiv:2005.05412* (2020).
8. Dagdigian, P. J., Wilcomb, B. E. & Alexander, M. H. Lih state-to-state rotationally inelastic cross sections in collisions with hcl and dcl. *The J. Chem. Phys.* **71**, 1670–1682 (1979).
9. Irikura, K. K. Experimental vibrational zero-point energies: Diatomic molecules. *J. physical chemical reference data* **36**, 389–397 (2007).
10. Krems, R. V. *Molecules in electromagnetic fields: from ultracold physics to controlled chemistry* (John Wiley & Sons, 2018).

4

SUB- AND SUPERLUMINAL PROPAGATION IN MEDIA OF THREE-LEVEL SYSTEMS

In Chapter 2 we gave an extensive derivation of the Bloch–Maxwell equations for the ensembles of three-level systems driven by strong control field and a weak probe pulse. This is particularly important for the understanding of the investigations done in article A3. Three different energy-level configurations Λ, V, and Ξ, even though described by similar equations, provide tremendously different responses in the context of pulse propagation. The Ξ-system in the regime of far-detuned two-photon absorption was identified as the optimal candidate for the observation of the superluminal pulse propagation. We also provided a convenient figure of merit to show the connection between the control field's parameters and the superluminality.

As in the case of the two-level system, the density-matrix formalism along with the Bloch–Maxwell and GKLS equations were the key tools for this research, respectively capturing the effects of field propagation and atomic dynamics including the effect of dissipative processes.These are exceptionally important in the context of pulse propagation in the media in general and for superluminal propagation in particular. Optimization of the numerical approach was a subject of research as well as the simulations done for the article were time- and resource-costly.

4.1 SUPERLUMINAL PROPAGATION IN MEDIA OF THREE-LEVEL Ξ SYSTEMS

In article A3, we investigate superluminal light propagation in three-level atomic systems. We propose an all-optical approach to achieve superluminality using a two-photon resonance in a three-level Ξ-system, aiming to reduce the absorption and avoid the need for population inversion or nonlinear optical effects. In this work, we use the theory introduced in Sections 2.2 and 2.3. The research contributes to the understanding of light-matter interactions and could be useful in optical communication technologies.

Key elements of this work:

- Three configurations (Λ, V, and Ξ) are analyzed, and the Ξ-system is identified as optimal for achieving superluminal light propagation with minimal distortion.
- Numerical approach is developed for efficient simulations of light propagation in three-level systems.
- The trade-off between pulse advancement and transmission is investigated by the usage of a figure of merit to optimize optical factors.
- Numerical and analytical methods are employed to evaluate group velocities in rubidium vapors, showing that superluminal propagation can be achieved under specific conditions, making the findings relevant for future experimental implementations.

In the article, I contributed to the conception of the idea, followed by the dominant contributions to the development of the theory, results analysis, and manuscript preparation. I am fully responsible for the numerical solver implementation.

scientific reports

OPEN

Superluminal light propagation in a three-level ladder system

Piotr Gładysz[1]✉, Szymon Pustelny[2] & Karolina Słowik[1]

Superluminal light propagation is typically accompanied by significant absorption that might prevent its observation in realistic samples. We propose an all-optical implementation exploiting the two-photon resonance in three-level media to overcome this problem. With several computational methods, we analyze three possible configurations of optically-dressed systems and identify an optimal configuration for superluminal propagation. Due to the far-detuned operating regime with low absorption, this scenario avoids the usual need for population inversion, gain assistance or nonlinear optical response. Our analysis covers a broad parameter space and aims for the identification of conditions where significant pulse advancement can be achieved at high transmission levels. In this context, a figure of merit is introduced accounting for a trade-off between the desired group-index values and transmission level. This quantity helps to identify the optimal characteristics of the dressing beam.

Throughout the decades, the perspective of propagation of electromagnetic pulses with velocities greater than the speed of light in vacuum c has inspired the imagination of researchers. Theoretical predictions and experimental evidence of superluminal propagation were subjects of wide-ranging discussions, in particular in the context of Einstein's special relativity[1–3]. As a result of these debates and numerous follow-up works, a number of scenarios[4] for slow (subluminal)[5–7], fast (superluminal)[8–12], or tunable propagation velocity[13–17] were implemented. With this work, we propose a new, simple experimental scheme for superluminal propagation, adding to this extensive topic. The schematic superluminal pulse propagation in the time domain is shown in Fig. 1. The pulse propagating through the medium arrives faster (pulse advancement) and is also distorted and partially absorbed compared to the pulse propagating through the free space of the same length.

The group index describes the medium's optical properties and is linked to its dispersion. Specifically, normal dispersion results in subluminal propagation with $0 \leq v_g \leq c$.[18,19] Anomalous dispersion can lead to pulse velocities exceeding the vacuum speed of light $v_g > c$,[20,21] or negative $v_g < 0$.[11] The two latter cases are called superluminal light propagation. The terms *slow* and *fast* light can be described by the group refractive index n_g related to the pulse group velocity via $v_g = c/n_g$.[22]

Anomalous dispersion is a requirement for superluminal pulse propagation, but its observation in realistically long samples is often hindered by the associated high absorption[23–26]. In some experiments researchers address this issue[27,28], however, in general, this leads to distorted pulses and challenges in defining group velocity[29–31]. To overcome this problem, several schemes based on electromagnetically induced transparency (EIT)[32–35], optical saturation[36], gain assistance[8,10,37], four-wave mixing[38], and many more[12,15,39] have been proposed.

This work demonstrates that superluminal pulse propagation could be achieved in a significantly simpler scenario. It involves a coherent interaction between an atomic medium and two light beams (control and probe), modifying the medium's optical properties and the probe-pulse group velocity via the control field. In the proposed scheme, the probe and control fields are far detuned from single-photon transitions and are tuned near a two-photon transition, reducing absorption and limiting population transfer and pulse distortion. Under such conditions, the anomalous dispersion of the medium can be exploited without gain assistance and far from saturation. The predicted levels of pulse advancement are comparable to those achieved in gain-assisted schemes[9,40] for similarly high transmittance and low pulse distortion.

In the manuscript, we examine different energy-level schemes in a three-level system for superluminal pulse propagation and identify the ladder scheme as a good candidate, offering a small group index and low absorption. This scheme is then theoretically investigated in a broad range of control parameters to identify regimes where superluminal propagation with considerable pulse advancement can be achieved at high transmission levels with little pulse distortion. Several approaches are used to determine the group index of the medium. The approaches exploit elegant but approximate analytical methods, but also exact numerical treatment. While the analytical

[1]Institute of Physics, Faculty of Physics, Astronomy and Informatics, Nicolaus Copernicus University in Toruń, Grudziadzka 5, 87-100 Toruń, Poland. [2]Institute of Physics, Jagiellonian University, Łojasiewicza 11, 30-348 Kraków, Poland. ✉email: glad@umk.pl

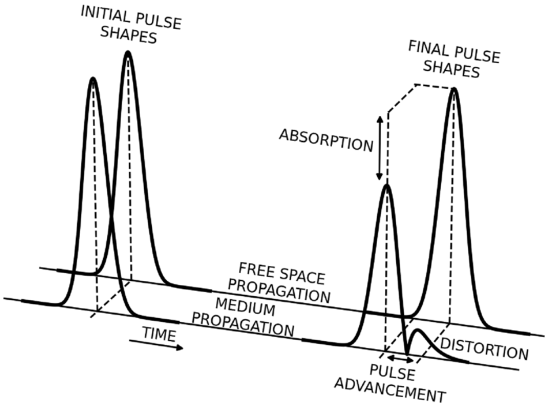

Figure 1. Schematic representation of the pulse propagating in the time domain through the free space (behind) and through the medium (in the front) of equal lengths. On the left-hand side, we present two identical Gaussian pulses (for z=0), while on the right-hand side, we show an unchanged shape in free propagation and a distorted one for the medium case (for z=L).

method works for monochromatic waves, the determination of the group velocity of a pulse requires analysis of its whole spectrum, which typically calls for numerical analysis. These approaches are used for the analysis of pulse velocity in rubidium vapors dressed with the control field. We highlight the trade-off between the negative group velocity of a pulse and its transmission coefficient. To quantify this trade-off, we introduce a figure of merit and use it to identify the optimal control-field parameters for the superluminal propagation of the probe.

Model

A two-level system is the simplest system with anomalous dispersion[41], but the associated strong on-resonance absorption limits its usefulness for the investigation of superluminal propagation. Therefore, we explore three-level media in the so-called vee (V), lambda (Λ), and ladder (Ξ) configurations (Fig. 2). In each scheme, selected pairs of levels are coupled with the probe Ω_p and control Ω_k fields. This allows controlling probe propagation with the control field. The medium is described using the density matrix ρ, whose evolution is governed by the Bloch equations. The matrix can be used to determine the medium's polarization at any time and position along the propagation direction, being the source term for the coupled first-order field propagation equation.

A derivation of the Bloch-Maxwell equations for one-dimensional media for the three cases is provided in Supplement Sec. S1. The resulting Bloch evolution equations have the form

$$\dot{\sigma}_{aa} = \mathrm{i}\Omega_{\mathrm{p}}\sigma_{\mathrm{ba}} - \mathrm{i}\Omega_{\mathrm{p}}\sigma_{\mathrm{ab}} - \mathrm{i}\Omega_{\mathrm{k}}\sigma_{\mathrm{ac}} + \mathrm{i}\Omega_{\mathrm{k}}\sigma_{\mathrm{ca}} + \mathscr{L}_{\mathrm{aa}}, \tag{1a}$$

$$\dot{\sigma}_{cc} = \mathrm{i}\Omega_{\mathrm{k}}\sigma_{\mathrm{ac}} - \mathrm{i}\Omega_{\mathrm{k}}\sigma_{\mathrm{ca}} + \mathscr{L}_{\mathrm{cc}}, \tag{1b}$$

$$\dot{\sigma}_{ba} = \alpha_p\mathrm{i}\delta_{\mathrm{p}}\sigma_{\mathrm{ba}} - \mathrm{i}\Omega_{\mathrm{p}}(1 - \sigma_{\mathrm{cc}} - 2\sigma_{\mathrm{aa}}) - \mathrm{i}\Omega_{\mathrm{k}}\sigma_{\mathrm{bc}} + \mathscr{L}_{\mathrm{ba}}, \tag{1c}$$

$$\dot{\sigma}_{ac} = -\alpha_k\mathrm{i}\delta_{\mathrm{k}}\sigma_{\mathrm{ac}} + \mathrm{i}\Omega_{\mathrm{p}}\sigma_{\mathrm{bc}} - \mathrm{i}\Omega_{\mathrm{k}}(\sigma_{\mathrm{aa}} - \sigma_{\mathrm{cc}}) + \mathscr{L}_{\mathrm{ac}}, \tag{1d}$$

$$\dot{\sigma}_{bc} = (\alpha_p\mathrm{i}\delta_{\mathrm{p}} - \alpha_{\mathrm{k}}\mathrm{i}\delta_{\mathrm{k}})\sigma_{\mathrm{bc}} + \mathrm{i}\Omega_{\mathrm{p}}\sigma_{\mathrm{ac}} - \mathrm{i}\Omega_{\mathrm{k}}\sigma_{\mathrm{ba}} + \mathscr{L}_{\mathrm{bc}}, \tag{1e}$$

where σ is the density matrix in the rotating frame, $\delta_{p,k}$ are detunings of the fields from resonances, and $\mathscr{L}$ is a decoherence term (see Supplement Sec. S2).

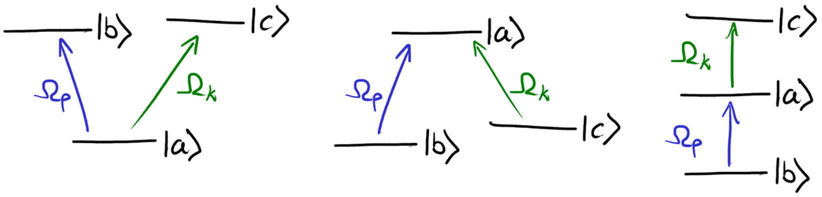

Figure 2. Investigated three-level configurations coupled by the probe (blue) and control (green) fields of Rabi frequencies Ω_p and Ω_k.

The equations describing the field propagation in the slowly-varying-envelope approximation read

$$(\partial_t \pm c\partial_z)\Omega_{p/k} = \pm\alpha_{p/k}\mathrm{i}\frac{\mathrm{N}\omega_{\mathrm{p/k}}\left|\mathrm{d}_{\mathrm{ba/ac}}\right|^2}{2\hbar\epsilon_0}\sigma_{\mathrm{ba/ac}}, \qquad (2)$$

where the left/right indices correspond to the probe/control fields N is the atomic concentration, $\omega_{p/k}$ are fields central frequencies, $d_{ba/ac}$ are values of the transition dipole moments, and ϵ_0 is electric permittivity in vacuum. The ± signs allow us to choose the propagation direction: minus for propagation in the direction of the axis and plus otherwise. We have introduced parameters $\alpha_{p/k}$ to keep track of the signs as follows: for the V system: $\alpha_p = \alpha_k = +1$, for the Λ system: $\alpha_p = \alpha_k = -1$, for the Ξ system: $\alpha_p = -1$, $\alpha_k = +1$. All the quantities are described in greater detail in Supplement Sec. S1.

Identification of the optimal three-level system

The purpose of this section is to identify the appropriate configuration to achieve superluminal propagation. Based on investigations of the electric susceptibility χ, we seek a balance between the adverse strength of absorption and the favorable slope of dispersion. Under such balanced conditions, the pulse propagates with a superluminal velocity and maintains its temporal shape.

Three-level systems

The electric susceptibilities $\chi_{ab/ba}$ for the three configurations are derived in Supplement Sec. S4 with a description of approximations and assumptions, and presented in the main text in Fig. 3 for selected parameters' values. The susceptibility functions sustain resonances whose nature is described in detail in the following paragraphs. Each of these resonances supports anomalous dispersion (dashed lines) being the necessary condition for superluminality. By Kramers-Krönig relations, the anomalous dispersion is in each case fundamentally linked to the accompanying absorption peak (solid lines)[2]. In the absence of the control field, the susceptibility sustains a single resonance for each of the three configurations (black lines in Fig. 3). The resonance corresponds to the transition between the levels $|a\rangle$ and $|b\rangle$, while the level $|c\rangle$ contributes little to the dynamics leading to a two-level system (TLS) regime. A relatively strong, near-resonant control field splits the resonance into a pair of symmetric resonances (red lines). This splitting is a consequence of the Autler-Townes (AT) or EIT effects[42]. A more interesting situation arises when the control field is significantly detuned from the single-photon transition between the $|a\rangle$ and $|c\rangle$ levels ($|\delta_k| \gg \gamma_{cc}, \gamma_{aa}$). With the negatively-detuned control field, $\delta_k < 0$ in V and Λ cases, and positively-detuned $\delta_k > 0$ in Ξ case, the resonances that arise at positive probe detunings ($\delta > 0$; right peaks in the plots)

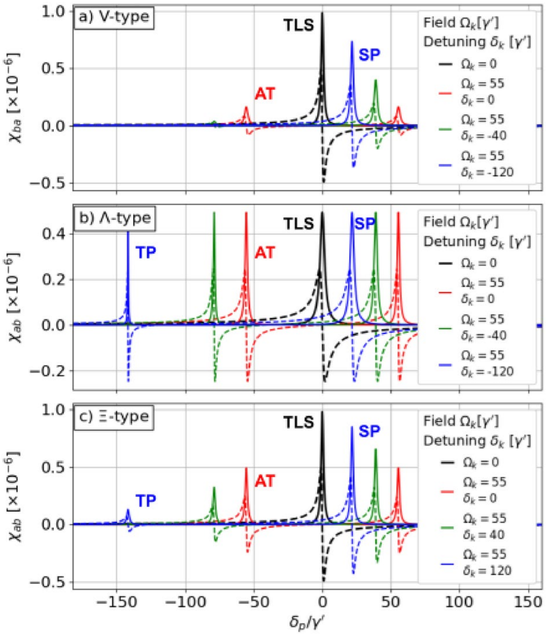

Figure 3. Real (dashed) and imaginary (solid) parts of the electric susceptibility as functions of the probe detuning for different energy-level schemes. The black curves illustrate the single-photon resonance in the absence of the control field (TLS regime), while other colors illustrate results for $\Omega_k = \gamma'$ and different δ_ks (AT, SP, TP regimes). The control field splits the single resonance (black) into two resonances (colors). For a) and b), the two-photon resonance condition reads $\delta + \delta_k = 0$ while for c) it is $\delta - \delta_k = 0$. Note that each absorption peak (solid lines) is accompanied by anomalous dispersion (dashed lines).

can be associated with single-photon transitions $|b\rangle \rightarrow |a\rangle$ (eg. blue curves, single-photon (SP) regime) while the resonances that arise at negative probe detunings (left peaks in the plots) - as a consequence of two-photon transitions $|b\rangle \rightarrow |c\rangle$ (eg. blue curves, two-photon (TP) regime). This classification reflects the appearance of $\mathrm{i}\delta$ (single-photon transition), and $\mathrm{i}(\delta \pm \delta_\mathrm{k})$ (two-photon transition) terms in expressions for electric susceptibilities (see Eqs. S24 in the Supplement). As the value of the control-field detuning $|\delta_k|$ increases, the single-photon resonance moves closer to the single-photon resonance obtained for $\Omega_k = 0$. This indicates that the system is weaker perturbed by the control field. The behaviour of the two-photon resonance strongly depends on the scheme of energy levels. The two-photon resonance amplitude and width are related to the decoherence rate γ_{bc} between the $|b\rangle$ and $|c\rangle$ levels. As derived in the Supplement Sec. S4, in the considered case γ_{bc} is given by $\frac{1}{2}(\gamma_{bb} + \gamma_{cc})$, 0, and $\frac{1}{2}\gamma_{cc}$ for the V, Λ, and Ξ configuration, respectively. This causes the different scaling of the resonance peaks we discuss now.

In the V system (Fig. 3a) with two short-living levels, a significant population transfer occurs from the ground level $|a\rangle$ to the excited state $|c\rangle$ due to the illumination with the strong control field $\left(\sigma_{aa} = \frac{\gamma_{cc}^2+4(\delta_k^2+\Omega_k^2)}{\gamma_{cc}^2+4(\delta_k^2+2\Omega_k^2)} + O[\Omega_p^2]\right)$. Such population distribution makes the system more vulnerable to decoherence[42]. Due to the relatively large decoherence rate γ_{bc}, the two-photon resonance amplitude decreases rapidly with the control-field detuning.

Due to the existence of two infinitely long-lived levels $|b\rangle$ and $|c\rangle$, the two-photon resonance is narrowest in the Λ system (Fig. 3b). The amplitude of the resonance is comparable to the single-photon resonance, and it does not depend on the detuning. In turn, strong two-photon absorption is observed. In practical implementations, the lifetime of the two lower-energy levels is limited by atomic collisions or the exchange of atoms with a reservoir. Consequently, under realistic conditions, the two-level absorption is suppressed compared to the single-photon absorption, decreasing with the detuning.

The Ξ system (Fig. 3c) has advantages over both V and Λ systems: The transfer of population ($\sigma_{bb} = 1 + O[\Omega_p^2]$) and the amplitude of the two-photon resonance are relatively small, corresponding to suppressed absorption. At the same time, the two-photon resonance width is narrow leading to a relatively steep derivative and, hence, large group velocities. This makes the Ξ-type system, driven by a weak probe field and strong, far-detuned control field particularly attractive for superluminal pulse propagation. Contrary to the intensively studied Λ configuration, the system has not been studied in detail in this context, so hereafter we focus our analysis on the Ξ system. Its electric susceptibility reads

$$\chi_{ab}(\delta) = \frac{N|d_{ab}|^2}{\hbar\epsilon_0} \frac{\mathrm{i}}{-\mathrm{i}\delta + \frac{\gamma_\mathrm{aa}}{2} + \frac{\Omega_\mathrm{k}^2}{-\mathrm{i}(\delta+\delta_\mathrm{k})+\frac{\gamma_\mathrm{cc}}{2}}} + \mathcal{O}[\Omega_p^2], \tag{3}$$

where δ plays the role of the probe detuning.

Relation to two-level media

Similar conditions can be achieved in a low-density two-level medium characterized with a single-photon resonance. However, such resonance is typically relatively strong resulting in full pulse absorption even for low medium densities. Ξ-type systems provide a more realistic platform for experiments as densities can be higher and fields can be stronger without inducing significant population transfer. We can analyze it more precisely in terms of saturation parameters in both cases. A large saturation parameter means strong population transfer that leads to pulse distortion.

For the two-level system, the Hamiltonian in the interaction picture reads

$$H \doteq \frac{\hbar}{2} \begin{bmatrix} \delta_{TLS} & -\Omega \\ -\Omega^* & -\delta_{TLS} \end{bmatrix}, \tag{4}$$

where δ_{TLS} is the detuning from the resonance and Ω is Rabi frequency. Based on this, we can simply write saturation parameter for some fixed spontaneous emission rate γ

$$S = \frac{2|\Omega|^2}{1 + \left(\frac{2\delta_{TLS}}{\gamma}\right)^2}. \tag{5}$$

This parameter directly corresponds to the population of the excited level in the steady state given by $\frac{S/2}{1+S}$.

To compare this result with our three-level ladder model we can perform adiabatic elimination of the middle level[43]. This can be done as the level is approximately empty due to the assumed huge values of single-photon detuning. We obtain an effective two-level Hamiltonian

$$H_\mathrm{eff}^{\Xi} \doteq \frac{\hbar}{2} \begin{bmatrix} (\delta_p + \delta_k) - \frac{|\Omega_k|^2}{\delta_p - \delta_k} & -\frac{\Omega_p \Omega_k}{\delta_p - \delta_k} \\ -\frac{\Omega_p^* \Omega_k^*}{\delta_p - \delta_k} & -(\delta_p + \delta_k) - \frac{|\Omega_p|^2}{\delta_p - \delta_k} \end{bmatrix}, \tag{6}$$

In analogy, we can write the effective saturation parameter for the ladder system. Let us assume comparable values of the spontaneous emission rates in both models $\gamma^{\Xi} \approx \gamma$, comparable fields values $|\Omega_p| \approx |\Omega_k| \approx |\Omega|$ and introducing $\delta_{TLS} = \delta_p + \delta_k$ as a two-photon detuning and $\Delta = \delta_p - \delta_k \approx -2\delta_k$ being of the order of the single-photon detuning. Since $\Delta \gg \delta_{TLS}$ we can neglect $|\Omega|^2/\Delta$ term and by comparison to the two-level description (Eqs. (4, 5) with Eq. (6)), express the resulting effective saturation parameter S^{Ξ} with respect to the S parameter

$$S^{\Xi} \approx \frac{2|\Omega|^4}{\Delta^2\left(1+\left(\frac{2\delta_{TLS}}{\gamma}\right)^2\right)} = \frac{|\Omega|^2}{\Delta^2} S \ll S. \tag{7}$$

Thus, we rather qualitatively show the intuitive result that the saturation in the ladder-type systems compared to the pure two-level one is much harder to achieve hence the population transfer is suppressed by the factor $\frac{|\Omega|^2}{\Delta^2}$ which is roughly of the order of $10^{-2} - 10^{-4}$. Indeed, experiments in three-level media are usually carried out far from the saturation regime[13,25].

Group index: approaches

The group velocity v_g and the group index n_g are related by the expression $v_g = c/n_g$. This paper mainly examines the group index, which is more convenient for calculations. The following section describes different approaches enabling the determination of the group index in optically-dressed media. The analytical derivation of the group index is based on an assumption of the monochromatic probe light. For a more realistic treatment, we additionally consider numerical and semi-analytical methods to incorporate the spectral shape of the probe pulse.

Analytical solution

The spectral components of the group index can be related to the electric susceptibility by[44]

$$n_g(\delta) = \Re\left(\sqrt{1+\chi_{ab}(\delta)}\right) + \omega_p \frac{\partial}{\partial \delta} \Re\left(\sqrt{1+\chi_{ab}(\delta)}\right). \tag{8}$$

The electric susceptibility of the Ξ-type medium is given by Eq. (3), which holds for $\Omega_k \gg \Omega_p$. For a more detailed discussion including nonlinear probe corrections see Supplement Sec. S5.1. The analytical formulation in (8) assumes spectrally narrow pulses; hence, we will use it as a benchmark for more realistic calculations considering spectrally broad pulses.

Numerical approach

The numerical method operates entirely in the time domain. It achieves the best simulation accuracy at the expense of the highest computational time among all the considered methods. We have implemented Eqs. (1) and (2) in a self-developed solver in Python based on the Lax-Wendroff and Runge-Kutta 4th order methods (see Supplement Sec. S3). It provides the full dynamics for both medium and fields conforming to the slovly-varying-envelope approximation.

Knowing the pulse's temporal profile at the end of the sample $\Omega_p(z = L, t)$, we calculate the group index in analogy to the optical refractive index, evaluating the difference in optical (here "group") paths for pulses propagating inside the medium and in free space: $n_g L - L = ct_g - ct_0$. Here, $t_g \equiv t_g(\delta_p, \Omega_k, L)$ is the time of travel of a fixed-carrier-frequency probe pulse through the given medium, while t_0 is the time for the same pulse travelling through empty space of the same length L. This yields[45]

$$n_g(\delta_p) = 1 + \frac{c}{L}(t_g(\delta_p) - t_0). \tag{9}$$

Evaluation of t_g has to be based on a reference point in the pulse, which we select as the maximum of the pulse. In optically-dense media the shape of a pulse may be distorted (see schematics shown in Fig. 1), which calls into question our ability to track the pulse maximum, and hence, the definition of group velocity[44,46]. In our study, we use Gaussian pulses in dilute media to ensure the preservation of pulse shape and carefully monitor population distribution and absorption rate.

The expression given by Eq. (8) describes individual spectral components of the group index. Contrary, (Eq. 9) is a recipe to evaluate the group index of a pulse with the carrier frequency detuning δ_p. The pulse could be spectrally broad as demonstrated in Sec. 5 and might have a nontrivial shape, with the restrictions described in the previous paragraph.

Fourier semi-analytical solution

The final group index evaluation method combines elements from frequency and time domains and ideas already presented. We Fourier transform (FT) the propagation equation for the probe field [Eq. (2)] and by using relation $\tilde{\sigma}_{ab} \propto \tilde{\Omega}_p \chi_{ab}$ (see Supplement) and (Eq. 3), we obtain

$$\left(\frac{\omega}{c} - \mathrm{i}\partial_z\right)\tilde{\Omega}_p = \frac{\omega_p}{2c}\chi_{ab}(\omega)\tilde{\Omega}_p, \tag{10}$$

where $\tilde{x} \equiv \mathrm{FT(x)}$. The solution is

$$\tilde{\Omega}_p = \tilde{\Omega}_{p0} \mathrm{e}^{\mathrm{i}[-\frac{\omega}{c} + \frac{\omega_\mathrm{p}}{2\mathrm{c}}\chi_{\mathrm{ab}}(\omega)]\mathrm{z}}, \tag{11}$$

where $\tilde{\Omega}_{p0} \equiv \tilde{\Omega}_p(z = 0, \omega)$ is the spectral shape of the pulse at the beginning of the sample. To obtain the shape of the pulse at the end of the medium, we inverse Fourier transform (IFT) the solution for $z = L$:

$$\Omega_p(L, t) = \mathrm{IFT}\left(\tilde{\Omega}_{p0} \mathrm{e}^{\mathrm{i}[-\frac{\omega}{c} + \frac{\omega_\mathrm{p}}{2\mathrm{c}}\chi_{\mathrm{ab}}(\omega)]\mathrm{L}}\right). \tag{12}$$

The introduced equations can only be calculated analytically for simple cases, otherwise, numerical Fourier transformations are used. The approach is based on the probe susceptibility χ_{ab} evaluated in the regime linear with the probe field Ω_p [Eq. (3)], and limited to relatively weak probes to avoid the distortion of the pulse and population transfer. This is the frequency-domain part of the approach. The time-domain part involves the same procedure as the fully numerical solution, with the group index found based on Eq. (9). We compare the temporal shapes of the probe fields at the end of the sample in the absence or presence of the control field. To find the field at the end, instead of heavy simulations of the pulse propagation, we perform faster calculations in the frequency domain. The evaluated group index based on Eq. (9) corresponds to the group velocity of a spectrally broadened pulse with the carrier frequency detuning δ_p and approaches the analytical result, Eq. (8), in the limit of monochromatic fields.

In summary, the analytical solution given by Eq. (8) describes the group index of individual Fourier components of the probe pulse. The group index of a spectrally broad pulse can be calculated with Eq. (9) either in the fully numerical method or using the Fourier semi-analytical solution. The most general numerical method provides insight into the full population dynamics and thus can be time-consuming. It allows us to verify the validity of the $\sigma_{bb} = 1$ assumption made for the other two methods. The Fourier approach, applied to the stationary case in the far-from-saturation regime, is a faster calculation method. In Supplement Sec. S3 the three methods are compared in detail.

Results

In this section, we evaluate the optimal parameters of the control field for observing superluminality by introducing a two-dimensional figure of merit. The calculations are made for rubidium vapor parameters.

Calculation parameters

The medium with length $L = 4.91$ cm ($9.28 \cdot 10^8$ a.u.) is filled with rubidium-87 vapor with states $|a\rangle = 5P_{\frac{3}{2}}$, $|b\rangle = 5S_{\frac{1}{2}}$ and $|c\rangle = 5D_{\frac{5}{2}}$ and transition wavelengths $\lambda_{ba} = 780$ nm, $\lambda_{ac} = 776$ nm (The magnetic structure of the levels is neglected.). The lowest level is a ground state for the Rb atom with infinite lifetime while the middle level has the lifetime of $\tau_a = 26$ ns ($1.08 \cdot 10^9$ a.u.) and the upper one of $\tau_c = 238$ ns ($9.84 \cdot 10^9$ a.u.)[47]. The spontaneous emission rates are $\gamma_{aa} = 2\pi/\tau_a = 2\pi \cdot 6.1$ MHz ($9.26 \cdot 10^{-10}$ a.u.) and $\gamma_{cc} = 2\pi/\tau_c = 2\pi \cdot 0.67$ MHz ($1.016 \cdot 10^{-10}$ a.u.). The electric dipole moments for transitions $|b\rangle \to |a\rangle$ and $|a\rangle \to |c\rangle$ are $d_{ba} = 5.1 \cdot 10^{-29}$ C m (6 a.u.) and $d_{ac} = 1.95 \cdot 10^{-29}$ C m (2.3 a.u.)[48]. The concentration N is set to 10^{11} atoms/cm^3 ($1.5 \cdot 10^{-14}$ a.u.).

Selection of optimal parameters of CW control field

We analyse the probe output field as a function of control-field parameters to identify promising superluminal regimes. The probe propagates along the z-axis [minus signs in Eq. (2)] and the control field in the opposite direction [plus signs in Eq. (2)]. This is a common approach to reduce the Doppler broadening in experiments on Ξ configuration systems[49]. The control parameters are the single-photon detuning δ_k and the amplitude $\mathcal{E}_k$ (or equivalently Ω_k), affecting medium dispersion and absorption.

To optimise the control-field conditions, we define a figure of merit (FOM) that combines the requirements of the group index being below 1 and of a high transmission coefficient

$$\beta(\delta_k, \Omega_k; M) = \underbrace{\left(1 - n_g(\delta^{\min}, \delta_k, \Omega_k)\right)}_{\text{superluminality}} \underbrace{\left(\mathrm{e}^{-\frac{\omega_\mathrm{p}}{2\mathrm{c}} \chi_\mathrm{ab}(\delta^{\min}, \delta_\mathrm{k}, \Omega_\mathrm{k})\mathrm{L}}\right)^M}_{\text{transmission}}. \tag{13}$$

For each set of control-field parameters δ_k and Ω_k, we adjust the probe-field detuning to maximize β: $\delta^{\min}$ is the probe detuning that minimizes the $n_g(\delta, \delta_k, \Omega_k)$ in the vicinity of the two-photon resonance. The transmission coefficient is evaluated as the probe amplitude at the end of the sample relative to its input value. The FOM is constructed as a product of two quantities: The left parenthesis evaluates how much the group index differs from the vacuum value and needs to be positive for superluminality, while negative values of β correspond to subluminal propagation. The higher the value of this parenthesis, the larger the group velocity of the pulse becomes. The right parenthesis describes transmission for the optimal detuning $\delta^{\min}$ of the probe field. The significance of transmission in the FOM is controlled by the parameter M. For $M = 0$ transmission is not taken into account and the FOM only considers the degree of superluminality. For $M = 1$, β has maximal values for transmissions below 40% while the value of $M = 4$ favours roughly 80% transmission, which better prevents pulse distortion.

We now construct FOM maps as functions of the control-field parameters (δ_k, Ω_k) in Fig. 4. The single-photon detuning δ_k is hundreds of times larger than the width of the middle level (γ_{aa}) to suppress the influence of the single-photon resonance. Figure 4a shows the control-field detuning and amplitude plane with solid contour lines for the constant group index and dashed for transmission. Figure 4b–d presents β for different values of M, with the colour scale indicating the FOM above or below half the maximal value shown in white. These plots guide the selection of control-field parameters for further investigation – the bluer the region, the better the conditions for the superluminal propagation. White lines mark the values of the group indices and transmission in the vicinity of the largest FOM values. For a higher value of M the FOM β is maximized at larger transmission coefficients. Smaller values of M prioritize the minimized group index in the first bracket in Eq. (13). Thus, we find a trade-off between transmission and superluminal propagation velocity.

Five pairs of parameters are selected for further analysis with the FOM evaluated for $M = 4$ (Fig. 5): **Point 1**, with the control-field Rabi frequency $\Omega_k = \gamma_{aa}$ and detuning $\delta_k = 300\gamma_{aa}$ lies in the blue region, where small absorption and a high negative group index are observed. The conditions are favorable for superluminal propagation. FOM = 248.

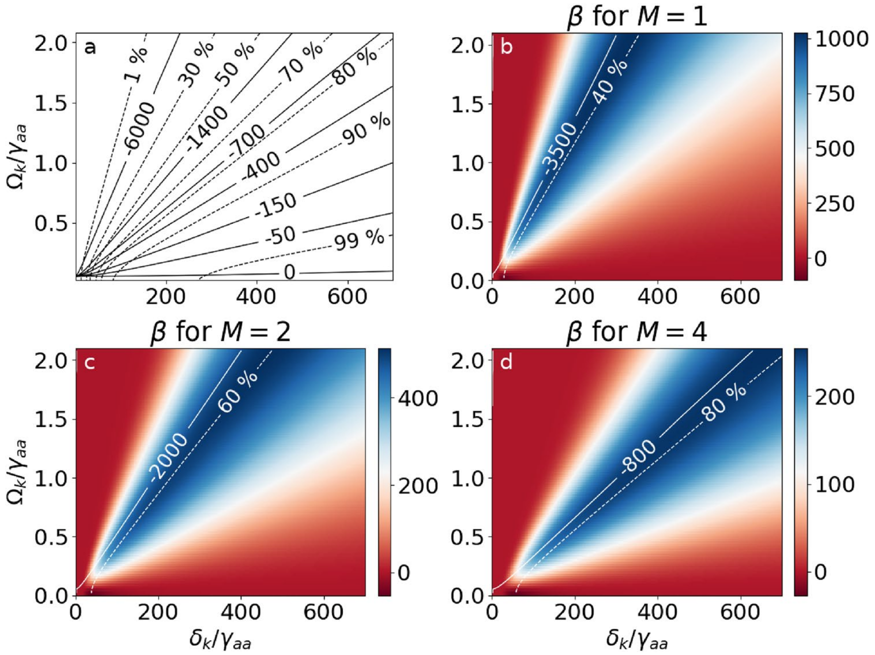

Figure 4. (**a**) Group index (solid lines) and transmission (dashed) as functions of the control-field Rabi frequency Ω_k and detuning δ_k. (**b**–**d**) $\beta(\delta_k, \Omega_k; M)$ for different values of M. Group index and transmission near the FOM maximum are marked with white lines.

Point 2 demonstrates that for a weaker control-field amplitude $\Omega_k = 0.5\gamma_{aa}$ a detuning $\delta_k = 150\gamma_{aa}$ can be chosen to achieve a similar FOM = 238 as for **Point 1**.

For **Point 3** keeping the same detuning as in **Point 1**, we significantly increase the value of the control field $\Omega_k = 1.5\gamma_{aa}$, which results in lower transmission but larger group index. FOM = 156.

For **Point 4** keeping the same amplitude of the control field as in **Point 1**, we significantly increase the detuning $\delta_k = 500\gamma_{aa}$. This leads to greater transmission, but the value of the group index is closer to 1. FOM = 168.

Point 5 belongs to the dark red region, where the parameter β is negative (FOM = -27) in contrast to the previously analysed cases. In this case, the two-photon transition is suppressed by the single-photon transition. For the control-field Rabi frequency $\Omega_k = 0.01\gamma_{aa}$ and $\delta_k = 50\gamma_{aa}$, the resulting group index is a small correction at the background given by the single-photon resonance and the superluminal propagation conditions are not achieved.

We additionally introduce the fractional advancement parameter (FA), which is a percentage value of the pulse advancement $t_{\text{adv}} = t_g - t_0$ with respect to the pulse temporal width. It can be calculated directly from the Eq. (9) as

$$FA = 100\% \frac{t_{\text{adv}}}{2t_{\text{HWHM}}} = 100\% \frac{L}{c} \frac{n_g - 1}{2t_{\text{HWHM}}}, \tag{14}$$

where t_{HWHM} is the temporal half-width-half-maximum of the pulse at the beginning of propagation.

For further calculations, we set the probe field $\Omega_p = 0.05\gamma_{aa}$. We can consider it as a relatively weak field that fulfils requirements for the previously derived equations. The time step is set to $\Delta t = 1.28 \cdot 10^{-4}\gamma_{aa}^{-1} = 3.34$ ps ($1.38 \cdot 10^5$ a.u.) and the spatial step $\Delta x = c\Delta t = 1.0$ mm ($1.89 \cdot 10^7$ a.u.). This gives 50 spatial points along the sample.

Broad and narrow pulse propagation analysis

We now investigate the propagation of the probe pulses under conditions defined by the five points above. Supplement Sec. S5.2 discusses monochromatic fields as a benchmark for other approaches. Such a wave has an infinitely narrow spectrum that provides the deepest dip in the group index curve, as demonstrated by the examples in Figs. 6 and 7 discussed below in detail. Here, we focus on Gaussian-shaped probe pulses as an important and experimentally feasible case. For a satisfactory resolution of numerical calculations described in Sec. 4.2 in the vicinity of the two-photon resonance we set $\Delta\omega_p = 0.01\gamma_{aa}$. Then, calculations for discretized detunings $\delta_p = -\delta_k + m \cdot \Delta\omega_p$ are performed for $m \in \{-30, -29, ..., 29, 30\}$, where $m = 0$ corresponds to the two-photon resonance condition ($\delta_p + \delta_k = 0$). The other methods (see Secs. 4.1 and 4.3) are less time-consuming, so we could perform calculations with higher spectral resolution.

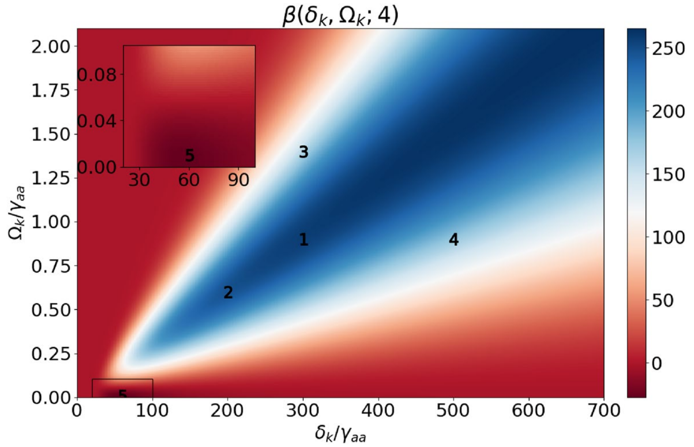

Figure 5. FOM β for $M = 4$ as a function of normalized detuning and Rabi frequency. Five points for further analysis are marked.

The control field modelled as a smoothed step pulse enters the sample first. After a stationary state is established, the probe pulse propagates in the opposite direction. The details of the control-field shape and parameters are discussed in Supplement Sec. S5.2. We performed calculations for Gaussian probe pulses with two different temporal lengths for all five (δ_k, Ω_k) pairs, corresponding to the Points in Fig. 5. Such pulses propagate through the medium, and at the end, we collect their temporal shapes. The resulting peak amplitudes and positions are used to evaluate group indices [Eq. (9)], which are directly comparable with the analogous results for monochromatic waves [Eq. (8)].

Long Gaussian pulse

We first discuss Gaussian pulses of spectral width narrow with respect to the spontaneous-emission rate, characterized by the temporal HWHM $= 50\tau_a = 1.3\,\mu$s ($5.4 \cdot 10^{10}$ a.u.). The left-hand side of Fig. 6 presents the pulses at the end of the sample obtained numerically (solid lines) and calculated by the Fourier approach (dashed lines). All the results are in very good agreement, as the requirements of negligible population transfer and control-field modulation are met. Since we present the shapes for different values of the detuning, we capture pulses on the side of the absorption line (e.g. the blue ones) which are subliminal, as well as the superluminal ones near the resonance (e.g. red ones). Black solid lines show reference pulses travelling through free space.

On the right-hand side, the corresponding group indices are presented as functions of detunings δ_p/γ_{aa}. Each point in black and along the red line corresponds to the group index of the Gaussian pulse with the carrier-frequency detuning δ_p and spectral width given above. On the contrary, each point along the blue curve, based on the analytical formula Eq. (8), describes a single-frequency component of the group index, which can be interpreted as the limiting case of pulses infinitely narrow spectrally. Results for the Gaussian pulses are slightly suppressed with respect to those of the monochromatic waves. The maximal values of *FA* obtained for resonant pulses are also marked on the right-hand side of Fig. 6.

For the most promising **Points 1** and **2**, the transmission on the two-photon resonance is around 80% as intended by setting the parameter $M = 4$, while the group index drops to $n_g^{\min} \approx -600$, which corresponds to the fractional advancement $FA \approx -3.8\%$. The similarity of these results can be explained by the fact that the absorption is tightly connected to the dispersion responsible for the group index. The two-photon resonance may be broadened due to the stronger control field; however, here this correction is marginal. For **Point 3**, as we go up in the FOM plot, the absorption is significantly greater, and the group index dip reaches $n_g^{\min} \approx -1200$ ($FA \approx -7.5\%$); hence we observe the mentioned trade-off. The opposite situation is presented for **Point 4**: as we go to the right from **Point 1** in the plot, the absorption and group index are suppressed, resulting in a minimal value of $n_g^{\min} \approx -200$ ($FA \approx -1.2\%$). The clearly subluminal propagation conditions provided by **Point 5**, intentionally chosen for demonstration purposes, lead to negligible absorption as the two-photon group index dip is a small correction on the left edge of a single-photon one. Additionally, we see discretization and discrepancy between numerical and analytical data. It indicates that our calculations at this point are at the numerical-accuracy limit: The arrival time difference as in Eq. (9) roughly corresponds to one time step Δt. All the calculations were performed for the same time and space steps $(\Delta t, \Delta z)$, and so the last results serve as a limit reference in this particular setup. Naturally, decreasing these steps would increase the calculation time as well as the accuracy of the results.

In all cases, the results confirm conditions for superluminal propagation in three-level ladder systems with Rb vapors, except for one intentionally poor choice of parameters (Point 5). The results show negative group velocities and approach the limiting values of the group index achievable for monochromatic waves. These findings make Rb vapors a promising candidate medium for achieving superluminal propagation in experiments.

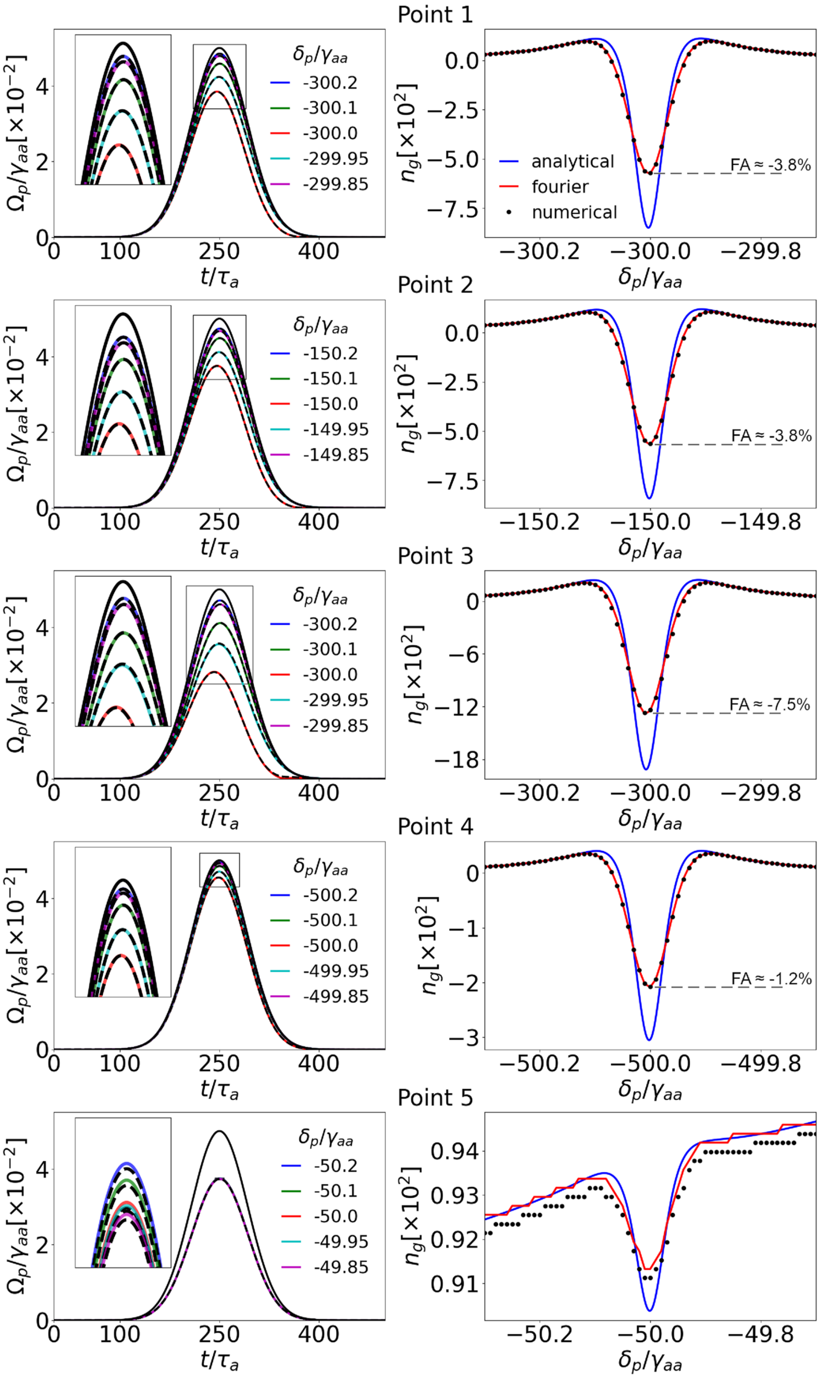

Figure 6. Transmitted-pulse temporal dependence (left column) and group-index spectral dependence versus the single-photon probe detuning (right column) at different two-photon resonance conditions for the long (spectrally narrow) pulse: **Point 1** $\Omega_k = \gamma_{aa}$, $\delta_k = 300\gamma_{aa}$; **Point 2** $\Omega_k = 0.5\gamma_{aa}$, $\delta_k = 150\gamma_{aa}$; **Point 3** $\Omega_k = 1.5\gamma_{aa}$, $\delta_k = 300\gamma_{aa}$; **Point 4** $\Omega_k = \gamma_{aa}$, $\delta_k = 500\gamma_{aa}$; **Point 5** $\Omega_k = 0.01\gamma_{aa}$, $\delta_k = 50\gamma_{aa}$. The colored solid lines shown in the left plots result from numerical calculations of pulses of different probe detunings δ_p near the two-photon transition. The dashed black lines are calculated with the Fourier approach for the same conditions. Solid black lines represent pulses travelling through free space of the same length and serve as reference. The right plots show resulting group indices for monochromatic waves (blue lines), Fourier (red lines), and numerical (dots) approaches. For the first four points, *FA* is also shown for the resonant pulse.

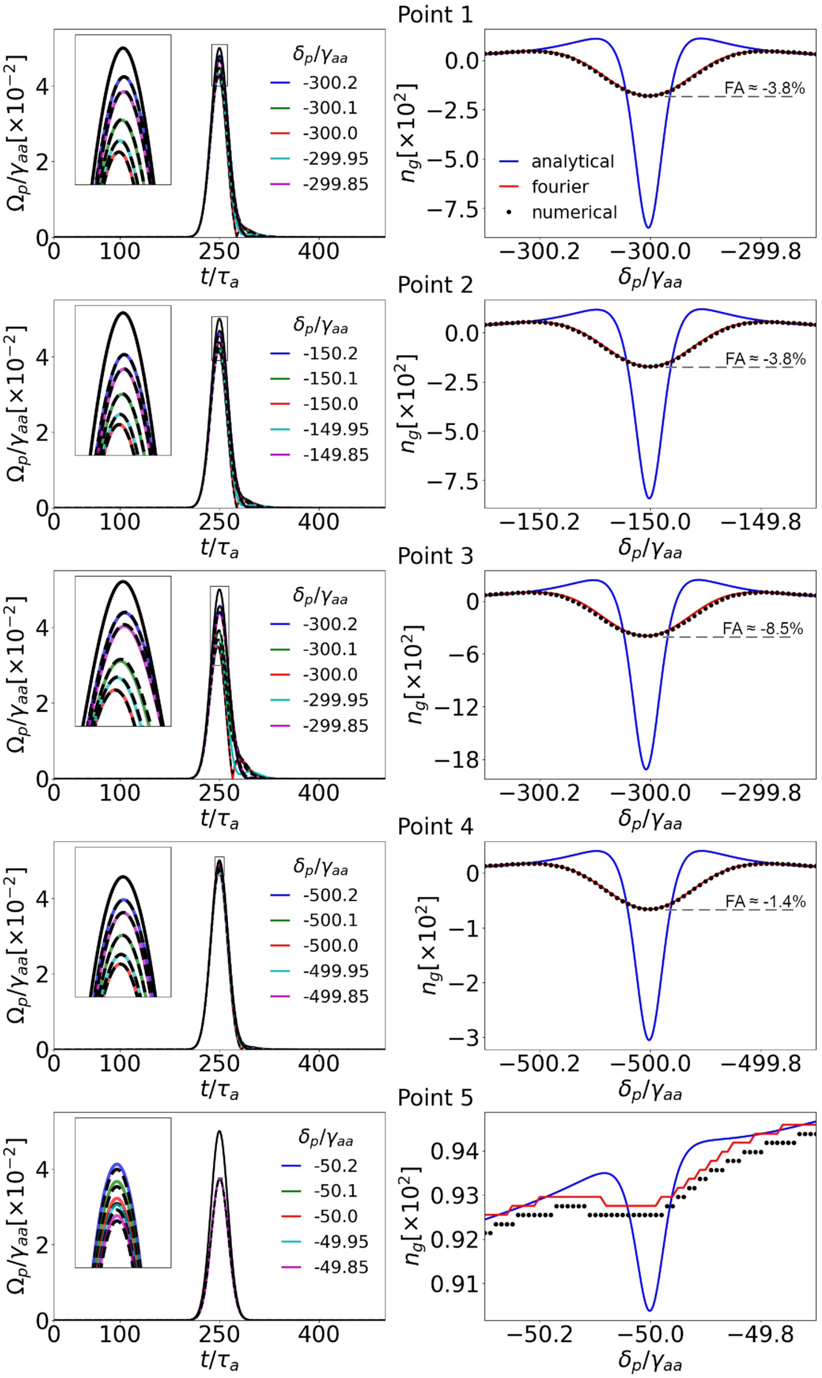

Figure 7. As Fig. 6 but for the short (spectrally broad) pulses.

Short Gaussian pulse

To understand the effect of the pulse spectral width, we examine Gaussian pulses with HWHM $= 15\tau_a = 0.39\,\mu$s ($1.6 \cdot 10^{10}$ a.u.), roughly three times shorter than the previous one. Consequently, different spectral components are subject to slightly different medium response.

All the calculations were performed similarly as in the previous subsection. Figure 7 shows the resulting shapes at the end of the sample (left column) and the group indices dependence on the probe carrier frequency (right column). The absorption is much weaker as the spectral width is larger, and hence smaller part of the pulse efficiently interacts with the medium. For the same reason, shape deformations may appear, as can be seen on the right side of the pulse in the two-photon resonance (red curves). This is a limitation for the group-index evaluation as the more deformed the final pulse is, the less meaningful the group velocity becomes[46]. The wide spectral shape affects the propagation velocity as well: The group-index curve is broadened and suppressed compared to the monochromatic case. Nevertheless, the Fourier-based and numerical calculations are still in perfect agreement as no underlying assumptions are violated. It is also worth noticing that for Point 3, we obtain $n_g^{\min} \approx -400$ which corresponds to $FA \approx -8.5\%$ at the transmission level well above 60%.

Superluminal discussion

The examples presented in this section provide clear evidence for the superluminal propagation of light near the two-photon resonance. Based on the above analysis, one can formulate several important conclusions.

First, the analysis of Gaussian-pulse propagation shows that the calculation of the group index, performed in analogy to the refractive index, is justified as long as the spectral profile of the pulse is considered. As expected, results for narrow-spectrum pulses match those for monochromatic light. A larger discrepancy between the numerical and analytical results for both the absorption coefficient and the group index is observed for spectrally wider pulses. This may originate from the fact that even though the central frequency of the beam is far detuned from the single-photon transition, the spectral tail of such a pulse may still induce the transition, resulting in non-negligible absorption. This violates the assumption of the analytical treatment and calls for a description beyond the analytical level from Sec. 4.1.

Second, the group refractive index and accordingly the pulse velocity can be controlled by changing the amplitude of the control field Ω_k or its detuning δ_k. By changing the control-field amplitude in exchange for a smaller transmission, we can significantly increase the group index and vice versa. Varying the control-field detuning allows one to switch between sub- and superluminal probe propagation.

Third, in the ladder scheme, the group index goes well below unity in the vicinity of the two-photon resonance. Simultaneously, different sets of parameters provide subluminal light propagation. Specifically, we can significantly reduce the pulse group velocity by simply detuning the probe field away from the two-photon resonance. The results are obtained in the case of probe light far detuned from the single-photon resonance, where the impact of the transition is small. Otherwise, for too small a separation between the dominant single-photon resonance and the two-photon resonance, the resulting group index is significantly increased. This can be seen in results for **Point 5**, with the group-index two-photon dip localized at the side slope of a single-photon one (Figs. 6 and 7).

Fourth, the results shown in Figs. 6 and 7 provide comparison between different approaches for Gaussian pulses. While pulse propagation can be simulated for different pulse shapes, group indices can be evaluated as long as there is a clearly distinguished point, which we can follow along the sample. For example, the rectangular shape is extremely difficult to investigate as the deformation on its edges would incorporate significant ambiguity in the position measurement. Hence, the propagation velocity would be indefinite.

Finally, with the medium in the ladder configuration, it is possible to use lower intensities of the probe field than in conventional two-level systems, where one operates in the linear absorption regime. This, given the concentration of the atoms in vapors and the sample size in a typical experiment (several centimetres), provides a promising scheme for experimental implementation. For this purpose, the introduced FOM map is a convenient tool for estimating propagation outcomes, especially for spectrally narrow pulses. As a quantity simple and fast to calculate, the FOM can be used to identify potentially interesting parameter regimes before performing time-consuming simulations.

Conclusions

The theoretical investigations presented in this work aimed at analysing superluminal light propagation in three-level systems under the two-photon absorption conditions. The analysis was performed with three different approaches, both analytical and numerical, concerning both the efficiency and correctness of the results. The results allowed us to formulate and verify the applicability conditions of the semi-analytical approach based on the spectral decomposition of the pulses. Based on these three approaches, the group index for different sets of the probe- and control-light parameters was calculated in a realistic scheme of rubidium vapor. To quantitatively compare the results for different control-field parameters, the figure-of-merit $\beta(\delta_k, \Omega_k; M)$ was introduced. It accounted for both the dispersion and absorption of the medium and allowed us to identify the conditions under which the optimal propagation was achieved.

The versatility of the numerical and the Fourier methods allows for future analysis of more complex scenarios. One can envision light propagation with a time-dependent control field, for which the properties of the medium change, e.g., switching between sub- and superluminal regimes for the probe pulses. Pulse reshaping effects could be discussed in the regimes in which the group velocity is no longer a valid quantity. Another interesting case is the nonlinear regime when the medium supports the refractive index dependence on the probe intensity in the Kerr effect, related to the formation of optical solitons, optical vortices or applications of optical switches and logic gates for all-optical computing.

Data availability

The data underlying the results presented in this paper are publicly available at https://doi.org/10.18150/Z5U8MG

Received: 19 October 2023; Accepted: 14 May 2024

References

1. Rayleigh, J. W. S. B. The collected optics papers of Lord Rayleigh (Optical Society of America, 1994).
2. Sommerfeld, A. & Brillouin, L. Wave propagation and group velocity (1960).
3. Born, M. & Wolf, E. Principles of optics, 7th (expanded) edition. *United Kingdom: Press Syndicate of the University of Cambridge* **461**, 401–424 (1999).
4. Wicht, A., Rinkleff, R.-H., Molella, L. S. & Danzmann, K. Comparative study of anomalous dispersive transparent media. *Physical Review A***66**, 063815 (2002).
5. Kasapi, A., Jain, M., Yin, G. & Harris, S. E. Electromagnetically induced transparency: propagation dynamics. *Phys. Rev. Lett.* **74**, 2447 (1995).
6. Alzetta, G. Induced transparency. *Phys. Today* **50**, 36–42 (1997).
7. Turukhin, A. *et al.* Observation of ultraslow and stored light pulses in a solid. *Phys. Rev. Lett.***88**, 023602 (2001).
8. Wang, L. J., Kuzmich, A. & Dogariu, A. Gain-assisted superluminal light propagation. *Nature* **406**, 277–279 (2000).
9. Stenner, M. D., Gauthier, D. J. & Neifeld, M. A. The speed of information in a 'fast-light'optical medium. *Nature* **425**, 695–698 (2003).
10. Dogariu, A., Kuzmich, A., Cao, H. & Wang, L. Superluminal light pulse propagation via rephasing in a transparent anomalously dispersive medium. *Opt. Express* **8**, 344–350 (2001).
11. Gehring, G. M., Schweinsberg, A., Barsi, C., Kostinski, N. & Boyd, R. W. Observation of backward pulse propagation through a medium with a negative group velocity. *Science* **312**, 895–897 (2006).
12. Manchaiah, D., Kumar, R., Ahmad, M. & Easwaran, R. K. Normal and anomalous dispersion study on probe light propagation in the presence of structured coupling light using electromagnetically induced transparency protocol. *JOSA B* **40**, 1904–1910 (2023).
13. Mikhailov, E. E., Sautenkov, V. A., Novikova, I. & Welch, G. R. Large negative and positive delay of optical pulses in coherently prepared dense rb vapor with buffer gas. *Phys. Rev. A***69**, 063808 (2004).
14. Han, D., Guo, H., Bai, Y. & Sun, H. Subluminal and superluminal propagation of light in an n-type medium. *Phys. Lett. A* **334**, 243–248 (2005).
15. Carreno, F., Calderón, O. G., Antón, M. & Gonzalo, I. Superluminal and slow light in λ-type three-level atoms via squeezed vacuum and spontaneously generated coherence. *Phys. Rev. A***71**, 063805 (2005).
16. Arif, S. M., Bacha, B. A., Wahid, U., Haneef, M. & Ullah, A. Tunable subluminal to superluminal propagation via spatio-temporal solitons by application of Laguerre fields intensities. *Phys. Lett. A***388**, 127041 (2021).
17. Tuan, A. N., Doan, T. T., Huy, B. N., Yen, N. L. T. & Minh, D. H. Knob of adjusting light group velocity in an inhomogeneously broadened degenerate two-level atomic medium by a magnetic field. *Laser Phys. Lett.***21**, 035208 (2024).
18. Hau, L. V., Harris, S. E., Dutton, Z. & Behroozi, C. H. Light speed reduction to 17 metres per second in an ultracold atomic gas. *Nature* **397**, 594–598 (1999).
19. Kash, M. M. *et al.* Ultraslow group velocity and enhanced nonlinear optical effects in a coherently driven hot atomic gas. *Phys. Rev. Lett.* **82**, 5229 (1999).
20. Basov, N., Ambartsumyan, R., Zuev, V., Kryukov, P. & Letokhov, V. Nonlinear amplification of light pulses. *Sov. Phys. JETP* **23**, 16–22 (1966).
21. Chu, S. & Wong, S. Linear pulse propagation in an absorbing medium. *Phys. Rev. Lett.* **48**, 738 (1982).
22. Brillouin, L. Wave propagation and group velocity, vol. 8 (Academic press, 2013).
23. Segard, B. & Macke, B. Observation of negative velocity pulse propagation. *Phys. Lett. A* **109**, 213–216 (1985).
24. Akulshin, A. M., Cimmino, A. & Opat, G. Negative group velocity of a light pulse in cesium vapour. *Quantum Electron.* **32**, 567 (2002).
25. Tanaka, H. *et al.* Propagation of optical pulses in a resonantly absorbing medium: Observation of negative velocity in rb vapor. *Phys. Rev. A***68**, 053801 (2003).
26. Landau, L. D. et al. Electrodynamics of continuous media, vol. 8 (Elsevier, 2013).
27. Keaveney, J., Hughes, I. G., Sargsyan, A., Sarkisyan, D. & Adams, C. Maximal refraction and superluminal propagation in a gaseous nanolayer. *Phys. Rev. Lett.***109**, 233001 (2012).
28. Jennewein, S., Sortais, Y. R., Greffet, J.-J. & Browaeys, A. Propagation of light through small clouds of cold interacting atoms. *Phys. Rev. A***94**, 053828 (2016).
29. Crisp, M. Concept of group velocity in resonant pulse propagation. *Phys. Rev. A* **4**, 2104 (1971).
30. Shin, H. *et al.* Reducing pulse distortion in fast-light pulse propagation through an erbium-doped fiber amplifier. *Opt. Lett.* **32**, 906–908 (2007).
31. Swaim, J. D. & Glasser, R. T. Faster light with competing absorption and gain. *Opt. Express* **26**, 10643–10648 (2018).
32. Artoni, M., La Rocca, G., Cataliotti, F. & Bassani, F. Highly anomalous group velocity of light in ultracold rubidium gases. *Phys. Rev. A***63**, 023805 (2001).
33. Bajcsy, M., Zibrov, A. S. & Lukin, M. D. Stationary pulses of light in an atomic medium. *Nature* **426**, 638–641 (2003).
34. Fleischhauer, M., Imamoglu, A. & Marangos, J. P. Electromagnetically induced transparency: Optics in coherent media. *Rev. Mod. Phys.* **77**, 633 (2005).
35. Yadav, K. & Wasan, A. Switching from sub-to superluminal light in a Y-type atomic system using wavelength mismatching. *Pramana* **93**, 1–6 (2019).
36. Agarwal, G. & Dey, T. N. Sub-and superluminal propagation of intense pulses in media with saturated and reverse absorption. *Phys. Rev. Lett.***92**, 203901 (2004).
37. Grochowska, P. & Zielińska-Raczyńska, S. Analysis of light propagation in an anomalously dispersive medium. *Physica Scripta***2014**, 014015 (2014).
38. Glasser, R. T., Vogl, U. & Lett, P. D. Stimulated generation of superluminal light pulses via four-wave mixing. *Phys. Rev. Lett.***108**, 173902 (2012).
39. Bharti, V. & Natarajan, V. Sub-and super-luminal light propagation using a Rydberg state. *Opt. Commun.* **392**, 180–184 (2017).
40. Cui, C.-L. *et al.* Resonant gain suppression and superluminal group velocity in a multilevel system. *Opt. Express* **20**, 10712–10720 (2012).
41. Szymanowski, C., Wicht, A. & Danzmann, K. On negative dispersion without absorption in bichromatically driven two-level systems. *J. Mod. Opt.* **44**, 1373–1392 (1997).
42. Khan, S., Bharti, V. & Natarajan, V. Role of dressed-state interference in electromagnetically induced transparency. *Phys. Lett. A* **380**, 4100–4104 (2016).
43. Brion, E., Pedersen, L. H. & Mølmer, K. Adiabatic elimination in a lambda system. *J. Phys. A: Math. Theor.* **40**, 1033 (2007).
44. Milonni, P. W. Fast light, slow light and left-handed light (CRC Press, 2004).
45. Gomez-Iglesias, A., O'Brien, D., O'Faolain, L., Miller, A. & Krauss, T. F. Direct measurement of the group index of photonic crystal waveguides via fourier transform spectral interferometry. *Appl. Phys. Lett.***90**, 261107 (2007).
46. Garrett, C. & McCumber, D. Propagation of a Gaussian light pulse through an anomalous dispersion medium. *Phys. Rev. A* **1**, 305 (1970).
47. Safronova, M. & Safronova, U. Critically evaluated theoretical energies, lifetimes, hyperfine constants, and multipole polarizabilities in rb 87. *Phys. Rev. A***83**, 052508 (2011).

48. Safronova, M., Williams, C. J. & Clark, C. W. Relativistic many-body calculations of electric-dipole matrix elements, lifetimes, and polarizabilities in rubidium. *Phys. Rev. A***69**, 022509 (2004).
49. Biraben, F., Cagnac, B. & Grynberg, G. Experimental evidence of two-photon transition without Doppler broadening. *Phys. Rev. Lett.* **32**, 643 (1974).

Author contributions

All authors equally contributed to the idea conception, theory development and results analysis. PG implemented the code and performed all simulations and calculations. All authors contributed to the preparation of the manuscript.

Funding

SP acknowledges the support of the Polish National Science Centre (NCN) within the SONATA BIS programme (grant number 2019/34/E/ST2/00440). PG is grateful for the support within the NCN PRELUDIUM programme (grant number 2021/41/N/ST2/02068). KS acknowledges the financing by the National Centre for Research and Development, Poland, project number QUANTERAII/1/21/E2TPA/2023 realized within the QuantERA ERA-NET Cofund in Quantum Technologies programme.

Competing interests

The authors declare no competing interests.

Additional information

Supplementary Information The online version contains supplementary material available at https://doi.org/10.1038/s41598-024-62220-x.

Correspondence and requests for materials should be addressed to P.G.

Reprints and permissions information is available at www.nature.com/reprints.

Supplement: Superluminal light propagation in a three-level ladder system

Piotr Gładysz[1,*], **Szymon Pustelny**[2], **and Karolina Słowik**[1]

[1]Institute of Physics, Faculty of Physics, Astronomy and Informatics, Nicolaus Copernicus University in Toruń, Grudziadzka 5, 87-100 Toruń, Poland
[2]Institute of Physics, Jagiellonian University, Łojasiewicza 11, 30-348 Kraków, Poland
[*]glad@doktorant.umk.pl

Here, we discuss in detail the following topics:
S1. Derivation of the Bloch-Maxwell equations.
We derive general equations for the evolution of the one-dimensional three-level media and for the propagation of the electric fields.
S2. Spontaneous emission and dephasing.
We evaluate the matrix forms of the operators corresponding to the spontaneous emission and dephasing processes in all three types of three-level systems considered in the main text.
S3. Numerical methods.
We discuss numerical methods used for simulations and briefly describe the parallelization of the calculations.
S4. Derivation of electric susceptibilities for three-level systems.
We provide a comparison of three-level configurations in terms of electric susceptibilities in each case.
S5. Validation of the approaches.
We present evidence that the approaches introduced in the main text are valid and give the same results under various conditions.

S1 Derivation of the Bloch-Maxwell equations

In our analysis, we focus on a 1D atomic medium, with atoms modelled as three-level systems. The medium is described with the formalism based on spatiotemporal density matrix $\rho(z,t)$, whose evolution is given by the Lindblad master equation that includes relaxation processes (spontaneous emission or dephasing)

$$\mathrm{i}\hbar\dot{\rho}(z,t) = [H(z,t),\rho(z,t)] + \mathscr{L}(\rho(z,t)), \tag{S1}$$

where $\hbar$ is the reduced Planck constant and $\mathscr{L}$ is the Lindblad operator. In the energy basis $\{|c\rangle, |a\rangle, |b\rangle\}$, the matrix representation of the Hamiltonian H is given by

$$H = \begin{bmatrix} \hbar\omega_c & -\vec{E}_k(z,t)\vec{d}_{ca} & 0 \\ -\vec{E}_k(z,t)\vec{d}_{ac} & \hbar\omega_a & -\vec{E}_p(z,t)\vec{d}_{ab} \\ 0 & -\vec{E}_p(z,t)\vec{d}_{ba} & \hbar\omega_b \end{bmatrix}. \tag{S2}$$

The above form of the Hamiltonian reveals that only electric-dipole interactions are considered in our treatment (the electric-dipole approximation). The electric-dipole moment elements $\vec{d}_{ij}$ are responsible for the transitions between the states $|i\rangle$ and $|j\rangle$, where $i, j \in \{a,b,c\}$ and $i \neq j$. In all cases, the transition between levels $|c\rangle$ and $|b\rangle$ is forbidden, $\vec{d}_{bc} = \vec{d}_{cb} = \vec{0}$. Additionally, for the V type medium, we set $\hbar\omega_a = 0$ while for the two other cases, $\hbar\omega_b = 0$ and the energies of the other levels are evaluated with respect to the corresponding ground state.

The general expression for the Lindblad operator is

$$\mathscr{L}(\rho) = 2\mathrm{i}\hbar\sum_{ij}\gamma'_{ij}\left[L_{ij}\rho L^{\dagger}_{ij} - \frac{1}{2}\left(L^{\dagger}_{ij}L_{ij}\rho + \rho L^{\dagger}_{ij}L_{ij}\right)\right], \tag{S3}$$

where $i, j \in \{a,b,c\}$ such that $\omega_j > \omega_i$ and $L_{ij} = |i\rangle\langle j|$ are flip operators, describing spontaneus emission, while γ'_{ij} are the corresponding relaxation rates. Dephasing can be included by setting $i = j$[1] (for more information see Sec. S2.4). For each type three-level system, there are only two non-zero rates describing spontaneous emission: γ'_{ab} and γ'_{ac}, γ'_{ba} and γ'_{ca}, γ'_{ba} and

γ'_{ac} for V, Λ, and Ξ, respectively. Since for all the cases the matrix forms of $\mathscr{L}(\rho)$ are significantly different, we derive their explicit forms in Sec. S2.

The levels $|a\rangle$ and $|b\rangle$ are coupled via the electric field of the probe light given by

$$\vec{E}_p(z,t) = \mathscr{E}_p(z,t)\vec{e}_p\cos(k_p z \pm \omega_p t). \tag{S4}$$

Similarly, the control field

$$\vec{E}_k(z,t) = \mathscr{E}_k(z,t)\vec{e}_k\cos(k_k z \pm \omega_k t) \tag{S5}$$

couples the $|a\rangle$ and $|c\rangle$ levels. Here $\mathscr{E}_p$ and $\mathscr{E}_k$ are the envelopes of the fields, $\vec{e}_p$ and $\vec{e}_k$ are the corresponding polarization vectors, ω_p and ω_k stand for the carrier frequencies, and k_p and k_k are the projections of the wavevectors onto the z-axis. Additionally, since we keep calculations general, we allow the fields to propagate in either of the two directions along the z-axis, which is represented by the ± signs in the argument of cosine functions.

To derive equations for each density matrix elements ρ_{ij}, we introduce the substitutions

$$\begin{aligned}
\rho_{aa}(z,t) &= \sigma_{aa}(z,t), && \text{(S6a)}\\
\rho_{bb}(z,t) &= \sigma_{bb}(z,t), && \text{(S6b)}\\
\rho_{ba}(z,t) &= \sigma_{ba}(z,t)\mathrm{e}^{\mp\alpha_p \mathrm{i}(k_p z \pm \omega_p t)}, && \text{(S6c)}\\
\rho_{ac}(z,t) &= \sigma_{ac}(z,t)\mathrm{e}^{\pm\alpha_k \mathrm{i}(k_k z \pm \omega_k t)}, && \text{(S6d)}\\
\rho_{bc}(z,t) &= \sigma_{bc}(z,t)\mathrm{e}^{\mp\alpha_p \mathrm{i}(k_p z \pm \omega_p t)}\mathrm{e}^{\pm\alpha_k \mathrm{i}(k_k z \pm \omega_k t)}, && \text{(S6e)}
\end{aligned}$$

where the lower or upper sets of signs should be used according to the propagation-direction choice from Eqs. (S4) and (S5). To distinguish different three-level systems, we introduced the parameters α_p and α_k that define signs for different cases:

- for V system: $\alpha_p = \alpha_k = +1$,
- for Λ system: $\alpha_p = \alpha_k = -1$,
- for Ξ system: $\alpha_p = -1,\ \alpha_k = +1$.

The substitution allows us to perform the rotating-wave approximation (RWA) and simplify the evolution [Eq. (S1)] by removing the rapidly oscillating terms. The resulting set of the Bloch equations is

$$\begin{aligned}
\dot{\sigma}_{aa} &= \mathrm{i}\Omega_p\sigma_{ba} - \mathrm{i}\Omega_p\sigma_{ab} - \mathrm{i}\Omega_k\sigma_{ac} + \mathrm{i}\Omega_k\sigma_{ca} + \mathscr{L}_{aa}, && \text{(S7a)}\\
\dot{\sigma}_{cc} &= \mathrm{i}\Omega_k\sigma_{ac} - \mathrm{i}\Omega_k\sigma_{ca} + \mathscr{L}_{cc}, && \text{(S7b)}\\
\dot{\sigma}_{ba} &= \alpha_p\mathrm{i}\delta_p\sigma_{ba} - \mathrm{i}\Omega_p(1-\sigma_{cc}-2\sigma_{aa}) - \mathrm{i}\Omega_k\sigma_{bc} + \mathscr{L}_{ba}, && \text{(S7c)}\\
\dot{\sigma}_{ac} &= -\alpha_k\mathrm{i}\delta_k\sigma_{ac} + \mathrm{i}\Omega_p\sigma_{bc} - \mathrm{i}\Omega_k(\sigma_{aa}-\sigma_{cc}) + \mathscr{L}_{ac}, && \text{(S7d)}\\
\dot{\sigma}_{bc} &= (\alpha_p\mathrm{i}\delta_p - \alpha_k\mathrm{i}\delta_k)\sigma_{bc} + \mathrm{i}\Omega_p\sigma_{ac} - \mathrm{i}\Omega_k\sigma_{ba} + \mathscr{L}_{bc}, && \text{(S7e)}
\end{aligned}$$

where we introduced the Rabi frequencies $\Omega_p = \mathscr{E}_p\vec{e}_p\cdot\vec{d}_{ba}/2\hbar$ and $\Omega_k = \mathscr{E}_k\vec{e}_k\cdot\vec{d}_{ac}/2\hbar$ of the probe and control fields, respectively. We also assumed real values of the electric dipole moments, $\vec{d}_{ij} = \vec{d}_{ji}$ and preservation of atomic population ($\sum_i \sigma_{ii} = 1$). The detunings from single-photon resonances are defined as $\delta_p = \omega_p - \omega_{ba}$ for the probe field and $\delta_k = \omega_k - \omega_{ac}$ for the control field.

The propagation of the fields along the medium can be fully described by the wave equation

$$\left(-\partial_z^2 + \frac{1}{c^2}\partial_t^2\right)\left[\vec{E}_p(z,t) + \vec{E}_k(z,t)\right] = -\mu_0\partial_t^2\vec{P}(z,t). \tag{S8}$$

Here, $\vec{P}$ stands for the polarization induced in the medium by the fields and μ_0 is the vacuum permeability. The relation between this macroscopic quantity and the quantum state of the medium is given by $\vec{P}(z,t) = N\,\mathrm{Tr}\left(\rho\vec{d}\right)$, where N is the concentration of atoms. We can now apply RWA and the slowly-varying-envelope approximation (SVEA) to Eq. (S8). The latter is used if one can assume that the field envelopes $\mathscr{E}_{p,k}$ change slowly in time (space) compared to the rapid oscillations at the carrier frequency. In such a case, time derivatives of σ_{ij} can be neglected, as $|\dot{\sigma}_{ij}| \ll |\omega\sigma_{ij}|$, and the wave equation can be separated into a set of first-order equations for the probe and control fields[2]

$$(\partial_t \pm c\partial_z)\,\Omega_p = \pm\alpha_p \mathrm{i}\frac{N\omega_p|d_{ba}|^2}{2\hbar\varepsilon_0}\sigma_{ba}, \tag{S9a}$$

$$(\partial_t \pm c\partial_z)\,\Omega_k = \pm\alpha_k \mathrm{i}\frac{N\omega_k|d_{ac}|^2}{2\hbar\varepsilon_0}\sigma_{ac}, \tag{S9b}$$

where ε_0 is the vacuum permittivity. As a result, probe- and control-field dynamics depend on the coherences in the medium originating from the interaction with the fields. Equations (S7) and (S9) are known in the literature as Bloch-Maxwell equations.

S2 Spontaneous emission and dephasing

In the considered case, the Bloch equations, given in Eqs. (S7), contain terms with $\mathscr{L}_{ij}$. The terms are derived from the master equation Eq. (S3) and are responsible for spontaneous emission. Here, we derive the exact forms of these terms for all the energy-level schemes considered in the manuscript.

S2.1 V-type

The spontaneous emission is described by the two flip operators $L_{ab} = |a\rangle\langle b|$ and $L_{ac} = |a\rangle\langle c|$ (the transition between the levels $|c\rangle$ and $|b\rangle$ is forbidden). Hence, the Lindblad operator takes the form[3]

$$\begin{aligned}\mathscr{L}^V(\rho) = 2\mathrm{i}\hbar\Bigg\{&\gamma'_{ab}\left[L_{ab}\rho L^\dagger_{ab} - \frac{1}{2}\left(L^\dagger_{ab}L_{ab}\rho + \rho L^\dagger_{ab}L_{ab}\right)\right] \\ &+\gamma'_{ac}\left[L_{ac}\rho L^\dagger_{ac} - \frac{1}{2}\left(L^\dagger_{ac}L_{ac}\rho + \rho L^\dagger_{ac}L_{ac}\right)\right]\Bigg\}.\end{aligned} \tag{S10}$$

The matrix form of the operator in the eigenbasis $\{|c\rangle, |a\rangle, |b\rangle\}$ is

$$\mathscr{L}^V \doteq \mathrm{i}\hbar\begin{bmatrix} -2\gamma'_{ac}\rho_{cc} & -\gamma'_{ac}\rho_{ca} & -(\gamma'_{ab}+\gamma'_{ac})\rho_{cb} \\ -\gamma'_{ac}\rho_{ac} & 2\gamma'_{ab}\rho_{bb}+2\gamma'_{ac}\rho_{cc} & -\gamma'_{ab}\rho_{ab} \\ -(\gamma'_{ab}+\gamma'_{ac})\rho_{bc} & -\gamma'_{ab}\rho_{ba} & -2\gamma'_{ab}\rho_{bb} \end{bmatrix}. \tag{S11}$$

Usually, this matrix is presented in a different form with use of the rewritten variables as below

$$\mathscr{L}^V \doteq \mathrm{i}\hbar\begin{bmatrix} -\gamma_{cc}\rho_{cc} & -\gamma_{ac}\rho_{ca} & -\gamma_{bc}\rho_{cb} \\ -\gamma_{ac}\rho_{ac} & \gamma_{bb}\rho_{bb}+\gamma_{cc}\rho_{cc} & -\gamma_{ab}\rho_{ab} \\ -\gamma_{bc}\rho_{bc} & -\gamma_{ab}\rho_{ba} & -\gamma_{bb}\rho_{bb} \end{bmatrix}, \tag{S12}$$

where $\gamma_{cc} = 2\gamma'_{ac}$, $\gamma_{bb} = 2\gamma'_{ab}$, $\gamma_{ab} = \gamma'_{ab} = \frac{1}{2}\gamma_{bb}$, $\gamma_{ac} = \gamma'_{ac} = \frac{1}{2}\gamma_{cc}$, and $\gamma_{bc} = \gamma'_{ab} + \gamma'_{ac} = \frac{1}{2}(\gamma_{bb}+\gamma_{cc})$. Here, γ_{ii} is the relaxation rate of the state $|i\rangle$, while γ_{ij}, $i \neq j$, are the terms responsible for the decay of coherences, i.e., the off-diagonal elements of the density matrix. If spontaneous emission is the only source of decoherence, we can express the decoherence rates by the spontaneous emission rates:

$$\mathscr{L}^V \doteq \mathrm{i}\hbar\begin{bmatrix} -\gamma_{cc}\rho_{cc} & -\frac{1}{2}\gamma_{cc}\rho_{ca} & -\frac{1}{2}(\gamma_{bb}+\gamma_{cc})\rho_{cb} \\ -\frac{1}{2}\gamma_{cc}\rho_{ac} & \gamma_{bb}\rho_{bb}+\gamma_{cc}\rho_{cc} & -\frac{1}{2}\gamma_{bb}\rho_{ab} \\ -\frac{1}{2}(\gamma_{bb}+\gamma_{cc})\rho_{bc} & -\frac{1}{2}\gamma_{bb}\rho_{ba} & -\gamma_{bb}\rho_{bb} \end{bmatrix}. \tag{S13}$$

S2.2 Λ-type

For the Λ energy configuration, the following flip operators are important for the spontaneous emission: $L_{ba} = |b\rangle\langle a|$ and $L_{ca} = |c\rangle\langle a|$. Thus, we have

$$\begin{aligned}\mathscr{L}^\Lambda(\rho) = 2\mathrm{i}\hbar\Bigg\{&\gamma'_{ab}\left[L_{ba}\rho L^\dagger_{ba} - \frac{1}{2}\left(L^\dagger_{ba}L_{ba}\rho + \rho L^\dagger_{ba}L_{ba}\right)\right] \\ &+\gamma'_{ac}\left[L_{ca}\rho L^\dagger_{ca} - \frac{1}{2}\left(L^\dagger_{ca}L_{ca}\rho + \rho L^\dagger_{ca}L_{ca}\right)\right]\Bigg\},\end{aligned} \tag{S14}$$

which in the matrix form is given by

$$\mathscr{L}^{\Lambda} \doteq \mathrm{i}\hbar \begin{bmatrix} 2\gamma'_{ac}\rho_{aa} & -(\gamma'_{ab}+\gamma'_{ac})\rho_{ca} & 0 \\ -(\gamma'_{ab}+\gamma'_{ac})\rho_{ac} & -2(\gamma'_{ab}+\gamma'_{ac})\rho_{aa} & -(\gamma'_{ab}+\gamma'_{ac})\rho_{ab} \\ 0 & -(\gamma'_{ab}+\gamma'_{ac})\rho_{ba} & 2\gamma'_{ab}\rho_{aa} \end{bmatrix}. \tag{S15}$$

Here, we can rewrite this matrix in analogy to the V scheme, but an additional assumption is needed. Usually, the lower levels are energetically close to each other in comparison with the upper level, and we assume $\gamma'_{ab} \approx \gamma'_{ac}$. Under these assumptions, we have new substitutions $\gamma_{aa} = 2(\gamma'_{ab}+\gamma'_{ac})$, $\gamma_{ab} = \gamma_{ac} = \gamma'_{ab}+\gamma'_{ac} = \frac{1}{2}\gamma_{aa}$, and $\gamma_{bc} = 0$. These lead to the final matrix form of the Λ-scheme Lindblad operator

$$\mathscr{L}^{\Lambda} \doteq \mathrm{i}\hbar \begin{bmatrix} \frac{1}{2}\gamma_{aa}\rho_{aa} & -\frac{1}{2}\gamma_{aa}\rho_{ca} & 0 \\ -\frac{1}{2}\gamma_{aa}\rho_{ac} & -\gamma_{aa}\rho_{aa} & -\frac{1}{2}\gamma_{aa}\rho_{ab} \\ 0 & -\frac{1}{2}\gamma_{aa}\rho_{ba} & \frac{1}{2}\gamma_{aa}\rho_{aa} \end{bmatrix}. \tag{S16}$$

S2.3 Ξ-type

As previously, only two flip operators ($L_{ba} = |b\rangle\langle a|$ and $L_{ac} = |a\rangle\langle c|$) describe the spontaneous emission in the Ξ system:

$$\begin{aligned} \mathscr{L}^{\Xi}(\rho) = 2\mathrm{i}\hbar\Big\{ & \gamma'_{ab}\left[L_{ba}\rho L^{\dagger}_{ba} - \frac{1}{2}\left(L^{\dagger}_{ba}L_{ba}\rho + \rho L^{\dagger}_{ba}L_{ba}\right)\right] \\ & \gamma'_{ac}\left[L_{ac}\rho L^{\dagger}_{ac} - \frac{1}{2}\left(L^{\dagger}_{ac}L_{ac}\rho + \rho L^{\dagger}_{ac}L_{ac}\right)\right]\Big\} \end{aligned} \tag{S17}$$

and the matrix form is

$$\mathscr{L}^{\Xi} \doteq \mathrm{i}\hbar \begin{bmatrix} -2\gamma'_{ac}\rho_{cc} & -(\gamma'_{ab}+\gamma'_{ac})\rho_{ca} & -\gamma'_{ac}\rho_{cb} \\ -(\gamma'_{ab}+\gamma'_{ac})\rho_{ac} & -2\gamma'_{ab}\rho_{aa}+2\gamma'_{ac}\rho_{cc} & -\gamma'_{ab}\rho_{ab} \\ -\gamma'_{ac}\rho_{bc} & -\gamma'_{ab}\rho_{ba} & 2\gamma'_{ab}\rho_{aa} \end{bmatrix}. \tag{S18}$$

By substituting $\gamma_{aa} = 2\gamma'_{ab}$, $\gamma_{cc} = 2\gamma'_{ac}$, $\gamma_{ab} = \gamma'_{ab} = \frac{1}{2}\gamma_{aa}$, $\gamma_{ac} = \gamma'_{ab}+\gamma'_{ac} = \frac{1}{2}(\gamma_{aa}+\gamma_{cc})$, and $\gamma_{bc} = \gamma'_{ac} = \frac{1}{2}\gamma_{cc}$, we obtain

$$\mathscr{L}^{\Xi} \doteq \mathrm{i}\hbar \begin{bmatrix} -\gamma_{cc}\rho_{cc} & -\frac{1}{2}(\gamma_{aa}+\gamma_{cc})\rho_{ca} & -\frac{1}{2}\gamma_{cc}\rho_{cb} \\ -\frac{1}{2}(\gamma_{aa}+\gamma_{cc})\rho_{ac} & -\gamma_{aa}\rho_{aa}+\gamma_{cc}\rho_{cc} & -\frac{1}{2}\gamma_{aa}\rho_{ab} \\ -\frac{1}{2}\gamma_{cc}\rho_{bc} & -\frac{1}{2}\gamma_{aa}\rho_{ba} & \gamma_{aa}\rho_{aa} \end{bmatrix}. \tag{S19}$$

S2.4 Extended description

To include the additional dephasing processes, we can modify the matrices (S13), (S16), and (S19) by adding the dephasing matrix

$$\mathscr{L}^{\mathrm{dep}} \doteq \mathrm{i}\hbar \begin{bmatrix} 0 & -\gamma^{\mathrm{dep}}_{ac}\rho_{ca} & -\gamma^{\mathrm{dep}}_{bc}\rho_{cb} \\ -\gamma^{\mathrm{dep}}_{ac}\rho_{ac} & 0 & -\gamma^{\mathrm{dep}}_{ab}\rho_{ab} \\ -\gamma^{\mathrm{dep}}_{bc}\rho_{bc} & -\gamma^{\mathrm{dep}}_{ab}\rho_{ba} & 0 \end{bmatrix}, \tag{S20}$$

where $\gamma^{\mathrm{dep}}_{ij}$ stands for the dephasing rates obtained from the master equation for the given dephasing operator, e.g., $L^{\mathrm{dep}} = \frac{1}{\sqrt{2}}\left(|i\rangle\langle i| - |j\rangle\langle j|\right)$ where i and j correspond to the involved states.

Despite the similar form of the Lindblad equations in different systems, the dynamics they represent turns out different. In the Λ-type model, spontaneous emission does not disrupt the coherences between the lower levels, and hence the coherent effects are the strongest. In the Ξ- and V-type systems, spontaneous emission influences the coherences, and hence the coherent effects are weaker. Based on Eqs. (S13, S16, and S19), in the V-type the suppression of coherence between the $|b\rangle$ and $|c\rangle$ states is the fastest among the three configurations due to the dependence on the spontaneous emission rates from both upper levels, while in the Ξ-type only the highest level contributes. These observations are reflected in the susceptibility profiles shown in the main text in Fig. 2 in Sec. 3.

S3 Numerical methods

For the propagation problem presented in the paper, we solve the Bloch-Maxwell equations [Eqs. (1) and (2) in the main text]. This can be done analytically for a few simple cases, but in general, the numerical approach is required. The calculations of the dynamics can be made in the discrete-time domain by solving the equations for the whole medium in successive time steps.

The equations describing the evolution of the medium [Eqs. (1)] are position-dependent. In the considered case, the medium consists of non-interacting three-level systems, and hence the dynamics of each of them can be calculated separately with the use of the Runge-Kutta fourth-order method[4]. This approach provides an accuracy proportional to the fourth order of the time step $(\Delta t)^4$.

For the calculations of the evolution of the probe and control pulses, we use the Lax-Wendroff method[5]. It is based on finite differences and has an accuracy proportional to the squared time step $(\Delta t)^2$. The general approach is based on solving the equation

$$\partial_t f(z,t) + A\partial_z f(z,t) = s(z,t), \tag{S21}$$

where A is a constant, f is a solution we are looking for, and s is a source term. For the solution, we introduce the discretization $t \to t_p = t_0 + p\Delta t$ for $p = 0,1,2,\ldots$ and $z \to z_q = z_0 + q\Delta z$ for $q = 0,1,2,\ldots,n$. Additionally, we choose $\Delta z = A\Delta t$. To simplify, we write $f(z,t) = f(t,z) \to f(t_p, z_q) \equiv f_{p,q}$. To calculate $f_{p+1,q}$ for all q, we use the formula[6]

$$f_{p+1,q} = f_{p,q} \pm \frac{1}{2}(f_{p,q+1} - f_{p,q-1}) + \frac{1}{2}(f_{p,q+1} - 2f_{p,q} + f_{p,q-1}) + \Delta t s_{p,q}, \tag{S22}$$

where the ± sign has to be set to minus for propagation along the z-axis and to plus otherwise. Since it is a first-order differential equation, we have to know the initial conditions $f_{0,q}$ for all q and the boundary conditions $f_{p,0}$, $f_{p,n}$ for all p.

Comparing Eq. (S21) with Eq. (2), we can adapt the described method to the considered case. Specifically, the function s can be identified as a solution of the Bloch equations, precisely the coherences σ_{ij} from Eq. (2) driving the probe and control field.

We also implemented multiprocessing in the code so that we can calculate real-life samples in minutes instead of hours or days. Instead of calculating everything in a loop, we divide the medium into smaller pieces and do the calculations separately, exchanging only the values from the overlapping points on the edges between them. To calculate a point $f_{p+1,q}$, according to Eq. (S22), we have to know three points ($f_{p,q-1}$, $f_{p,q}$, and $f_{p,q+1}$) from the previous time step (see Fig. S1).

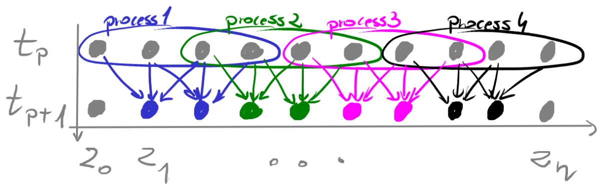

Figure S1. Representative ten space points and four processes (different colors). Each point in time step t_{p+1} requires three points from the previous step t_p (presented by arrows). Because of that, if we divide the medium into four parts, to perform proper calculations each part has to contain two more points from t_p than the resulting field has in t_{p+1}. The boundary conditions provide values for the edge points for all times t_p, so that the same number of points in space is used for each time step. This process repeats for all time steps used in the calculations.

S4 Derivation of electric susceptibilities for three-level systems

In the frequency domain, Eqs. (2) can be rewritten in terms of the electric susceptibility of the medium[2]. The probe-field susceptibility χ_p can be evaluated by a direct comparison of medium linear polarization components at the probe-field frequency $P(\delta) = \varepsilon_0 \chi(\delta)\mathscr{E}_p(\delta)$ and the microscopic description $P(\delta) = N\,\mathrm{Tr}[\sigma_{ab}(\delta)d_{ba}]$ for the Λ and Ξ systems and $P(\delta) = N\,\mathrm{Tr}[\sigma_{ba}(\delta)d_{ab}]$ for the V system. For convince, here the quantities are given using detuning $\delta = \omega - \omega_{ab}$ and ωs are spectral components of the pulse.[1] The vector notation is omitted since we assume that all vectors are co-linear. In our analysis, $\sigma_{ab(ba)}$ is assumed to give rise only to the relevant component of the polarization at the probe frequency, i.e., it does not couple other transitions.

The spectral components of the density-matrix elements $\sigma_{ij}(\delta)$ correspond to the stationary solutions obtained by replacing the derivatives in Eqs. (1) by zeros. The resulting expression for electric susceptibility for the probe field reads as

$$\chi_p(\delta, \delta_k, \Omega_p, \Omega_k) = \frac{N|d_{ab}|^2}{\hbar\varepsilon_0}\frac{\sigma_p^{\mathrm{stat}}(\delta, \delta_k, \Omega_k, \Omega_p)}{\Omega_p}, \tag{S23}$$

---

[1] The Fourier variable ω which we work with in the frequency domain may be confused with the carrier frequency of the probe pulse ω_p (similarly, the detuning δ can be confused with the detuning from the central frequency δ_p). This is only valid for monochromatic beams; when considering a pulse with many spectral components, ωs are distributed around the carrier frequency ω_p. We emphasize this difference with different symbols.

Table S1. Summary and comparison of different approaches used in this work.

Approach	analytical	numerical	Fourier-based
Calculation domain	frequency	time	frequency and time
Access to medium dynamics	no	$\sigma_{ij}(z,t)$	no
Access to field dynamics	$\Omega_p(z,t)$	$\Omega_p(z,t)$, $\Omega_k(z,t)$	$\Omega_p(z,t)$
Group index evaluation	spectral components $n_g(\delta)$ [Eq. (4)]	index per pulse $n_g(\delta_p)$ [Eq. (5)]	index per pulse $n_g(\delta_p)$ [Eq. (5)]
Accurate for spectrally broad pulses	no	yes	yes
Calculation speed	high	low	moderate

where σ_p^{stat} is the stationary value of the proper coherences ($p =$ "ba" for the V-type while $p =$ "ab" for the Λ- and Ξ-type systems). We solve Eqs. (1) for the coherences $\sigma_{ba}^{\text{stat}}$ (or $\sigma_{ab}^{\text{stat}}$) with the assumption that the interaction with the control field and operation under the steady state provide that prior to switching on the probe field whole population resides in the state $|b\rangle$ in the Λ and Ξ configurations (as for the V-system see the discussion below) and other levels are empty. Next, we expand the stationary expression in the Taylor series with respect to the values of Ω_p, which we truncate at the terms that are linearly proportional. The truncation is valid for the probe field of the Rabi frequency much smaller than the spontaneous-emission rates, $\Omega_p \ll \gamma$. We find that the electric susceptibility for all three energy configurations is

$$\chi_{ba}^{V}(\delta) = \mathrm{i}\frac{N|d_{ab}|^2}{\hbar\varepsilon_0}\frac{\left(\frac{\gamma_{cc}^2}{4}+\delta_k^2+\Omega_k^2\right)-\left(-\mathrm{i}\delta_k+\frac{\gamma_{cc}}{2}\right)\frac{\Omega_k^2}{-\mathrm{i}(\delta-\delta_k)+\frac{\gamma_{bb}+\gamma_{cc}}{2}}}{\left(\frac{\gamma_{cc}^2}{4}+\delta_k^2+2\Omega_k^2\right)\left[-\mathrm{i}\delta+\frac{\gamma_{bb}}{2}+\frac{\Omega_k^2}{-\mathrm{i}(\delta-\delta_k)+\frac{\gamma_{bb}+\gamma_{cc}}{2}}\right]} + \mathscr{O}[\Omega_p^2], \tag{S24a}$$

$$\chi_{ab}^{\Lambda}(\delta) = \frac{N|d_{ab}|^2}{\hbar\varepsilon_0}\frac{\mathrm{i}}{-\mathrm{i}\delta+\frac{\gamma_{aa}}{2}+\frac{\Omega_k^2}{-\mathrm{i}(\delta-\delta_k)}} + \mathscr{O}[\Omega_p^2], \tag{S24b}$$

$$\chi_{ab}^{\Xi}(\delta) = \frac{N|d_{ab}|^2}{\hbar\varepsilon_0}\frac{\mathrm{i}}{-\mathrm{i}\delta+\frac{\gamma_{aa}}{2}+\frac{\Omega_k^2}{-\mathrm{i}(\delta+\delta_k)+\frac{\gamma_{cc}}{2}}} + \mathscr{O}[\Omega_p^2]. \tag{S24c}$$

In the main text, we present graphically the above equations in Fig. 2. Used parameters represent typical orders of magnitude in atomic alkali vapors. The concentration is set to $N = 6.6\cdot10^9$ atoms/cm^3 (for the **Hartree atomic unit system**, $\hbar = a_0 = m_e = e = 1$ used in the numerical calculations, the concentration is 10^{-15} a.u.). The spontaneous emission rates (γ_{aa}, γ_{bb}, and γ_{cc}) are calculated for each configuration based on the arbitrarily selected values $\gamma'_{ba} = \gamma'_{ac} = \gamma' = 2\pi\cdot1.6$ MHz ($2.5\cdot10^{-10}$ a.u.), and $\gamma'_{bc} = 0$ used in Eq. (S3) (see Sec. S2 for interpretation). This gives $\gamma_{aa} = 4\gamma'$ for the Λ configuration, $\gamma_{bb} = \gamma_{cc} = 2\gamma'$ for the V configuration, and $\gamma_{aa} = \gamma_{cc} = 2\gamma'$ for the Ξ configuration. The control field is set to $\Omega_k = 55\gamma' = 2\pi\cdot90.1$ MHz ($1.38\cdot10^{-8}$ a.u.). The dipole moments are calculated from the Weisskopf-Wigner theorem[2]

$$|d_{ab}|^2 = \frac{3\pi\varepsilon_0\hbar c^3}{\omega_{ab}^3 n}\gamma_{ab}, \tag{S25}$$

where γ_{ab} is the optical-coherence (σ_{ab}) relaxation rate due to spontaneous emission, and n is the refractive index of the medium. Analogously, we can find the value of $|d_{ca}|^2$.

S5 Validation of approaches

Here, we provide the comparisons of the methods presented in Sec. 4 of the main text. A concise summary is presented in Table S1. We discuss the impact of the probe field on the electric susceptibility, the accuracy of the Fourier transformation method compared to the direct-propagation approach, and the validity of the monochromatic-wave approach. We use the parameters for rubidium atoms as presented in Sec. 5.1 of the main text.

S5.1 Electric susceptibility with probe field

In the main paper, we calculated signals using Eq. (3). In the equation, we neglect the higher-order corrections, e.g., the terms proportional to Ω_p^2, as they are small under our conditions. Here, instead of using the Taylor expansion and neglecting the higher-order terms, we assume large single-photon detuning δ_p so that the whole population remains in the ground state $|b\rangle$, $\sigma_{bb}^{\text{stat}} \approx 1$ (this is true in many physically relevant cases). In consequence, the populations of the upper states are negligible, $\sigma_{aa}^{\text{stat}} \approx \sigma_{cc}^{\text{stat}} \approx 0$, and no significant coherence can arise between the levels, $\sigma_{ac}^{\text{stat}} \approx 0$. Under such conditions, the electric susceptibility of the Ξ-type medium for the probe field is given by

$$\chi_{ab}(\delta_p) = \frac{N|d_{ab}|^2}{\hbar\varepsilon_0}\frac{\mathrm{i}}{-\mathrm{i}\delta_p + \frac{\gamma_{aa}}{2} + \dfrac{\Omega_k^2}{\underbrace{-\mathrm{i}(\delta_p+\delta_k)+\dfrac{\gamma_{cc}}{2}}_{\substack{\text{two-photon}\\ \text{resonance}\\ \text{term}}} + \underbrace{\dfrac{\Omega_p^2}{-\mathrm{i}\delta_k + \frac{\gamma_{aa}+\gamma_{cc}}{2}}}_{\substack{\text{probe-field}\\ \text{correction}}}}}. \tag{S26}$$

Contrary to Eq. (3), this expression includes the probe field Ω_p in all orders, taking into account nonlinear corrections to the medium response. Rewriting the denominator in Eq. (S26), we get

$$\begin{aligned} -\mathrm{i}(\delta_p+\delta_k)+\frac{\gamma_{cc}}{2}+\frac{\Omega_p^2}{-\mathrm{i}\delta_k+\frac{\gamma_{aa}+\gamma_{cc}}{2}} &= \\ -\mathrm{i}\left[\delta_p + \underbrace{\delta_k\left(1-\frac{\Omega_p^2}{\delta_k^2+\left(\frac{\gamma_{aa}+\gamma_{cc}}{2}\right)^2}\right)}_{\delta_k^{\text{eff}}}\right] &+ \underbrace{\frac{\gamma_{cc}}{2}+\frac{\frac{\gamma_{aa}+\gamma_{cc}}{2}\Omega_p^2}{\delta_k^2+\left(\frac{\gamma_{aa}+\gamma_{cc}}{2}\right)^2}}_{\gamma_{bc}^{\text{eff}}}, \end{aligned} \tag{S27}$$

where the probe field acts as a correction to the detuning δ_k and moves the two-photon resonance towards the single-photon resonance (an effective detuning δ_k^{eff}). Additionally, the resonance is broadened by the probe field (the effective rate γ_{bc}^{eff}). It should be noted, however, that, for the investigated case of $\delta_k \gg \frac{\gamma_{aa}+\gamma_{cc}}{2}$, the peak shift is the dominant effect.

S5.2 Comparison of results for monochromatic waves

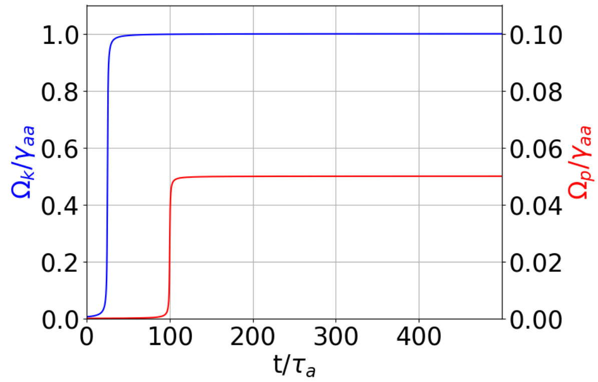

Figure S2. Probe- and control-field envelopes (respectively red and blue lines). Both shapes are presented right before entering the medium (probe for $z = 0$ and control for $z = L$). For the probe field $t_m = -100/\gamma_{aa}$ while for the control field $t_m = -25/\gamma_{aa}$. For both pulses $a = 2\gamma_{aa}$.

We check the simplest possible case of monochromatic wave propagation in order to compare all three approaches introduced in Sec. 4 of the main paper.

Let us first note that considering the propagation of monochromatic waves is numerically ambiguous as the field needs to have a beginning and end. One may think of the step function as an approximation of a real-life realization of such a problem, however, a fast switching of the field has numerical consequences and leads to unwanted oscillations known as the "switching-on effect". Instead, we use the *arctan* function, for which we can control the slope of a rising-field envelope. At the beginning of the medium ($z = 0$), the field can be described by

$$f(t) = \Omega \left[\frac{1}{\pi} \arctan(a(t+t_m)) + \frac{1}{2} \right], \tag{S28}$$

where Ω is the maximum amplitude of the field, a is the slope parameter given in units of [1/s], and t_m is the shift of the pulse in time. Additionally, as we are interested in the steady state, we switch on the control field first and wait until the dynamics of the medium stabilizes. Next, we turn on the probe field and again await the steady state. The envelopes of the representative control and probe fields are presented in Fig. S2. The control field propagates in the negative z-direction and the probe field propagates in the positive direction.

S5.2.1 Weak probe field

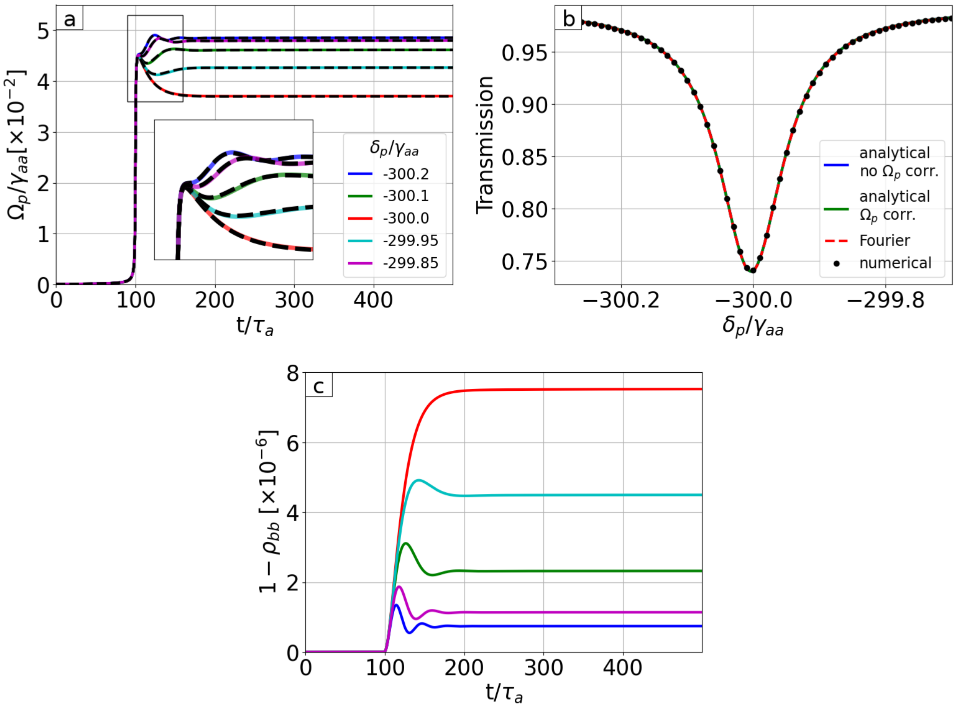

Figure S3. a) Shapes of the probe fields (solid colored lines) calculated numerically and obtained by the Fourier-based method (dashed black lines) at the end of the medium for different probe detunings. b) Absorption in spectral domain calculated based on: analytical [without (blue line) and with (green line) probe-field correction], Fourier (dashed red line), and numerical (black dots) approaches. c) Temporal change of population of the ground state $|b\rangle$.

For the consecutive calculations, we use parameters described in the main text as **Point 1**: control field $\Omega_k = \gamma_{aa}$, and detuning $\delta_k = 300\gamma_{aa}$. The probe field is also set to the same value $\Omega_p = 0.05\gamma_{aa}$. Once the steady state is reached, we measure the amplitude of the probe field at the end of the sample. All the calculations are done for a fixed detuning of the control field δ_k and for a range of detunings of the probe field δ_p around the two-photon resonance ($\delta_k + \delta_p = 0$). The resulting probe field envelopes at the end of the sample can be compared with those calculated with the Fourier-based method.

All the outcomes are presented in Fig. S3. First of all, in Fig. S3a we see pulse shapes for several detunings evaluated numerically (colored lines) and from the Fourier-based method (dashed lines). We can see a perfect agreement between these two methods. This suggests that the assumption $\sigma_{bb} \approx 1$ holds in that case. Indeed, Fig. S3c shows the transfer of population from state $|b\rangle$ for the point in the middle of the medium. The value is less than 0.001%.

In Fig. S3b we compare the transmission of the pulse obtained from the numerical calculations (black dots) with analytical results. We use the Lambert-Beer law

$$\Omega_p(L) = \Omega_p(0)\mathrm{e}^{-\frac{\omega_p}{2c}\,\mathrm{Im}(\chi_{ab})L}, \tag{S29}$$

where χ_{ab} is given by Eq. (S26). Since we intend to examine the importance of the probe-field correction, we plot transmission calculated with and without this correction (respectively, green "analytical Ω_p corr." and blue "analytical no Ω_p corr.". On top of that, we also plot the results from the Fourier-based method (dashed red). All the methods return indistinguishable results as all the curves are the same.

S5.2.2 Strong probe field

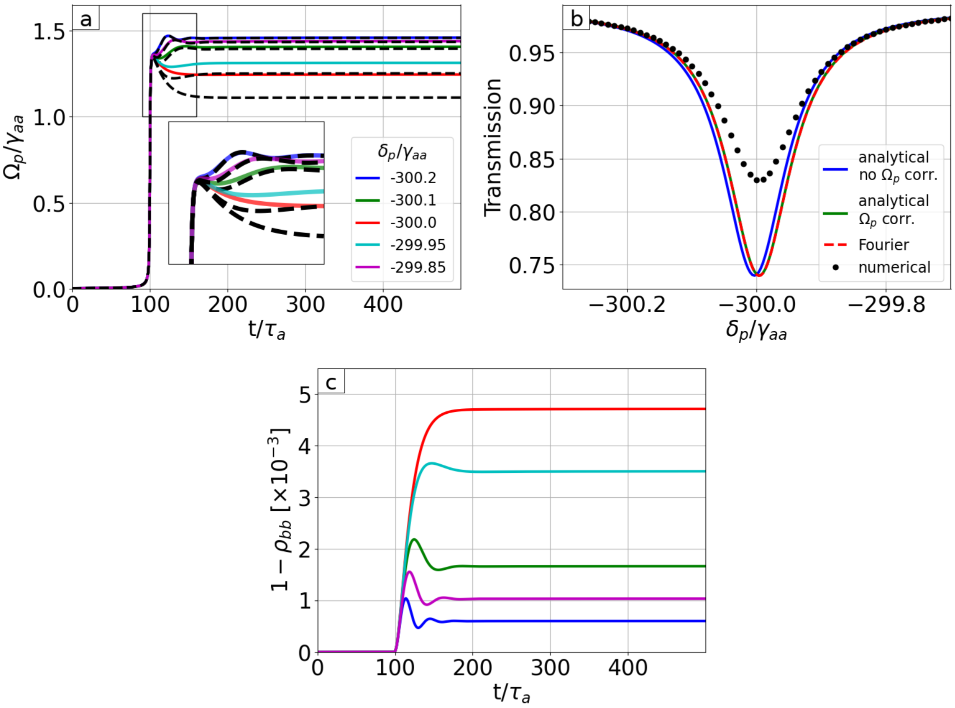

Figure S4. a) Pulse shapes at the end of the medium calculated numerically (solid lines) and determined using the Fourier approach (black dashed lines). The clear differences between the results of the two approaches indicate significant absorption of the control field along the process. b) Absorption in the spectral domain calculated using analytical [without (blue line) and with (green line) probe-field correction], Fourier (red line), and numerical (black dots) approaches. The resonance shift is evident and calculated correctly by incorporating the Ω_p-correction (the red plot is on top of the green one). c) Population of the ground state due to the action of the probe field, indicating the transfer of population to the excited state.

For a strong probe field, the nonlinear Ω_p-dependent correction in Eq. (S26) may modify the optical response of the medium. To investigate this, in the following, we discuss the test case of $\Omega_p = 1.5\gamma_{aa} > \Omega_k$ while all other parameters are the same as above. Note that the probe field is far-detuned with $\delta_p \approx -300\gamma_{aa}$.

As shown in Fig. S4a and S4b, for the strong probe field, the analytical and Fourier approaches are no longer valid near the resonance. This is due to the significant absorption of the control field, which modifies the properties of the medium. Near the resonance, the control field may be significantly absorbed, hence the medium response to the probe field is weaker. However, even for the case of the strong fields, the transfer of population to the excited states is negligible (less than 0.5%), as shown in Fig. S4c). From Fig. S4b, we can see that the probe-field correction is required at least for the proper description of the resonance position, as we can clearly see a resonance shift concerning the calculations neglecting the probe field.

We demonstrated that the assumption of the small probe field is valid unless the field intensity is not comparable to the control field. However, even in the opposite case, the assumption of negligible population transfer holds but the absorption of the control field starts to be important significantly changing the probe absorption.

References

1. Tempel, D. G. & Aspuru-Guzik, A. Relaxation and dephasing in open quantum systems time-dependent density functional theory: Properties of exact functionals from an exactly-solvable model system. *Chem. Phys.* **391**, 130–142 (2011).

2. Scully, M. & Zubairy, M. *Quantum Optics, Sixth Printing* (Cambridge University Press Cambridge, 2008).

3. Breuer, H.-P. & Petruccione, F. *The theory of open quantum systems* (Oxford University Press, 2007).

4. Runge, C. Über die numerische auflösung von differentialgleichungen. *Math. Annalen* **46**, 167–178 (1895).

5. Lax, P. Systems of conservation laws. Tech. Rep., Los Alamos National Lab (1959).

6. LeVeque, R. J. *Numerical methods for conservation laws*, vol. 214 (Springer, 1992).

5

SUMMARY

Throughout this thesis the interactions between light and matter are investigated, focusing on two-level systems with broken inversion symmetry and inversion-symmetric three-level systems. By developing a comprehensive theoretical framework, the dynamics of light-matter interactions are explored, particularly the generation of low-frequency radiation and phenomena like superluminal propagation in the media of such systems.

The work naturally divides into two parts. The first one focuses on the interaction of light with polar systems, offering analytical solutions for a new class of Hamiltonians. Previously, such solutions were limited to specific like the Jaynes–Cummings and Rabi ones. In this thesis, the focus is on the semi-classical description as most interesting phenomena occur under strong electromagnetic fields. It is shown how permanent dipole moments influence the optical properties of atomic systems, their coupling strengths with the field, relaxation constants and energy shifts. Additionally, the generation of radiation with an optically tunable Rabi frequency is characterized.

The second part extends the investigation to three-level systems, specifically focusing on the group velocity of the propagating pulses. The possibility of superluminal propagation in the ladder configuration has been confirmed. A new experimentally feasible scheme is proposed to achieve superluminal velocities in rubidium vapors.

Overall, this work enriches our understanding of light-matter interactions across different symmetries and provides a foundation for future research in quantum optics and related areas. The theory included in this thesis opens up a broad area for further investigation, with several ongoing projects aimed at deepening our understanding of the topic.

As an outlook, the nonlinear scaling of Rabi frequency suggests a method for enhancing coherence in molecular ensembles subject to fields strongly varying in space. In the regime of Rabi frequency being weakly dependent on the field amplitude, the coherence within the ensemble may remain stable against fluctuations both in laser intensity and the positioning of the quantum systems.

Furthermore, the developed theory of polar systems incorporates the impact of permanent dipole moments and strong fields into the detuning parameter, which may enable exceptionally accurate calculations of the resonance position in atomic systems. This advancement would pave the way for investigating weak processes occurring in narrow spectral windows, such as excitation via driving fields far-detuned to match multiphoton resonances.

Looking ahead, further generalizations of the proposed theory could encompass inversion breaking in many-level systems, alongside investigations of typical processes associated with three-level systems, such as EIT, STIRAP, and superluminal propagation. Additionally, exploring multiphoton transitions in the strong/ultrastrong coupling regime as well as nontrivial system-reservoir interactions present an exciting avenue for future research, building on the foundations established in this work.

BIBLIOGRAPHY

[1] G. F. Thomas, "Effects of permanent dipole moments on the collision-free interaction of a two-level system with a laser and a static electric field", *Physical Review A*, vol. 33, no. 2, p. 1033, 1986.

[2] M. A. Kmetic and W. J. Meath, "Perturbative corrections to the rotating-wave approximation for two-level molecules and the effects of permanent dipoles on single-photon and multiphoton spectra", *Physical Review A*, vol. 41, no. 3, p. 1556, 1990.

[3] A. Brown, W. J. Meath, and P. Tran, "Rotating-wave approximation for the interaction of a pulsed laser with a two-level system possessing permanent dipole moments", *Physical Review A*, vol. 63, no. 1, p. 013 403, 2000.

[4] O. Kibis, G. Y. Slepyan, S. Maksimenko, and A. Hoffmann, "Matter coupling to strong electromagnetic fields in two-level quantum systems with broken inversion symmetry", *Physical review letters*, vol. 102, no. 2, p. 023 601, 2009.

[5] I. Y. Chestnov, V. A. Shahnazaryan, A. P. Alodjants, and I. A. Shelykh, "Terahertz lasing in ensemble of asymmetric quantum dots", *Acs Photonics*, vol. 4, no. 11, pp. 2726–2737, 2017.

[6] S. A. Moses, J. P. Covey, M. T. Miecnikowski, D. S. Jin, and J. Ye, "New frontiers for quantum gases of polar molecules", *Nature Physics*, vol. 13, no. 1, pp. 13–20, 2017.

[7] F. Barachati, S. De Liberato, and S. Kéna-Cohen, "Generation of rabi-frequency radiation using exciton-polaritons", *Physical Review A*, vol. 92, no. 3, p. 033 828, 2015.

[8] G. Scala, K. Słowik, P. Facchi, S. Pascazio, and F. V. Pepe, "Beyond the rabi model: Light interactions with polar atomic systems in a cavity", *Physical Review A*, vol. 104, no. 1, p. 013 722, 2021.

[9] W. J. Meath and B. Jagatap, "On the effects of permanent molecular dipole moments in two-photon molecular excitations: An analytic generalized rotating wave approximation treatment including both the direct permanent dipole and the virtual state excitation mechanisms", *Journal of Physics B: Atomic, Molecular and Optical Physics*, vol. 44, no. 20, p. 205 401, 2011.

[10] ——, "On the effects of permanent molecular dipoles in the simultaneous absorption of two photons: Full generalized rotating wave approximation versus analytical results", *The Journal of Chemical Physics*, vol. 139, no. 14, 2013.

[11] W. J. Meath, "On the optimization, and the intensity dependence, of the excitation rate for the absorption of two-photons due to the direct permanent dipole moment excitation mechanism", *AIP Advances*, vol. 6, no. 7, 2016.

[12] M. Koppenhöfer and M. Marthaler, "Creation of a squeezed photon distribution using artificial atoms with broken inversion symmetry", *Physical Review A*, vol. 93, no. 2, p. 023 831, 2016.

[13] M. Antón, S. Maede-Razavi, F. Carreño, I. Thanopulos, and E. Paspalakis, "Optical and microwave control of resonance fluorescence and squeezing spectra in a polar molecule", *Physical Review A*, vol. 96, no. 6, p. 063 812, 2017.

[14] K. Gawarecki, P. Machnikowski, and T. Kuhn, "Electron states in a double quantum dot with broken axial symmetry", *Physical Review B*, vol. 90, no. 8, p. 085 437, 2014.

[15] N. V. Vitanov, A. A. Rangelov, B. W. Shore, and K. Bergmann, "Stimulated raman adiabatic passage in physics, chemistry, and beyond", *Reviews of Modern Physics*, vol. 89, no. 1, p. 015 006, 2017.

[16] L. Deng, Y. Niu, and S. Gong, "Detuning-induced stimulated raman adiabatic passage in two-level systems with permanent dipole moments", *Physical Review A*, vol. 98, no. 6, p. 063 830, 2018.

[17] B. Gadway and B. Yan, "Strongly interacting ultracold polar molecules", *Journal of Physics B: Atomic, Molecular and Optical Physics*, vol. 49, no. 15, p. 152 002, 2016.

[18] M. Macovei, M. Mishra, and C. H. Keitel, "Population inversion in two-level systems possessing permanent dipoles", *Physical Review A*, vol. 92, no. 1, p. 013 846, 2015.

[19] C. M. Dion, A. Keller, O. Atabek, and A. D. Bandrauk, "Laser-induced alignment dynamics of hcn: Roles of the permanent dipole moment and the polarizability", *Physical Review A*, vol. 59, no. 2, p. 1382, 1999.

[20] Y. Noguchi, Y. Miyazaki, Y. Tanaka, N. Sato, Y. Nakayama, T. D. Schmidt, W. Brütting, and H. Ishii, "Charge accumulation at organic semiconductor interfaces due to a permanent dipole moment and its orientational order in bilayer devices", *Journal of Applied Physics*, vol. 111, no. 11, 2012.

[21] M. Tanaka, M. Auffray, H. Nakanotani, and C. Adachi, "Spontaneous formation of metastable orientation with well-organized permanent dipole moment in organic glassy films", *Nature Materials*, vol. 21, no. 7, pp. 819–825, 2022.

[22] D. Braak, "Integrability of the Rabi model", *Physical Review Letters*, vol. 107, no. 10, p. 100 401, 2011.

[23] L. Brillouin, *Wave propagation and group velocity*. Academic press, 2013, vol. 8.

[24] J. W. S. B. Rayleigh, *The theory of sound*. Macmillan, 1896, vol. 2.

[25] M. Born and E. Wolf, "Principles of optics, 7th (expanded) edition", *United Kingdom: Press Syndicate of the University of Cambridge*, vol. 461, pp. 401–424, 1999.

[26] C. Garrett and D. McCumber, "Propagation of a gaussian light pulse through an anomalous dispersion medium", *Physical Review A*, vol. 1, no. 2, p. 305, 1970.

[27] A. Kasapi, M. Jain, G. Yin, and S. E. Harris, "Electromagnetically induced transparency: Propagation dynamics", *Physical review letters*, vol. 74, no. 13, p. 2447, 1995.

[28] S. E. Harris, "Electromagnetically induced transparency", *Physics today*, vol. 50, no. 7, pp. 36–42, 1997.

[29] J. P. Marangos, "Electromagnetically induced transparency", *Journal of modern optics*, vol. 45, no. 3, pp. 471–503, 1998.

[30] A. Turukhin, V. Sudarshanam, M. Shahriar, J. Musser, B. Ham, and P. Hemmer, "Observation of ultraslow and stored light pulses in a solid", *Physical Review Letters*, vol. 88, no. 2, p. 023 602, 2001.

[31] G. Juzeliūnas and P. Öhberg, "Slow light in degenerate fermi gases", *Physical review letters*, vol. 93, no. 3, p. 033 602, 2004.

[32] L. Wang, A. Kuzmich, and A. Dogariu, "Gain-assisted superluminal light propagation", *Nature*, vol. 406, no. 6793, pp. 277–279, 2000.

[33] M. D. Stenner, D. J. Gauthier, and M. A. Neifeld, "The speed of information in a 'fast-light'optical medium", *Nature*, vol. 425, no. 6959, pp. 695–698, 2003.

[34] B. Macke and B. Ségard, "Propagation of light-pulses at a negative group-velocity", *The European Physical Journal D-Atomic, Molecular, Optical and Plasma Physics*, vol. 23, pp. 125–141, 2003.

[35] G. M. Gehring, A. Schweinsberg, C. Barsi, N. Kostinski, and R. W. Boyd, "Observation of backward pulse propagation through a medium with a negative group velocity", *Science*, vol. 312, no. 5775, pp. 895–897, 2006.

[36] T. Stievater, X. Li, D. G. Steel, D. Gammon, D. Katzer, D. Park, C. Piermarocchi, and L. Sham, "Rabi oscillations of excitons in single quantum dots", *Physical Review Letters*, vol. 87, no. 13, p. 133 603, 2001.

[37] T. Faust, J. Rieger, M. J. Seitner, J. P. Kotthaus, and E. M. Weig, "Coherent control of a classical nanomechanical two-level system", *Nature Physics*, vol. 9, no. 8, pp. 485–488, 2013.

[38] J. Lisenfeld, G. J. Grabovskij, C. Müller, J. H. Cole, G. Weiss, and A. V. Ustinov, "Observation of directly interacting coherent two-level systems in an amorphous material", *Nature communications*, vol. 6, no. 1, p. 6182, 2015.

[39] G. Margiani, S. Guerrero, T. L. Heugel, C. Marty, R. Pachlatko, T. Gisler, G. D. Vukasin, H.-K. Kwon, J. M. Miller, N. E. Bousse, *et al.*, "Extracting the lifetime of a synthetic two-level system", *Applied Physics Letters*, vol. 121, no. 16, 2022.

[40] J. v. Neumann, "Wahrscheinlichkeitstheoretischer aufbau der quantenmechanik", *Nachrichten von der Gesellschaft der Wissenschaften zu Göttingen, Mathematisch-Physikalische Klasse*, vol. 1927, pp. 245–272, 1927.

[41] M. O. Scully and M. S. Zubairy, *Quantum Optics*. Cambridge University Press, 1997.

[42] M. Goeppert-Mayer, "Über elementarakte mit zwei quantensprüngen", *Annalen der Physik*, vol. 9, pp. 273–294, 1931, Dissertation, University of Göttingen.

[43] A. S. Davydov, *Quantum Mechanics, Part 1*, trans. by D. ter Haar. Pergamon Press, 1965, p. 299.

[44] D. J. Griffiths, *Introduction to Quantum Mechanics*, 3rd. Cambridge University Press, 2017.

[45] H.-P. Breuer and F. Petruccione, *The Theory of Open Quantum Systems*. Oxford University Press, 2002.

[46] G. Lindblad, "On the generators of quantum dynamical semigroups", *Communications in Mathematical Physics*, vol. 48, no. 2, pp. 119–130, 1976.

[47] B. Dalton, R. McDuff, and P. Knight, "Coherent population trapping", *Optica Acta: International Journal of Optics*, vol. 32, no. 1, pp. 61–70, 1985.

[48] M. A. Sillanpää, J. Li, K. Cicak, F. Altomare, J. I. Park, R. W. Simmonds, G. Paraoanu, and P. J. Hakonen, "Autler-townes effect in a superconducting three-level system", *Physical review letters*, vol. 103, no. 19, p. 193 601, 2009.

[49] I.-C. Hoi, A. F. Kockum, T. Palomaki, T. M. Stace, B. Fan, L. Tornberg, S. R. Sathyamoorthy, G. Johansson, P. Delsing, and C. Wilson, "Giant cross–kerr effect for propagating microwaves induced by an artificial atom", *Physical review letters*, vol. 111, no. 5, p. 053 601, 2013.

[50] Y.-x. Liu, H.-C. Sun, Z. Peng, A. Miranowicz, J. Tsai, and F. Nori, "Controllable microwave three-wave mixing via a single three-level superconducting quantum circuit", *Scientific Reports*, vol. 4, no. 1, p. 7289, 2014.

[51] H. Xu, X.-K. Song, D. Wang, and L. Ye, "Quantum sensing of control errors in three-level systems by coherent control techniques", *Science China Physics, Mechanics & Astronomy*, vol. 66, no. 4, p. 240 314, 2023.

[52] C. Bottcher and C. Feuillade, "Collisional relaxation times in a three-level maser", *Chemical Physics*, vol. 26, no. 2, pp. 319–326, 1977.

[53] M. Fleischhauer and A. S. Manka, "Propagation of laser pulses and coherent population transfer in dissipative three-level systems: An adiabatic dressed-state picture", *Physical Review A*, vol. 54, no. 1, p. 794, 1996.

[54] B. Sanchez and T. Brandes, "Matrix perturbation theory for driven three-level systems with damping", *Annalen der Physik*, vol. 516, no. 10, pp. 569–594, 2004.

[55] C. Liu, Z. Dutton, C. H. Behroozi, and L. V. Hau, "Observation of coherent optical information storage in an atomic medium using halted light pulses", *Nature*, vol. 409, no. 6819, pp. 490–493, 2001.

[56] P. Gładysz, *Low-frequency propagation*, GitHub repository, Accessed: 2024-09-27, 2020. [Online]. Available: `https://github.com/gladysz-piotr/Low-frequency_propagation.git`.